PHOTOELECTROCHEMICAL SYSTEMS FOR HYDROGEN PRODUCTION

by

Peter H. Aurora

A dissertation submitted in partial fulfillment
of the requirements for the degree of
Doctor of Philosophy
(Mechanical Engineering)
in The University of Michigan
2010

Doctoral Committee:

Professor Levi T. Thompson, Jr., Co-Chair
Professor Volker Sick, Co-Chair
Professor Rachel S. Goldman
Research Fellow John A. Turner, National Renewable Energy Laboratory

DEDICATION

To my loving parents and my sisters

ACKNOWLEDGMENTS

First want to express my extreme gratitude to professor levi thompson, for introducing me to the field of photocatalysis. His guidance provided me with many opportunities to develop myself both professionally and personally. The support and mentorship he has provided will not be forgotten. I would like to extend my sincere appreciation and thanks to professor Volker Sick for his guidance and advice during my doctoral degree process. I also want to thank the rest of my doctoral committee; professors Rachel Goldman and Dr. John Tuner. Their advice and constructive criticism of my work were extremely helpful.

My interactions both professionaly and socialy with current and former members of the Thompson Research Group were also crucial to my professional development. I am thankful to Dr. Chang Hwan Kim, Dr. Saemin Choi, Dr. Paul Rasmussen, Dr. Alice Sleightholme, Dr. Fan Shi, Dr. Valarie Thomas, Dr. Gallen Fisher, Dr. Easwar Ranganathan, Dr. Randolph mcgee, Dr. André Taylor, Dr. William Johnson, Dr. Maha Hammoud, Dr. Worajit (Sai) Setthapun, Leon Webster, Neil Schweitzer, Tafaya Ransom, William Northrop, Joshua Schaidle, Adam Lausche, Richard (Memie) Ezike, Kana Okada, Joshua Grilly, Aaron Shinkle, Priyanka Pande, Binay Prasad, Chandra Setu, Dr. Xaohui Chen and Gang Wang. In addition, I would like to thank the following undergraduate students: Patrice Langford, Abhinav Shrestha, Adrew Olive, Paul Rhee,

Yemina Leszczuk and Josue Lopez whom I had the pleasure to work with during my year of graduate school.

I would like to specifically acknowledge Saemin and Chang for providing motivation and friendship. Specifically, Chang served as a mentor during the early stages of my graduate studies, performed much of the high-resolution transmission electron microscopy analysis, and assisted with the synthesis of Au catalysts. Saemin was also very willing to provide assistance when called upon and introduced me to his unique problem solving approach rooted in his extensive knowledge base in industry. I would like to acknowledge Tim, Valarie, Maha, Josh S., and Randy for their insightful discussions and to Adam reading and editing this dissertation. I would like to extend thanks to barbara overholt as well, for her help in editing the grammar of my work. Finally, I would like to thank Paul for helping me with the fabrication of the photocatalyst and his dedication, which often spilled over into late nights and weekends.

I would like to acknowledge the following individuals outside of the research group: Brian Johnson for his help using the evaporator in the Burn's clean room, Dr. Erol Seeker for his aid preparing titania by sol-gel method, Eranda Nikolla, Saadet Albayrak, Sigrun Karlsdottir, Vladislava Tomeckova, Paul Arias, Alberto Lopez, Steven Bush, Jason Martz, and Dr. Susan Montgomery for their lasting friendship.

My deepest gratitude is to my loving parents for emphasizing even from my early years in education, the importance of dedication in learning. I would like to thank my sisters Marleni, Giovana and Liliana for supporting me always in my endeavors. Finally, I would like to give special thanks to Megan for all her support and love.

TABLE OF CONTENTS

LIST OF FIGURES

LIST OF TABLES

ABSTRACT

A major challenge to the use of photoelectrochemical (PEC) cells in the production of hydrogen from water and solar energy is the low photoanode efficiency. These low efficiencies are largely due to high semiconductor oxide bandgaps; losses associated with recombination of the charge carriers and low photocatalytic activities. The goal of this research is to advance the understanding and development of efficient and stable photoelectrochemical cells for renewable hydrogen production. To this end, three main strategies were investigated for improving the photoanode performance: producing the semiconducting oxide (i.e. titanium dioxide, TiO_2) in the form of long nanotube arrays, incorporating gold nanoparticles onto the surface, and combining this photocatalyst with a solar cell.

Highly ordered TiO_2 nanotube (TiNT) arrays were fabricated using an anodization process. By varying the anodization conditions, TiNTs with different dimensions were fabricated. Increasing the nanotube length resulted in increased photocurrents up to lengths that exceeded the diffusion length of electrons in TiO_2 (~20 μm). Gold nanoparticles with average diameter ranging from 3-12 nm were deposited onto selected TiNTs using a modified deposition precipitation method. The pH of the solution used during the Au loading is the crucial parameter determining the gold particle size and metal loading. Furthermore, small gold nanoparticles (less than 5 nm) significantly

improved the electrocatalytic properties of TiO_2 by adding active sites for water oxidation. Studies relating Au particle size and hydrogen rate per active Au species suggested that for Au particles bigger than 5 nm the most active sites might be located on the surface of the metal, and for Au particles smaller than 5 nm the most active sites seemed to be at the perimeter in contact with the oxide support.

Efficiencies for PEC cells were calculated and the Au/TiNT photoelectrodes shown efficiencies in excess of 1.2 %, which are one order of magnitude higher than the efficiencies reported for TiO_2 powder photoelectrodes. In addition, this efficiency is about 100% higher than the efficiencies reported in the literature for photoanodes made similar nanotube arrays.

The novel Au/TiNT photocatalyst was combined with Si solar cells in a hybrid arrangement. In this tandem cell the photocatalyst film and the solar cell were connected in series (adding the voltage produced by each component) and gave a conversion efficiency of 1.6 %.

CHAPTER 1
INTRODUCTION

1.1 MOTIVATION

Environmental challenges including global climate change and air pollution, as well as depletion of fossil fuels, encourage the development for new sources of energy with two desirable characteristics; first, they should be renewable, and second, they should not produce greenhouse gases or pollutants.

Hydrogen is considered to be an ideal energy carrier for the future. Traditionally, hydrogen has been produced by the steam reforming of fossil fuels, which produces hydrogen and carbon dioxide, CO_2, with the latter being released to the atmosphere [1]. Alternatively, hydrogen fuel can be produced using renewable resources. And if this H_2 is used in a fuel cell to produce electricity the final life cycle is environmentally friendly [1-3]. Solar and wind energies are the two major sources of renewable energy and they are also promising sources for clean hydrogen production. On Earth, hydrogen is not naturally present in molecular form (H_2), but is present and very abundant in many other forms including water, natural gas, petroleum and biomass.

Solar-hydrogen, or hydrogen generated from water using solar energy, is a renewable and environmentally safe energy carrier due to the following reasons [1]:

- Production of solar-hydrogen is relatively simple, so the cost of solar-hydrogen is expected to be acceptable for consumer applications.

- The only raw material used in the production of solar-hydrogen is water, which is a renewable resource.
- Large areas of the globe have ready access to solar energy, which is the only required energy source for solar-hydrogen generation.

Photoelectrochemical (PEC) water decomposition using solar energy is one of the most promising methods for the generation of hydrogen [1,3]. PEC cells are being developed for the efficient conversion of water into hydrogen using solar light as the energy source. A major challenge for the use of PEC is the low energy conversion efficiency (i.e. solar to hydrogen efficiency).

This dissertation evaluates the performance of photocatalysts and photoelectrochemical systems for stable and efficient hydrogen production. This chapter introduces the need for renewable H_2 production and discusses how photoelectrochemical hydrogen can meet that need. Information about materials for PEC cells and types of PEC cell is given. The research goals and organization of the dissertation are outlined as well.

1.2 SOLAR HYDROGEN TECHNOLOGIES

1.2.1 Hydrogen Generation and Use

Hydrogen is a key feedstock for the production of a large number of chemicals that have a direct socioeconomic impact. Most of the H_2 produced (in 2003 57% of the total H_2 production) was consumed by the chemical industry in the Haber-Bosch process for ammonia synthesis [4,5]. Ammonia is important for the production of agricultural

fertilizer, which is responsible for sustaining roughly 40% of the global population [4], and also for the production of ammunition. About 27% of all H_2 produced is used during the production of fuels such as gasoline and heating oils [5]. Other uses for H_2 include the hydrogenation of edible oils by the food industry, the production of electronics, refined metals, vitamins, cosmetics, and glass.

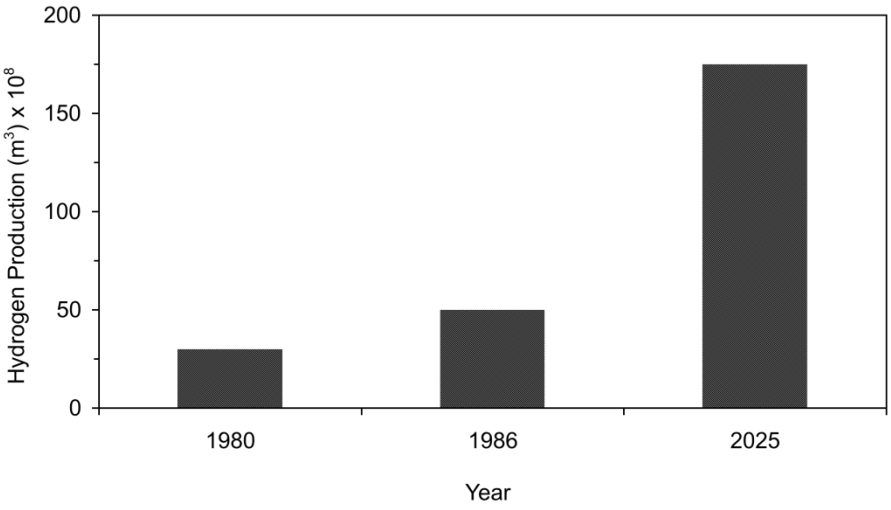

Figure 1.1: Past and future (predicted) global hydrogen production trends. The data was obtained from reference [6].

The worldwide hydrogen demand is expected to increase in the next several decades. As shown in Figure 1.1, it is predicted that there will be a greater than 300% increase in global H_2 production between 1986 and 2025. This increase is mainly driven by increased H_2 consumption by the chemical and petrochemical industries. It is expected that H_2 will satisfy approximately 10% of our energy needs by the year 2030 [7]. As it was mentioned above, in nature hydrogen does not exist in molecular form, therefore, to meet the existing demand, the H_2 must be produced

Table 1.1: Hydrogen production methods from fossil fuels. One kilogram of H_2 is roughly equivalent to one gallon of gasoline in terms of energy content [8 and references within].

Production Technique	Energy Efficiency (%)	Estimated H_2 Price	
		($/MMBtu)	($/kg)
Methane Steam Reforming[1]	83	5.54	0.75
Methane Partial Oxidation[2]	70-80	7.32-10.37	0.98-1.39
Methane Autothermal Reforming	71-74[3]	16.88[4]	1.93[4]
Coal Gasification[1]	63	6.83	0.92

[1]CO_2 sequestration not included in estimated H_2 price
[2]Current process for hydrocarbons (i.e., coke off-gas and residual oil)
[3]Higher end includes ion transport membrane technology
[4]Cost estimates for cyclic ATR process

Several methods for H_2 production, from both fossil fuels (i.e., natural gas, coal, and oil) and alternative fuel sources are given in Table 1.1 and Table 1.2, respectively [4-7]. The simplest method is by the electrolysis of water resulting in the direct formation of H_2 and O_2. However, the low efficiencies and high costs associated with electrolysis along with other alternative sources such as photovoltaics and biomass conversion currently makes the electrolysis method impractical for large-scale H_2 production.

Currently, hydrogen production from fossil fuels via catalytic reactions (i.e. reforming and gasification) is more efficient compared to alternative processes and accounts for 96% of all H_2 produced [9].

Technologies for the utilization of hydrogen are at a more advanced stage today than the technologies for the efficient production of hydrogen from renewable resources like solar energy, wind, tidal energy or geo-thermal energy. There is interest in the development of more efficient and inexpensive technologies for the production of

hydrogen from renewable resources. This will bridge the gap between the production and consumption.

Table 1.2: Hydrogen production methods from alternative energy sources and nuclear energy. One kilogram of H_2 is roughly equivalent to one gallon of gasoline in terms energy content [8 and reference within].

Production Technique	Energy Efficiency (%)	Estimated H_2 Price	
		($/MMBtu)	($/kg)
Direct Biomass Gasification[1]	40-56[2]	9.4-16.3	1.21-2.42
Biomass Pyrolysis	56[1,3]	9.4-16.3	1.26-2.19
Electrolysis	25[4]	19-22[5]	2.56-2.97[5]
Electrolysis (coupled with nuclear heat)	45-55[4]	14.5	--
Electrolysis (coupled with concentrated solar power)	--	26-42	--
Electrolysis (coupled with wind power)	--	21	--
Thermonuclear Sodium Iodine Cycles (at 850 °C)	42	14.9	2.01
Thermonuclear Sodium Iodine Cycles (at 950 °C)	52	13.9	1.87
Biosynthetic/ Photo-biological	24	41.04	5.52
Photocatalytic Water Splitting	10-14	37.0	4.98

[1]Not proven on a large-scale process.
[2]Higher end for fast internal circulation fluidized bed process
[3]Estimated for steam reforming of bio-oil after pyrolysis
[4]Includes efficiency of electricity
[5]Based on electricity price of 4 cents/kWh

1.2.2 Methods of Hydrogen Production from Water Using Solar Energy

Hydrogen can be produced from water and solar energy in several ways. Some methods are briefly described below [10 and references within].

1.2.2.1 Solar Electrolysis

Electricity generated by a photovoltaic array is passed through an electrolyzer to

produce of H_2 and O_2. Water decomposition by electrolysis consists of two partial reactions that take place at the two electrodes. The electrodes in the electrolyzer are separated by an ion-conducting electrolyte, and H_2 and O_2 are produced at the cathode and the anode respectively. Normal operating conditions for commercial electrolyzer are ~ 1 A/cm^2, which corresponds to voltages higher than 2 V with an energy efficiency of 50 %. Coupling this efficiency to commercial photovoltaic array with 14% (Si solar panels) yields a solar-to-hydrogen efficiency of 7%. To increase the energy efficiency of this system will require a better catalyst or decrease the current densities.

1.2.2.2 Direct thermal decomposition of water

In this method water is heated to a high temperature (above 2200 °C), some of the water vapor dissociates into hydrogen and oxygen. It may be possible to utilize this reaction for the production of hydrogen by separating the product gases generated. Theoretically, at low pressures and high temperatures, thermal decomposition can reach efficiencies as high as 80%. However, such extreme temperatures and pressures are not practically feasible. Kogan *et al.* [11] have estimated a theoretical efficiency of 40% for more practical conditions (2 mbar and 2200 °C).

1.2.2.3 Thermochemical hydrogen production

Water is decomposed into H_2 and O_2 through combinations of chemical reactions that are carried out at high temperatures. Water and heat (from sunlight) are the inputs to the system, and only the elemental constituents (H_2 and O_2) and waste heat are generated. In order to obtain high conversion efficiencies high temperature need (T >800°C) to be used, which is the main disadvantages of this process. The maximum

temperature requirements for most thermochemical cycles lie within a temperature range of 650 to 1100°C. Efficiencies between 30 and 50% have been reported [11]. Between 2000-3000 different theoretical cycles have been proposed and evaluated [10]. They can all be subdivided into four basic steps: water splitting reaction, hydrogen production, oxygen production, and material regeneration. Amongst all the possible thermochemical cycles the Mark 1, Mark 15, ZnO/Zn, UT-3, Fe_3O_4/FeO and Iodine-Sulfur processes are the only few, which have been studied extensively [10].

1.2.2.4 Photochemical hydrogen production

Similar to a thermochemical system this process also employs a system of chemical reactions that split water, however, the driving force is not thermal energy but light. In this sense, this system is similar to the photosynthetic system present in green plants. One of the main difficulties in this method is that hydrogen requires two electrons and oxygen produces four electrons to carry out the redox process. The highest efficiency reported was ~7 % [12].

1.2.2.5 Photoelectrochemical hydrogen production

Light incident on a semiconductor electrode generates electron-hole pairs. The holes carry out the oxidation of H_2O to O_2 and H^+ ions, while the electrons reduce the H^+ ions to H_2 in gaseous form. Depending on the type of semiconductor material, the operating current density for a PEC cell is 2 –20 mA/cm^2 [15]. At these current densities, the voltage required for electrolysis is much lower than in a commercial electrolyzer, and therefore, the corresponding electrolysis efficiency is much higher. The highest efficiency reported to date, ~ 18 % was obtained with a very high efficiency solar cell and a very

active catalyst for water splitting [14].

1.2.2.6 Biological and biochemical hydrogen production

This method uses the ability of microorganisms to produce hydrogen via consumption of carbon dioxide. This method has the advantage of producing hydrogen at lower temperatures (~ room temperatures). One of the fundamental ways to produce H_2 is the biophotolysis, which is a process that uses micro-algae-cynobacteria and green algae to produce H_2 in the presence of sunlight and water. The microalgae use two classes of enzymes to produce hydrogen: hydrogenase and nitrogenase. Nitrogenase enzyme works in the absence of nitrogen gas to reduce protons to molecular hydrogen. Efficiencies between 4 and 8% have been reported [10].

1.3 PHOTOELECTROCHEMICAL (PEC) CELLS

Photoelectrochemical cells combine photovoltaics and electrolysis into one step to dissociate water. One of the major advantages, of a direct conversion PEC system over a photovoltaic array combined with an electrolyzer, is that the area available for electrolysis approximates that of the solar cell. In addition, the high operating current densities and voltages of commercial electrolyzers limit the efficiency of hydrogen production by a PV-electrolysis system [14,15]. A PEC system not only eliminates most of the costs of the electrolyzer, but also it has the possibility of increasing the overall efficiency (lower operating conditions) of the process leading to a further decrease in costs [15].

A PEC cell consists of a semiconductor electrode called photoelectrode (PE) and a metal counter electrode immersed in an aqueous electrolyte. When semiconductor

electrode absorbs light it generates electricity. This electricity is then used for water electrolysis. Figure 1.2 shows the schematic representation of a PEC cell developed by Fujishima and Honda [13].

The following processes take place in the cell when an n-type photoelectrode is illuminated (the process is analogous for p-type photoelectrodes):

1. *Photogeneration of charge carriers* (electron and hole pairs): Illumination results in the intrinsic ionization of n-type semiconducting materials over the bandgap leading to the formation of electrons (e^-) in the conduction band and holes (h^+) in the valence band. The bandgap, E_g, is the smallest difference between the top of the valence band and the bottom of the conduction band.

$$2h\nu \rightarrow 2e^- + 2h^+ \tag{1.1}$$

The generation of electrons and holes may take place when the energy of the photons is equal to or greater than the semiconductor E_g. An electric field at the electrode/electrolyte interface is required to avoid recombination of these charge carriers. This may be achieved through modification of the potential at that interface [2].

2. *Charge separation and migration* of the holes (photoanode, PA) to the interface between the semiconductor and the electrolyte, and *transport* of the electrons to the bulk of the semiconductor.

3. O*xidation of water* to O_2 gas and H^+ by the holes at the photoanode:

$$2h^+ + H_2O_{(liquid)} \rightarrow \frac{1}{2}O_{2(gas)} + 2H^+ \tag{1.2}$$

This process takes place at the photoanode/electrolyte interface.

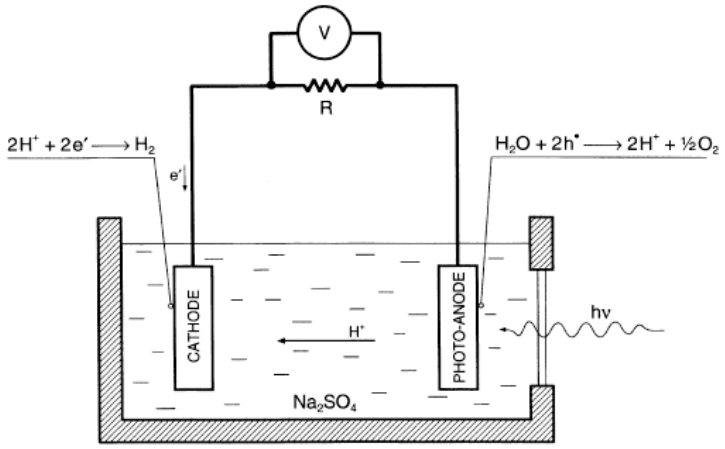

Figure 1.2: Schematic of a photoelectrochemical cell structure for water photoelectrolysis [13]. The photoanode is made of a semiconducting material and the cathode is a metal (i.e platinum).

4. Transport of the H^+ ions from the photoanode to the cathode through the electrolyte and the transport of electrons from the photoanode to the cathode through external circuit.

5. Reduction of H^+ ions to H_2 by electrons at the cathode:

$$2H^+ + 2e^- \rightarrow H_{2(gas)} \tag{1.3}$$

Then the overall reaction of a PEC cell may be expressed in the form:

$$2h\nu + H_2O_{(liquid)} \rightarrow \tfrac{1}{2}O_{2(gas)} + H_{2(gas)} \tag{1.4}$$

The energy for reaction (4) is given by E^o:

$$E^o = \frac{\Delta G^o_{(H_2O)}}{2N_A} = h\nu = 1.23 \text{ eV} \tag{1.5}$$

In the theoretical limit, electrochemical decomposition of water takes place when the voltage of the cell is equal or grater than 1.23 eV. Figure 1.3, PEC cell circuit, shows the charge transfer within the cell, where E_{CB} is the conduction band (CB) energy, E_{VB} valence band (VB) energy, E_g bandgap energy, and E_F Fermi energy.

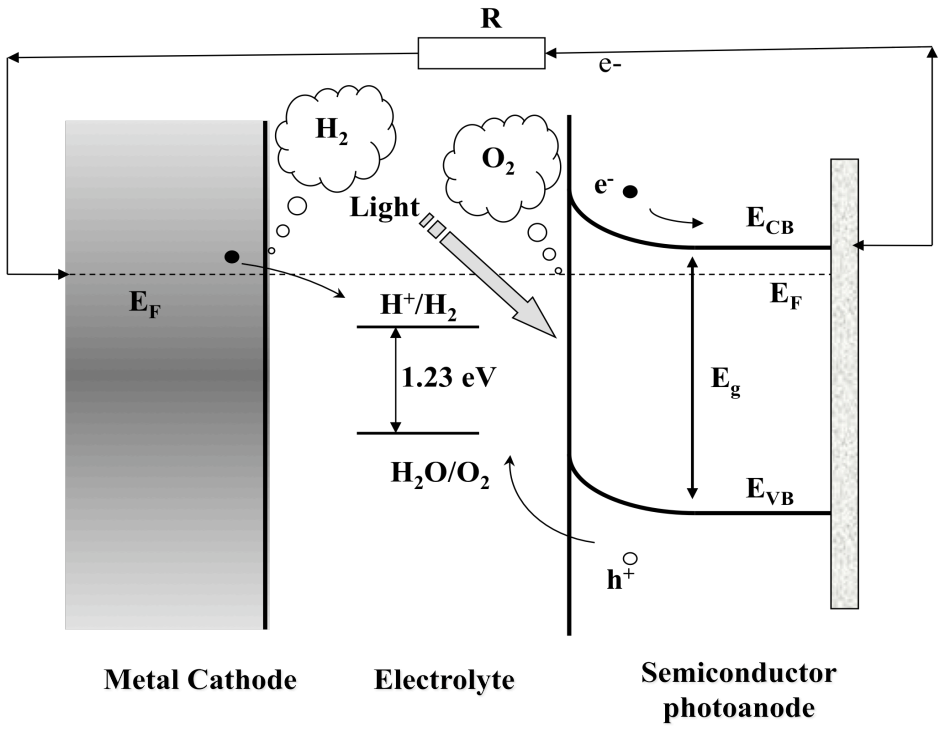

Figure 1.3: Electrical circuit illustrating charge transfer within a photoelectrochemical cell formed with a semiconducting photoanode and metallic cathode in aqueous electrolyte [1,3,14,21].

1.3.1 Photoelectrochemical Cell Band Model Representation

The band structures of both electrodes (the photoanode of an n-type semiconductor and metallic cathode) at different stages in the formation of the electrochemical chain of the PEC are shown schematically in Figure 1.7. These figures show the band structure, illustrating various energy quantities, including: work function

(*Φ*, minimum energy needed to remove an electron from a solid to a point immediately outside the solid surface); band levels of the electrodes (conduction and valence band) before and after the contact is established (compared to the water redox potentials H^+/H_2 and O_2/H_2O redox couples); band bending (local change in electron energy at interface due to space charge effects); and Fermi level (E_F, top of the available electron energy levels at low temperatures, also called chemical potential).

Figure 1.4 shows the energy diagram before contact between the electrolyte and the electrodes, is made. There is a formation of a double layer at the interface between the electrode and the electrolyte.

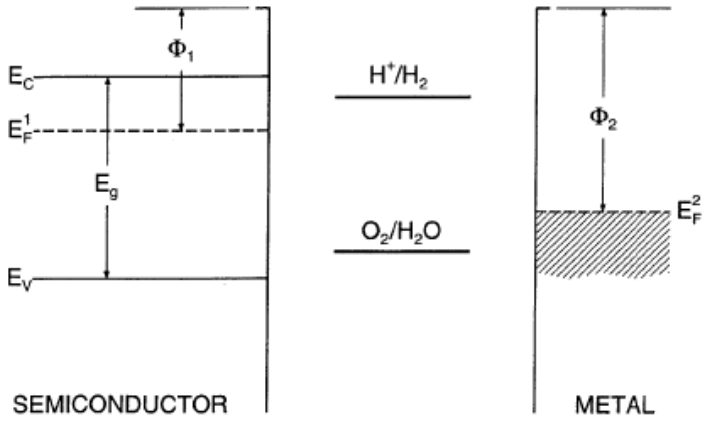

Figure 1.4: Band energy diagrams of PEC components at different stages during the photoelectrochemical process. PEC cell components, anode (semiconductor) cathode (metal) and electrolyte before galvanic contact [3].

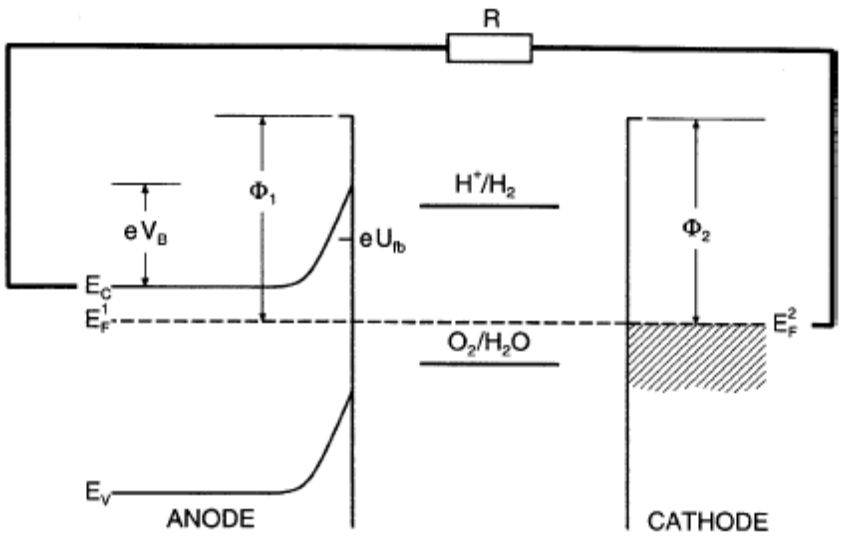

Figure 1.5: Band energy diagrams of PEC components at different stages during the photoelectrochemical process. Galvanic contact with no illumination [3].

As seen in Figure 1.5, the contact between the two electrodes (in the absence of light) results in electronic charge transfer from the lower work function (semiconductor) to the higher work function (metal) material. These charge transfers will occur until the work functions of both electrodes become equal [3]. The excess charge does not lie on the surface (like in metals) but extends into the electrode. This region is called space charge region, and for an n-type semiconductor, electrons will be transferred to the electrolyte and the space charge region will be positively charge (depletion region). The charge transfer results in a change in the semiconductor surface's electrical potential by V_B, leading to upward band bending. This energy is not enough for water decomposition because the H^+/H_2 energy level is above the E_F of the cathode.

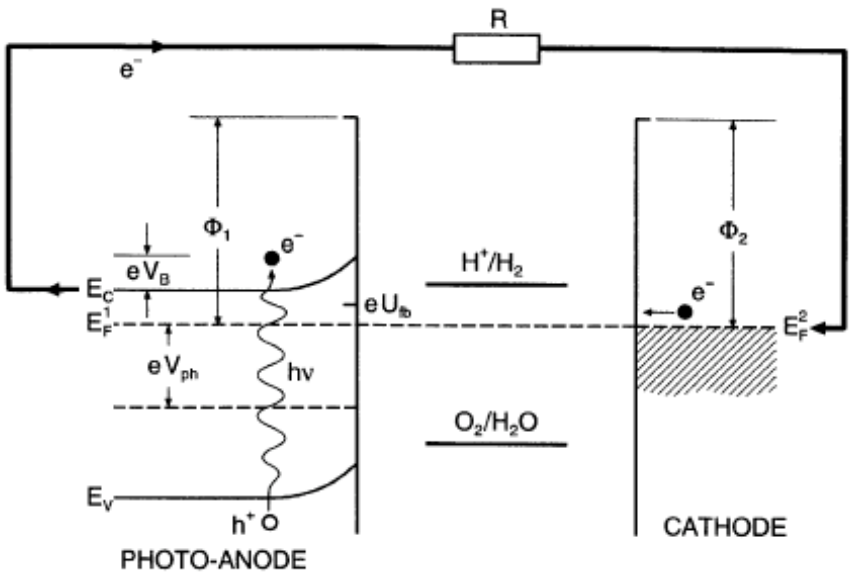

Figure 1.6: Band energy diagrams of PEC components at different stages during the photoelectrochemical process. Effect of light on the electronic structure of the PEC components [3].

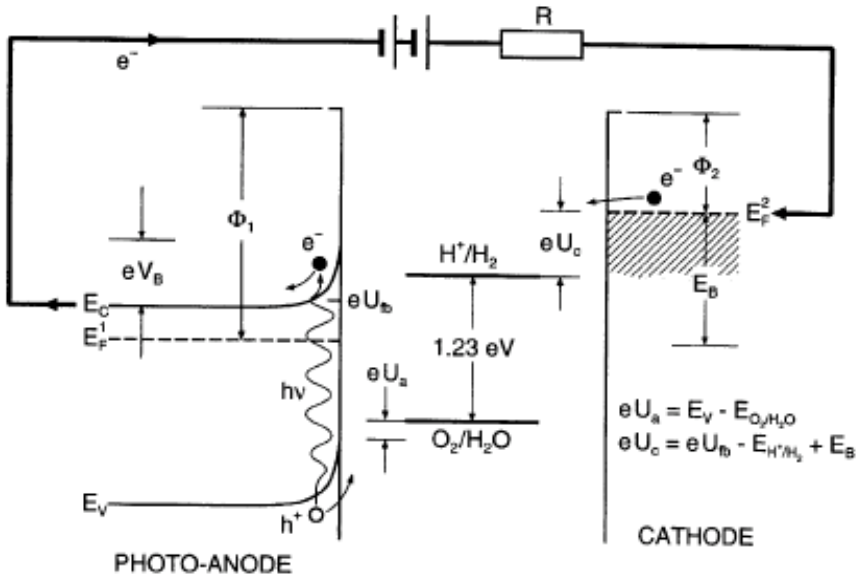

Figure 1.7: Band energy diagrams of PEC components at different stages during the photoelectrochemical process. Light effect on the band energies with applied bias voltage [3].

As seen in Figure 1.6, the application of light results in the lowering of the surface potential of the photoanode and the lowering of the H^+/H_2 potential. However, the latter still is above the E_F level of the cathode [1]. Consequently, Figure 1.7 shows that the application of an anodic bias is required to elevate the cathode E_F level above the H^+/H_2 energy level, thus making the process of water decomposition possible [3].

1.4 MATERIALS FOR PHOTOELECTROCHEMICAL CELLS

Most PEC cells for hydrogen production use titanium dioxide (TiO_2, also called titania) or related solid solutions like $SrTiO_3$ as photoanodes. Titanium dioxide is the preferred material because of its stability in aqueous environment. However, it has disadvantages such as large bandgap (>3.0 eV which it only allows absorption in the ultraviolet (UV) region of the solar spectrum) and low photocatalytic activities [14-18]. The typical open circuit voltage (V_{oc}) of a TiO_2 PEC cell is approximately 0.7 to 0.9 V [3]. Thus, in order to use this material, as a photoanode for water splitting extra bias has to be supplied to the cell. This bias can be:

- External bias voltage.
- Internal bias, using different concentrations of H^+ ions in the two electrode systems, so the two half-cell compartments use electrolytes at different pH.
- Use of two (or more) photoelectrodes - at one of the electrodes the oxidation of H_2O to O_2 and H^+ would take place, while the other photoelectrodes will merely generate additional photovoltage for water splitting [19].
- Imposition of internal bias voltage through the use of a PV unit in conjunction with the photoanode (hybrid electrode) [20].

1.4.1 Water Photoelectrolysis

The ideal voltage for water splitting is 1.23 eV. However, do to the existence of inefficiencies associate with overvoltages at the anode and the cathode, higher voltage is needed. These overvoltages can create activation barriers, which can only be reduced by the use of catalysts with high activities. Platinum and nickel are good catalysts for hydrogen evolution. However, there are not catalytic materials of comparable efficiency for oxygen production from water. Even the best catalysts (i.e. RuO_2) create overvoltage in the oxidation of water [21].

A good semiconductor for water photoelectrolysis must generate more than 1.23 eV and should have good catalytic properties for the water oxidation reaction, and it has to be stable against corrosion [1,3,24]. For such an ideal semiconductor the conduction band level should be more negative than the hydrogen reduction level ($E_{H+/H2}$), while the valence band should be more positive than the water oxidation level ($E_{H2O/O2}$) for efficient water photoelectrolysis [1,3,14,21].

1.4.2 Solar Conversion

The bandgap of a photoelectrode has a critical impact on the energy conversion efficiency of the PEC cell. Only the photons with energy equal to or larger than that of the bandgap may be absorbed and used for conversion. In general, the maximum conversion efficiency of photovoltaic (PV) devices may be achieved at bandgaps in the range of 1.0-1.4 eV [20]. In practice, the energy needed for conversion is higher than the thermodynamic limit. Including the energy losses which are unavoidable for the electron hole separation and the internal resistances of the cell, a bandgap of ~1.8 eV is the

minimum for a semiconductor that can perform this reaction at reasonable rates [19]. These losses include:

- polarization within the PEC
- recombination of the photogenerated electron-hole pairs
- resistance of the electrodes
- resistance of the electrical connections
- voltage losses at the contacts

The sum of these losses is about 0.6 - 1 eV; this energy is not available for conversion. Therefore, the optimum bandgap for water splitting is > 1.8 eV. Semiconductor materials that have a bandgap in this range (i.e. GaP) are susceptible to corrosion. Figure 1.8 shows the solar spectrum indicating the location of the ideal energy needed for water oxidation and the visible portion.

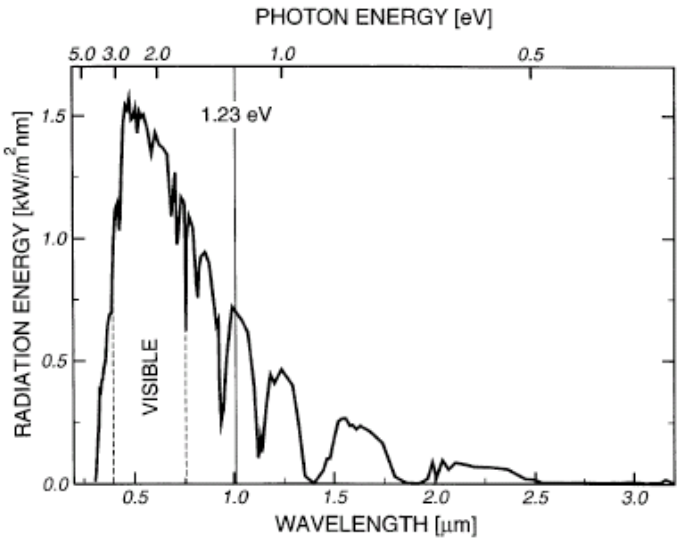

Figure 1.8: Solar light spectrum (AM 1.5) in terms of radiation energy vs. photon wavelength [2]. The 1.23 eV line indicates the theoretical water splitting energy.

The maximum amount of energy of the solar spectrum lies in the visible region (below 3.0 and above 1.4 eV, refer to Figure 1.8). Hence, in order to increase the efficiency of the solar devices an ideal semiconductor should have a bandgap within this energy range.

1.4.3 Materials Aspects for Photoelectrochemical Cells

The material used for photoanodes has to satisfy specific functional requirements with respect to semiconducting and electrochemical properties. These requirements are: (1) the high solar energy absorption (low bandgap), (2) minimum energy losses due to recombination, (3) high charge transfer at the photoelectrode/electrolyte interface, (4) and stability in aqueous solutions [3].

1.4.3.1 Bandgap

The bandgap is one of the critical properties of photoelectrodes materials; it determines the amount of solar energy absorbed and available for conversion. Figure 1.9 shows bandgap energies for different semiconductor photoanode candidates. The bandgap energies are compared to the vacuum level (the vacuum level refers to the energy of a free stationary electron that is outside of any material [22]) and to the standard hydrogen electrode (SHE) level in an aqueous solution of pH = 1. At this pH, a few materials (i.e. ZnO, TiO_2, SiC) have a bandgap to perform a spontaneous reaction. Other semiconductors (i.e. Fe_3O_2, WO_3, SnO_2) have conduction band energies less than the hydrogen production level (reduction reaction H^+/H_2), which indicates that anodes made with these semiconductors would need an external bias to split water. Unfortunately, materials with the right bandgap width, such as GaP (E_g = 2.23 eV) and

GaAs (E_g = 1.4 eV), are not stable in aqueous environments with significant corrosion by water. Two promising oxide materials, which are corrosion resistant and have bandgaps large enough to oxidize water, are TiO_2 and $SrTiO_3$. However, these large bandgap materials would only use the UV portion of the solar spectrum. This issue can be addressed by the following means:

- Formation of a sandwich-type electrode involving an upper layer of material that exhibits high corrosion resistance, such as TiO_2, and a sublayer of a narrow bandgap material (hybrid photoelectrode), hybrid PEC cell.
- Reduction of the bandgap width of oxide materials that are known to have high resistance to corrosion and photocorrosion, such as TiO_2. This reduction may be accomplished through the following procedures [1]:
    - Increasing the concentration of intrinsic defects, resulting in stronger interactions between defects and an alteration of the lattice parameters.
    - Doping with aliovalent ions resulting in the formation of mid-gap bands, which alters the electronic structure so that substantially lower energy gaps are required for ionization than that of the undoped material.

1.4.3.2 Flat Band Potential

The flat-band potential, E_{fb}, is the potential that has to be imposed over the electrode/electrolyte interface in order to make the bands flat (Figure 1.10). The process of water photoelectrolysis takes place when the flat-band potential is higher than the redox potential of H^+/H_2 couple [20]. The flat band potential frequently has been considered to be a specific property of the material (related to different phases and

crystallographic orientations). This potential is equal to the curvature of the bands in the absence of any potential applied to the interface. The flat band potential may be modified to the desired level through surface chemistry [2].

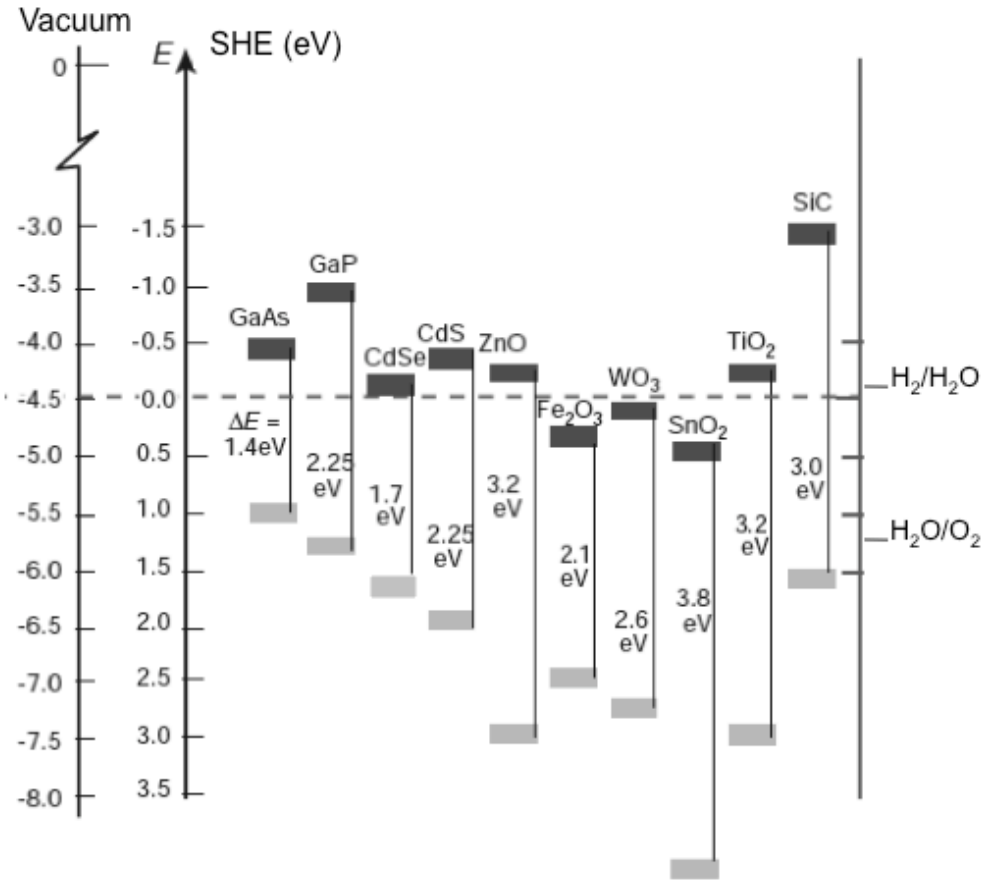

Figure 1.9: Diagram showing bandgap energies of different oxide materials and relative energies with respect to vacuum level and SHE level in electrolyte pH = 1 [25]. Lower edge is the valence band and the upper edge is the conduction band.

Figure 1.11 shows the flat band potential for several oxide materials versus the bandgap. Cells incorporating photoanode materials with negative flat band potentials relative to the redox potential H^+/H_2 couple (which depends on the pH) can split the water molecule without the imposition of a external bias.

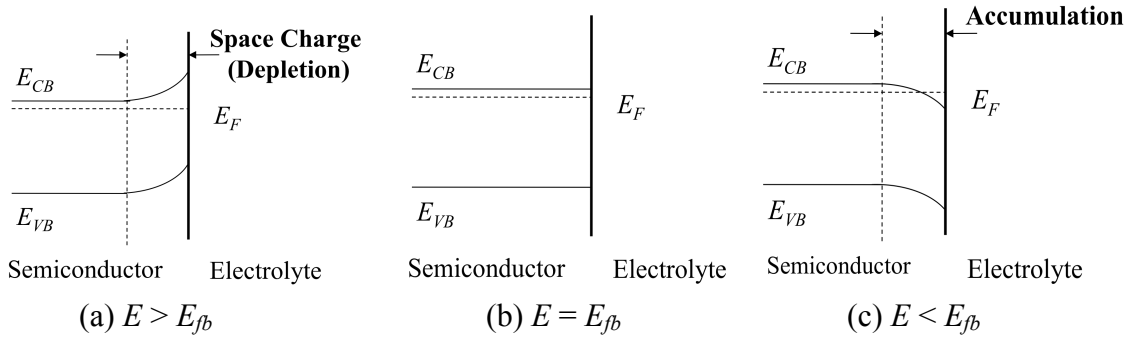

Figure 1.10: Effect of varying the applied potential on the band edges of the n-type semiconductor, (a) potential positive to the E_{fb}, (b) potential that make the band flat, E_{fb}, and (c) potential negative to the E_{fb}.

1.4.3.3 Schottky Barrier

A drop in the potential within the interface layer of the solid, formed as a result of concentration gradients, surface states, and adsorption states, is called the Schottky barrier. This barrier prevents the recombination of charge carriers (electron-hole pair) [27]. The recombination of electron-hole pairs reduces the photocurrent available for decomposition of water. Hence, the formation of the Schottky barrier is a desirable phenomenon. The barrier allows the separation of electrons and holes. The consequence of this separation is that electrons are transported into the bulk of the solid, forming an n-type semiconductor, while holes are transported toward the water-electrode interface, resulting in the formation of a p-type surface layer [2]. In the case of the n-type semiconductor, the band edges near the interface are curved upwards allowing the holes to move to higher energy levels. On the other hand, the electrons move to the bulk of the semiconductor at a lower energy than the interface. This effectively separates the electron-hole pair.

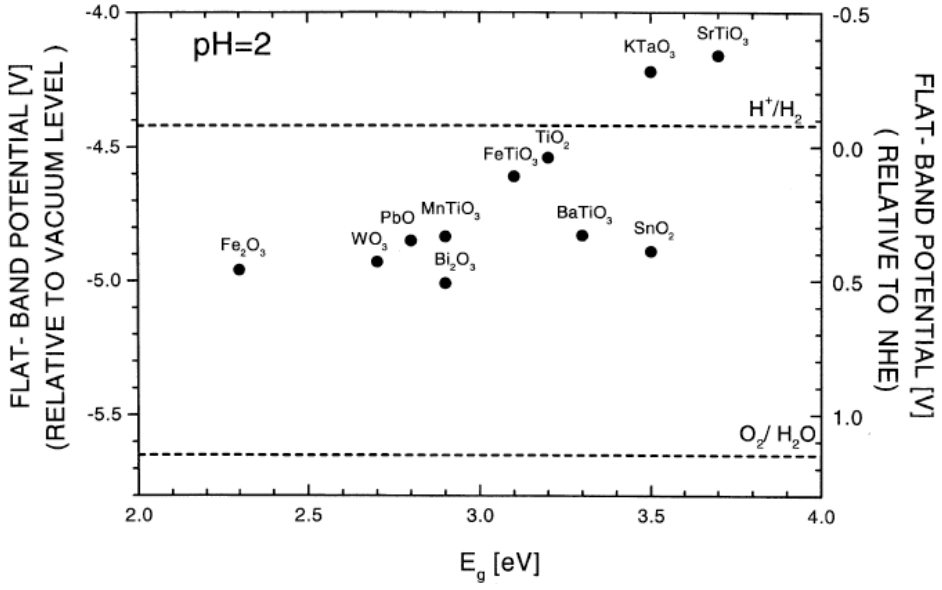

Figure 1.11: Flat band potential versus bandgap for different semiconductor oxides [23] measurements where done at pH = 2.0.

1.4.3.4 Electric Resistance

The ohmic resistance losses (external and internal circuits) in the PEC are associated with the:

- Electrodes
- Electrolyte
- Electrical leads (wires)

The dominant contributors are resistances of the electrodes and electrolyte, which are several orders of magnitude larger than the resistances of the metallic parts of the circuit. Lower resistances can be achieved by increasing the carrier concentrations, n and p, by doping with impurities. However, the mobilities decrease when the carrier concentration is increased. Hence, optimal doping is required to have maximum

conductivity. Formation of nonstoichiometric TiO_2 (TiO_{2-x}) results in an oxygen deficiency, which leads to an increase in the concentration of negative carriers. However, in a PEC cell, contact of the photoanode with oxygen is expected to increase the resistance due to quenching of defects [28].

An alternative method to reduce the resistance is through minimization of the thickness of the photoelectrode by fabrication of a thin film. This method has the advantage that the substrate can be made of Ti metal [2].

The resistance of the electrolyte can be decreased by increasing the concentration of high mobility ions in the solution, like H^+, OH^-, K^+, and Cl^- [3]. The resistances of electrical contact wires and measuring equipment should be kept at minimum by avoiding too many contacts between wires of different materials and corrosion at the electrode.

1.4.3.5 Helmholtz Potential Barrier

When a semiconductor material is immersed in a liquid electrolyte, charge transfer at the solid/liquid interface results in charging of the surface layer of the semiconductor. Charge transfer from the semiconductor to the electrolyte leads to the formation of a surface charge and results in upwards band bending, forming a potential barrier [23]. This barrier is similar to that of the solid/solid interface (like in PV solar cells). This surface charge is compensated by a charge of the opposite sign, which is induced in the electrolyte within a localized layer, known as the Helmholtz layer. It is ~ 1 nm thick and is formed of oriented water molecule dipoles and electrolyte ions adsorbed at the electrode surface [29]. The height of this potential barrier, known as the Helmholtz barrier, is determined by the nature of the aqueous environment of the electrolyte and the

properties of the photo-electrode surface [23]. The performance characteristics of PEC cells depend, to a large extent, on the height of the Helmholtz barrier.

1.4.3.6 Chemical Potential (Fermi Energy)

The Fermi energy, E_F, is a characteristic of the Fermi-Dirac statistics of electrons in a material. The Fermi energy may be referenced quantitatively by comparison to the energy of either the bottom of the conduction band or the top of the valence band. The E_F level may be referenced to the energy level where the electrons are free of electrostatic interactions, which is outside the solid surface (E_o also called vacuum level). The difference between these two levels (E_F and E_o) is termed the work function, ϕ, [1].

The E_F is used to characterize semiconducting properties of solids with respect to their ability to donate or accept electrons. The Fermi energy also is a key quantity in the evaluation of the charge transfer accompanying chemical reactions, especially in catalysis. In chemistry, chemical equilibrium typically is described in terms of the chemical potentials of reactants and reaction products. In this case, the E_F is equivalent to the chemical potential of electrons, which describes the electroactivity of a solid and together with its ability either to accept or donate electrons during chemical reaction [2,3].

There is a growing body of empirical data indicating that the E_F in the bulk is quite different from E_F at the surface [3]. This difference is due to segregation-induced concentration gradients at interfaces (surfaces and grain boundaries) and the resultant electrical potential gradients. These gradients have a significant impact on the functional properties of solids, including photosensitivity. Therefore, quantitative analysis of surface versus bulk properties is a critical issue in the interpretation of photo-induced effects [2].

1.4.3.7 Corrosion Photocorrosion Resistance

The electrons and holes generated in the semiconductor can also cause a chemical reaction between the electrolyte and the semiconductor itself, thus altering the chemical nature of the semiconductor and destroying its semiconducting properties. This is called photocorrosion [3]. Photocorrosion of the semiconductor alters, in particular, the chemical composition of the electrode at the interface between the electrolyte and photoelectrode, where the charge transfer reactions take place, and deteriorates the semiconducting properties of the photoanode. The semiconductor may itself be reactive towards the electrolyte and react with it even in the absence of the light generated charge carriers. This is called chemical corrosion [2,3].

Some oxide materials, like TiO_2, SnO_2, WO_3 are resistant to photocorrosion and chemical corrosion, while ZnO is stable only as a photocathode. Group III-IV and II-VI compounds and Cu_2O are not stable and corrode, although their bandgaps are in the optimal range [29]. In particular, titania is a widely used material because of its exceptional chemical resistance in solution. Mixed oxides such as $SrTiO_3$ are also used as photoanodes; these materials are corrosion resistant and offer the possibility of tailoring their band gap by altering their composition.

1.4.3.8 Microstructure

It is anticipated that future commercial photoelectrodes will be polycrystalline rather than single-crystal [3]. So far, little is known of the effect of interfaces, such as surface linear defects caused by grain boundaries, on the photoelectrochemical properties of photoelectrodes. There is a need for the understanding of the effect of the microstructure of polycrystalline photoelectrodes, specifically that of surface structural

defects, on the photoelectrochemical properties. Also, there is need for the development of interface processing technologies leading to the optimization of the energy conversion efficiency of photoelectrodes of polycrystalline materials [28].

1.4.4 Types of Photoelectrochemical Systems

The principle of charge transfer reaction at the semiconductor-electrolyte interface forms the basis for the various photoelectrochemical systems. These syste,s can be categorized according to the net free energy change in the overall system [21,30].

1.4.4.1 Electrochemical photovoltaic cells ($\Delta G = 0$)

In these cells the optical energy is converted into electric energy, with zero change in the free energy of redox electrolyte. The reaction occurring at the counter electrode is opposite to the photoelectrode. Therefore the light energy is converted directly to electrical energy, without a change in the solution composition or electrode material. The electrodes only serve as a shuttle for the charge transfer mechanism. The dye-sensitized solar cells (DSSC) are this category [30].

1.4.4.2 Photoelectrolysis cells or Photoelectrochemical cells ($\Delta G > 0$)

In this case two redox couples are present and the net change takes place in the system. The photoelectrolysis cells and some electrochemical storage solar cells belong to this category. The optical energy is converted into chemical energy [21]. In this work we used the term PEC cells for the photoelectrolysis cells for hydrogen production. It was shown previously that in PEC cells oxygen and hydrogen gas evolve separately [3], in the photoanode and cathode respectively.

1.4.4.3 Photocatalytic Cells ($\Delta G < 0$)

In this case the change in free energy is negative and the optical energy provides the activation energy for the chemical reaction [21]. In this cell both redox reactions (oxidation and reduction) occur on the surface of the photocatalyst. Therefore the photocatalyst particle exhibits the function of both anode and cathode [3].

1.4.5 Configuration of PEC Cells ($\Delta G > 0$)

The PEC systems reported in the literature may be categorized as:

- Single photoelectrode (photoanode or photocathode)
- Hybrid photoelectrode (multijunction PEC)
- Photoelectrode sensitized through:
    a. Doping by foreign ions
    b. Incorporation of particles of noble metals
    c. Deposition of dye
- Bi-photoelectrode (n-type and p-type photoanode and photocathode, respectively)

The single photoelectrode PEC system (i.e. Fujishima and Honda, Figure 1.2) has a single active light-absorbing electrode. The counter electrode is a non-photoactive metal. The bi-photoelectrode system is based on the use of semiconducting materials as both photoelectrodes. In this case n- and p- type materials are used as photoanode and photocathode respectively. The advantage of this configuration is that energy is generated in both electrodes, resulting in an overall voltage sufficient to decompose water without the application of a bias. The hybrid photoelectrode system has only one photoelectrode that is electrolytically active (i.e. an electrode where the reaction of water splitting takes place); however, there are other photoactive electrodes in the cell that act as photovoltaic

cells (producing electricity from light) without carrying out chemical reaction. These electrodes generate a photovoltage that acts as an internal bias. Both the bi-photoelectrode and the hybrid photoelectrode systems allow a substantial increase in solar energy conversion.

Substantial research has been devoted to enhancing the absorption properties of semiconductor oxides such as TiO_2 by adding foreign ions to reduce their bandgap [29-41], allowing the material to absorb more sunlight. Semiconducting photoanodes may also be sensitized by incorporation of small particles of noble metals, such as Au, Ag and Pt, thus forming a dispersed system involving nanoscale particles [18], which can change the optical, electrical, electrochemical and photoelectrochemical properties of the semiconductor electrode.

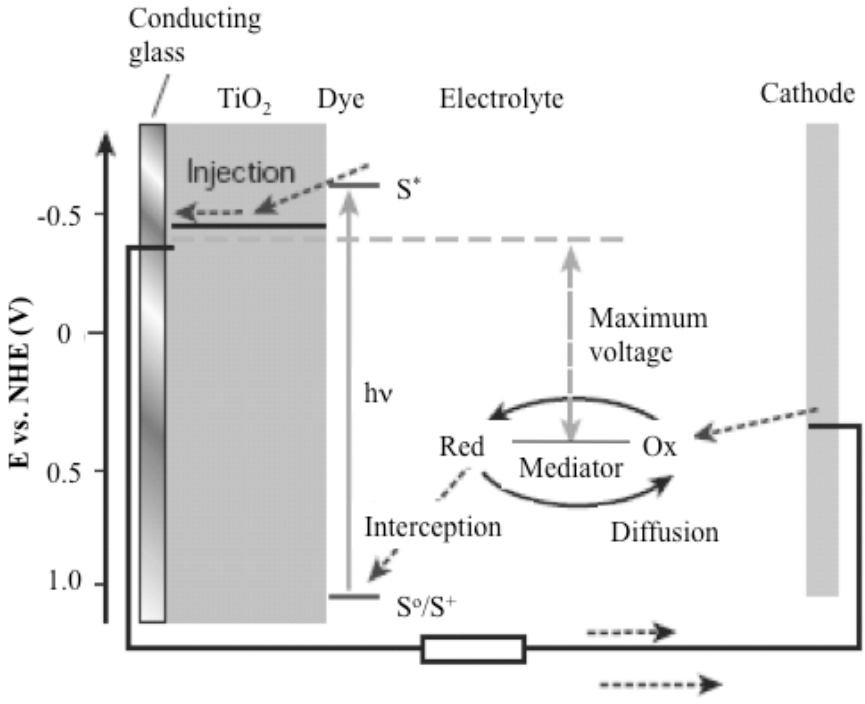

Figure 1.12: Schematic representation of the operation of a dye-sensitized PEC [25]. Photoelectrode made of mesoporous dye-sensitized TiO_2. The mediator is regenerated at the cathode giving a final $\Delta G = 0$.

Also, the conversion efficiency of a photoelectrode can be increased substantially through dye-sensitization of photoelectrodes [24]. The photosensitizer, which is an organic dye, is physically attached to the surface of the photoelectrode. Light absorption by the dye leads to the transformation of the dye molecules from the ground state (S) to the excited-state (S*) (Figure 1.12). The transition from the excited state (S*) to a higher oxidation state (S^+) results in the formation of electrons. Consequently, the oxidized dye molecule reacts with water, resulting in the formation of O_2 at the photo-anode and H_2 at the cathode [25]. Accordingly, dye-sensitized semiconducting photo-electrode exhibits two functions, these being (i) absorption of light by the dye and (ii) charge transport by the semiconductor.

1.4.5.1 Doped Semiconductor Materials

Titanium Dioxide (TiO_2)

Fujishima and Honda were the first to report successful PEC splitting water [13]. They used a semiconductor electrode based on rutile TiO_2. Both rutile and anatase crystal of TiO_2 have been largely studied for PEC and photocatalytic applications. TiO_2 is substantially less expensive than other photosensitive materials and the different process technologies for TiO_2 production are relatively straightforward and uncomplicated compared to those required for other semiconductors. The main drawback of TiO_2 is its large bandgap, 3.0 eV for rutile and 3.2 eV for anatase (only allows UV absorption). The properties of TiO_2 can be altered by varying the defect chemistry and associated electronic structure through the introduction of extrinsic defects and/or the alteration of the concentration of intrinsic defects [42]. To improve the PEC efficiency, it is desirable

to red-shift bandgap of the photoelectrode to use less energetic but more intense visible part of the solar spectrum.

It has been reported that nitrogen-doped TiO_2 ($TiO_{2-x}N_x$) shows a narrower bandgap and better photocatalytic activity under visible light than undoped TiO_2 [32,39,40]. The nitrogen doped TiO_2 shifts the bandgap down toward 2.3-2.4eV, showing a photoresponse in the visible light region toward [41,42]. Efficient photocatalytic or photoelectrochemical response of TiO_2 with other anion materials has also been reported [42]. Carbon-modified TiO_2, Sulfur-doped TiO_2, and $TiN_xO_yF_z$ are novel and interesting materials (good photocatalytic response to light) used for air and water purification, are also potentially candidates for PEC water splitting [34]. S-doped TiO_2 was reported to be photocatalytically active under visible light [34,43].

Khan et al. synthesized TiO_2 by controlled combustion of Ti metal in a natural gas flame. This material, in which carbon substitutes for some of the lattice oxygen atoms, absorbs light at wavelengths below 535 nm and has lower band-gap energy than rutile (2.3eV) [34]. Nakano et al. reported band gap states (~0.86, ~1.3 and ~2.34 eV) in C-doped TiO_2 films that were prepared by oxidative annealing of sputtered TiC; in particular the pronounced 2.34 eV band contributes to band gap narrowing and the additional two levels can be active as an efficient generation-recombination center [36].

It has been reported that the mechanism for visible light response for N-doped TiO_2 arises from the formation of an N-induced (occupied) midgap level (N 2p) slightly above the valence band edge [44,45]. The replacement of oxygen by C, N or other aliovalent ions and the elimination of oxygen vacancies ia crucial to tailor the photocatalytic reactivity of TiO_2 in the visible region [45]. The bandgap of the TiO_{2-x} can

be reduced the bandgap from 3.2 to 2.0 eV [44,45]. However, this might also result in energy losses through the modification of other properties such as [1]:

- Increased stability of the ionized surface oxygen species, leading to increased energy losses due to reduced charge transfer at the electrode/electrolyte interface
- Reduction in the lifetime of the electron-hole pairs generated, leading to an increase in energy losses due to recombination
- Formation of segregation-induced potential barrier in the surface layer, leading to the generation of retarding effect on the charge transport
- Increased ohmic resistance of the TiO_{2-x} photoelectrode
- Increased electrical potential barrier across the Helmholtz layer due to the enhanced adsorption of dipoles
- Formation of a bi-dimensional surface structure, which exhibits extraordinary properties that may retard the charge transport across this structure
- Insignificant overlap of the electron wave functions of the dopants in TiO_{2-x}.

Tungsten Trioxide (WO_3)

Tungsten trioxide has a relatively narrow bandgap (E_g ~ 2.5 eV) and is basically capable to split water using visible light. The resistance of WO_3 against photocorrosion in aqueous solutions has been confirmed over an acidic range of pH, including strongly acidic solutions [43,46]. The maximum photocurrents obtained for water splitting using WO_3 photoanodes (under visible light) have recently been considerably improved to reach almost 5 mA/cm^2, which should give an efficiency of ~ 2%[43].

WO_3 films doped with transition metal, such as Pt, Ru, Ni, Co, Cu and Zn, Pt and Ru were found to improve upon the photocurrent of WO_3, but only in small

concentrations. Since neither of these materials (transition metals) absorb light, adding too much of either most likely reduces photon absorption, leading to lower photocurrent. Small doping benefits the catalytic properties of the surface without affecting the photon absorption, giving greater photocurrents compared to pure WO_3 [43].

Radecka and coworkers have demonstrated that the incorporation of Ti ions into WO_3 lattice leads to the decrease of recombination process of electron and hole couples, and also addition of Ti shifts the flat band potential towards more positive values [38].

Ferric Oxide (Fe_2O_3)

Ferric oxide in the hematite phase has a bandgap between 2.0 and 2.3 eV, it is a low cost photoanode material and has high stability in aqueous solutions. However, ferric oxide has relatively slow charge transfer kinetics and high rate of hole-electron recombination resulting in low conversion efficiencies and the onset of the photocurrent shifts to positive potentials [47]. The conduction band of Fe_2O_3 is more negative than the redox potential for hydrogen reduction [48,49]. Because of this, the photoelectrolysis of the water using Fe_2O_3 photoanode would require a substantial external bias, which might be provided by a photovoltaic cell connected in series to form a tandem-cell device.

Thin films of Fe_2O_3, without dopants, have been extensively studied with reported energy conversion efficiencies of up to 2% for water splitting using external bias [43]. The effect of doping α-Fe_2O_3 thin-films with Ti, Al, Sn, Pt, Ni, In, Cr, Cu and Li has also been extensively studied [47]. Photocurrents of typically 5-6 mA/cm^2 have been achieved with Ti/Al-doped Fe_2O_3 thin-films (1-μm thin films) [43].

Zinc Oxide (ZnO)

Zinc oxide has a bandgap of 3.2 eV and is relatively stable in aqueous solutions. ZnO films have been doped aiming to have an improvement in the photocatalytic activity under visible illumination and increased stability. Cobalt as a dopant showed the greatest improvements in terms of visible light photocurrent. Cerium-doped samples proved to be the most stable ones. Fe, Ni, Ru and Mn doped samples also showed improvements versus pure ZnO [43,51].

Other material such as $GaInP_2$ (E_g ~ 1.83 eV), InN (E_g ~ 1.4 eV), Sn_xN_y (E_g ~ 1.8 eV) $CIGS_2$ (E_g ~ 1.4-1.9 eV) have also been studied. Even though they can generate sufficient energy to start an electrochemical reaction, the energy position of the band edges may prevent it from doing so [43]. Due to its favorable bandgap, materials like these ones remains a very promising material for efficient for PEC water splitting [35,52,53].

1.4.5.2 Multiple Bandgap Photoelectrochemistry

Energetic constraints imposed by single bandgap semiconductors have limited the photoelectrochemical solar-to-electric energy efficiency to 10-16% [54]. Considering factors involved with producing photocurrent or photovoltage using semiconductors of various bandgaps with solar energy of various wavelengths and intensities one can calculate the maximum theoretically achievable efficiency for various bandgaps. This relationship gives a parabolic curve for efficiency versus bandgap, with a maximum theoretical efficiency of about 30 % for a bandgap of 1.4 eV (see Figure 1.13) [56]. However, a semiconductor with this bandgap would give a voltage of ~0.7 V (assuming

its flat band potential matched the reduction potential of water), which is not sufficient to split water [54], therefore a much larger bandgap is needed. In contrast, multiple bandgap systems are capable of better utilizing the solar radiation [55-62]. Multiple bandgap solid-sate solar cells have achieved more than 40 % conversion efficiency [14]. In a multiple bandgap cell (multijunction cell), the topmost layer absorbs the more energetic photons and transmits lower energy photons, which are absorbed by layers underneath.

Conversion efficiencies can be enhanced, and calculations predict that a 1.64 eV and 0.96 eV two-bandgap system has maximum efficiencies of 38 % and 50 %, for 1 and 1000 suns concentration, respectively. Similar calculations indicate that the maximum energy conversion efficiency increases to a limit of 72 % for a 36-bandgap solar cell [55].

Present solid-state multijunction photovoltaics exist in two modes: either splitting (in which the solar spectrum is optically separated prior to incidence on the cells) or stacked devices. The latter mode has been developed as either monolithic (integrated) or mechanically (discrete cells layered with transparent adhesive) stacked cells. Most monolithic stacked multijunction photovoltaics under development use III-V semiconductors in at least one of the layers, and take advantage of the variations in bandgap [53,57].

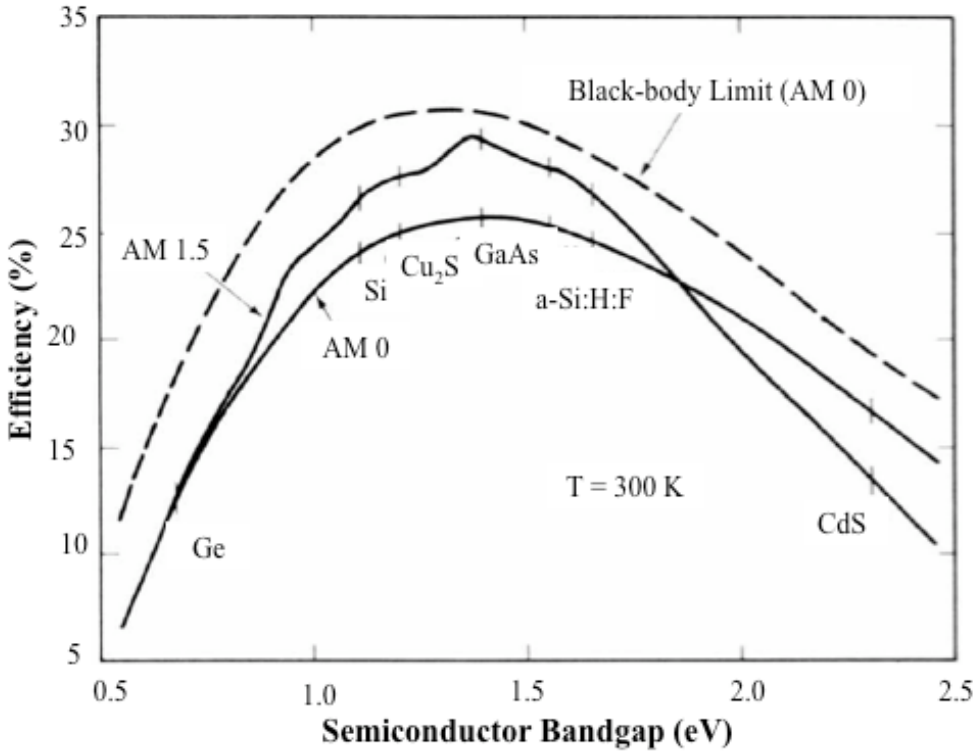

Figure 1.13: Theoretical calculated energy conversion efficiencies of solar cell materials vs. bandgap for single junction cells [54].

Figure 1.14 shows a schematic of a multiple bandgap PEC cell. In these multijunction devices the unstable (in aqueous solution) material is located at the bottom junction and a stable and protective one on the top junction. The monolithic structure minimizes the amount of active area needed while simultaneously decreasing the amount of semiconductor material, which will decrease the cost of produced hydrogen. The difficulty in this approach is in matching the light absorption characteristics of the two materials. Since the cells are in series, the lowest component cell current will limit the photogenerated current. Therefore, for maximum efficiency, the solar spectrum must be split equally between all the junctions in the PEC water-splitting device [58].

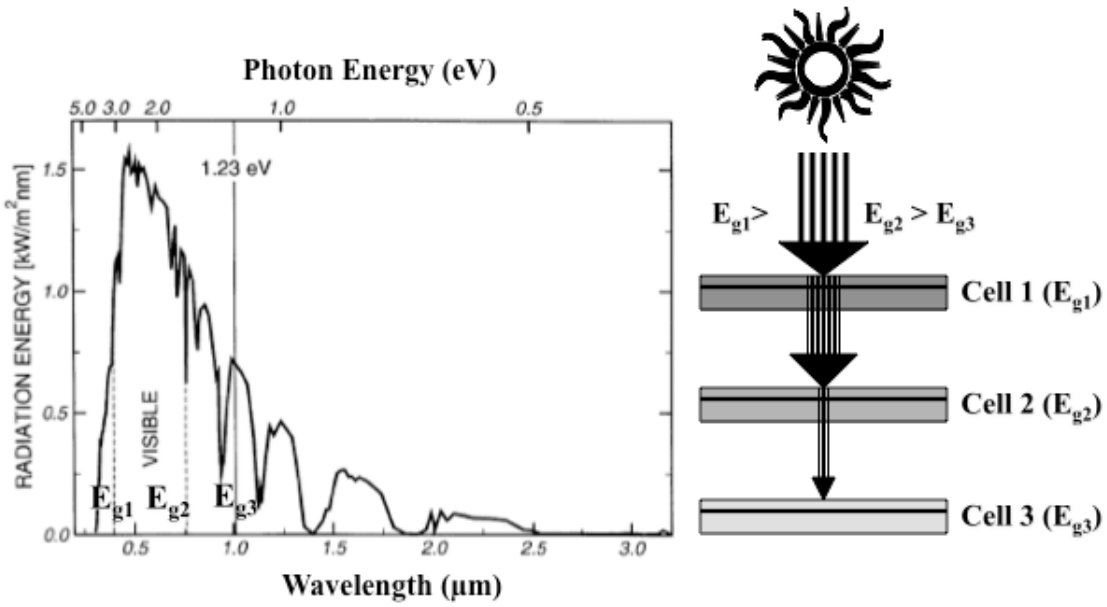

Figure 1.14: Schematic representation of a multijuntion cell. In this tandem photoanode, the top cell converts the higher energy photons and transmits the remainder onto layers with smaller bandgap cell, for more effective utilization of the solar spectrum [adapted from 3 and 14].

The first report of a hybrid photoelectrode was by Morisaki *et al.* (refer to Figure 1.15) [58]. The light reaches first the TiO_2 layer, which absorbs photons having energy equal or greater than its band gap, while the rest is transmitted to the silicon solar cell. Photons having energy between the band gap of TiO_2, 3.2 eV, and the band gap of silicon, 1.2 eV, are absorbed by the silicon solar cell. The photovoltaic cell provides the additional voltage required for biasing the cell for water electrolysis.

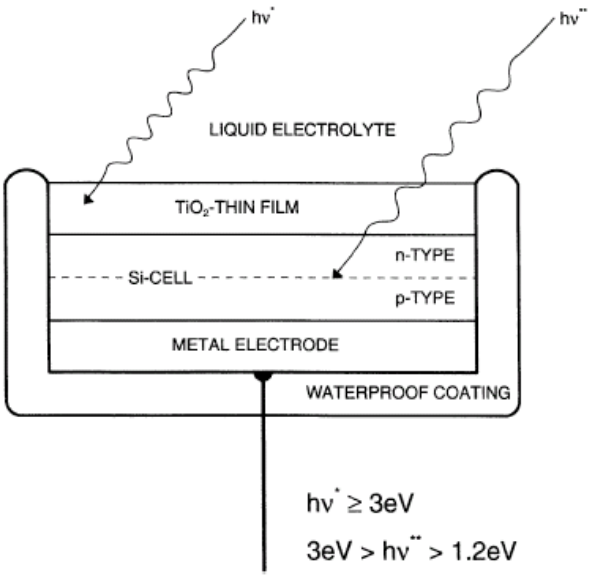

Figure 1.15: Hybrid photoelectrode involving a TiO_2 photoanode and a Si solar cell [58]. The top most film is TiO_2 and works as a photocatalyst for water oxidation. The Si solar cell gives the extra bias voltage for water oxidation.

Turner *et al*. designed a tandem PEC cell consisting of a gallium indium phosphide ($GaInP_2$) with GaAs tunnel-diode interconnection (Figure 1.16). Platinum deposited on the solar cell was used to catalyze the water oxidation [59]. The tandem cell gave 16 % solar-to-hydrogen (STH) conversion efficiency (based on hydrogen evolution and the lower heating value of hydrogen). Licht *et al*. designed the highest efficiency multijunction PEC cell reported to date. The cell containing illuminated AlGaAs/Si and RuO_2/Pt to evolve hydrogen and oxygen, respectively (refer to Figure 1.17). The resultant solar photoelectrolysis cell drove sustained water splitting at 18.3% conversion efficiency [14].

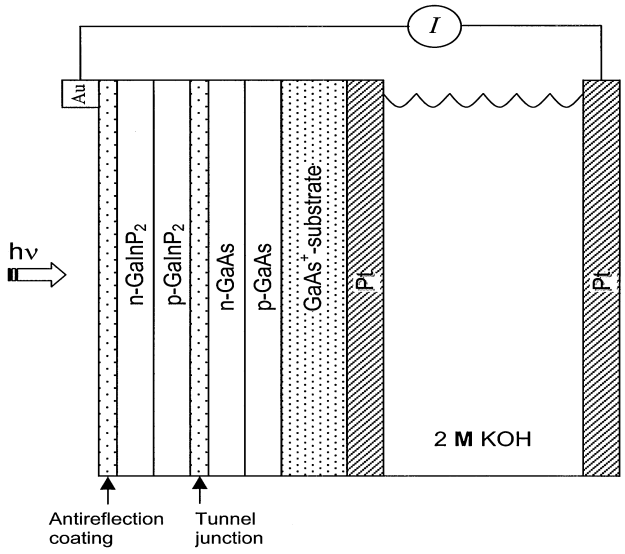

Figure 1.16: Schematic presentation of the components in n/p-GaInP/GaAs(Pt)/ KOH/Pt/PV electrolysis cell [15]. The Pt film on the photoelectrode works as a catalyst for water oxidation. The photoelectrode is illuminated from the back.

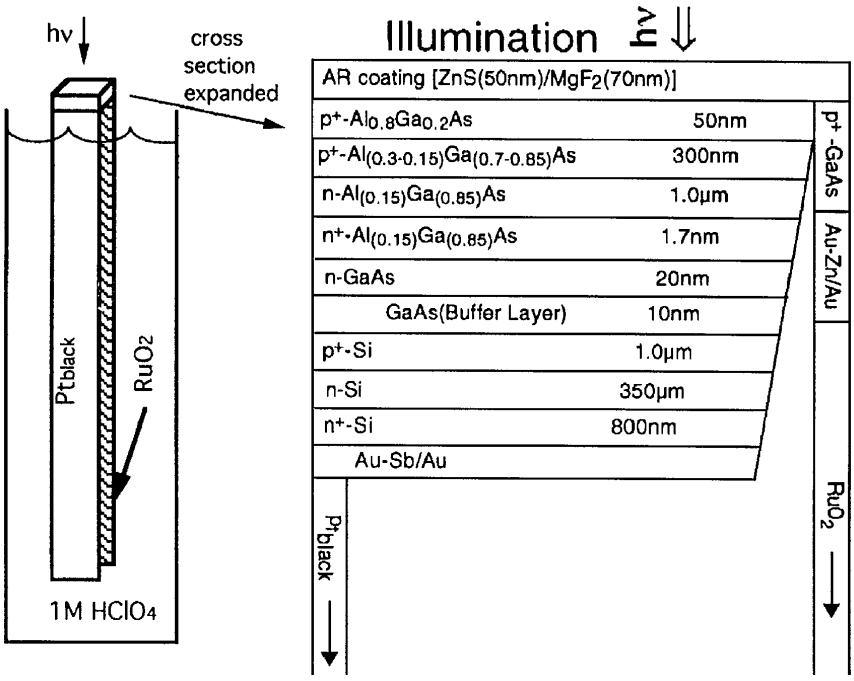

Figure 1.17: Schematic representation of the AlGaAs/Si RuO_2/Pt_{black} PEC cell [41]. In this cell the RuO_2 is the catalyst for water decomposition and it is not in contact with the light.

1.5 RESEARCH GOALS AND ORGANIZATION OF THE TEXT

The main focus of this research is to advance the understanding and development of efficient and stable photoelectrochemical cells for renewable hydrogen production. The specific objectives are to:

1. Identify and characterize semiconductor materials with an appropriate bandgap for water oxidation and that are stable in aqueous environments. Titanium dioxide and iron oxide based photoanode were fabricated and tested in a PEC cell.
2. Develop techniques and strategies to improve photoanode performance. Different structures of the oxides (nanoparticulates, nanowires and nanotubes) were studied and their influence on the performance of the PEC cells was characterized and analyzed. The addition of catalytically active sites to the oxide nanostructures was also investigated.
3. Evaluate the effects of different morphologies of the semiconductor nanostructures and supported metal particles on PEC cell performance.
4. Fabricate multijunction PEC cells and evaluate their performance for H_2 production. The combination a highly active photocatalysis for water oxidation with solar cells in a tandem system was analyzed in order to obtain higher efficiencies.

The text is divided into five chapters. A summary of the remaining four chapters follows:

Chapter 2: TiO_2 Photocatalyst Synthesis and Characterization

The preparation methods and techniques used for fabrication of the photocatalysts are described. The photocatalysts include nanostructured powders, nanotube films, and nanotube-supported active metals. The advantages of using titanium dioxide and its

electrochemical and photoelectrochemical properties are also discussed. The textural properties and bulk structures of the resulting materials, along with the surface structure and dispersion of the gold catalyst were evaluated using characterization techniques inlcuding X-ray diffraction, thermal gravimetric analysis, scanning electron microscopy, transmission electron microscopy, UV-Visible spectroscopy, and cyclic voltammetry.

Chapter 3: TiO_2 Photoelectrode Characterization and Performance Evaluation

Chapter 3 discusses the performance characterization of the different photoelectrodes and photocatalysts. Electrochemical characterization methods including linear sweep voltammetry, chronoamperometry and cyclic voltammetry were utilized. The role of the supported metal as well as the physical and chemical properties of the metal active sites on photocatalyst performance are also discussed, and a proposed location of the additional active sites for water oxidation is discussed. Efficiencies of the different photoelectrodes are also presented and analyzed.

Chapter 4: Hybrid Photoelectrochemical Systems

The results from a preliminary evaluation and secondary testing of hybrid photoelectrochemical cells are described in Chapter 4. Photoelectrochemical characterization based on linear sweep voltammetry and chronoamperometry are presented and analyzed. Energy efficiencies calculations are also presented.

Chapter 5: Other Materials for PEC cells: Hematite

Experiments using iron oxide (hematite) as a photocatalyst are presented in this chapter. Preliminary material characterization as well as photoelectrochemical evaluation

for the iron oxides nanotubes and metal nanoparticle loaded on these nanotubes is described.

Chapter 6: Summary, Conclusions and Recommendations for Future Work

An overall summary and conclusions relevant to this research are presented. Recommendations for future work are also suggested. The conclusions of this work should guide the future development of photoelectrochemical cells.

1.6 REFERENCES

1. C. W. Forsberg, Chemical Engineering Progress Magazine (2005) 20-22.
2. J. Nowotny, C. C. Sorrell, L. R. Sheppard, T. Bak, International Journal of Hydrogen Energy 30 (2005) 521-544.
3. T. Bak, J. Nowotny, M. Rekas, C. C. Sorrel, International Journal of Hydrogen Energy 27 (2002) 991-1022.
4. Stanford Research Institute, Chemical Economics Handbook. Chemical Economics Service Dept. of Business and Industrial Economics Stanford Research Institute, Stanford, Calif., 2004, v. (loose leaf).
5. M.D. Fryzuk, Nature 427 (2004) 498-499.
6. F. Ullmann, and Wiley InterScience (Online service), Ullmann's Encyclopedia of Industrial Chemistry. John Wiley & Sons Inc., New York, 2004.
7. U.S D.O.E.-E.I. Administration. 2006.
8. T. E. King. 2007. Carbide and Nitride Supported Water-gas Shift Catalysts. In Chemical Engineering. University of Michigan, Ann Arbor, MI
9. J.L.G. Fierro, and M.A. Peña, in: M., Fernández-García, and J.A. Anderson, (Eds.), Supported Metals in Catalysis Imperial College Press, London. 229-282.
10. Y. Goswami, K. Boer, (Eds.), Advances in Solar Energy, American Solar Energy Society (ASES), Boulder, CO, 2003, v. 13. 405-458.
11. A. Kogan, E. Spiegler, and M. Wolfshtein, International Journal of Hydrogen Energy, 25 (2000) 739-745.
12. D. F. Katakis, C. Mitsopoulou, J. Konstantatos, E. Vrachnou, and P. Falaras, Journal of Photochemical Photobiological Advances in Chemistry, 68, (1992) 375-388.
13. A. Fujishima Akira and K. Honda, Nature 238 (1972) 37-38.
14. S. Licht, in: A. J. Bard and M. Stratmann, (Eds.), Solar Photoelectrochemical Generation of Hydrogen Fuel: Encyclopedia of Electrochemistry, Wiley-VCH, Weinheim, Germany, 2002 v. 6, 346-357.
15. O. Khaselev, A. Bansal, and J. A. Turner, International Journal of Hydrogen Energy 26 (2001) 127-132.
16. N. Lewis and G. Crabtree (Eds.), Basic Research Needs for Solar Energy Utilization, Report of the Basic Energy Sciences Workshop on Solar Utilization, US Department of Energy (2005).
17. P. V. Kamat, Physical Chemistry C 111 (2007) 2834.
18. A. J. Nozik, Applied Physics Letters 29 (3) (1976) 150-153
19. H. Morisaki, T. Watanabe, M. Iwase, K. Yawaza, Applied Physics Letters, 29 (6) (1976) 338-340.

20. H. Gerischer, Semiconductor Electrodes and their Interaction with Light, Photoelectrochemistry, Photocatalysis and Photoreactors, Fundamentals and Developments, NATO ASI Series, 146 (1984) 39-106.

21. S. Chandra, Photoelectrochemical Solar Cells, Electrocomponent Science Monographs, Gordon and Breach Science Publisher, 1985, v. 5.

22. H. Ishii, K. Sugiyama, E. Ito, and K. Seki, Advanced Materials 11 (1999) 8.

23. J. L. Gray, The Physics of Solar Cells, Handbook of Photovoltaic Science and Engineering, John Wiley & Sons, 2003, 61-112.

24. M. Gratzel, Nature, 414 (2001) 338-344.

25. M. Gratzel, Journal Photochemistry and Photobiology C, 4 (2003) 145-153.

26. Y. V., Pleskov and Y. Y. Gurevich, Semiconductor Photoelectrochemistry, Consultants Bureau, New York, 1986.

27. V. Urade, 2004. Photoelectrochemical Generation Hydrogen. School of Chemical Engineering, Purdue University.

28. J. Nowotny, C. C. Sorrel, T. Bak, and L. R. Sheppard, International Journal Hydrogen Energy 78 (2005) 593-602.

29. A. G. Agrios and P. Pichat, Journal of Applied Electrochemistry 35 (2005) 665-663.

30. M. Sharon, in: A. J. Bard and M. Stratmann (Eds.), Encyclopedia of Electrochemistry, Volume 6: Semiconductor Electrodes and Photoelectrochemistry, Wiley-VCH, Weinheim, Germany, 2002 v. 6, 287-316.

31. A. Aroutiounian, and V.M. Shahnazaryan, Solar Energy, 78 (2005) 581-592.

32. R. Asahi, T. Morikawa, T. Owaki, K. Aoki, and Y. Taga, Science 293 (5528) (2001) 269-271.

33. E. Baborini, A. M. Conti, I. Kholmanov, P. Piseri, A. Podesta, Milani Paolo, C. Cepek, O. Sakho, R. Macovez, and M. Sancrotti, Advaced Materials. (Weinheim, Ger.) 17 (2005) 1842-1846.

34. S. Khan, M. Al-Shahry, and W. Ingler, Science 297 (2002) 2243-2245.

35. T. Lindgren, M. Larsson, and S. Lindquist, Solar Energy Materials and Solar Cells 84 (2004) 147-157.

36. Y. Nakano, T. Morikawa, T. Ohwaki, and T. Yasunori, Applied Physics Letters 87 (2005).

37. T. Ohno, Mitsui T., Matsumua M., Green Chemistry Letters Review 32 (2003) 364-365.

38. M. Radecka, P. Sobas, M. Wierzbicka, and M. Rekas, Physica B, 364 (2005) 85-92.

39. Sakthivel S., and Kisch H., Chemical Physics 4 (2003) 487-490.

40. P. G.Wu, C. H. Ma, and J. K. Shang, Applied Physics A 81 (2005) 1411-1417.

41. S. Licht, J. Physical Chemistry B 105 (2001) 6281-6294.

42. P. R. Mishra, P. K. Shukla, A. K. Singh, and O. N. Srivastava, International Journal of Hydrogen Energy 28 (2003) 1089-1094.

43. A. Luzzi, Photoelectrolytic Production of Hydrogen, IEA Agreement on the Production and Utilization of Hydrogen, IEA/H2/TR-02/ 2004.

44. H. Irie, Y. Watanabe, and K. Hashimoto, Journal of Physcal Chemistry B 107 (2003) 5483-5486.

45. R.Nakamura, T. Tanaka, and Y. Nakato, Journal of Physical Chemistry B 108 (2004) 10617-10620.

46. C. Santato, M. Ulmann, and J. Augustynski, Advanced Materials 13 (2001) 511-514.

47. J. C. Sartoretti, M. Ulmann, B. D. Alexander, J. Augustynski, and A. Weidenkaff, Chemical Physics Letters 376 (2003) 194-200.

48. A. Kay, C. Ilkay, and Michael Gratzel, Jounral of the American Chemical Society. 128 (2006) 15715.

49. A. Kokorin, and D. Bahnemann (Eds.), Chemical Physics of Nanostructured Semiconductors, Utrecht: Boston, MA, 2003, 83-110.

50. W. B. Ingler, and S. U. M. Khan, International Journal of Hydrogen Energy 30 (2005) 821-827.

51. T. F. Jaramillo, S. H. Baeck, A. Kleiman-Shwarsctein, and E. W. McFarland, Macromolecular Rapid Communication 25 (2004) 297-301.

52. A. M. Fernandez, N. Dheree, J. A. Turner, L. G. Arriaga, and U. Cano, Solar Energy Materials & Solar Cells 85 (2005) 251-259.

53. R. C. Valderrama, P. J. Sebastian, M. Miranda-Hernandez, J. Pantoja Enriques, and S. A. Gamboa, Journal of Photoelectrochemistry and Photobiology A 168 (2004) 75-80.

54. A. Goetzberger, C. Hebling, and H-W Schock, Material Science and Engineering 40 (2003) 1-46.

55. S. Litch, in: A. J. Bard and M. Stratmann, Encyclopedia of Electrochemistry, Semiconductor Electrodes and Photoelectrochemistry, Wiley-VCH, Weinheim, Germany, 2002 v. 6 358-394.

56. S. Maheshwar, in: A. J. Bard and M. Stratmann, Encyclopedia of Electrochemistry, Semiconductor Electrodes and Photoelectrochemistry, Wiley-VCH, Weinheim, Germany, 2002 v. 6, 346-357.

57. E. L. Miller, R. E. Rocheleau, and S. Khan, International Journal of Hydrogen Energy, 29 (2004) 907-914.

58. H. Morisaki, T. Watanabe, M. Iwase, and K. Yawaza, Applied Physics Letters 29 (6) (1976) 338-340.

59. O. Khaselev, J. A. Turner, Science 280 (5362)(1998) 425-427.

60. E. L. Miller, B. Marsen, D. Paluselli, and R. Rocheleau, Electrochemistryand Solid-State Letters 8 (2005) A247-A249.

61. E. L. Miller, D. Paluselli, B. Marsen, and R. Rocheleau, Hawaii Natural Energy Institute, University of Hawaii, II.E.2 Photoelectrochemical Hydrogen Production, DOE Hydrogen Program, FY 2004 Progress Report.

62. E. L. Miller, D. Paluselli, B. Marsen, R. E. Rocheleau, Solar Energy Material & Solar Cells 88 (2005) 131-144.

CHAPTER 2

TITANIUM DIOXIDE PHOTOCATALYSTS SYNTHESIS AND CHARACTERIZATION

2.1 INTRODUCTION

As the most promising photocatalyst [1-4], TiO_2 is expected to play an important role in solving many environmental and pollution challenges, through its effective utilization in photovoltaic and water-splitting devices [1].

Titanium dioxide (TiO_2) has been produced commercially since the early 1900's, and it has been widely used as a pigment and in sunscreens, paints, ointments, toothpaste, etc. Since Fujishima and Honda discovered the phenomenon of photocatalytic splitting of water on a TiO_2 electrode under ultraviolet (UV) light, enormous efforts have been devoted to developing TiO_2 for this purpose. This has led to many promising applications in areas ranging from photovoltaics and photocatalysis to photo-electrochromics and sensors [1-3]. These applications depend not only on the properties of the TiO_2 material itself but also on the modifications of the TiO_2 as a support (e.g., with inorganic and organic dyes) and on the interactions of TiO_2 with the environment.

There are three main TiO_2 structures: rutile, anatase and brookite. If the particle sizes of the three crystalline phases are equal, rutile is the most stable phase for

particles above 35 nm in size [2], anatase is the most stable phase for particles below 11 nm and brookite has been found to be the most stable or nanoparticles in the 11–35 nm range [1,2].

Rutile and anatase TiO_2 are n-type semiconductors due to the presence of oxygen vacancies [2]. Their conductivity increases with increasing O_2 partial pressure at temperatures above 600 °C [2]. The release of O_2 from the lattice creates Ti^{3+} sites, which are responsible for the electronic conductivity. Unlike metals, semiconductors lack continuum interband states to assist the recombination of electron-hole pairs, which assures a sufficiently long lifetime of the charge carriers to diffuse. The differences in lattice structures between anatase and rutile cause different densities and electronic band structures, leading to different bandgaps. Bandgaps for bulk anatase and rutile are 3.2 and 3.0 eV, respectively [3]. These bandgaps only allow the absorption of the UV portion of the solar spectrum, which in terms leads to lower energy conversion efficiency for PEC fabricated using TiO_2.

The electrochemical properties of TiO_2 depend on its crystallinity and phase [4]. For example, the anatase phase is preferred in charge separation devices such as PEC cells and dye sensitized solar cells (DSSC), while rutile is used in gas sensors, MOSFET devices, and dielectric layer applications [2,4]. For solar cell applications, the anatase structure is preferred over the rutile structure, because anatase exhibits higher electron mobility, lower dielectric constant [2]. These phases exhibit different activities for photocatalytic reactions, which could be a consequence of the differing conduction band energies. The conduction band energy, E_{CB}, for rutile TiO_2 is essentially coincident with the reversible hydrogen potential at all pH values, whereas for anatase TiO_2 the E_{CB} is

more negative by 0.20 V [2].

Titanium dioxide can be prepared in the form of powder, crystal, or thin films. Both powders and films can be built up from crystallites ranging from a few nanometers to several microns thick [3]. Some of these preparation methods are sol-gel, precipitation, hydrolysis, solvothermal, combustion synthesis, electrochemical synthesis, gas phase methods, chemical vapor deposition (CVD), physical vapor deposition (PVD) and spray pyrolysis deposition. Four of these methods have been used in this research to fabricate nanostructured titanium dioxide.

The energy conversion efficiencies for TiO_2 photoelectrodes in solar applications (i.e. PEC cells) are limited by high recombination of charge carriers, formed during illumination, and low photocatalytic rates. Efforts have been dedicated to overcome these limitations by modifying the morphological and crystalline structures of TiO_2 as well as changing its surface by addition of different metals. Nanostructured TiO_2 in the form of wires, ribbons and tubes has been fabricated and tested [1-11]. The best performance (conversion efficiencies in excess of 0.6 %) has been reported for highly ordered TiO_2 nanotubes. Grimes [4] and Schmucki [11] have reported TiO_2 nanotubes as long as 250 μm with different diameters and thicknesses.

This chapter describes details regarding the fabrication and characterization of a novel photocatalyst based on titanium dioxide. Two strategies have been explored for improving the photoelectrochemical properties of TiO_2: (1) producing the photocatalyst in the form of nanotubes to improve collection efficiencies and (2) incorporating nanocrystalline gold onto the nanotubes to improve photocatalytic activities.

2.2 EXPERIMENTAL

This section summarizes the methods and techniques used to prepared and characterized powders and nanotube-films photocatalysts.

2.2.1 Powder Titanium Dioxide: Hydrolysis of Titanium Tetrachloride

High surface area TiO_2 powders were prepared using the hydrolysis of titanium tetrachloride ($TiCl_4$). Titanium hydroxide was precipitated at pH 5.0 from aqueous $TiCl_4$ [5]. A volume of 5.0 mL of $TiCl_4$ (98% v/v Sigma Aldrich) was added to 18 mL of hydrochloric acid (HCl, ACS grade Fisher Scientific) solution (0.65M) under vigorous stirring in a dried environment (liquid nitrogen was poured in open dewars to eliminate the moisture in the air inside the hood). The transparent solution was titrated by addition of ammonium hydroxide, NH_4OH (12 wt%, Sigma Aldrich) under continuous stirring until the pH reaches 5.0. After aging the suspension for 30 minutes, the precipitate material was filtered and washed with deionized water (DI) to eliminate the residual chlorine ions [6]. Then, the cake was dried at 80°C in a vacuum oven over night. The dried white material was crushed to a fine powder, and then calcined to crystallize the oxide.

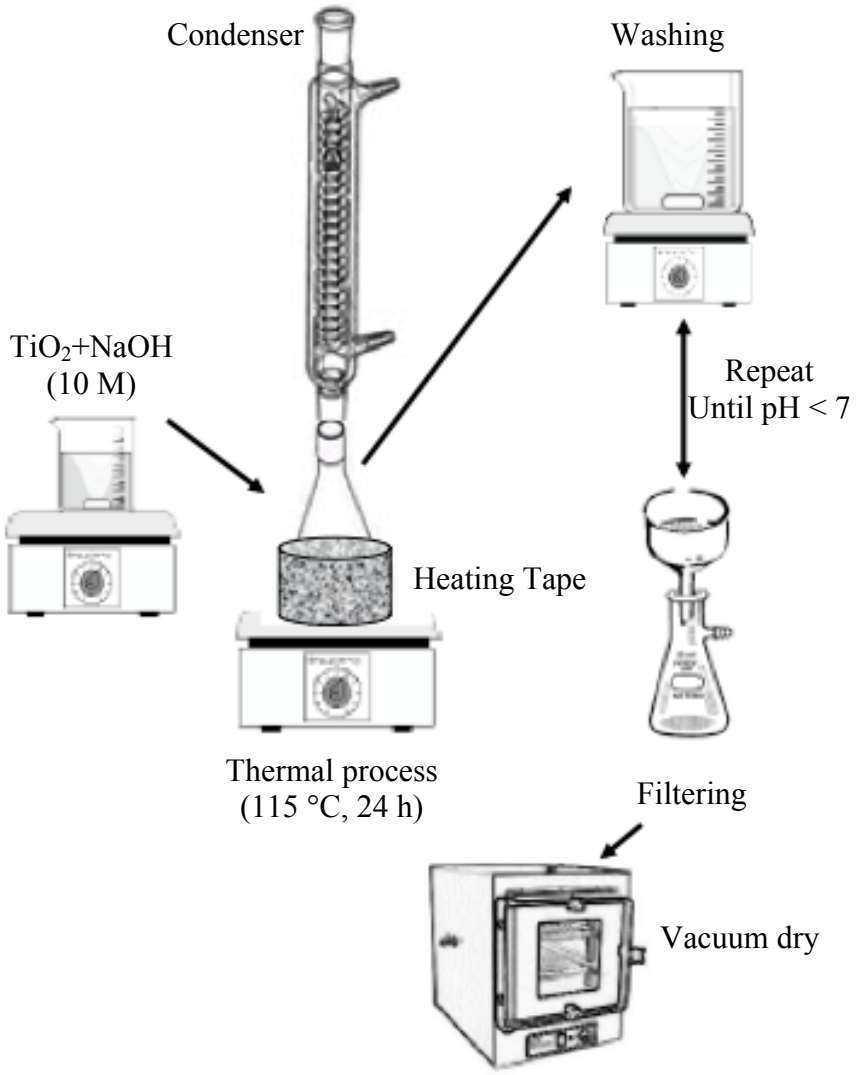

Figure 2.1: Schematic illustration of the hydrothermal system used to synthesize disordered TiO_2 nanotubes in powder form.

2.2.2 Powder Titanium Dioxide: Sol-Gel Method

Titanium dioxide powders were prepared using the sol-gel method [7-9]. In order to prepare 1.0 g of TiO_2, 4.3 mL of titanium n-butoxide (Alfa Aesar) was mixed with 20.6 mL of ethanol (anhydrous 87%, Fisher Scientific). The solution was stirred vigorously at room temperature. A volume of about 1.2 mL of HCl (~ 5.5 M) was added

to the titanium n-butoxide-ethanol solution under continuous stirring. Gel formed within 10 minutes after the addition of the acid solution. The gel was dried in air for 12 h at 110 °C. Finally, the gel was calcined at 450-500 °C to remove organic residuals and to crystallize the remaining powder [9].

2.2.3 Synthesis of Disordered TiO_2 Nanotubes Powders (*tint*)

A hydrothermal method was used to prepare disordered TiO_2 nanotubes (*tint*) [10]. Two grams of titanium dioxide P25 powder (75 % anatase and 25 % rutile, Degussa) were dissolved in 200 mL of 10 M NaOH (Alfa Aesar). Then the mixture was transferred to a flask and connected to a condenser (Figure 2.1). The solution was maintained at 115 °C for 24 hhh under constant stirring. The final product was washed with 200 mL of DI water and then filtered several times. The final wash was done with small volumes of 1 M nitric acid (80%, ACS grade Fisher Scientific) until the final pH was neutralized (pH~ 7). The solid material was dried in a vacuum oven at 100 °C over night. The dried material was then calcined to crystallize the powder.

2.2.4 Synthesis of Highly Ordered TiO_2 Nanotube Films

An anodization method was used to fabricate ordered titanium dioxide nanotubes (TiNT) [11,12]. Three different electrolytes were used: 0.25 wt% hydrofluoric acid (HF, 50% v/v Fisher Scientific) in DI water, 0.5 wt% hydrofluoric acid in glycerol (Fisher Scientific, less than 0.1 wt% H_2O), and 0.3 wt% ammonium fluoride (NH_4F, Sigma Aldrich, 98+%) in 98 wt% ethylene glycol (Fisher Scientific, less than 0.2 wt% H_2O) and balance DI water.

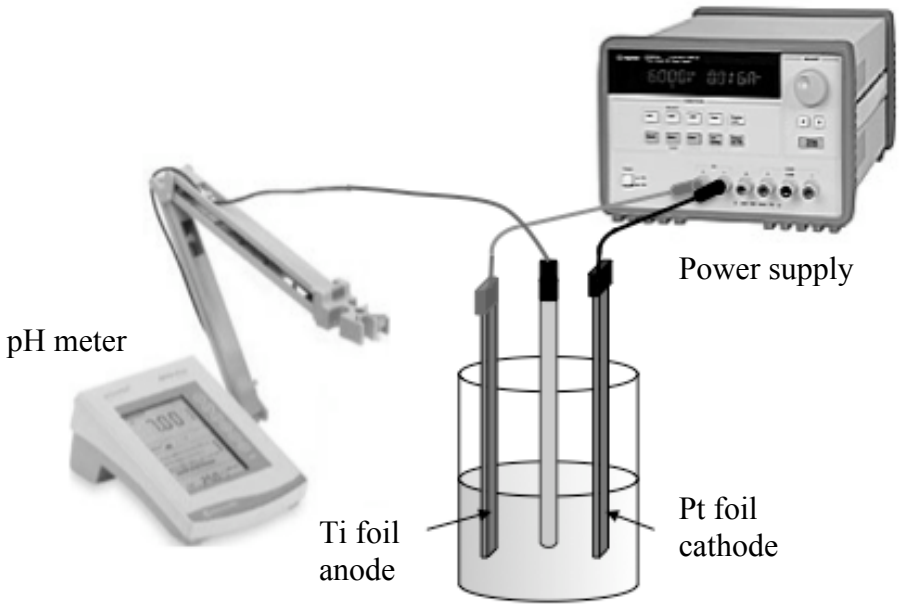

Figure 2.2: Schematic representation of the two-electrode anodization cell used to fabricate titanium dioxide nanotubes (TiNT) films.

The anodization was carried out at room temperature using a two-electrode cell (Figure 2.2), with a Ti foil or a thin Ti film deposited on glass substrates as the anode and Pt foil as the cathode. The titanium foils (Sigma Aldrich 99.7% purity, 0.127 mm thickness) were cut into 2.5 × 0.9 cm^2 pieces. To clean the metal surface (Ti foils and Ti films) the metal pieces were sonicated in ethanol, then acetone and finally water for 10 minutes each time; then dried in air for 30 minutes at 90°C.

The electrodes were connected to a power supply (Agilent, E36474, maximum voltage 60V). During anodization, the voltage was increased from open circuit potential to the final potential at a rate of 0.1 V/s, and then held at the final potential for a defined period of time. The final potential and the anodization time were also varied to study the influence of these parameters on the final nanotube dimensions. After anodization, the samples were rinsed with ethanol to remove any electrolyte left on the surface of the film. Some of the anodized nanotubes had surface debris covering the entrance of the tubes,

which were removed by sonication in ethanol. After the cleaning step, the films were dried under vacuum at 90 °C for 30 minutes. Finally, the TiNT films were calcined to remove remaining organic compounds and to crystallize the samples.

2.2.5 Synthesis of Supported Gold Catalysts

TiO_2 supported gold catalysts were prepared with 0.1 to 5.0 wt% gold via regular and modified deposition-precipitation (DP) methods. The support materials included powder TiO_2 (P25, Alfa Aesar, and catalysts prepared in our laboratory), *tint*, and TiNT films.

2.2.5.1 Gold Loading: Powder Catalysts

Gold nanoparticles were deposited onto the TiO_2 powders using a deposition-precipitation method [13-15]. The powdered support was transferred to 100 mL of DI water and stirred. Subsequently, the temperature of the solution was increased and maintained at 40-50 °C for about 1 h. 1.0 M Na_2CO_3 was added to the TiO_2 solution until the pH increased to ~10.0, as measured by a pH meter. A volume (the amount depends on the desired Au nominal loading) of ~ 0.002 M $HAuCl_4 \cdot 3H_2O$ (Sigma Aldrich) in DI water was slowly added to the support in suspension. During this period, the pH of the suspension was maintained at 10 via the drop-wise addition of aqueous Na_2CO_3. The temperature of the suspension was maintained at 40-50 °C for 1 h in order to age the suspension. The solution supernatant was separated from the catalyst solid using 0.45 μm filter paper (Fisher). The filtered solid was then washed with DI water and filtered several times. Finally, the material was dried in a vacuum oven (– 12 psi of vacuum, Isotemp 280A, Fisher Scientific) at 80 °C for over night.

2.2.5.2 Gold Loading: Ordered TiO_2 Nanotubes

The DP method was modified to deposit Au on the TiNT film surfaces [0]. After calcination the films were immersed in DI water (6.0 mL) under vigorous stirring. The Au precursor solutions consisted of $HAuCl_4 \cdot 3H_2O$ in DI water; the solution concentration was varied (0.5-2.0 mg/mL) to achieve different Au loadings. To help the deposition of the metal inside the nanotubes, the films were continuously spun in water using a small electric motor. Subsequently, the temperature of the water was maintained at 40-50 °C for 30 minutes. The Au gold precursor solution was slowly added to the DI water. The solution pH was regulated adding small amounts of 0.01 M Na_2CO_3 solution. After adding the Au precursor solution, the temperature of the loading solution was maintained at 40 °C for 1 h. The stirring and spinning of TiNT film was also kept constant for the duration of the aging period. After the deposition of Au, the substrates were rinsed various times by spinning the film in clean DI water for 30 minutes, then transferred to a vacuum (at -12 psi of vacuum) oven maintained at 80 °C and dried overnight.

2.3 BULK MATERIAL CHARACTERIZATION

2.3.1 Macro and Nano-Structural Characterization

Micro- and nano-structural properties of the materials were characterized using X-ray diffraction (XRD), scanning electron microscopy (SEM), and transmission electron microscopy (TEM).

2.3.1.1 X-Ray Diffraction Analysis

The XRD studies were done using a rotating anode X-ray diffractometer (Miniflex Rigaku) with a Cu $K\alpha$ radiation source with a Ni filter (λ = 1.5 Å). Samples were mounted on glass slides using double sided tape, and patterns were recorded over diffraction angles (2θ) from 10 to 90 at 5 °/min with a 0.5 degree step size The multi-function software, JADE, was used to interpret the diffraction patterns.

2.3.1.2 Scanning Electron Microscopy

SEM micrographs were taken for both powder and film photocatalysts. The powders were coated with a thin layer of Au-Pd using an Anatech Hummer VI Sputter Coater. In the case of the TiNT films, a small portion of the film was cut and loaded onto the metal support without any further metal coating. Cross-sectional images of the nanotubes were taken from layers cracked while cutting the sample film. SEM micrographs were used to determine the average diameters and lengths of the TiNTs.

2.3.1.3 Transmission Electron Microscopy

TEM was performed on the powder and film photocatalysts using conventional TEM bright field (BF) imaging using a JEOL 3011 transmission electron microscope operating at 400 kV. This technique was used to characterize the morphology of surface Au particles, as well as aided in measuring their size distribution. In the case of the Au/TiO_2 powder catalyst the materials were crushed using a mortar and pestle to achieve a finer powder. The powders were loaded onto a grid consisting of an ultra thin carbon film on a perforated carbon support film (*OD* = 3 mm, 400 mesh, TedPella Inc). In the case of the Au/TiNT films, the tubes were removed from the substrate by scraping the

film; the very small flakes were supported directly on the grid. The carbon support layer lying over the holes was less than 3 nm in thickness and was ideal for high-resolution microscopy. This method avoided the use of solvents and any concurrent modification of sample.

2.3.2 Elemental Analysis

Inductively Coupled Plasma Spectroscopy using a Varian 710-ES ICP Optical Emission Spectrometer was used to determine the Au loadings. For this technique, atoms in the plasma emit light with characteristic wavelengths for each element, and this light was recorded by calibrated optical spectrometers and quantified. The spectrometer was capable of analyzing elements in the parts per million (ppm) level.

The powder catalyst samples were digested using hydrofluoric acid (HF, Fisher Scientific, 50% v/v). Approximately 10-20 mg of catalyst was placed in polypropylene test tubes. Afterwards, 3 mL HF was added to dissolve the solid samples for 24 h at ambient temperature. This method is commonly applied for trace metal analysis in soil samples [18]. Each test tube was then visually inspected to ensure complete dissolution. Afterwards, 2 mL of the digested sample was extracted and placed in a separate test tube and diluted with DI water to a 2:14 dilution factor. This mixture was then tested for Au metal content.

The gold content in the nanotubes films was estimated by measuring the Au remaining in the supernatant after Au deposition. Approximately 2 mL of the supernatant was added to a polypropylene test tube and diluted with DI water to a 2:14 dilution factor. This mixture was analyzed for Au content using the ICP spectrometer. The amount of Au loaded on the TiNT films was calculated based on the difference between

the concentration before and after deposition. In addition, to investigate the accuracy of the measurement using the supernatant as compared to using the actual powder, eight TiNT films were loaded with different amounts of Au. The photocatalyst was then removed from the metal substrate by scraping the nanotube film. The flakes were crashed and the powder obtained was dissolved in HF for 24 h. After dilution in DI water, the Au content of the solutions were measured and compared with that from the supernatants used for Au loading.

2.3.3 Optical Characterization

The transmission and absorption properties of the photocatalysts were assessed by using UV-Vis spectroscopy (50 Bio UV-Visible Spectrophotometer, Varian Inc.). The absorption coefficient (α) was determined using the following equation [20]:

$$\alpha = 2.303\frac{A}{d} \tag{2.1}$$

where A is absorbance and d is the film thickness. Absorbance is also called the optical density, and it is related to the optical transmission (T) by the following relationship:

$$A = -\log\left(\frac{I}{I_o}\right) = -\log T \tag{2.2}$$

The absorption data was analyzed using the Tauc plots method [19]. In the high absorption regions α obeys the following relation [19, 20]:

$$\alpha h\nu = B\left(h\nu - E_g\right)^n \tag{2.3}$$

In equation (2.3), B is a constant, h is the Plank constant, ν is light frequency, and E_g is the optical bandgap energy of the material. The index n may assume one of the values, 2, 3, ½ and 3/2 indicating the type of electronic transitions [20]. Tauc plots of $(\alpha h\nu)^n$ versus $h\nu$ were obtained for the different photocatalysts tested.

2.3.4 Surface Area Measurements

The electrochemical surface areas of the photoelectrodes were calculated using data obtained from cyclic voltammetry (CV) [21]. A computer-controlled potentiostat (Gamry Instruments Series G750) was used to record the CV scans.

The total nanotube-films and powder-films electrode areas were accomplished using a 3-electrode cell: the working electrode was the photoanode; the counter electrode was a Pt foil; the reference electrode was a saturated mercury/mercury oxide electrode (saturated KOH, Koslow Scientific Company) Hg/HgO (0.0998 V vs. SHE), and the electrolyte was 1.0 M potassium hydroxide (KOH, ACS grade Fisher Scientific). The voltammograms were taken in a narrow voltage range (20-40 mV vs SHE) using different scan rates (0.5-200 mV/s). The current in the middle of the potential range was then plotted as a function of the scan rate. Charging of the double layer is the only process that takes place in this voltage range, since the plot is linear. The slope of this line has units of capacitance, and it is called film capacitance. The capacitance of the film can be compared with a reference capacitance for TiO_2 (50 $\mu F/cm^2$) and then total surface area based on the double layer capacitance can be obtained [21].

The electrochemical surface areas of supported Au photocatalysts were also measured via voltammograms taken in the vicinity of the oxygen adsorption/desorption potentials. Oxygen is chemisorbed in a monatomic layer with a one-to-one stoichiometry to the surface Au metal atoms over the range of 0 to 1.4 V vs SHE [21]. The area under the adsorption (desorption) peak gives the charge accumulated, and the surface area is obtained by dividing this charge by the reference capacitance, which for Au is 390 mC/cm^2 [21]. The Au electrochemical surface area measurements were accomplished

using a 3-electrode cell: the working electrode was the photoanode; the counter electrode was a Pt foil; the reference electrode was a saturated mercury/mercury sulfate electrode (saturated K_2SO_4, Koslow Scientific Company) Hg/Hg_2SO_4 (0.658 V vs. SHE), and the electrolyte used was 0.1 M sulfuric acid (H_2SO_4, Fisher, ACS grade).

Surface areas and pore size distributions for the powder samples were also measured via BET N_2 physisorption using a Micromeritics ASAP 2010 instrument. All of the samples were degassed under vacuum at 300 °C until the static pressure fell below 5 μm Hg. Typically, this required 5 h of degassing. The surface area was determined using eight P/P_0 values ranging from 0.06 to 0.2 for N_2 physisorption.

2.3.5 Point of Zero Charge

The point of zero charge (PZC) for a material is defined as the pH value for which the net surface charge is zero, at some ambient temperature, applied pressure, and aqueous solution composition [22]. In solution, the hydroxyl groups at the surface of the oxide become protonated (positively charged) at pH values below the PZC, and deprotonated (negatively charged) above the PZC [23].

The point of zero charge (PZC) was calculated using the potentiometric mass titration method [22-25]. Titanium dioxide (P25, S_{BET} = 54 m^2/g) and TiNT powders (peeled from the substrate and grained, S_{BET} = 10 m^2/g) were used. About 18 mg of the oxides were suspended in 6 mL of DI water at ambient temperature for 20 h to reach an equilibrium pH value. A small volume of 0.01 M Na_2CO_3 (a weak base) was added to deprotonate a significant part of the surface sites, rendering the surface negative. This was repeated with varying volumes of the base solution. In order to protonate the oxide surface, small volumes of a 0.01 M H_2SO_4 (a strong acid) solution were added. This step

was also repeated with different amounts of the added acidic solution. The initial and final pH values were recorded for each experiment.

2.3.6 Photoelectrode Fabrication

The photoelectrodes were prepared using either the powder photocatalysts or the TiNT films.

The powders (TiO_2 and Au/TiO_2) were mixed with polyethylene glycol (PG, M.W. 10,000, Polysciences, Inc.) and grinded in a ball-milling machine (LABMill-8000, ACM, OD 1/4" balls) to form an even paste. The paste was then deposited onto conductive glass (Indium Tin Oxide, ITO, film, R_s = 8-12 Ω, Delta Technologies Limited) and non-conductive glass (quartz, GM Associates Inc.). The deposition on conductive glass was done using the doctor-blade technique [10]. Two pieces of thin tape (Scotch® Magic™ Tape, ~ 10 μm thick) were fixed to the edges of the glass; then a drop of the paste was placed between the tapes using a small pipette. The excess was removed using a glass rod. Samples were dried at 80 °C in vacuum. Spin coating was used to make a TiO_2 film on quartz. The photocatalyst films deposited on quartz and ITO glass were used for the optical and photoelectrochemical measurements, respectively.

The electrodes made with the TiNT films, were prepared by attaching the TiNT film to a glass substrate (Microscope slides, Fisher Scientific) using a Bisphenol A based epoxy (DeVon 5 Minute® Epoxy, Fisher Scientific). The excess surface of the film was painted with white enamel, leaving a small uncovered area of ~ 0.3 cm^2.

2.4 RESULTS AND DISCUSSION

2.4.1 Titanium Dioxide Powders Fabrication

High surface area titanium dioxide powder catalysts were prepared using the sol-gel precipitation method, $TiCl_4$ hydrolysis process, and hydrothermal method. The hydrothermal method produced very small disordered nanotubes and nanorods. While the sol-gel and $TiCl_4$ hydrolysis gave spherical like nanoparticles of TiO_2.

2.4.1.1 Titanium Dioxide Powder Catalyst

The sol-gel method, using titanium butoxide precursor, produced a gel composed of titanium hydroxide and other organic compounds. This gel was calcined to remove the organics in the mixture. The final particle size and surface area depended on the calcination temperature. Thermal treatment at 450°C in air for 4 h led to the formation of the anatase crystal phase.

Table 2.1: TiO_2 prepared by hydrolysis of $TiCl_4$. The powders samples were calcined in air for 3 h.

Calcination Temperature (°C)	TiO_2 Phase	BET surface area (m^2/g)	Crystallite Size (nm)
as-prepared	amorphous	463 ± 30	---
300	amorphous	353 ± 30	---
400	anatase	206 ± 30	8.2 ± 1
450	anatase	120 ± 20	13.6 ± 1

Very high surface area TiO_2 powders were fabricated using the hydrolysis of $TiCl_4$. After precipitation the powder was washed with DI water and diluted acid to obtain a final pH of about 7. Since the as-prepared powder was amorphous, it was

calcined in air for 4 h at 450 °C to crystallize the material. The thermal treatment changed the particle size and also the surface area, as summarized in Table 2.1.

Figure 2.3 shows XRD patterns at different calcination temperatures for titania prepared by the hydrolysis of $TiCl_4$. While the as prepared material is amorphous, initial anatase peaks appeared at 300 °C, and complete transformation to anatase occurs at 450°C. The initial surface area of the amorphous, as-prepared material was 463 m^2/g; calcination at 450 °C decreased the surface area to 120, possibly due to collapse of the micropores.

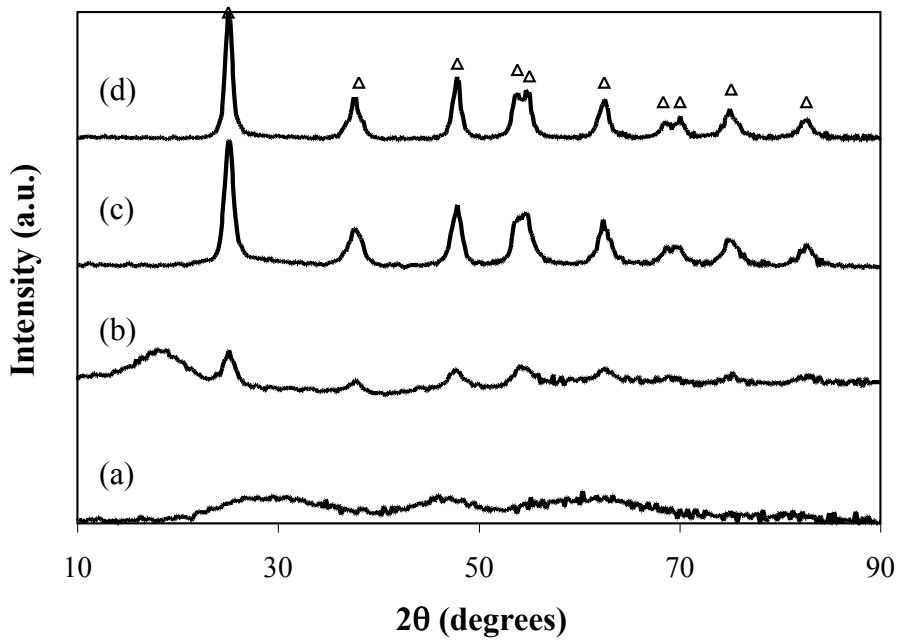

Figure 2.3: XRD patterns for TiO_2 fabricated by hydrolysis of $TiCl_4$ at different calcination temperatures (a) as-prepared, (b) 300 °C, (c) 400 °C, and (d) 450 °C. The (Δ) symbol indicates the anatase phase.

2.4.1.2 TiO_2 Disordered Nanotubes

Figure 2.4 shows a SEM micrograph of as-prepared titanium dioxide nanotube powders. The top inset is a TEM micrograph, which shows the dimension and structure

of the nanotubes. The as-prepared *tint* catalyst is an amorphous, white powder; in order to obtain crystallinity the powder was calcined in air for 4 h. Similar to the TiO_2 powder, the crystalline structure of the oxide changes with calcination temperature. The *tint* surface area also decreased with increased calcination temperature, due to an increase in particle size as summarized in Table 2.2.

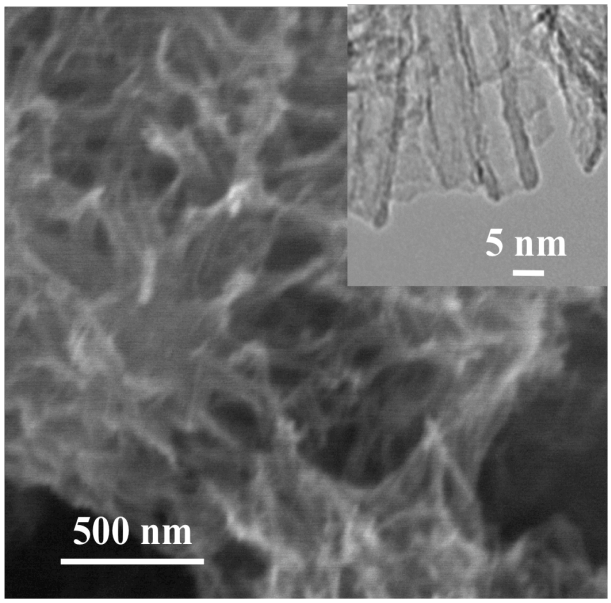

Figure 2.4: SEM micrograph of disordered titania nanotubes powder (*tint*). The inset is a TEM micrograph showing the details of the nanotube structure. The average external diameter was 10 nm.

Table 2.2: Summary of the fabrication parameters and the dimensions of disordered TiO_2 nanotubes. The powders were calcined in air for 3 h.

Fabrication Parameters		**Nanotube Dimensions**		
Calcination Temperature (°C)	**BET surface area (m^2/g)**	***OD* (nm)[1]**	***t* (nm)[2]**	***L* (μm)[3]**
As prepared	391 ± 40	5-10	1-2	0.3-0.6
400	291 ± 30	5-10	1.2	0.3-0.6
500	277 ± 30	8-12	1-3	0.2-0.5
600	226 ± 30	12-20	1-3	0.2-0.5
700	168 ± 30	12-20	2-5	0.1-04
750	77 ± 20	15-25	---	0.1-0.3

[1] *OD*: average outer diameter
[2] *t*: average wall thickness
[3] *L*: average length

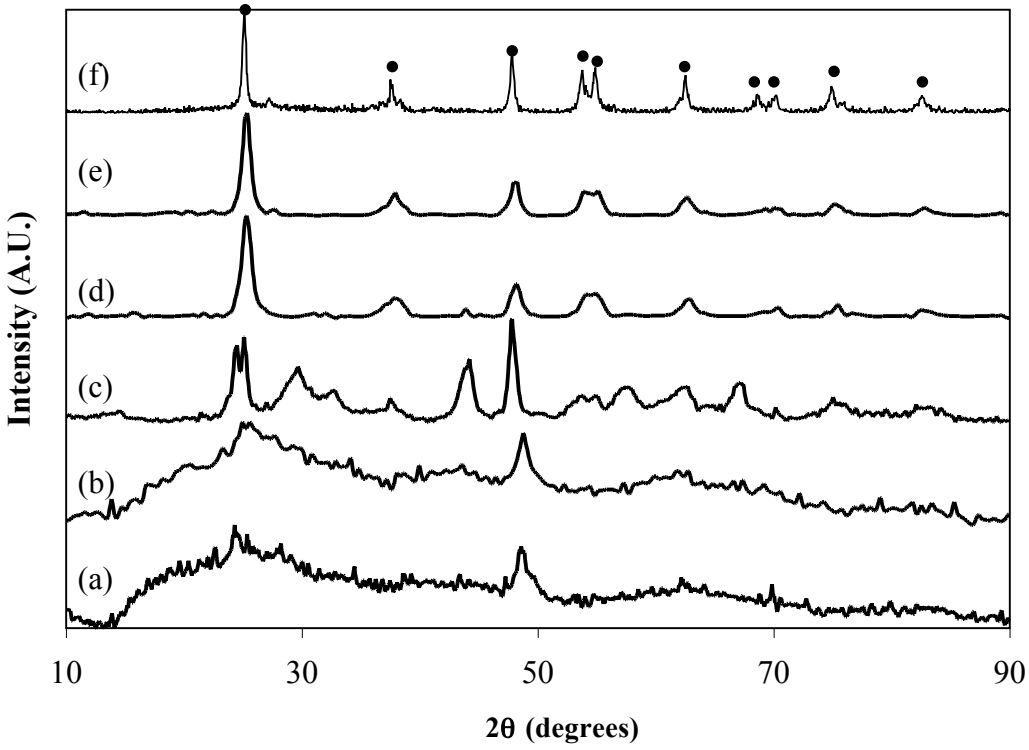

Figure 2.5: X-ray diffraction patterns for disordered TiO_2 nanotube powders calcined at different temperatures (a) as-prepared, (b) 400 °C, (c) 500 °C, (d) 600 °C, (e) 700 °C and (f) P25. Calcination was done in tube furnace with constant airflow for 3 h. The (•) symbol indicates the anatase phase.

Figure 2.5 shows XRD patterns for disordered TiO_2 nanotubes without thermal treatment and for nanotubes calcined at different temperatures. The transformation of the initial amorphous material to crystalline anatase phase does not start until the calcination temperature is 500 °C and the powder is completely transformed to anatase at 600 °C. Increasing the calcination temperature beyond 600 ° C led to the transformation of the anatase to rutile.

Furthermore, when the calcination temperature exceeds 700 °C the tubes collapsed and were converted into thicker nanorods. Figure 2.6 shows SEM micrographs of *tint* structures calcined at different temperatures.

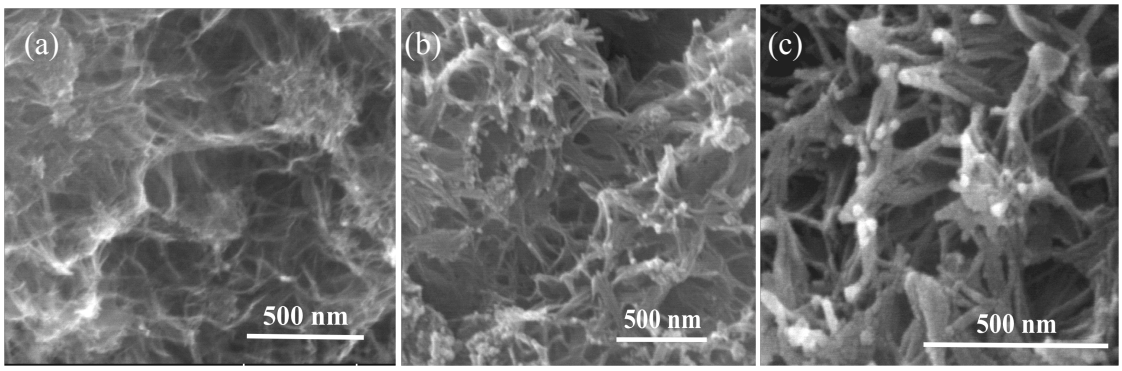

Figure 2.6: SEM micrographs for disordered TiO_2 nanotubes showing the change in structure. Sample (a) as-prepared, (b) calcined at 500 °C, and (c) calcined at 750 °C. Calcination was done under continuous airflow for 3 h.

2.4.2 Highly Ordered TiO_2 Nanotubes

Anodization of the Ti metal in acidified fluoride solution resulted in formation of highly ordered nanotubes. The mechanism of nanotube formation and results obtained by changing the anodization parameters are discussed in the following sections.

2.4.2.1 Nanotube Formation Mechanism

It has been proposed that the TiO_2 nanotubes grow as a result of a competition between an electrochemical oxide formation and a chemical dissolution of the oxide by the fluoride ions [4,26-29].

First, an oxide layer is formed due to interactions of the metal with O^{2-} or OH^- ions in the electrolyte. The overall reaction for oxidation of Ti can be represented as [29]:

$$Ti + 2H_2O \rightarrow TiO_2 + 4H^+ + 4e^- \tag{2.4}$$

Due to the applied electric field, the Ti-O bonds are broken - this step is called field-assisted dissolution, and metal Ti^{4+} cations dissolve in the electrolyte [4]. The free O^{-2} anions migrate towards the metal/oxide interface, to interact with the metal. At the same time, chemical dissolution of oxide in HF (or fluoride solution) electrolyte takes place, which plays a key role in the formation of nanotubes rather than a nanoporous structure. The following reaction represents the initiation of the pore formation center:

$$TiO_2 + 4H^+ + 6F^- \rightarrow TiF_6^{2-} + 2H_2O \tag{2.5}$$

Field-assisted dissolution dominates over chemical dissolution due to the relatively large electric field across the thin oxide layer. Small pits are formed on the oxide surface due to the localized dissolution of the oxide (pore formation center). These pits convert into bigger pores and as a result the pore density increases. The pore growth occurs due to the inward movement of the oxide layer at the pore bottom (barrier layer). The Ti^{+4} ions migrating from the metal to the oxide/electrolyte interface dissolve in the electrolyte [4,28,29], as illustrated in Figure 2.7.

Nanotube growth (film thickness) ceases when the chemical dissolution rate of the oxide at the top surface becomes equivalent to the rate of inward movement of the metal/oxide boundary at the bottom of the tube [4].

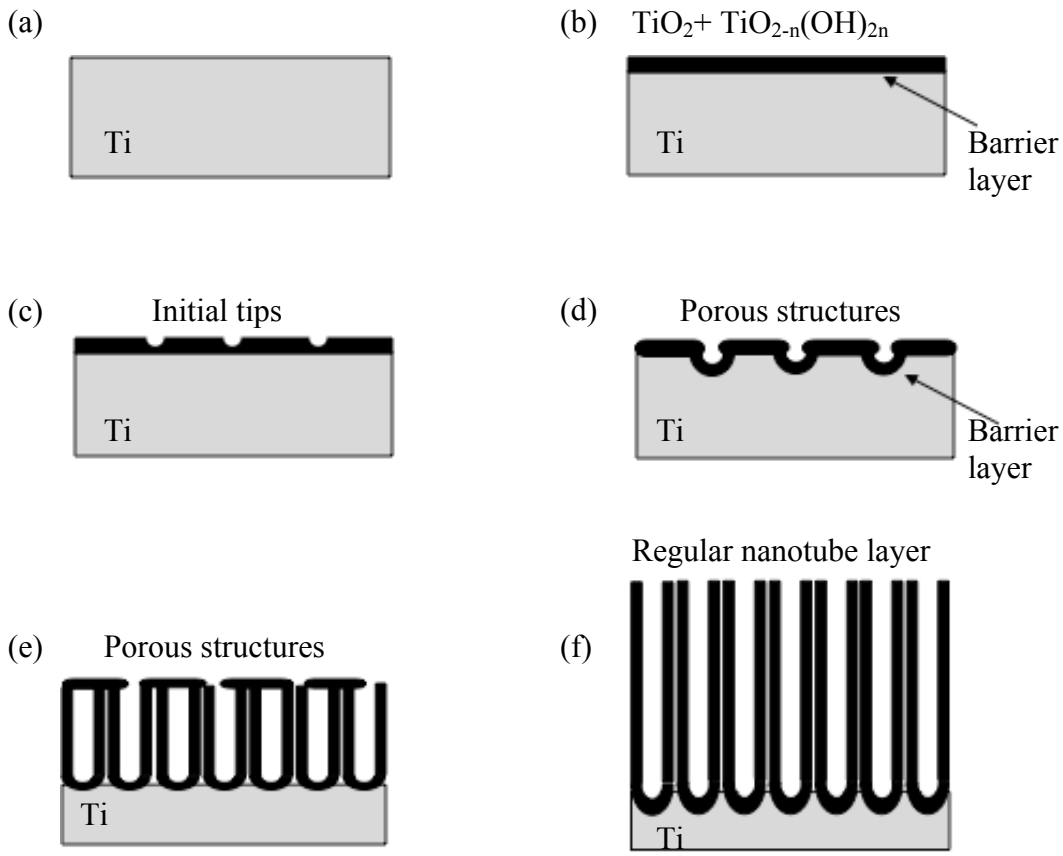

Figure 2.7: Schematic representation of the evolution of a nanotube array at constant anodization voltage: (a) initial Ti metal, (b) oxide layer formation, (c) pit formation on the oxide layer, (c) growth of the pit into scallop shaped pores, (d) metallic part between the pores undergoes oxidation and field assisted dissolution, (e) initial porous structure, and (f) fully developed nanotube array [4,29].

Higher anodization voltages increase the oxidation rate and the field-assisted dissolution; therefore longer nanotubes can be grown before equilibrating with the chemical dissolution [4,27]. The chemical dissolution is the key for the formation of

nanotubes. This dissolution reduces the thickness of the oxide layer (barrier layer) keeping the electrochemical etching process active. If the electrochemical etch proceeds faster than the chemical dissolution, the thickness of the barrier layer increases, which reduces the electrochemical etching to the rate determined by chemical dissolution. The chemical dissolution rate is determined by the fluoride concentration and solution pH [27-29]. Increases in pH and F^- concentration increase the dissolution rate.

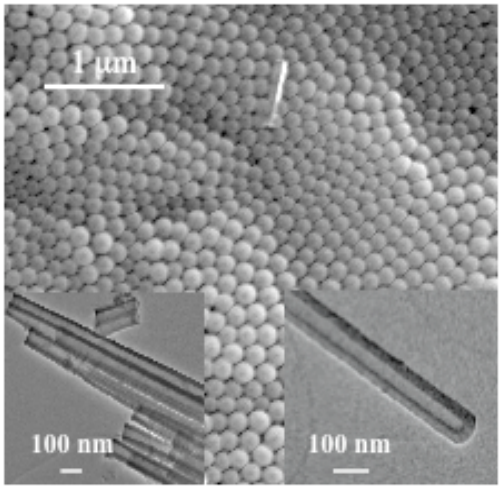

Figure 2.8: SEM micrographs showing the bottom view of the nanotubes. Lower left inset shows a TEM picture of the nanotubes, and the lower right inset is a TEM of a single nanotube. These nanotubes were anodized at 40 V for 3 h with ethylene glycol electrolyte.

Also, there is a pH gradient established between the pore tip and the bottom of the pore, where the dissolution due to the lower pH values leads to accelerated TiO_2 dissolution and pore penetration into the Ti substrate [30,31].

2.4.2.2 Anodization Results

Nanotubes produced using the anodization method have very smooth walls and well-defined shapes with semispherical bottoms closing them (Figure 2.8 and Figure 2.9).

Long nanotubes were obtained using the appropriate electrolyte (see following section for more detail). While long tubes are desired, a disadvantage of long anodization times is the appearance of debris covering most of the surface and blocking access to the nanotubes. This debris or nanograss is due to thinning of the tube walls closer to the top entrance by the chemical dissolution process [27]. This reduction in wall thickness leads to the collapse of tube tops [29]. In order to remove this debris, further cleaning by sonication for about 3 min was needed. Sonication cleans about 65 to 90% of the total top entrance areas of the nanotubes films. Visual inspection using SEM was used to characterize the cleanliness of the tubes. Figure 2.9.b shows the nanotubes after sonication; the inset shows the open tube entrances.

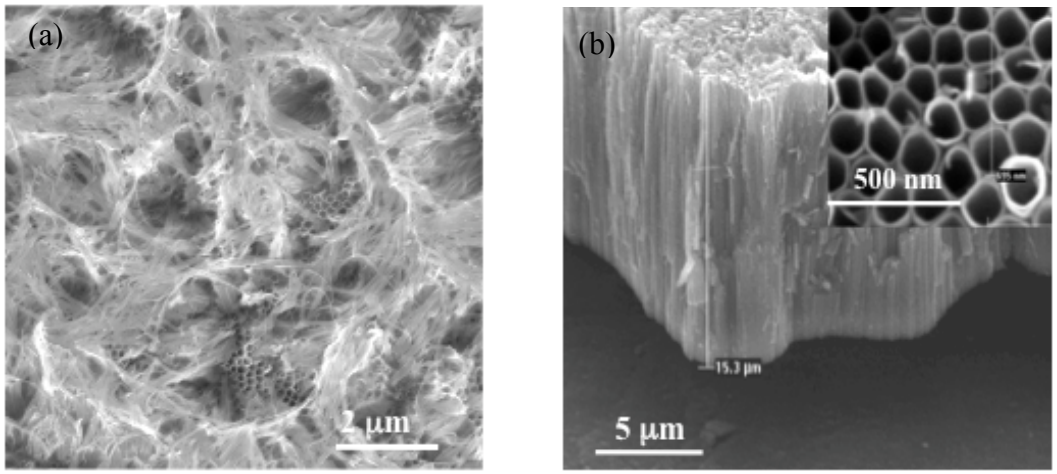

Figure 2.9: (a) SEM micrograph for an as-prepared TiNT sample electrode. (b) Nanotube film after sonication. Inset shows the cross section view of the nanotubes. The anodization was done at 40 V for 4 h; and the electrolyte used contained 0.3 wt % NH_4F, 2 wt% DI water and ethylene glycol.

2.4.2.3 Different Anodization Electrolytes

Different solvents were used to prepare the anodization electrolytes; the final nanotube structures depended on the electrolyte used. Figure 2.10 shows SEM micrographs of TiNT films fabricated with (a) water, (b) glycerol, and (c) ethylene glycol, respectively.

Table 2.3: Summary of anodization conditions and nanotube dimensions for the three electrolytes used for the fabrication of highly ordered TiO_2 nanotubes. The dimensions were measured for the as-prepared samples.

Anodization Parameters				**Nanotube Dimensions**		
Electrolyte	**Fluoride Ions (F^-)**	**Time (h)**	**Voltage (V)**	***OD* (nm)[1]**	***t* (nm) [2]**	***L* (µm)[3]**
Water	0.25-0.5 wt% HF	0.5-2	5-25	80-100	10-20	0.3-1.2
Glycerol	0.25-0.5 wt% HF	0.5-10	5-60	30-100	5-20	0.5-3
Ethylene Glycol	0.25-0.5 wt% HF and NH_4F	0.5-30	5-60	40-200	10-40	1-125

[1] *OD*: average external diameter
[2] *t*: average wall thickness
[3] *L*: average length

Short nanotubes were fabricated with the water-based electrolyte, however, when the applied voltage was higher than 25 V and the anodization time was increased to more than 2 h, the tubes did not grow more than 1.0 µm. It appears that with H_2O after 1 h of anodization the electrochemical oxide formation and a chemical dissolution equilibrate, and there is no further increase in nanotube length. The nanotube diameters obtained with the water-based electrolyte were approximately 100 nm. Besides their short length, the walls of the tubes were also corrugated (Refer to Figure 2.9.a) presenting ripples; it has been reported that these features correlate with current oscillations observed during anodization [28]. The amount of HF was also varied from 0.1-0.5 wt%. Increasing the HF

concentration led to shortened anodization times, and concentration higher than 0.5 wt% led to rapid oxidation of the Ti metal without nanotube formation.

In contrast to the results obtained with H_2O, when using glycerol/HF mixtures tubes have very smooth walls and smaller diameters (~50 nm) [32]. It has been reported that the smoothness of the walls could be originated from damping local spikes in the flux of reaction species (locally different pH values) within the tube when using highly viscous electrolytes [28]. The initial currents with glycerol were about one third lower to those recorded for water electrolyte and the final equilibration currents were as low as 1-3 mA for the same concentration of F^- ions. Lower current also led to longer anodization times (up to 10 h) and longer tubes (up to 125 μm). Increasing the applied voltage (40 - 60V) yielded tubes with diameters up to ~ 80 nm.

The third solvent used was ethylene glycol (EG). The viscosity of EG is higher than that for water, but lower than that for glycerol. Also its electric conductivity is higher than glycerol, which allowed the use of higher currents than for glycerol electrolytes. These higher currents led to shorter anodization times to grow tubes with the same length. The increase in voltage (40-60 V) gave nanotubes with average diameter up to 200 nm.

In summary, organic electrolytes were able to produce longer and smoother nanotubes compared to the ones obtained with water-based electrolyte. Table 2.3 gives a summary of the nanotubes dimensions obtained with the three electrolytes.

The dependence of results on viscosity suggests that the dominant growth limitation factor is diffusion of the reactants to the pore tip or reaction products away from the tip [11,32]. The lower current densities in the viscous electrolytes indicated

diffusion control of the process and hence dependence of the diffusion constant on the viscosity [32]. Therefore, a lower current density with lower local acidification and lower amount of competing chemical dissolution is obtained for the viscous electrolytes.

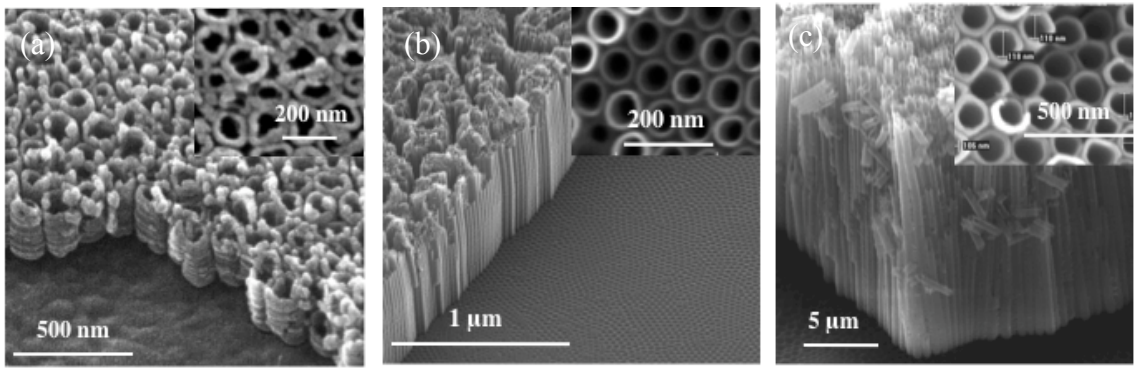

Figure 2.10: SEM micrographs for TiNT films fabricated with (a) water and 0.25 wt% HF, and 20 V for 1 h, (b) glycerol and 0.5 wt% HF, and 20 V for 3 h, and (c) ethylene glycol and 0.25 wt% NH_4F, and 60 V for 2 h. The samples were sonicated to remove debris.

Also, with organic electrolytes the availability of oxygen is more difficult in comparison to water and results in a reduced tendency to form oxides. This may in turn allow for thinner or lower quality barrier layers through which ionic transport may be enhanced [28,30]. The incorporation of organic components from the electrolyte into the anodic oxide film is known to lower the relative permittivity of the film and increase its dielectric breakdown potential [30]. The higher breakdown potential of the oxide in nonaqueous electrolytes allows for a larger range of anodization potential in which nanotube arrays can be achieved [30,34].

Nanotube films were also fabricated using different combinations of DI water, glycerol and ethylene glycol. Glycerol was only used in the early stages of this study and discarded because its use led to longer anodization periods compare to the ones for water

and ethylene glycol. Various amounts (from 10 to 0 wt%) of water were added to ethylene glycol based electrolytes to study its influence in the formation of nanotubes. The addition of water to ethylene glycol electrolytes resulted in shorter anodization times and higher current densities than the ones obtained with only ethylene glycol for the same applied voltage. In general decreasing the water content in the electrolyte with no more than 2% yielded large diameter, longer and smoother nanotube arrays. Therefore, the electrolyte used for the rest of the research work was composed of 2.0 wt% DI water and 0.25 wt% NH_4F balance in ethylene glycol.

2.4.2.4 Anodization Parameters

Various nanotube films were grown using Ti foils and the ethylene glycol based electrolyte at different anodization parameter conditions. First, the anodization time was varied while the applied voltage was kept at 40 V. Then, the anodization voltage was changed while the anodization times were kept to 4 h. The results showed that the dimensions of the nanotubes depended on both of these parameters. The applied voltage appears to govern the nanotube thickness and diameter. Figure 2.11.a shows a near linear relationship between tube diameter and voltage. The line slope was approximately 4, which gives a relationship between the diameter and the applied voltage according to equation 2.6 (in this eaquation OD is the outer diameter and V_{app} is the applied voltage). The influence of voltage on the nanotube length seems to also follow a linear relationship (refer to Figure 2.11.b), however the length seems to level off after it reaches 35 μm. Additionally, the wall thickness seems to obey a linear relationship given in equation 2.7 (see Figure 2.12), where t is the wall thickness. Similar results have been reported by Yosuda *et al*. [29].

$$OD \sim 4V_{app} \tag{2.6}$$

$$t \sim 2.2V_{app} \tag{2.7}$$

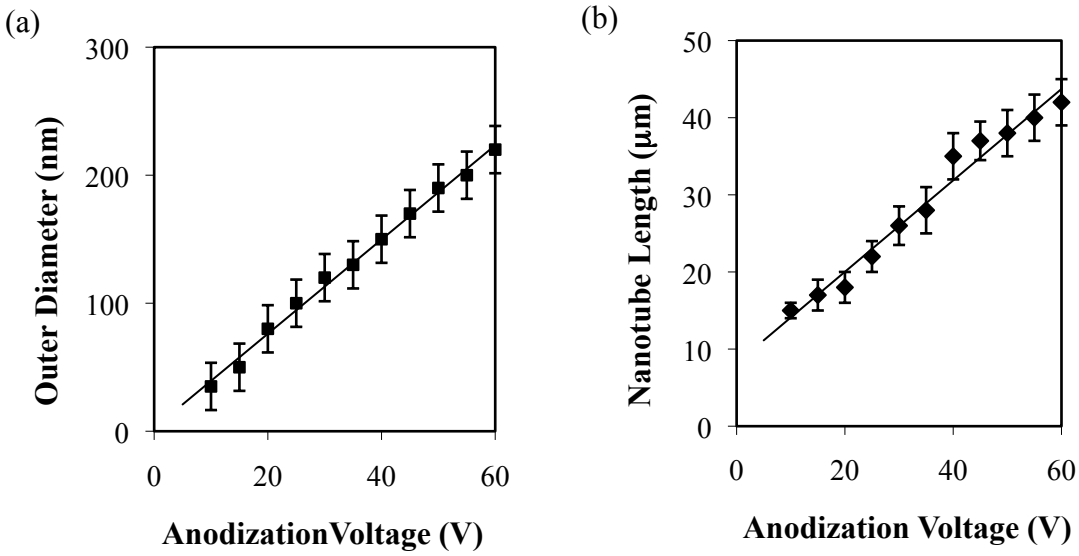

Figure 2.11: Influence of anodization voltage on the final geometry of the nanotubes plots: (a) nanotube outer diameter and (b) nanotube length vs. anodization voltage. The anodization time was 4 h.

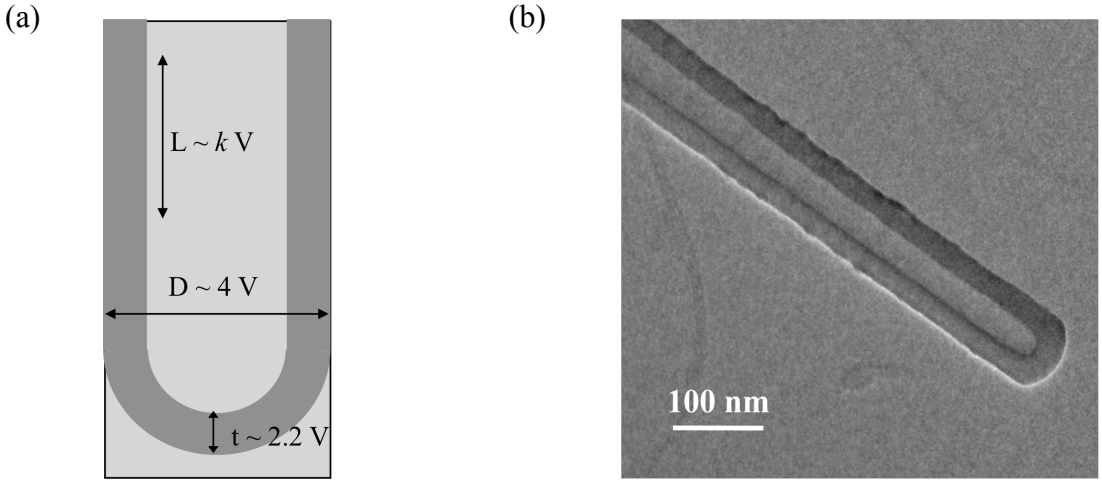

Figure 2.12: (a) Schematic representation of the nanotube dimension dependence on the applied potential [27]. (b) SEM of a single nanotube, fabricated at 25 V for 2 h, *OD* ~ 105 nm, *t* ~ 55 nm and *L*~ 6 µm; these dimension are in agreement with the relationships given in (a).

Figure 2.13 shows a plot of nanotube length versus anodization time, which indicates a rapid increase in length up to ~ 25 h. Nanotubes as long as 125 μm were obtained for this anodization time (see Figure 2.14). Longer periods of anodization did not increase the length of the tubes indicating that equilibrium has been reached between oxidation and dissolution. This cessation in nanotube growing may also be related to limited diffusion of electrolyte to the bottom of the very long nanotubes.

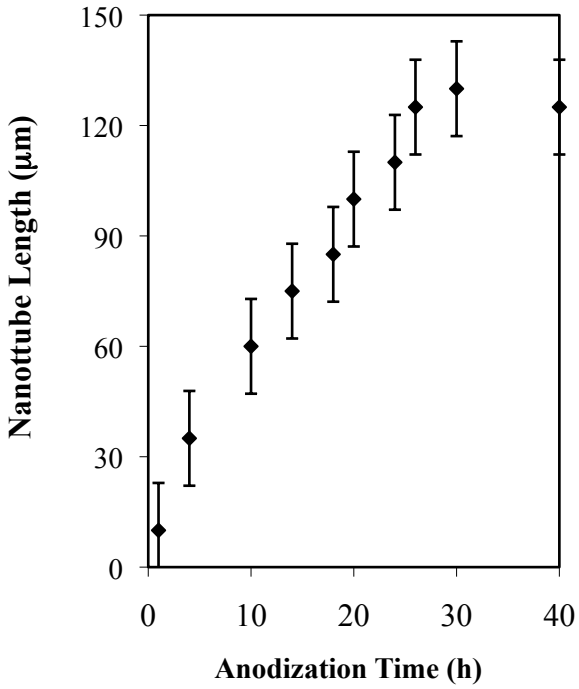

Figure 2.13: Nanotube length versus anodization time for the as-prepared samples fabricated using ethylene glycol based electrolyte at 40 V. Data was taken from as-prepared nanotube films.

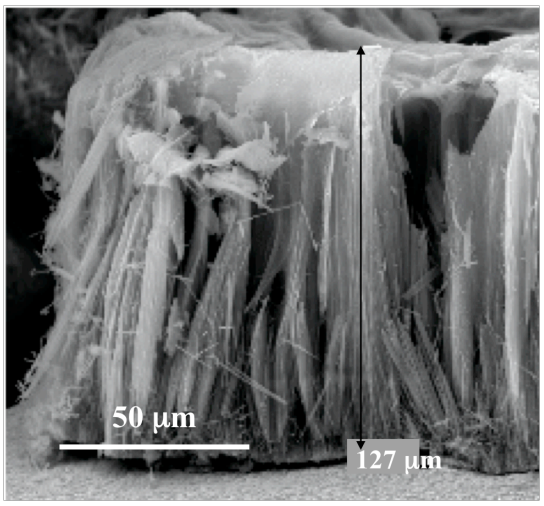

Figure 2.14: SEM micrograph showing exceptionally long TiNTs. The anodization time was 30 h and the voltage was 40 V. The electrolyte used was 98 wt% ethylene glycol and 0.3 wt% NH_4F.

2.4.3 Structural Characterization

As prepared TiNTs are amorphous, and crystallinity is obtained by high temperature calcination. Figure 2.15 shows SEMs of the as-prepared TiNTs and TiNTs calcined at 500°C. These nanotube films were fabricated with 2 wt% DI water, 0.3 wt% NH_4F electrolyte balanced in ethylene glycol. The films were calcined at different temperatures in dry air for 3 h. X-ray diffraction patterns for TiNTs are shown in Figure 2.16. The XRD patterns indicate that the as-prepared TiNTs were amorphous, characteristic peaks for Ti metal (from the substrate) were observed as well. Calcining the nanotubular arrays resulted in transformation of the amorphous material into crystalline phases. Thermal treatments above 300 °C started to convert the amorphous nanotubes into anatase; large peaks from the Ti substrate were also detected. At 500 °C most of amorphous TiO_2 was transformed into anatase. Above 500 °C, the rutile phase appeared in the XRD pattern. Calcination treatments that led to a complete conversion to rutile have not been successful, as the tubes tend to suffer from significant morphological

deterioration at approximately 700 °C [27]. Also, the signal from the Ti support decreases above 500°C and completely disappears at 800 °C.

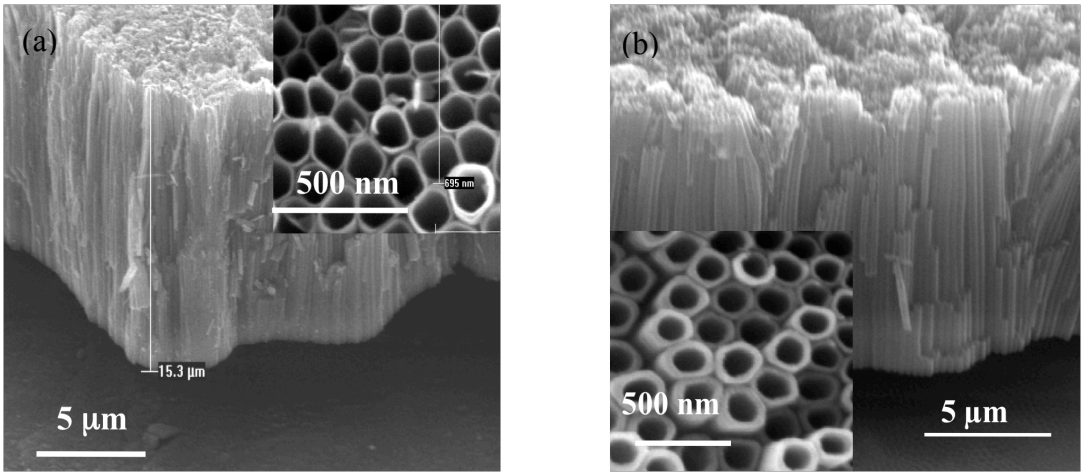

Figure 2.15: SEM micrographs for TiNTs (a) as-prepared and (b) calcined at 500°C in dry air for 3 h. The insets show the nanotube top view. The tubes were anodized at 40 V applied voltage for 4 h in ethylene glycol.

The heating and cooling rates affected the final structure and integrity of the nanotubes. Figure 2.17 shows SEM micrographs of nanotubes calcined at different heating rates. Faster heating rates (i.e. 10 °C/min) led to the destruction of the nanotubes. In order to keep the tubular structure and smoothness of the tubes, they were calcined with heating and cooling rates of 1°C/min.

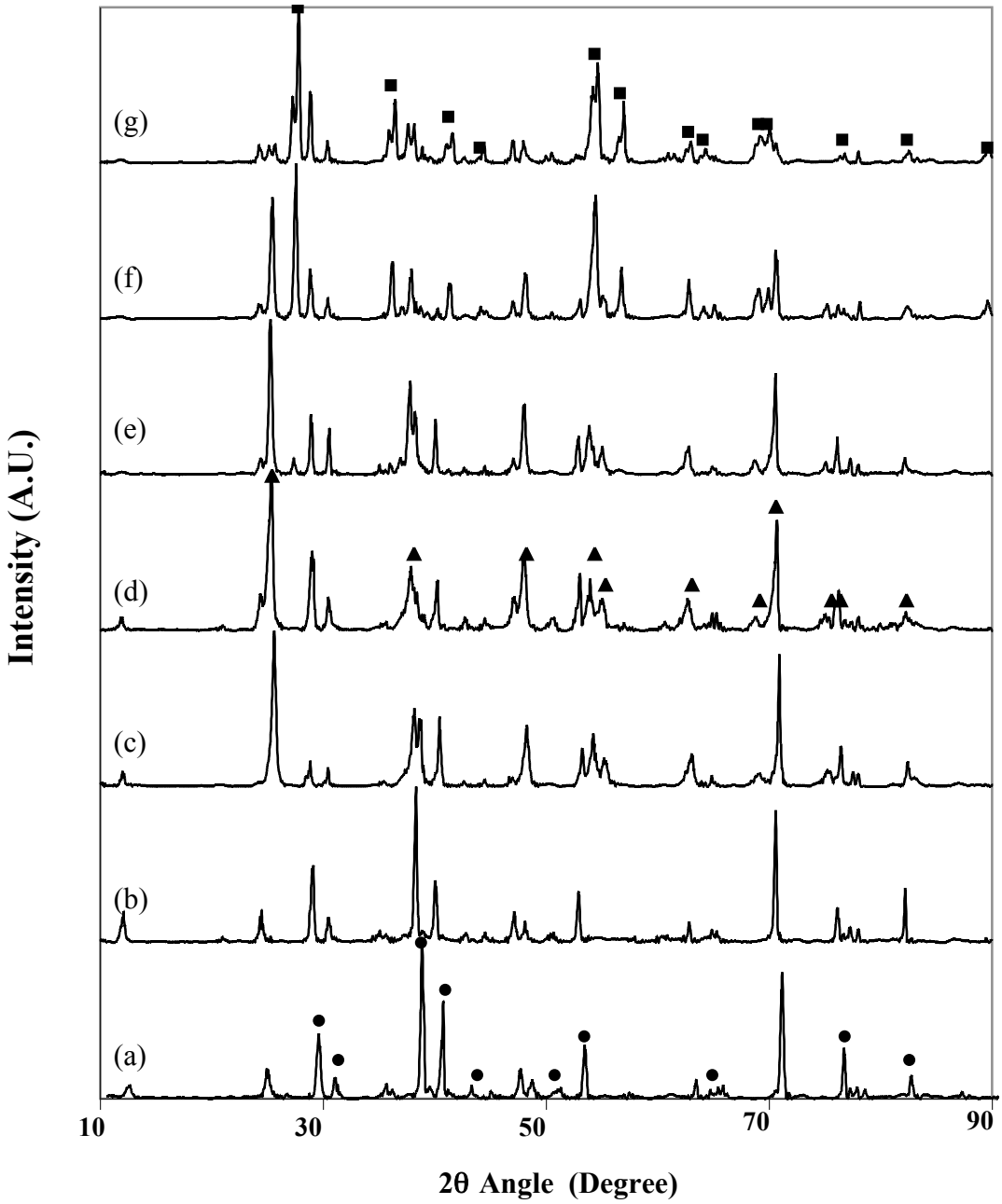

Figure 2.16: XRD diffraction patterns for TiNT films calcined in air for 3 h (a) as-prepared, (b) 300 °C, (c) 400 °C, (d) 500 °C, (e) 600 °C, (f) 700 °C, and 800 °C. The heating and cooling rates were of 1°C/min. The following symbols represent (•) Titanium, (Δ) Anatase, and (■) Rutile.

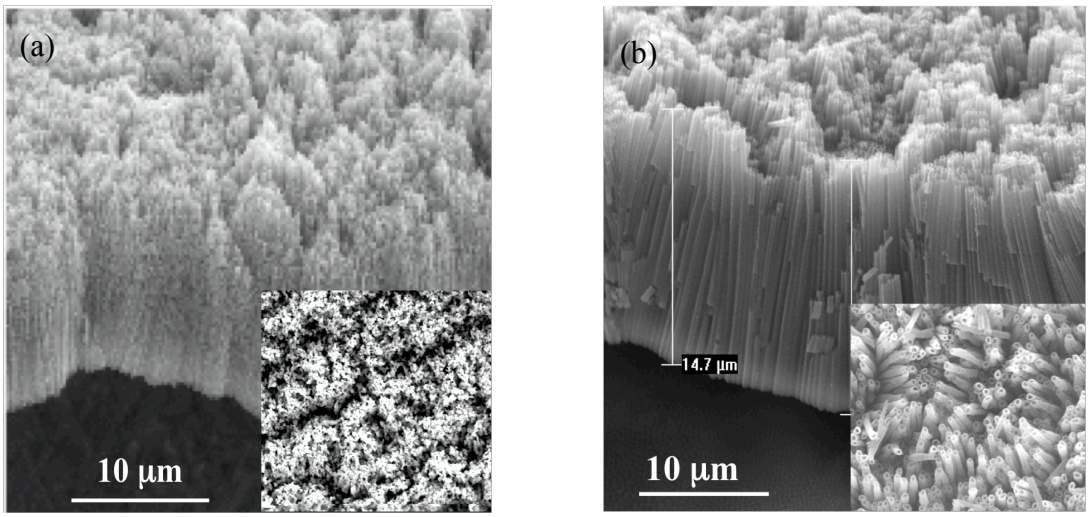

Figure 2.17: SEM Micrographs for nanotube films calcined in air at 500 °C for 3 h with a heating and cooling rate of (left) 10 °C/min and (right) 1 °C/min. The tubes were anodized at 40 V applied voltage for 4 h in ethylene glycol.

The specific temperatures and calcination rates can significantly affect the resulting crystallite size and the tube morphology under adequate annealing conditions. For example, the anatase crystallite sizes increased with temperature until 650°C, then decreased beyond this point. However for the rutile phase, the grain sizes increased with temperature up to 650 °C, and then stayed the same (Figure 2.18). The nanotube array structures were stable up to ~700 °C. Between 700 and 750 °C the samples seemed to start to crack. Above this temperature the tubular structure completely collapsed leaving dense rutile crystallites (Figure 2.19).

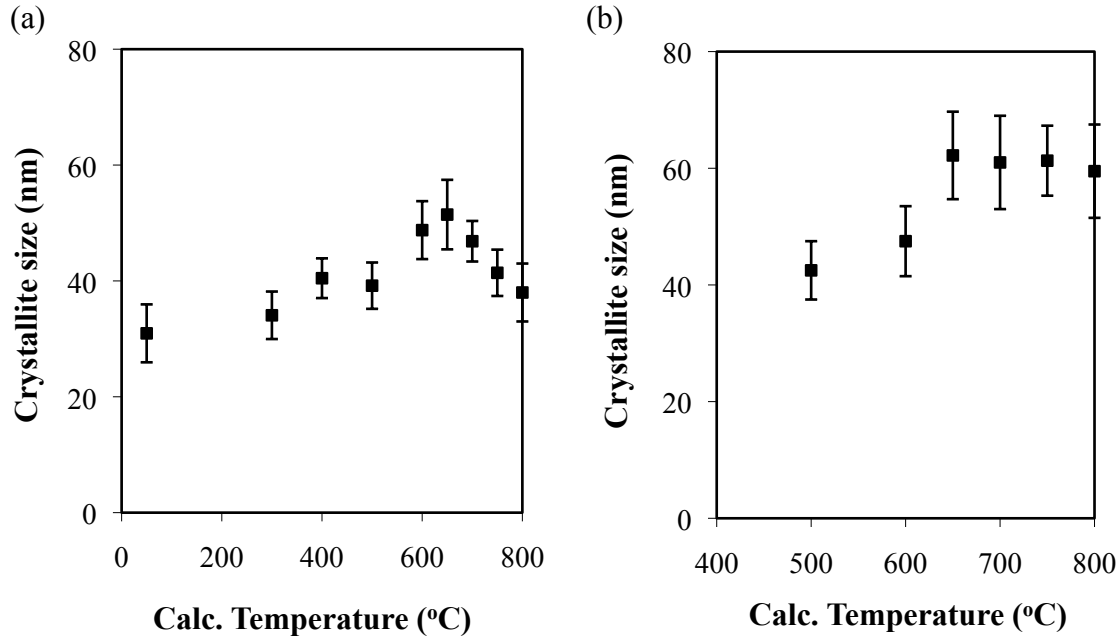

Figure 2.18: Crystallite size data for TiNT calcined at different temperatures, (left) anatase, (right) rutile phase. Nanotubes were fabricated at 40V for 4 h in ethylene glycol. The temperature rate was 1°C/min for all the cases.

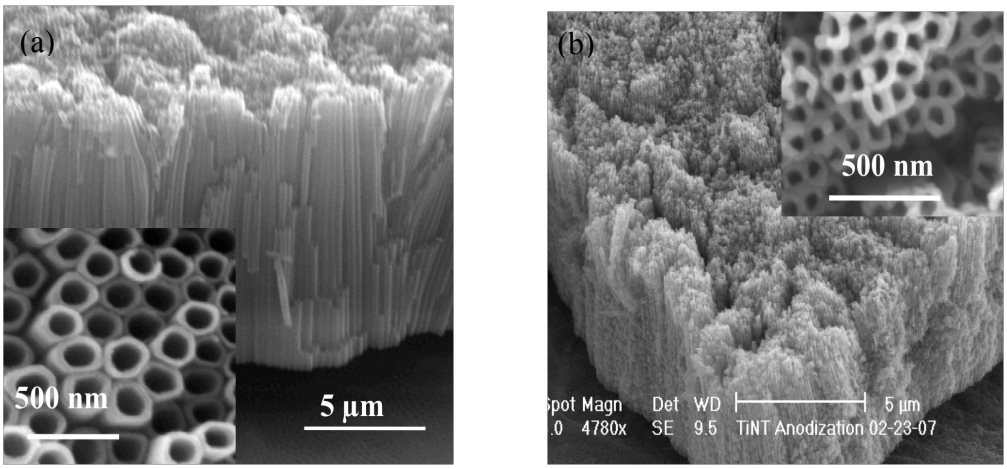

Figure 2.19: SEM micrographs for TiNTs calcined at (a) 500 °C and (b) 750 °C in air for 3 h. The calcination heating and cooling rates were 1°C/min. The TiNT films were anodized at 40 V for 4 h.

Grimes *et al*. have shown, using high resolution TEM and elemental analysis, anatase crystals were formed at the nanotube-Ti substrate interface region as a result of the oxidation of the metal at lower calcination temperatures. At higher temperatures, the rutile crystallites originate from the oxide layer (formed by oxidation of Ti metal) underneath the nanotubes. Therefore, nanotubes calcined at temperatures between 500 and 600 °C, might be considered as anatase crystallites stacked in a cylindrical shape on a rutile surface substrate [1,4]. This has been confirmed by using X-ray diffraction of nanotubes and the substrate after removing the tube array using sonication and calcining it in air for 3 h.

Table 2.4: BET surface areas for the different photocatalysts studied in this research work.

Catalyst	**Preparation Method**	**Calcination Temperature (°C)**	**Crystalline Phase**	**S_{BET} (m^2/g)**
TiO_2	Alfa Aesar	---	Anatase	164 ± 20
TiO_2	P25	---	75 % Anatase, 25 % Rutile	54 ± 10
TiO_2	Hydrolysis TCl_4	600	Anatase	226 ±40
TiO_2	Sol-gel	450	Anatase	90 ± 15
tint	Hydrothermal	600	Anatase	226 ± 40
TiNT	Anodization	500	Anatase	20 ± 5
Au/TiO_2	P25	---	---	54 ± 10
Au/*tint*	Hydrothermal	---	---	174 ± 20
Au/TiNT	Anodization	---	---	12 ± 3

2.4.3.1 Surface Areas

An important property of a catalyst is its surface area. In the case of powder catalysts the physical surface areas were measured by the BET method. The surface areas (S_{BET}) for the different catalysts fabricated in this research project are summarized in Table 2.4. Surface areas for Au loaded onto TiO_2 supports are also shown (more detail

regarding Au supported catalyst follows this section). The addition of Au nanoparticles to the TiO_2 did not change the surface area of the final product (Au/TiO_2). The BET surface areas for the TiNT and Au/TiNT films were also measured. To accomplish that, the TINT films were removed from the substrate and ground to form a powder. This powder was then analyzed using N_2 physisorption.

2.4.4 Gold Deposition on TiO_2 Powders

Haruta developed the deposition-precipitation (D-P) method [14]. This method offers better results in terms of catalytic activity than the impregnation method, which leads to large Au particles [15,40]. However, this method is not easily reproducible because there are many parameters that affect the surface chemistry during preparation. For example, the Au particle size of gold depends on the temperature and the pH [15]. Another disadvantage is that the DP method works well with oxides with point of zero charge greater than 5.0, like TiO_2 (PZC ~ 5.8), but it is not suitable for silica (PZC ~ 2.0), tungsta (PZC ~ 1.0) [36], or activated carbon [37]. In addition, in the DP method the total amount of Au present in solution cannot be deposited on the support. In fact, on the most commonly studied support, TiO_2, the maximum gold loading is much lower (3 wt.%) than the nominal amount of gold present in solution (13 wt.%) when the pH is in the range 7–10, but it is higher (8 wt%) at a pH closed to the PZC of the oxide (PZC ~ 6) [36]. An increase of the gold loading could be achieved by decreasing the pH of the solution below 6, but that occurs at the expense of the gold particles size, which strongly increases [37-40].

TEM has been used to determine gold particle size distribution and ICP-OES was used to determine the Au loadings.

Table 2.5: Summary of Au loadings for different TiO_2 supports. The nominal loadings used were 2 and 5 wt%. The DP method was used and the pH solution was kept at 10.

Support	Nominal Loading	
	2 wt %	5 wt %
	Actual Loading (wt%)	
P25[1]	1.2 ± 0.3	2.4 ± 0.4
AA[2]	0.8 ± 0.2	3.2 ± 0.6
TiO_2 (p)[3]	1.3 ± 0.3	2.7 ± 0.5
TiO_2 (s-g)[4]	1.2 ± 0.3	2.4 ± 0.4
tint[5]	0.3 ± 0.1	0.9 ± 0.3

[1] TiO_2 from Degussa, used as received.
[2] TiO_2 from Alfa Aesar, used as received.
[3] Titania prepared by precipitation of $TiCl_4$.
[4] Titania prepared by the sol-gel method.
[5] TiO_2 nanotube powder prepared by the hydrothermal process.

2.4.4.1 Gold Supported on TiO_2 Powders

Gold nanoparticles have been deposited onto TiO_2 and *tint* supports. The target loadings were 2 and 5 wt%. The actual Au loading varied depending on the support used. Table 2.5 shows a summary of the actual Au loadings for the different supports used.

The powder supports changed color with the incorporation of Au nanoparticles. The color ranged from dark purple to grey. Reports have shown that the color change (in alumina, silica, magnesia and titania) was related to the metal particle size [37]. Thermal decomposition of the chloroaurate ion on silica gives mauve products, although, when its concentration is so high that reduction is needed to form the metallic state, the color is dark red to brown [37]. The color change seems to depend on the support used as well as gold concentration, particle size and size distribution. It was speculated that the gold 5d orbitals interacted with those of the support cations to give the observed effects [36,37]. TEM studies on the catalysts loaded with Au nanoparticles have indicated that average

particles as small as 3.8 nm were correlated to a dark purple [36,37]. The powder catalysts change color from pink to light gray as the particle sizes increase from 4 to greater than 8 nm.

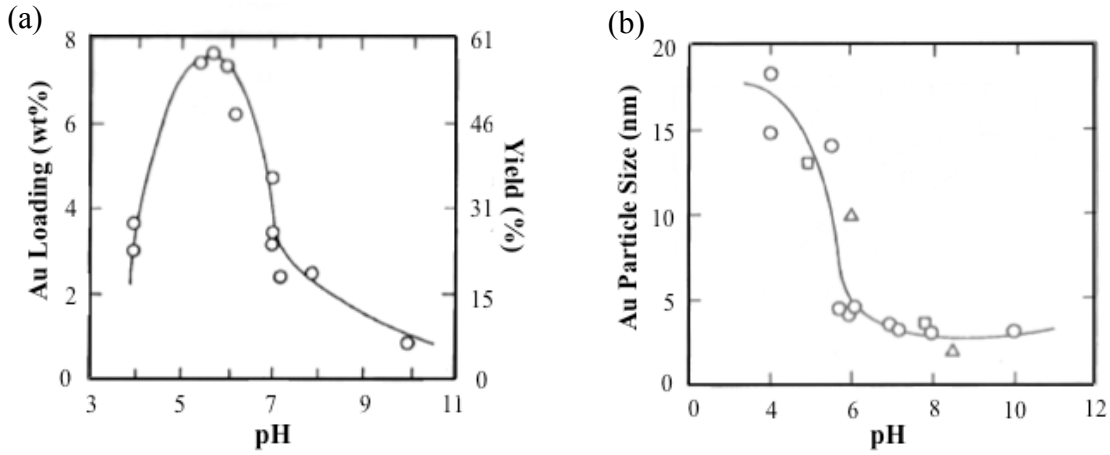

Figure 2.20: Gold (a) loading versus solution pH and (b) particle size versus solution pH plots for Au/TiO_2 catalysts. The different symbols in (b) represent data from different authors compiled in reference [36]. NaOH was added to the suspension to control the solution pH. The preparation was accomplished at 70 °C. The nominal loadings were 13 wt% in each case [36].

The literature suggests that loading at a pH of 10 gives Au particles smaller than 5 nm. However, this pH leads to low Au uptakes. Figure 2.20 shows the influence of pH on the Au loading and Au particle size. As illustrated above, for that Au/TiO_2 powder high loading can be obtained at pH close to the PZC of titania, however the particle size increases at the same time at this pH.

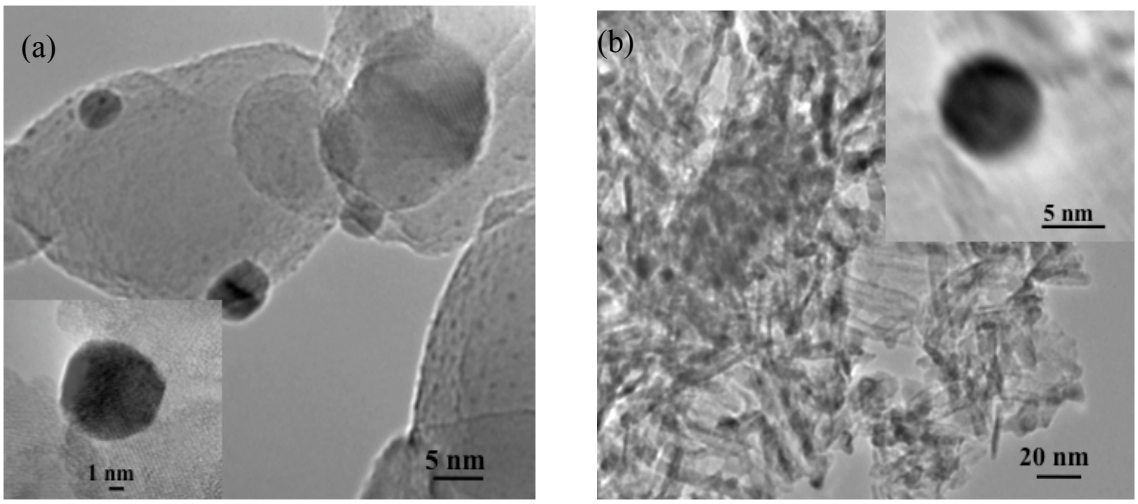

Figure 2.21: TEM micrographs for (a) Au/TiO_2 (P25) and (b) Au/*tint* powder photocatalysts. The nominal Au loadings were 5 wt% in both cases. The insets illustrate a magnification of characteristic Au particles.

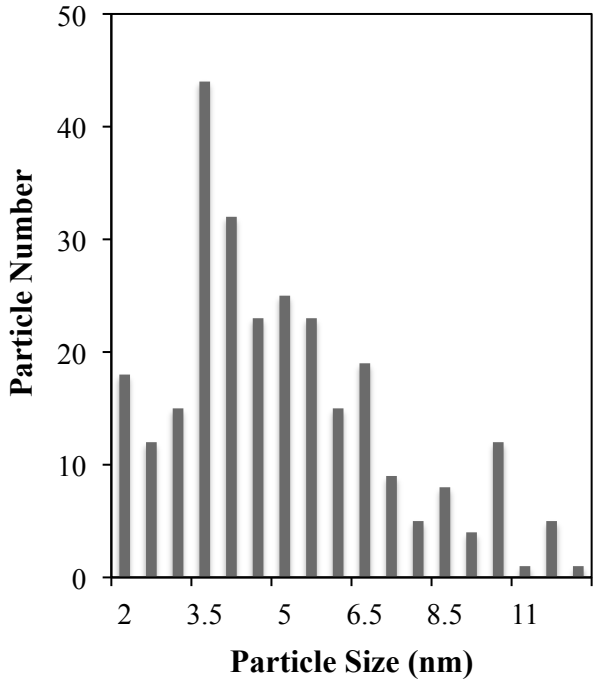

Figure 2.22: Au particle size distribution for Au/TiO_2 (P25). The measured metal loading was 2.4 wt%. Measuring the diameter of about 500 particles from TEM micrographs completed the particle size distribution.

Figure 2.21 shows TEM pictures of selected TiO_2 powder based materials, (a) P25 and (b) *tint*, loaded with Au nanoparticles, the nominal Au loading was 5 wt% in both cases. The particle size was calculated using the TEM micrographs by measuring 400-600 particles and averaging their diameters. Figure 2.22 shows the Au particle distribution for the Au/TiO_2 (P25) material with a 2.5 wt% Au loading.

The results obtained using TiO_2, regarding loadings and particle size, were very similar to the results already published for Au/TiO_2 [36,37]. However, the Au/*tint* case was somewhat different. The Au loading and Au dispersion were low compared to the TiO_2 (see Table 2.5). These results could be explained by the fact that there might be Na and/or Cl on the surface of the *tint* that blocks sites for the adsorption of the $AuCl_4^-$ complex [16].

2.4.5 Gold Deposited onto Ordered TiO_2 Nanotubes

Gold was supported on TiNT films; the early work was done following results already obtained using titania powders. However, the deposition process had to be modified for the TiNT films. The influence of the loading method and the deposition parameters are presented below.

2.4.5.1 Influence of the Loading Method

Gold was deposited on TiNTs using a modified deposition-precipitation method. The support is a film and cannot be dissolved to make a solution without destroying the sample. The first attempt to deposit Au on TiNTs films was done by immersing in stirred DI water and heated to 40°C, then the Au solution was added. The pH of the solution was varied by titration with Na_2CO_3 solution. This method led to the formation of large Au

particles (particles bigger than 20 nm) and high loadings (wt > 5 wt%) due to the relative larger amounts of Au. Figure 2.23 shows TEM micrographs of Au nanoparticles loaded on TiNTs. The average particle sizes for these two samples were 15 nm (Figure 2.23.a) and 25 nm (Figure 2.23.b), and the target loadings were between 18 and 20 wt%.

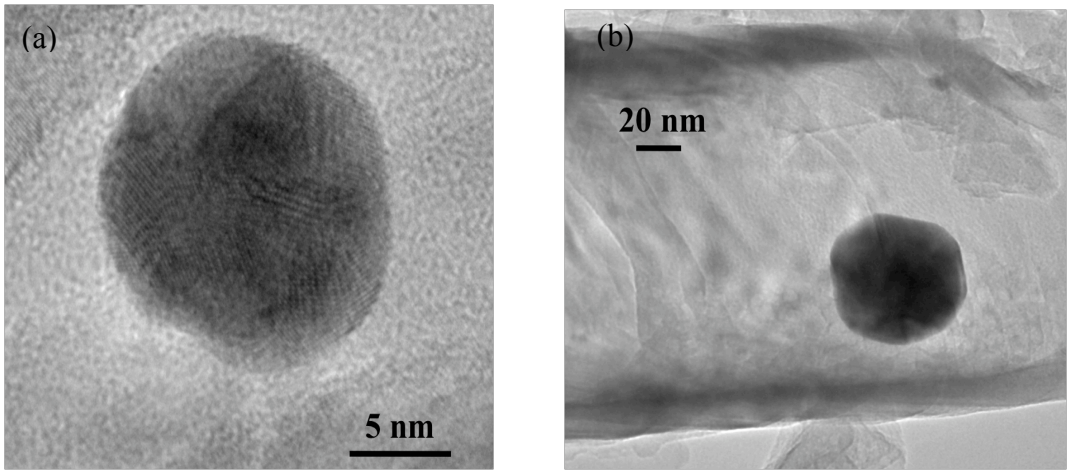

Figure 2.23: TEM micrographs for Au supported on TiNT films. The Au loadings were (a) 4.5 wt% and (b) 6.5 wt%. The average particle sizes were (a) 12 nm and (b) 18 nm.

Further modification of the DP process was needed. A small electric motor was used to spin the TiNT film (motion perpendicular to horizontal bench surface) inside of the solution. This addition helped collection of the Au precursor on the surface of the support. The amount of Au precursor added was also decreased from 30 to 20 wt% (Au precursor concentration 2 mg/mL). Figure 2.24 shows that the latter changes increased the Au dispersion and helped reduce the particle size. The loading final Au loading decreased to values below 5 wt%.

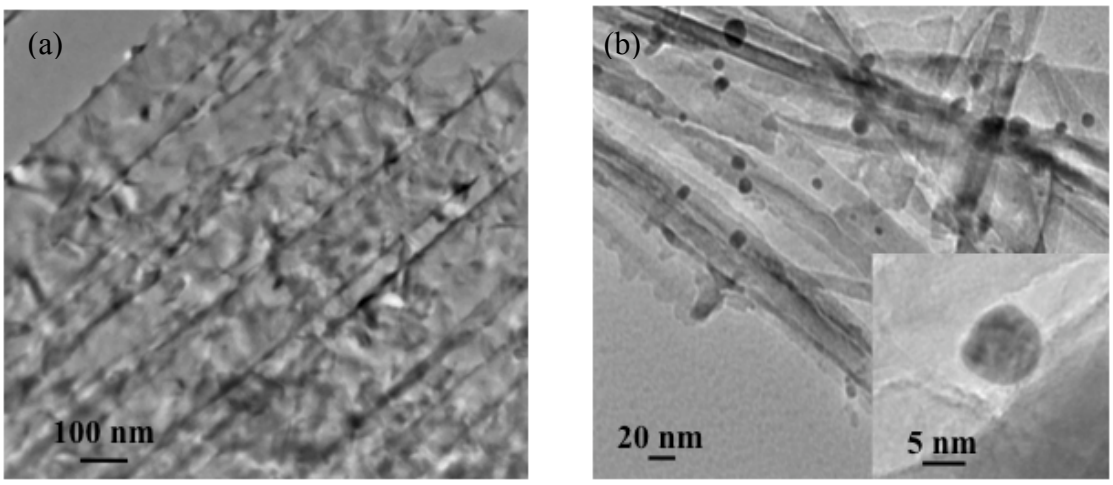

Figure 2.24: TEM micrographs for Au supported on TiNTs with Au loadings (a) 0.6 wt% and (b) 1.2 wt%. The solution pH was kept at ~10 in both cases. Na_2CO_3 was used as titration solution.

The results obtained with these preliminary experiments led us to optimize the DP process for TiNT films. Since then and for the rest of the research work, the DP was done using the electric motor and concentrations of the Au precursor not higher than 2 mg/mL.

2.4.5.2 Effect of the Deposition-Precipitation Parameters

The photocatalyst preparation conditions had a significant effect on the microstructures of the final product. These parameters include pH, temperatures of preparations and washing, and use of different titration solutions (i.e. sodium hydroxide).

It has been reported that temperature affects the rate of precipitation and therefore could affect the particle size [37]. The loading and washing temperature used in our experiments was 40 °C. Changes in the preparation and washing temperatures (from room to 80 °C) showed no significant variation in the final product; similar results have also been seen on powder Au/TiO_2 and Au/CeO_2 catalysts [15,36].

After precipitation, the materials were aged. This time allows the Au precursor to deposit onto the TiNT surfaces. Longer aging periods (more than 2 h) resulted in bigger gold particles (bigger than 25 nm) as compared to shorter (1 h) periods of time (smaller than 10 nm). A possible explanation of this phenomenon could be that some Au colloids present during deposition may serve as a nucleation sites for colloidal growth; this could explain the gold particle size increases with the gold loading and with time [42].

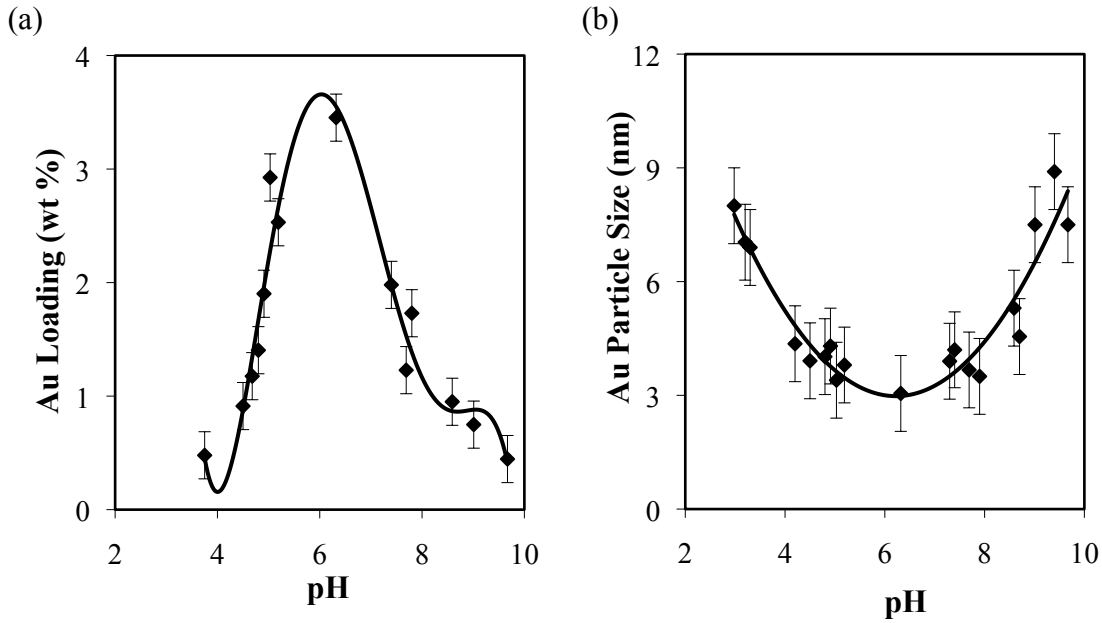

Figure 2.25. (a) Gold loading versus solution pH for Au/TiNT, and (b) average gold particle size versus solution pH plots. The catalysts were prepared by deposition-precipitation adding Na_2CO_3 to control the solution pH. The solution temperature was retained at 40 °C. The catalysts were dried in vacuum at 90 °C.

The use of different base titration solutions (NaOH or Na_2CO_3) did not affect particle size. These results are also similar to previous reports on Au/TiO_2 powders [36]. Figure 2.25.a and Figure 2.26 show Au loading versus solution pH for Na_2CO_3 and NaOH titration solutions, respectively. In addition, changing the nanotubes dimensions

led to similar Au loading as a function of solution pH trends. Figure 2.27 shows Au loading as function of pH for nanotubes with average *OD* = 80 nm and *OD* = 200 nm.

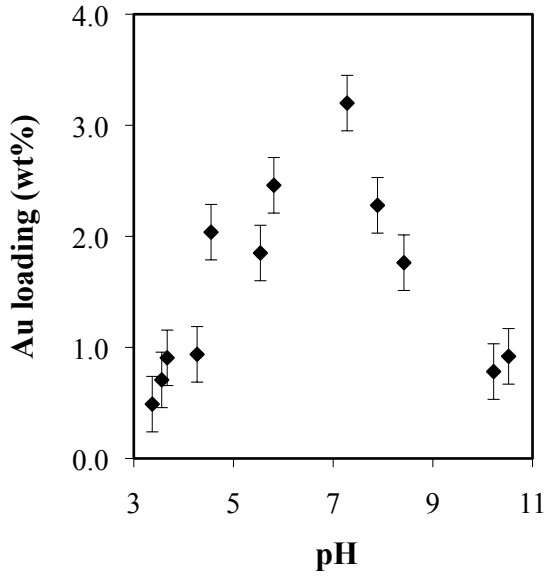

Figure 2.26: Gold loading versus solution pH for Au/TiNT The catalysts were prepared using DP method at 40 °C. The pH was controlled using NaOH to titrate the solution. Samples were dried under vacuum over night.

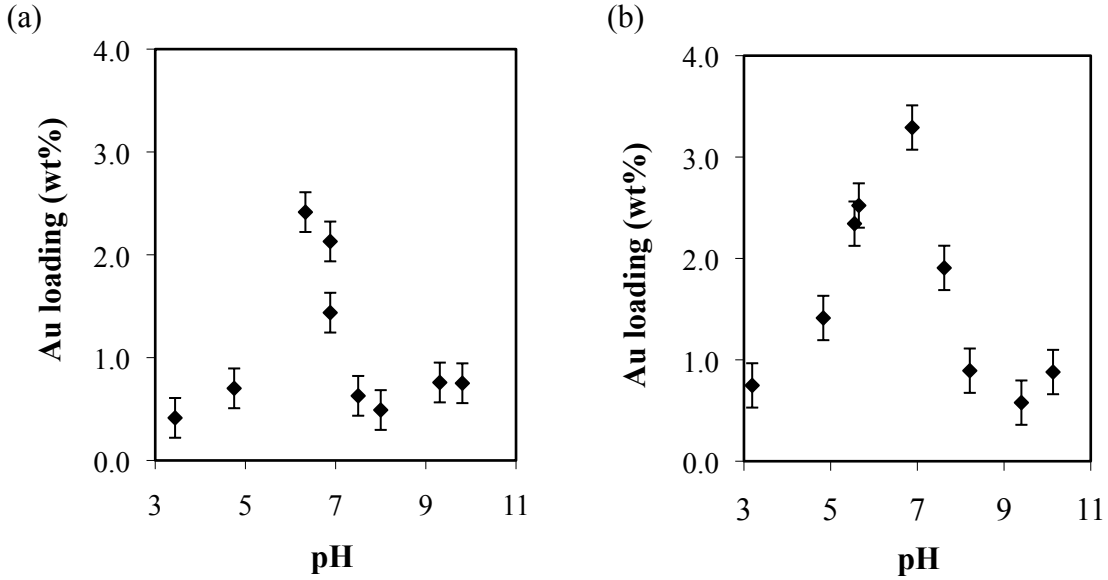

Figure 2.27: Gold loading versus solution pH for Au/TiNT. (a) Nanotube dimensions *OD* = 80 nm and *L* = ~ 12 μm, (b) Nanotube dimensions *OD* = 200 nm and *L* = ~ 18 μm.

The pH of the deposition solution can influence the rate of precipitation and the size of precipitates [14-16,36]. During preparation, the pH was controlled using a Na_2CO_3 solution. The pH of the solution was varied from 3 to 10.5, and the pH of the Na_2CO_3 was 11.7.

There are few studies reporting the influence of pH on the gold loading for Au/TiO_2 powders. Haruta *et al*. [35-37] showed that gold loading on TiO_2 decreases at pH higher than its PZC. These results are in line with the fact that for DP the highest loading is obtained at pH close to the PZC of the support (for oxides with PZC > 5).

The PZC of TiO_2 and TiNTs were measured using the mass titration method. Figure 2.28 illustrates a plot of the initial versus final solution pH during the titration process. The horizontal plateau of the plot indicates the PZC, which in the case of P25 is 5.9. On the other hand, for TiNT there is not a clear plateau; in this case the point where there is a change in slope will indicate the PZC [23]. This is a characteristic for materials with surface areas lower than 5 m^2/g, like TiNT (S_{BET} = 10 m^2/g). Therefore, the PZC for TiNT was stimated to be 6.2. These two PZC values are in agreement with the literature values for PZC (4.5- 6.8) for titania (4.5-6.7)[38,39].

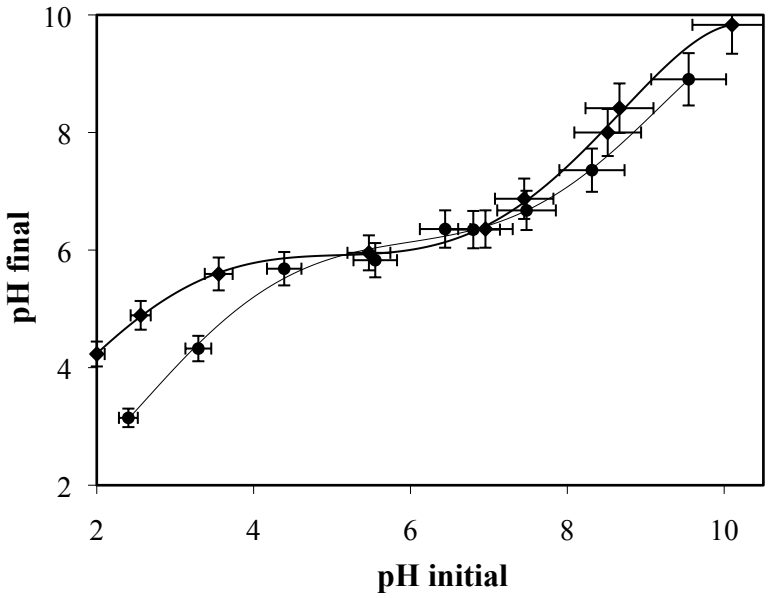

Figure 2.28: Curves for the potentiostatic mass titration final solution pH versus initial solution pH for (◆) TiO_2 (P25) and (●) TiNTs. The plateau (change slope) in the curve indicates the point of zero charge (PZC).

Studies varying the loading solution pH were done for Au/TiNT photocatalysts. The results of these experiments are presented in Figure 2.25.a. This figure shows an increase in Au loading as the pH increases up to pH ~ 6, after this value the amount of Au drops as the pH increases past the PZC. Similar results have been shown for Au/TiO_2 (Figure 2.20.a).

The influence of the solution pH on the particle size in Au/TiNT photocatalysts was also studied. TEM was used to determine the particle size distribution. Figure 2.29 shows TEM micrographs of Au/TiNT used to calculate the gold average particle size. Figure 2.25.b illustrates the particle size variation as a function of solution pH. And Figure 2.30 shows the Au particle size distribution for an Au/TiNT photocatalyst with 1.45 wt % Au.

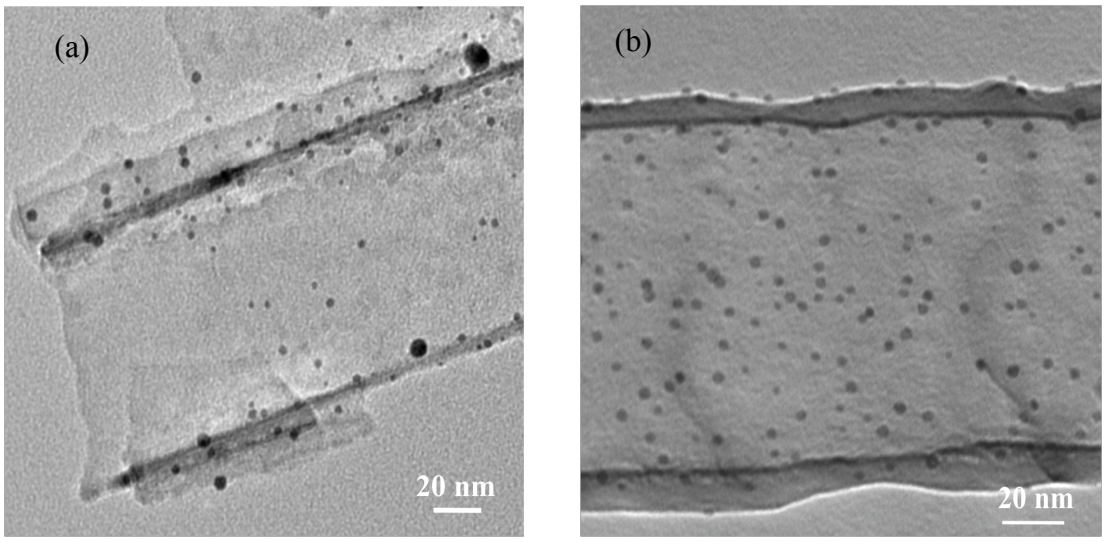

Figure 2.29: TEM micrographs showing Au/TiNT with different gold loadings and particle sizes, (a) pH= 8.1, 0.85 wt % Au, (b) pH = 6.1, 2.4 wt % Au. The nanotube dimensions were *L* ~15 μm, and *OD* ~ 150 nm. TiNT fabricated in ethylene glycol electrolyte at 40 V for 4 h and calcined at 500 °C for 3 h in air.

Previous work on Au/TiO_2 powders indicated [14,36,37] that the Au particle size decreases as pH increases until 7-8 (see Figure 2.20). In contrast, for the Au/TiNTs the Au nanoparticle size decreases as pH decreases reaching a minimum at pH 6-7. After that the size increases with increasing pH. Our results suggest that the best conditions for Au loading on TiNT films correspond to pH about 6-7, particle size ~ 3 nm and 3.5 wt% Au.

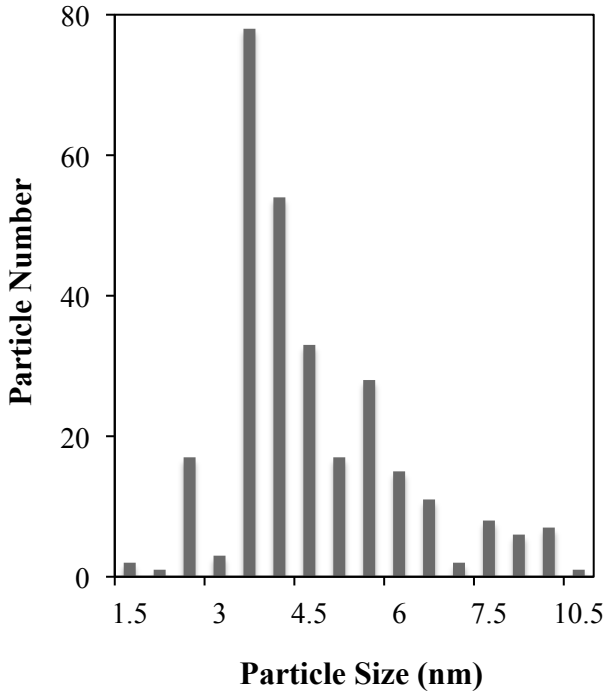

Figure 2.30: Particle size distribution for a representative Au/TiNT catalyst with 2.4 wt% Au loading. TEM micrographs were used to measure the diameters of the gold particles.

2.4.5.3 Gold Deposition Mechanism

The DP method for powders involves placing the support in contact with an aqueous solution of $HAuCl_4$. The solution pH has been raised by the addition of a base, so that upon heating an acidic precursor is formed on the support [36]. The nature of the gold species in solution varies with pH. Three kinds of processes appear to occur as the pH is increased [40]: (i) displacement of Cl^- from a complex anion by water, giving a neutral species; (ii) loss of a proton from a neutral hydrated ion; and (iii) hydrolysis by replacement of Cl^- by OH^- . The following reactions detail the progress of the hydrolysis of the $AuCl_4^-$ ion as the pH is raised [40]:

$$\left[AuCl_4\right]^- + H_2O \leftrightarrow AuCl_3\left(H_2O\right) + Cl^- \tag{2.8}$$

$$AuCl_3(H_2O) \leftrightarrow [AuCl_3(OH)]^- + H^+ \quad (2.9)$$

$$[AuCl_3(OH)]^- + H_2O \leftrightarrow AuCl_2(H_2O)(OH) + H^+ + Cl^- \quad (2.10)$$

$$AuCl_2(H_2O)(OH) \leftrightarrow [AuCl_2(OH)_2]^- + H^+ \quad (2.11)$$

$$[AuCl_2(OH)_2]^- + H_2O \leftrightarrow [AuCl(OH)_3]^- + H^+ + Cl^- \quad (2.12)$$

$$[AuCl(OH)_3]^- + H_2 \leftrightarrow [Au(OH)_3]^- + H^+ + Cl^- \quad (2.13)$$

$$[Au(OH)_4]^- \leftrightarrow [Au(OH)_3]^- + OH^- \quad (2.14)$$

Other reports based on XANES (X-ray near edge structure spectroscopy) and EXAFS (X-ray fine structure spectroscopy) have shown very similar results [42]. These studies indicate that the neutral $AuCl_3 \cdot H_2O$ is the major species at pH 3–4. In addition at pH 7, which is most often selected in the DP method of catalyst preparation, $AuCl(OH)_3^-$ is prevalent. At pH 10 and above, the $Au(OH)_4^-$ anion is the dominant species [42].

The PZC of TiO_2 (P25) is reported to be in the range of 4.3-6.5 (similar values were obtained in this work), so anionic species should adsorb by electrostatic attraction at lower pH. Neutral species will not adsorb in this manner [36-40]. On the other hand, the low gold uptake observed at lower pH (i.e. ~3.0) may reflect the difficult of the neutral species to interact with the positively charged surface [40]. When the surface is only negatively charged (pH > PZC), because of deprotonation of surface OH^-, the predominant species in solution are probably $AuCl(OH)_3^-$ and/or $Au(OH)_4^-$ and simple electrostatic attraction would not occur. In this case some other mechanism is probably in effect. A neutral $Au(OH)_3 \cdot H_2O$ may exist in solution in equilibrium with the anion, and this may interact with the surface. Gold uptake decreases progressively as the pH is

raised above 8. It seems that there is equilibrium between the adsorbed species and those in solution, in which the solution side is more favored as the pH is increased [36].

Something unusual with other method is that with the DP method for powder catalyst preparation is that in the pH range where gold uptake from solution is very high, somewhat large gold particles are formed. It may be that during the stages leading to the formation of metallic Au from the precursor (below pH 6–7) the support surface and/or the adsorbed complexes still retain some chloride ions, and this encourages mobility and aggregation, giving large Au particles. Above pH 8 the adsorbed precursor is substantially chlorine-free, the adsorption of chloride ions is less favorable, and excessive particle growth does not occur.

For Au/TiNT film photocatalyst the Au uptake seemed to be similar to the Au uptake for powder catalysts. Anionic Au species appear to be adsorbed on the TiNT surfaces by electrostatic interaction. However, the neutral species also present in the solution are not being used, giving a low Au uptake. At pH above but still close to the PZC there is gold complex formation [42]:

$$TiOH + \left[AuCl(OH)_3\right]^- \rightarrow Ti - \left[O - Au(OH)_3\right] + H^+ + Cl^- \qquad (2.15)$$

This increased on Au uptake at pH greater than the PZC has been related to the existence of great numbers of neutral hydroxyl [40-42]. On the other hand, the amount of hydroxyl groups available on the TiNT surface is lower at pH > PZC. This limits the number of adsorption sites, and can explain the restricted gold content obtained in the samples. The amount of chloride ions at pH close to the PZC decreases due to the hydrolysis of the Au complex, leading to small Au particles in contrast to Au particles obtained at pH lower than the PZC [36,40,42]. However, at pH > PZC, the particles

found on Au/TiNT are also large, even though there is no Cl^- remaining. It seems that there is another mechanism involved, which makes the Au particles to agglomerate and make large Au particles.

2.4.6 Optical Properties of Titanium Dioxide

One of the requirements for a good PEC material is that its bandgap must make efficient use of the solar spectrum. Adding the standard potential to split water (1.23 V) and the other overpotentials presented in a PEC cell, the voltage needed to efficiently split water is ~2.0 V [43]. Therefore semiconductors with a bandgap between 1.6 and 2.4 eV are desired. Recent and current research activities concentrate on only pure doping the anion or cation site of TiO_2 [44-50], or the design of alternative materials with suitable energy levels and bandgaps, to make photocatalysts active in visible light. An alternative option is to change the surface of the support by adding metal nanoparticles [36,51-55].

2.4.6.1 Surface Plasmon Resonance

Localized surface plasmons (SP) are collective oscillations of the conduction electrons in metal particles [57]. Movement of the conduction electrons upon excitation with incident light leads to a buildup of polarization charges on the particle surface. This acts as a restoring force, allowing a resonance (surface plasmon resonance, SPR) to occur at a particular frequency, which is termed the dipole surface plasmon resonance frequency [57]. Nanoparticles of noble metals such as gold and silver exhibit widely varying absorption profiles in the visible light region because of pronounced surface plasmon absorption [58,59].

Surface plasmons are sensitive to the properties of nanoparticles, such as shape

and size. Shifts in plasmon resonance are caused by changes in the local index of refraction, such as a change induced upon adsorption of molecules on a metal nanoparticle surface [57-60]. A strong electromagnetic field generated by the free electron oscillation near the metal surface interacts with molecules in the field. This interaction can cause unique enhancement of optical processes, such as fluorescence, Raman scattering, absorption, and photocurrent enhancement [58].

The resonance wavelength strongly depends on the size and shape of the nanoparticles, the interparticle distance, and the dielectric property of the surrounding medium [61,62]. There are two types of SP: localized (localized surface plasmon resonance, LSPR) and propagating (surface plasmon polariton; SPP), depending on the form of noble metal. LSPR occurs in small nanoparticles (10–200 nm), in which light absorption (and amplification of the electric field) has been shown to depend strongly on particle size, shape and local dielectric environment, while SPP is associated with smooth thin films of silver and gold with thicknesses in the range of 10–200 nm [57]. Normally the metal particles sizes in these systems exceed 10 nm for the plasmon resonance to affect light trapping [54,55]. On the other hand, if the Au particles are smaller than 10nm, the photocatalytic activity of the Au/TiO_2 system might increase.

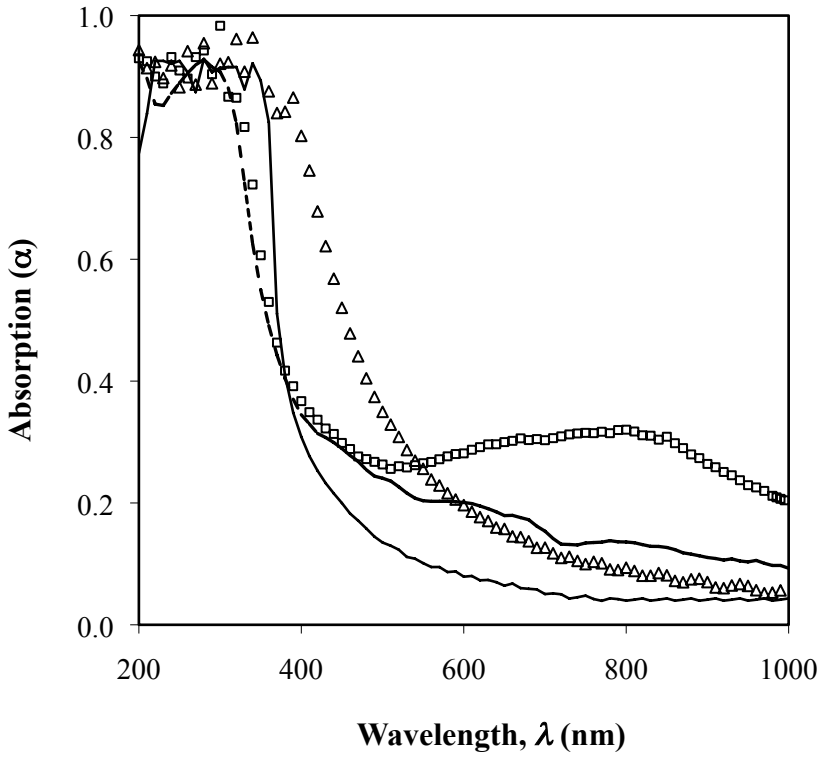

Figure 2.31: Optical absorption as a function of wavelength for (−) TiNT and Au/TiNT films. The pH of the solutions during the metal loading was (□) 3.4, (△) 6.8 and (×) 8.9. Previous results have indicated that the corresponding Au average particle size for these pH values are ~ 11, 4, and 8 nm respectively.

2.4.6.2 Optical Absorption Measurements and Bandgap

The optical properties of TiO_2 and Au supported TiO_2 powders and films were assessed using UV-Vis spectroscopy measurements. The transmission of semi-transparent films (TiO_2, Au/TiO_2, TiNT and Au/TiNT) deposited on quartz was measured. The absorption was calculated using equation (2.1) and (2.2), and the Tauc equation (2.3) was used to calculate average bandgap for the different films.

Figure 2.31 shows a plot of absorption versus wavelength for four TiNT films fabricated on a quartz glass. The data were corrected using the optical absorption for clean quartz without any coating. The solution pH used during the deposition was varied

from 3 to 10 in order to change the particle sizes and study the influence of Au nanoparticles size on the absorption and bandgap of the TiNT and Au/TiNT system. It was shown previously that Au particle size on TiNT increases if the metal deposition was done at pH further from the PZC (both directions but especially at low pHs). Based on those results, the average Au particles size for the plots shown in Figure 2.31 were ~ 11, 3, and 8 nm for 3.4, 6.8 and 8.9 respectively. The absorption plots indicate visible light absorption for TiNT films with 8 and 11 nm average Au nanoparticles. Especially in the case of 11 nm Au particles, the absorption curve has a peak at around 780 nm. This absorption peak is due to the SPR of the metal nanoparticles. The absorption peaks seem to be shifted to the right (compare to published results [60-63]), this could be attributed to the dimensions of the TiNT support [58] and the refraction index of titania.

By analyzing the data using Tauc plots of $(ah\nu)^n$ versus $h\nu$, the optical bulk bandgap (E_g) was determined [19]. In this Tauc equation (3) α is the measured absorption coefficient and n is ½ for indirect transitions (the case of TiO_2), Figure 2.32 shows the Tauc plots for TiO_2 and Au/TiO_2, and TiNT and Au/TiNT. The bandgap for both TiO_2 and TiNT were 3.26 and 3.21 eV respectively. These values are consistent with the bandgaps reported for anatase [2]. On the other hand, the values of E_g for the oxides loaded with Au were 3.08 and 3.03 for the powder and the film respectively.

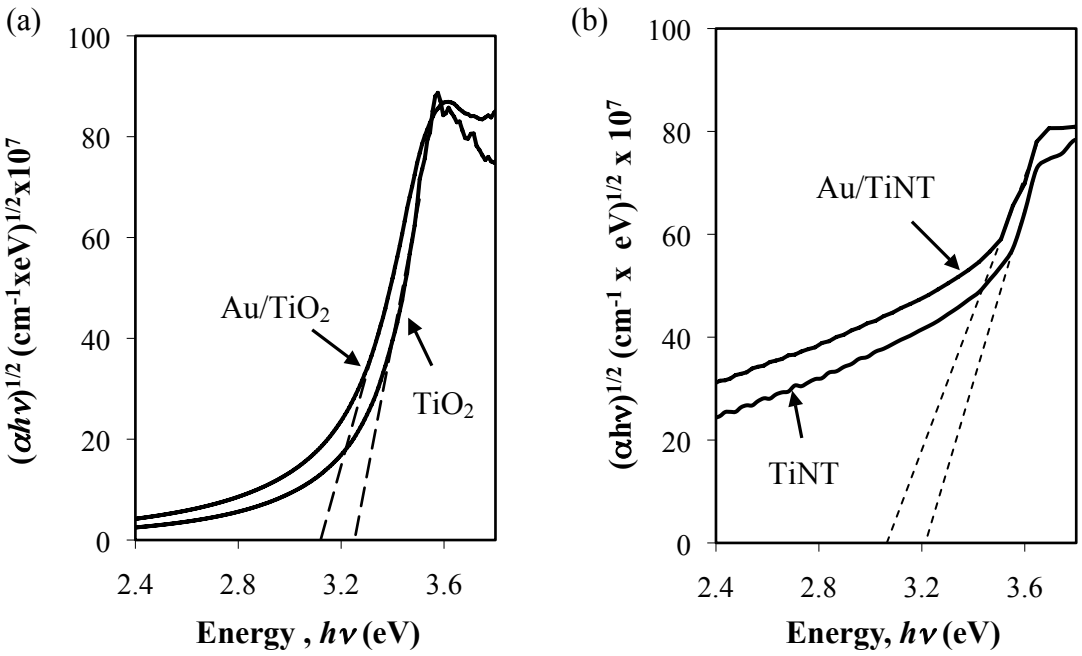

Figure 2.32: Indirect bandgap measurements using Tauc plot. (a) TiO_2 and Au/TiO_2 (2.8 wt% Au, Au particle size ~ 5.5 nm). (b) TiNT and Au/TiNT films (2.3 wt% Au, Au particle size 4.5 nm). The intersection of the extrapolation line (dashed) with the energy axis indicates the E_g of the material.

Tauc plots were also developed for TiNT loaded at pH lower than the PZC of titania. Figure 2.33 shows these plots, which indicate that the E_g for the Au/TiNT system with larger Au particles decreases more so than the one with smaller Au sizes. It is important to note that the actual bandgap of titania does not decrease when large metal nanoparticles but the total Au/TiNT system bandgap (like in the case of a multijunction solar cell with different bandgap semiconductors)

On the other hand smaller Au particles (less than 8 nm) seemed to reduce the E_g of TiO_2. This E_g reduction allowed the TiO_2 to absorb more light in the visible portion of the spectrum. Debeila *et al.* [56] have been reported similar results. They suggested that the light absorption of Au-modified TiO_2 shifts to longer wavelengths because of the existence of Au impurity energy levels. It seems that during process of Au loading on

TiO_2 surfaces the different Au complexes create oxygen defective states similar to the ones in reduced titania (i.e. created during thermal treatment) leading to a small reduction of E_g of TiO_2 [2]. This bandgap reduction is expected to result in an improvement in the water oxidation activities [17].

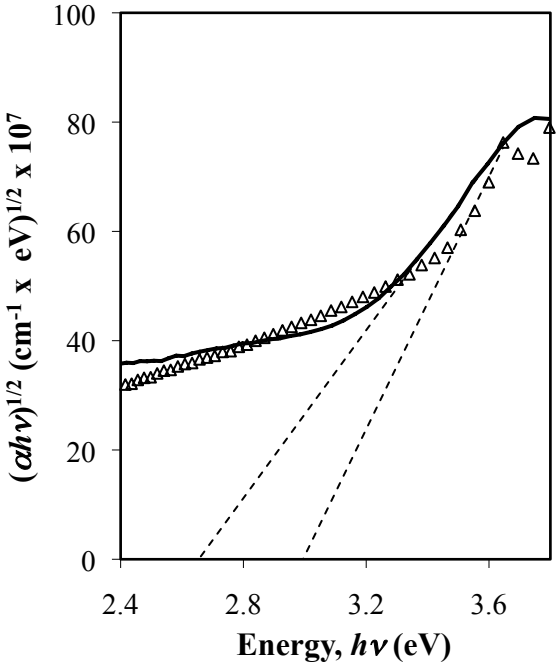

Figure 2.33: Tauc plots for Au/TiNT films (−) pH = 3.4, and (Δ) pH = 6.8, the average Au nanoparticles size corresponding to these pH values are ~11 nm and 4 nm respectively.

2.4.7 Electrochemical Characterization

2.4.7.1 Total Nanotube Surface Area

One way to measure the electrochemically active surface area of a photocatalyst is using cyclic voltammetry [21]. Figure 2.34 shows representative voltammograms for the TiNT films at 100 mV/s scan rate. The flat region (indicated by the arrows) corresponds to double layer charging and was used to determine the surface areas. Figure 2.35 shows

CVs recorded at different scan rates over the capacitive potential region. The scan rate was varied from 0.5 to 200 mV/s. The current increased as scan rate increased. The current and the CV midpoint was measured at plotted versus scan rate. Figure 2.36 shows the capacitive current versus scan rate for a sample electrode. In this plot two regions can be easily distinguished, each line has a different slope. The two line segments (Figure 2.36.a) observed can be correlated with the morphology of highly porous/rugged structures [64]. The changes in slope observed in the high scan rate domain is attributed to the top area of the nanotubes, and the slope obtained in the low scan rate could be attributed to the more porous and difficult-to-access regions (Figure 2.36.b), inner tube. These findings are consistent with those reported by Trasatti and Da Silva [21,64] for TiO_2 and CuO films. Therefore, in order to find the electrochemical surface (active) area of the TiNT electrode, the internal and external capacities need to be included. This value is then divided by the reference capacitance value of 50 mF/cm^2 and the surface area of the electrode can be estimated [21].

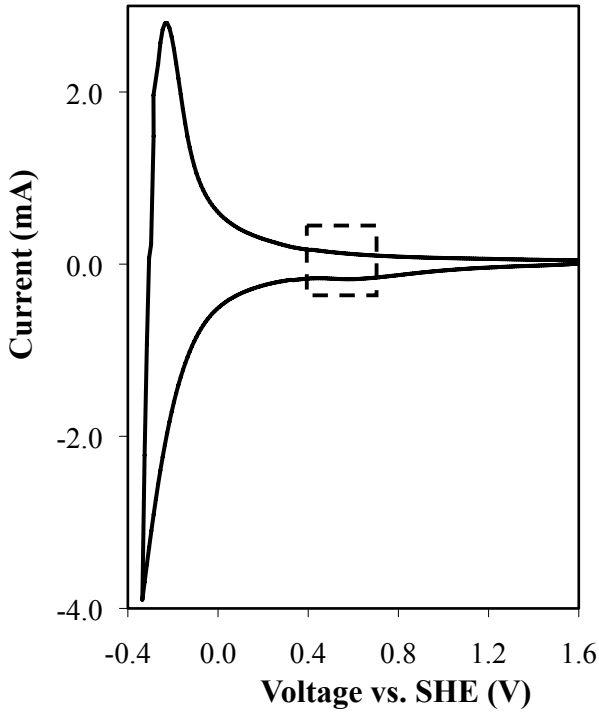

Figure 2.34: Cyclic voltammogram for a representative TiNT film. The dashed rectangle indicates the location of the double layer region used to record CVs for the surface area measurement. Scan rates of 50 mV/s and 1.0 M KOH were used.

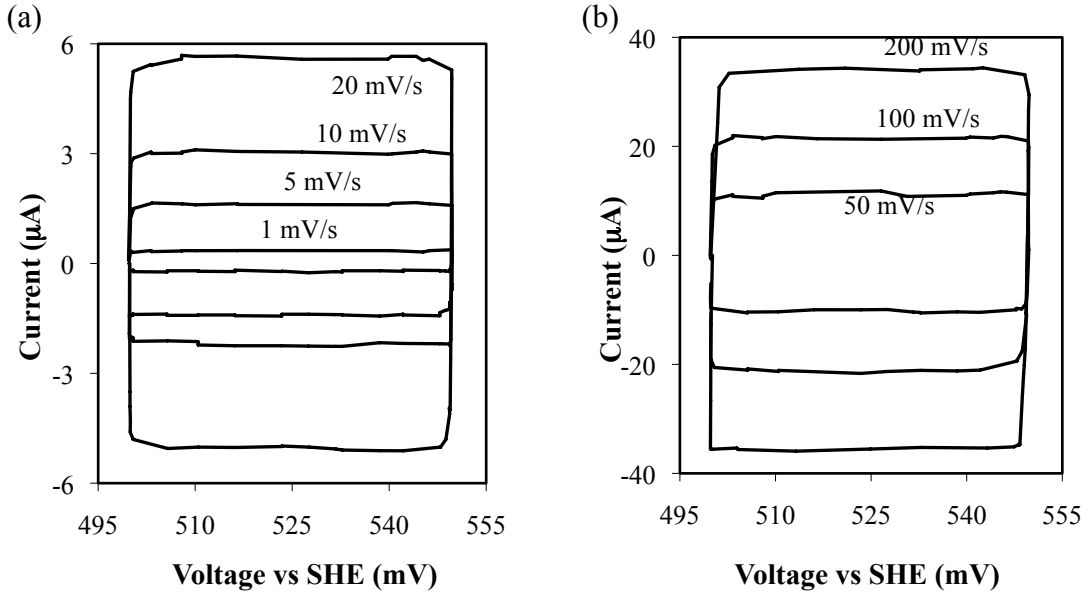

Figure 2.35: Cyclic voltammograms covering the capacitance interval as a function of potential scan rate. (a) Low scan rates and (b) high scan rates. These CVs were used to calculate the electrochemical surface areas of TiNT films.

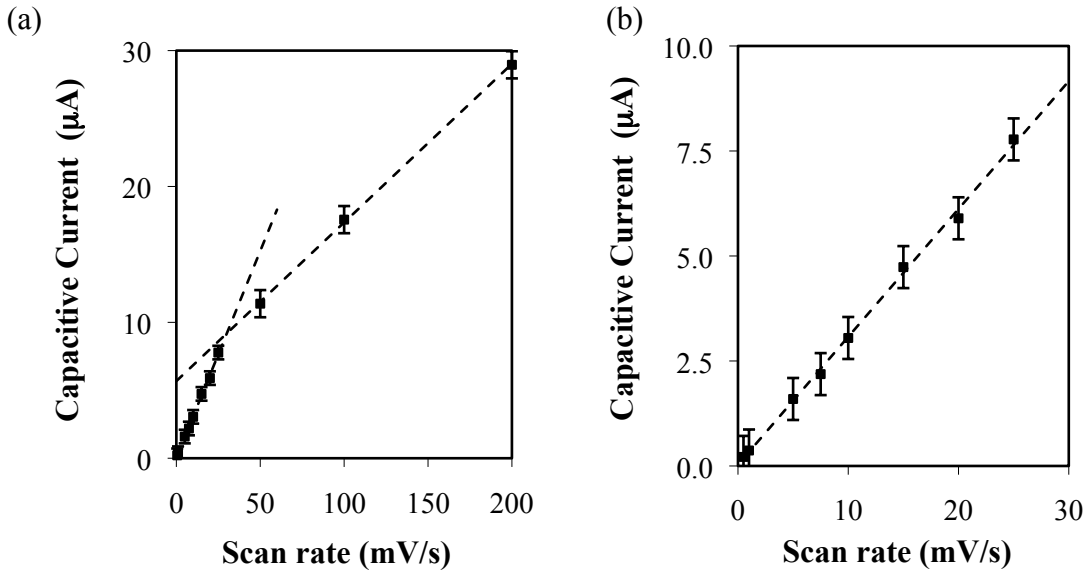

Figure 2.36: (a) Dependence of the capacitive current as a function of scan rate plots for a TiNT electrode. (b) Magnification of the current vs. scan rate at lower scan rate.

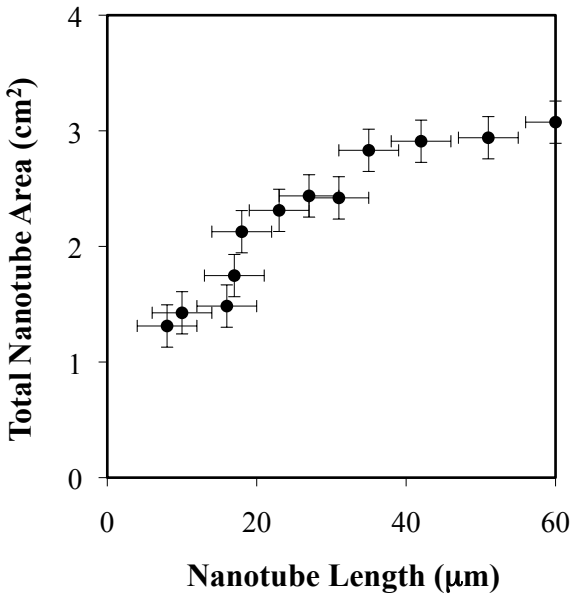

Figure 2.37: TiNT electrochemical surface area as a function of nanotube length. TiNT films were fabricated at 40 V applied bias voltage and ethylene glycol based electrolyte. The nanotube dimension were L ~15 μm and OD ~ 150 nm.

The TiNT film electrochemical surface areas depended on the nanotubes geometry. For a constant outer diameter (OD ~ 150 nm) the TiNT total surface area

(measured by CV) increases, as the nanotubes got longer. Figure 2.37 shows a plot of the TiNT electrochemical area as a function of nanotube length. It is important to note here that even though very long nanotubes (L > 60 μm) were fabricated, they were broken during ultrasonic cleaning leading to shorter tubes. Figure 2.37 suggests the existence of a critical length of ~ 40 μm, after where the nanotube surface area levels off. In addition, it is worth mentionimg that the nanotube walls are thicker in the lower parts of the tubes than the portions closer to the nanotube entrance (Figure 2.38); in other words the internal nanotube diameter (ID) changes from the bottom to the top of the tube. This change in thickness is more pronounced in nanotubes longer than 30 μm, and walls thicker than 50 nm have been observed. This reduction in ID for longer tubes reduces their final internal area. Based on the latter arguments, increasing the nanotube lengths further than 30 μm does not result in further internal nanotube surface areas.

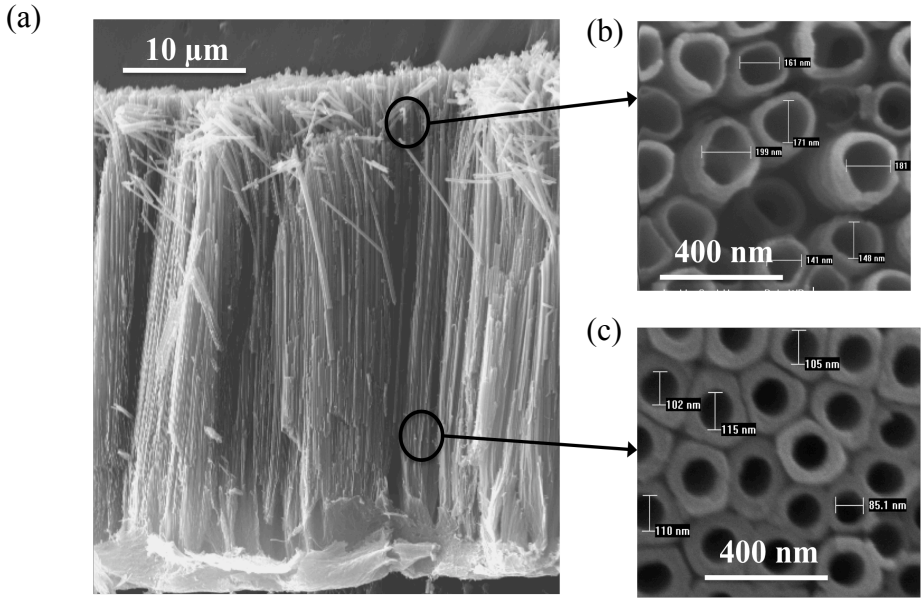

Figure 2.38: SEM micrographs of a TiNT film. (a) Lateral view of the nanotubes showing the length and two sections (b) top and entrance part nanotube diameters and (c) bottom section diameter. Nanotubes were fabricated with 60 V and ethylene glycol electrolyte for 8 h.

There has been some debate whether liquids (KOH electrolyte used in the PEC cell, H_2SO_4 used for Au surface measurement, and Au precursor solution used during the Au loading) can easily diffuse inside of the TiNTs. In order to address this question, a quick calculation was done using the Young-Laplace equation (2.14). This equation describes the capillary pressure difference sustained across the interface between two static fluids, such as water and air, due to the surface tension [66-68]

$$\Delta p = p_{LV} = \gamma\left(\frac{1}{r_1} + \frac{1}{r_2}\right) \tag{2.16}$$

In equation (2.14) p_{LV} (p_L-p_V) is the pressure difference between liquid (p_L) side and the vapor (p_V) side of the meniscus, V represents the vapor (gas, air) phase and its initial pressure p_o (atmospheric pressure), γ is the surface tension of the liquid (for water ~ 72 mN/m), and r_1, r_2 are the radii of curvature of any two normal section of the meniscus. For a cylindrical pore (nanotube) [67]:

$$C = \left(\frac{1}{r_1} + \frac{1}{r_2}\right) = \frac{2}{R} \quad \text{and} \quad R = \frac{r}{Cos\theta} \tag{2.17}$$

Where R is the meniscus radius of curvature in a cylindrical pore, r is the radius of the cylindrical pore and θ the contact angle (for TiO_2 the reported contact angle is 72 ± 1°). Figure 2.1 shows a schematic representation of the diffusion of liquid inside of the TINT. Then equation 2.14 can be represented as [66,67]:

$$\Delta p = p_{LV} = \frac{2\gamma Cos\theta}{r} \tag{2.18}$$

The capillary pressure at which the liquid is forced inside of the nanotube can be calculated using equation 2.16. In order to calculate how much is the nanotube filed with liquid, it was assumed that the remaining air inside of the tube behaves like an ideal gas [68]. If assume that the liquid will compress the air at constant temperature (isothermal

compression). The compression ends when the final pressure of the air is equal to the compressing liquid (p_L). The final length of air inside of the tubes was calculated using the TiNT ID and equation 2.17. Then, the liquid filling fraction can be calculated. These values (for nanotubes with different internal diameters) are summarized in Table 2.6. The results reported in this table suggest that the liquid (in which the nanotube film is immersed) should fill at least 85% of the total length of the tube depending on its internal diameter.

$$p_1V_1 = p_2V_2 \text{ for this case } p_oV_1 = p_LV_2 \tag{2.19}$$

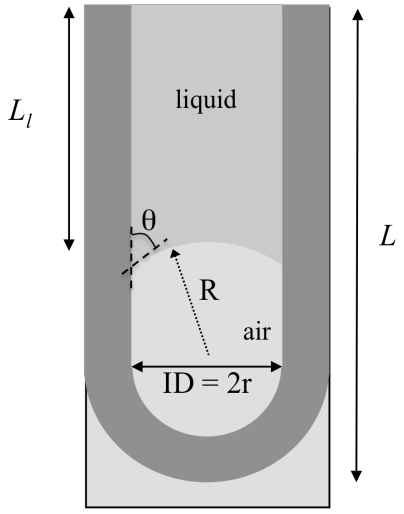

Figure 2.39: Schematic representation of the capillary diffusion of liquid inside of the TiNT. The two phases inside of the tube are liquid (electrolyte) and gas (air).

Table 2.6: Summary of the parameters used for the calculation of the fill fraction of liquid inside of the TiNTs.

TiNT ID (nm)	TiNT *r* (nm)	ΔP (bar)	p_L (bar)	TiNT L (μm)	Liquid L (μm)	Fill (%)
50	25	17.8	18.8	12	11.4	95
90	45	9.9	10.9	15	13.6	91
140	70	6.4	7.4	18	15.6	86

Electrochemical surface areas were also calculated for TiO_2 films (P25 powder deposited on ITO conductive glass).

Table 2.7 summarizes the total electrochemical surface areas for TiNT films areas for 3 different nanotube diameters and for films made with TiO_2 powders. In the case of nanotube films the total surface area changes slightly as the nanotube dimensions change. However, the specific surface area (equivalent to S_{BET} in m^2/g) is similar for the three cases.

Table 2.7: Summary of electrochemical surface areas for various TiNT and TiO_2 photoelectrodes. The areas were calculated using CV.

Nanotube Dimensions		TiNT Area (cm^2)	TiNT Mass (mg)	Specific Area (m^2/g)
OD (nm)	Length (μm)			
80	12	1.28 ± 0.2	1.1 ± 0.1	0.12 ± 0.03
150	15	1.58 ± 0.3	1.5 ± 0.1	0.10 ± 0.03
200	18	1.78 ± 0.3	1.6 ±0 .1	0.11 ± 0.03
TiO_2 (powder) film		Total Elec. Area (cm^2)	TiO_2 Mass (mg)	Specific Area (m^2/g)
Size (nm)[1]	Film Thickness (μm)			
10-15	20	1.12 ± 0.1	1.8 ± 0.1	0.06 ± 0.01

[1] Nanoparticle average size

2.4.7.2 Gold Surface Area

Gold surface areas were also measured electrochemically using cyclic voltammetry. Scans were taken around the oxygen adsorption/desorption peaks and 100

mV/s. The first experiments were done with Au wires, to find the location of the oxygen peaks. After that the Au/TiO_2 powders deposited on conductive glass were scanned. Figure 2.40 shows the CV for an Au/TiO_2 electrode deposited on a conductive glass, the gold loading was 5 wt % (sample was obtained from AuTek). The oxygen adsorption peak is located at about 0.8 V (vs. SHE). The area under the oxygen peak was integrated; this area is proportional to the charge accumulated on the metal during oxygen adsorption, and therefore proportional to the Au surface area.

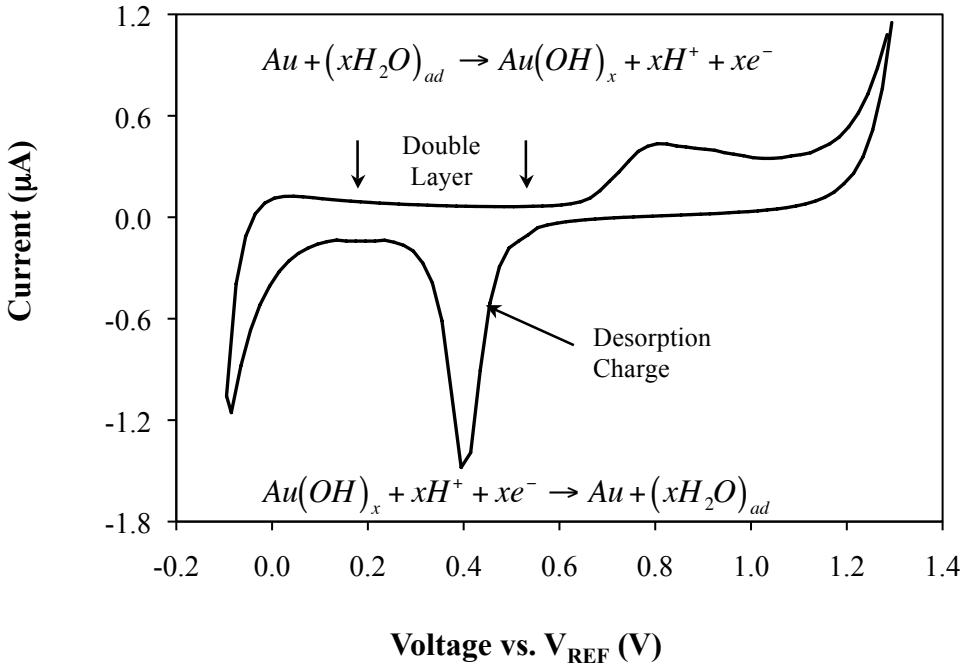

Figure 2.40: Cyclic voltammogram of Au/TiO_2 deposited on a conductive (ITO) glass using 0.01 M H_2SO_4 as the electrolyte with a scan rate of 100 mV/s. The shaded area indicted the charge accumulated during oxygen desorption.

After the preliminary work performed with Au wires and electrodes made with Au/TiO_2 powders the Au/TiNT electrodes were tested. Because, the gold loading and

metal particle size were lower than the powder based electrodes, the oxygen peaks in the CVs were also smaller. Figure 2.41 shows the CVs for different electrodes, bigger peaks are obtained for higher gold loadings. Figure 2.42 shows plots of the Au surface area as a function of Au particle size and Au loading. For Au loading between 1.5 and 3 wt% the Au area increases as the metal particle size decreases. And increasing the Au loading increases the Au total area. However, for Au particle size bigger than 6 nm the Au area does not increase as much, which could be a consequence of the existence of larger particles (bigger than 10 nm) as well.

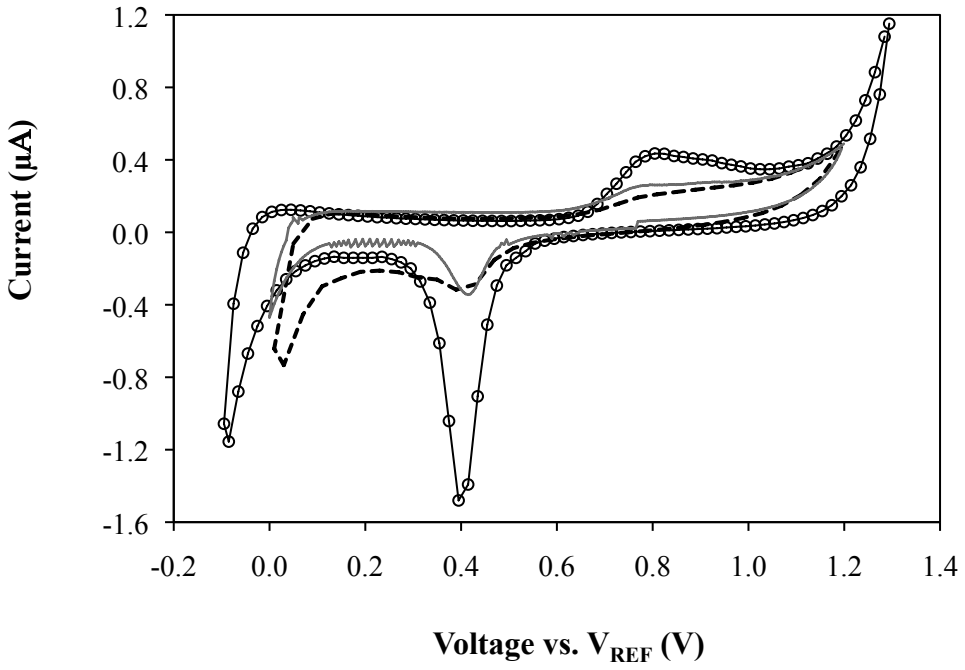

Figure 2.41: Cyclic voltammograms plots for Au/TiNT photoelectrodes with different Au loading. Gold loading (o) 2.1, (---) 1.8, (−) 0.8 wt%. Gold particle size (a) 3.8, (b) 6.2, and (c) 9.3 nm. The electrolyte used was 0.01 M H_2SO_4 and an 100 mV/s scan rate.

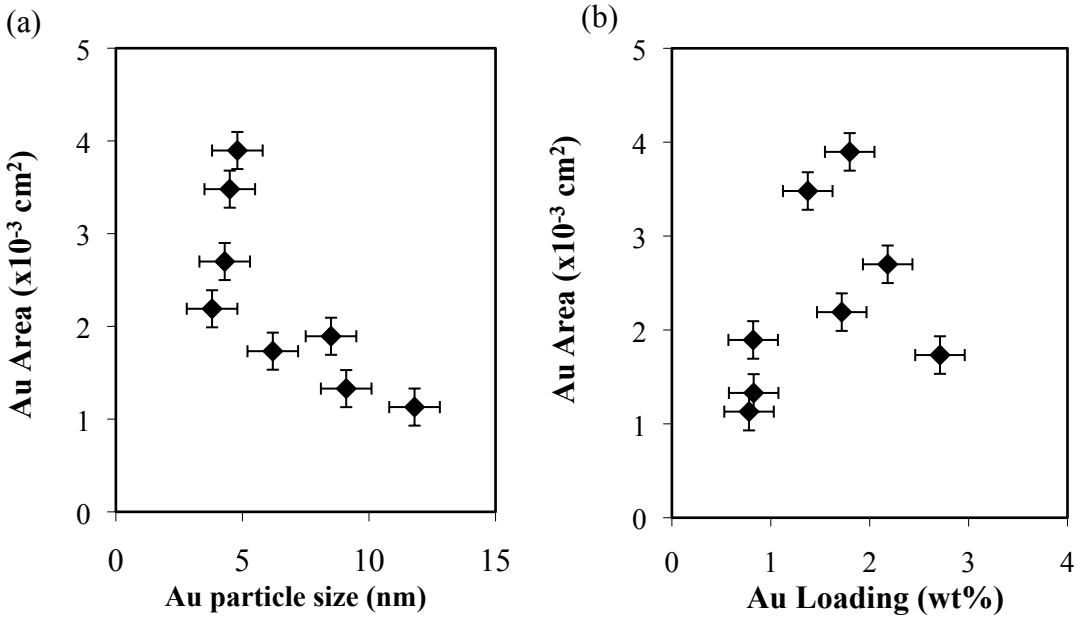

Figure 2.42: Gold electrochemical surface area versus (a) Au particle size and (b) Au loading. The Au gold was done via CV analysis. The nanotubes dimensions $L \sim 15$ μm and $OD \sim 150$ nm.

2.5 SUMMARY AND CONCLUSIONS

In this chapter results regarding fabrication and characterization of the different photocatalysts was presented. Characterization techniques such as XRD, SEM, TEM, ICP, BET, CV, and UV-Vis were used.

High surface area titania powders were fabricated by the precipitation of $TiCl_4$ and hydrothermal method (disorder TiO_2 nanotubes). The nanoparticles size (nanotube dimension for the case of the *tint*) and S_{BET} changes with thermal treatment in air.

Highly ordered TiO_2 nanotubes were sensitized using an anodization process. It was shown that the dimensions of the TiNTs strongly depended on the anodization parameters. Relatively short nanotube arrays were obtained when water is used as solute for the acid electrolyte. Longer, smoother tubes are obtained when organic solvents were used in combination with low concentrations of fluoride ions. The voltage had the most significant effect on the nanotube diameter, while the anodization time increased the nanotube length. To obtain crystallinity the as-prepared amorphous nanotubes were calcined in air, at elevated temperatures, for several hours. At temperatures between 450 and 550°C the nanotube were converted into anatase, and at temperatures higher than 550°C the nanotube started to transform to rutile. At temperatures higher than 750°C the structure of the nanotubes cracked and finally collapsed at temperatures higher than 850°C.

Gold nanoparticles were successfully loaded in TiNTs using a modified deposition precipitation method. The deposition of gold on TiO_2 nanotubes was different from the deposition of gold on powders. Even though, the gold deposited on the nanotubes follows the reported TiO_2 powder trend, the Au particle size distribution as a function of pH was different. The smallest Au particles were observed at pH close to the PZC of TiO_2. These results suggested that the gold loading process is not the same for TiO_2 powders and TiNT films, different surface and bulk defects in the TiNT could have influence the growing of Au particles. Results presented in this work suggested that the best loading conditions (high loading and small particle size) were obtained when the pH was in the range of pH 6-7.

The addition of gold nanoparticle changed the optical properties of titania. For instance, visible light absorption was enhanced when the Au particles were bigger than 10 nm. This absorption enhancement resulted as a consequence of surface plasmon resonance. Further, Au/TiO_2 with average particle size larger than 10 nm has shown to have a bandgap 0.5 eV lower than TiO_2. On the other hand, Au particles as small as 3 nm slightly decreased the bandgap of the oxide support (between 0.1-0.2 eV). The latter could be consequence of the existence of impurity energy levels between the energy bands of TiO_2 that were created during the fabrication of the photocatalyst.

A capacitive current with respect to the voltage ramp rate was observed. This allowed us to identify two different regions, inner and outer surface, in the electrode, which gave a better estimation of the surface area. The total surface are of the nanotubes depended on their dimensions. In particular, the TiNT surface area was higher for longer tubes. However, that only occurs up to nanotube lengths ~ 40 μm. After that the surface area level offs. Even though the diffusion liquid in the tubes does not change considerably for long nanotubes, the nanotube internal diameter (close to the bottom of the tube) reduces when the anodization times are too long (used to grow long nanotubes).

Finally, the electrochemical surface area of gold in the photoelectrodes was calculated based on cyclic voltammetry. The results shown that the Au area depended on the metal loading and Au particle size.

2.6 REFERENCES

1. X. Chen and S. S. Mao, Chemical Reviews 107 (2007) 2891-2959.
2. A. Fujishima, X. Zhang, T. Donald, Surface Science Reports 63 (2008) 515-582.
3. O. Carp, C. L. Huisman, A. Reller, Progress in Solid State Physics 32 (2004) 33–177.
4. G. K. Mor, O. K. Varghese, M. Paulose, K. Shankar, C. A. Grimes, Solar Energy Materials and Solar cells 90 (2006) 2011-2075.
5. S. Sakthivel and H. Kisch, ChemPhysChem 5 (2003) 487-490.
6. Y. Li, Y. Fan and Y. Chen, Journal of Materials Chemistry, 12 (2002) 1387–1390.
7. P. Yang, C. Lu, N. Hua, and Y. Du, Materials Letters (2002) 57-794.
8. V. Brezova, A. Beazkova, L. Karpinsky, J. Groskova, V. Jorik, and M. Cepan, Journal Photochememistry and Photobiology A: Chemistry (1997) 109-177.
9. I. M. Arabatzis, S. Antonaraki, T. Stergiopoulos, A. Hiskia, E. Papaconstantinou, M. C. Bernard, Journal Photochemistry Photobiology A: Chemistry (2002) 149-237.
10. T. Kasuga, M. Hiramatsu, A. Hoson, T. Sekino, and K. Niihara, Advanced Materials. 11 (1999) 1307.
11. J. Macak and P. Schmuki, Electrochimical Acta 52 (2006) 1258–1264.
12. H. E. Prakasam, K. Shankar, M. Paulose, O. K. Varghese, and C. A. Grimes, Journal Physical Chemistry C 111 (2007) 7235-7241.
13. C. H. Kim, L. T. Thompson, Journal of Catalysis 244 (2006) 248.
14. M. Haruta, M. Date, Applied Catalysis A: General 222 (2001) 427.
15. C. H. Kim, L. T. Thompson, Journal of Catalysis 230 (2005) 66.
16. C. H. Kim. 2005. Catalytic and Surface Properties of Nanocrystalline Gold Water Gas Shift Catalysts. In Chemical Engineering. University of Michigan, Ann Arbor, MI.
17. P. Aurora, P. Rhee, L. Thompson, Journal of the Electrochemical Society 157 (2010) 152-155.
18. T. E. Tim. 2007. Carbide and Nitride Supported Water-gas Shift Catalysts. In Chemical Engineering. University of Michigan, Ann Arbor, MI
19. Z. Chen, T. F. Jaramillo, T. G. Deutsch, A. Kleiman-Shwarsctein, A. J Forman, N. Gillard, R. Garland, K. Takanabe, C. Heske, M. Sunkura, E. W. McFarland, K Domen, E. L. Miller, J. Turner, H. N. Dinh, Journal of Materials Research 25 (2010) 3-16.
20. M. Anwar and C. A. Hogarth, Physica Status Solidi 109 (1988) 469-478.

21. S. Trasatti, and O. A.Pettri, Journal of Electroanalytical Chemistry 327 (1992) 353-376.

22. G. Sposito, Environmental Science & Technology 32 (1998) 2815-2819.

23. J. Park, and J. R. Regalbuto, Journal of Interface and Colloidal Science 175 (1995) 239-252.

24. K. Bourikas, J. Vakros, C. Kordulis, and A. Lycourghiotis, Journal of Physical Chemistry B 107 (2003) 9441-9451

25. L.A. De Faria and S. Trasatti, Journal of Electroanalytical Chemistry 340 (1992) 145-152.

26. K. Shankar, J. I. Bashman, N. K. Allen, O. K. Varghese, G. K. Mor, X. Feng, M. Paulose,J. A. Seabold, K. Choi, and C. A. Grimes, Journal of Physical Chemistry C 113 (2009) 6327.

27. A. Ghicov and P. Schmuki, Chemical Communications (Cambridge, United Kingdom) 2009, 2791-2808.

28. J. M. Macak, H. Hildebrand, U. Marten-Jahns, and P. Schmuki, Journal of Electroanalytical Chemistry 621 (2008) 254–266.

29. K. Yasuda, J. M. Macak, S. Berger, A. Ghicov, and P. Schmuki, Journal of the Electrochemical Society 154 (2007) 472-478.

30. S. Berger, J. Kunze, P. Schmuki, A. T. Valota, D. J. LeClere, P. Skeldon, and G. E. Thompson, Journal of the Electrochemical Society 157 (2010) 18-23.

31. L. V. Taveira, J. M. Macák, H. Tsuchiya, L. F. P. Dick, and P. Schmuki, Journal of the Electrochemical Society 152 (2005) 405-410.

32. J. M. Macak, H. Tsuchiya, L. Taveira, S. Aldabergerova, and P. Schmuki, P. Angewandte Chemie, International Edition 44 (2005) 7463-7465.

33. K. Shankar, G. K. Mor, H. E. Prakasam, S. Yoriya, M. Paulose, O. K. Varghese, and C. A. Grimes, Nanotechnology 18 (2007) 065707.

34. Y. Song, R. Lynch, D. Kim, P. Roy, and P. Schmuki, Electrochemical and Solid-State Letters 12 (2009) 17-20.

35. M. Haruta, S. Tsubota, T. Kobayashi, H. Kageyama, M. J. Genet, and B. J. Delmon, Journal of Catalysis 144 (1993) 175.

36. G. C. Bond, C. Louis, and D. T. Thompson (Eds.) Catalysis by Gold; Catalytic Science Series, v. 6, Imperial College Press, London, 2006.

37. G. C. Bond, and D. T. Thompson, Catalysis Reviews 41 (1999) 319.

38. M. Kosmulski, Journal of Colloid and Interface Science 298 (2006) 730–741.

39. M. Kosmulski, Advances in Colloid and Interface Science 99 (2002) 255–264.

40. F. Moreau, G. C. Bond, and A. O. Taylor, Journal of Catalysis 231 (2005) 105–114.

41. S. Tsubota, D. Cunningham, Y. Band, and M. Haruta, Studies in Surface Science and Catalysis 91 (1995) 227-231.

42. R. Zanella, L. Delannoy, and C Louis, Applied Catalysis A: General 291 (2005) 62–72.

43. J. Nowotny, C. C. Sorrell, L. R. Sheppard, T. Bak, International Journal of Hydrogen Energy 30 (2005) 521-544.

44. K. Okazaki, S. Ichikawa, Y. Meda, M. Haruta, and M. Kohyama, Applied Catalysis A: General 291 (2005) 45-54.

45. J. R. Bolton. IEA Agreement on the Production and Utilization of Hydrogen. National Renewable Energy Laboratory Golden, CO USA, 1996.

46. J. Nowotny, C. C. Sorrel, T. Bak, and L. R. Sheppard, International Journal of Hydrogen Energy 78 (2005) 593-602.

47. M. Gratzel, Nature 414 (2001) 338-344.

48. T. Lindgren, M. Larsson, and S. Lindquist, Solar Energy Materials and Solar Cells 84 (2004) 147.

49. V. M. Aroutiounian, V. M. Arakelyan, G. E. Shahnazaryan, Solar Energy 78 (2005) 581-592.

50. N. Yoshitaka, M. Takeshi, O. Takeshi, T. Yasunori, Applied Physics Letters 87 (2005) 52111.

51. T. Lana-Villarreal and R. Gomez, Electrochemical Communications 7 (2005) 1218–1224.

52. P. G. Wu, C. H. Ma and J. K. Shang, Applied Physics A: Material Science and Processing 81 (2005) 1411.

53. T. Ohno, T. Mitsui, M. Matsumua, M. Chemistry Letters 32 (2003) 364-365.

54. X. Hu, and D. J. Blackwood, Journal of Electroceramics 16 (2006) 593–598.

55. K. Yu, Y. Tianw, and T. Tatsuma, Jopurnal of Physical Chemistry A 8 (2006) 5417–5420.

56. M. Debeila, M. Raphulu, E. Mokoena, M. Avalos, V. Petranovskii, N. Coville, and M. Scurrell, Materals Science and Engineering A 396 (2005) 70-76.

57. S. Pillai, K. R. Catchpole, T. Trupke, and M. A. Green, Journal of Applied Physics 101 (2007) 093105.

58. L. Du, A. Furube, K. Yamamoto, K. Hara, R. Katoh, and M. Tachiya, Journal of Physiscal Chemistry C 113 (2009) 6454–6462.

59. E. W. McFarland and J. Tang, Nature 421 (2003) 616-618.

60. T. Toyoda, S. Tsugawa, and Q. Shena, Journal Of Applied Physics 105 (2009) 034314.

61. Yang Tian and Tetsu Tatsuma, Journal American Chemical Society, 127 (2005) 7632-7637.

62. S. Link and M. A. El-Sayed, Journal of Physical Chemistry B 103 (1999) 4212-4217.

63. E. Kowalska, O. Omar Prieto Mahaney, R. Abea and B. Ohtani, Physical Chemistry Chemical Physics 12 (2010) 2344–2355.

64. L. M. Da Silva, L. A. De Faria, and J. F. C. Boodts, Electrochimical Acta 47 (2001) 395 – 403.

65. S. Ardizzone, G. Fregonara, S. Trasatti, Electrochemical Acta 35 (1990) 263-267.

66. J. M Haynes, Materiaux et Constructions, 33 (1973) 209-213.

67. N. R. Tas, P. Mela, T. Kramer, J. W. Berenschot, and A. van der Berg, Nano Letters, 11 (2003) 1537-1540.

68. D. Mattia and Y. Gogotsi, Microfluid Nanofluid, 5 (2008) 289-305.

CHAPTER 3

TiO_2 PHOTOELECTRODE CHARACTERIZATION AND PERFORMANCE EVALUATION

3.1 INTRODUCTION

Efficiencies for PEC cells reported to date are low due to their slow kinetics for water oxidation, and also due to different problems related to charge carrier generation, separation and transport in the photoanode. Stable semiconducting oxides are among the most widely used materials for photoelectrochemical cells [1,2]. However, their high bandgap only allows absorption of the solar spectrum in the limited, high-energy UV region, and its photocatalytic activities for water oxidation are very low [2]. While optimizing the bandgap and absorption characteristics of the semiconducting oxide is important, there is arguably a greater need for the incorporation of catalytically active sites to increase hydrogen production rates. It has been reported that the water oxidation rates have to be increased by more than an order of magnitude to keep pace with the production of electrons and holes [3]. Also, because the particle size of powdered catalysts (e.g. commercially available oxides like TiO_2 P25 and Anatase Alfa Aesar) used as the photoanode, only about 5% of the generated carriers are used for the water-splitting reaction [4]; the rest of the charge carriers recombine before they can be utilized.

The process of electron transport networks proceeds by a trap-limited diffusion process [5], in which photogenerated electrons interact with different traps as they randomly travel towards the back of the electrode. These traps are defects in the semiconductor oxide. While the electrons are captured by Ti^{4+} sites (to form $Ti^{3+)}$, the cations from solution intercalate into the TiO_2 lattice to compensate for the loss of charge [6-9]. An electron may experience a million trapping/promoting events before it reaches the backside of the electrode or recombine with hole or react with an oxidizing species in the electrolyte [5-9].

In nanoparticle networks (i.e. powder TiO_2) the electrons have to overcome grain boundaries in their random walk to the back of the electrode. In this process photogenerated electrons and holes recombine before they can be used for water oxidation. In order to reduce these recombination losses, the diffusion length (average distance a carrier can move from point of generation until it recombines) of the minority carrier (holes in the case of TiO_2) has to be longer than the particle size or film thickness [10]. One way to increase the life of the charge carriers is by using nanowires or nanotubes, instead of discrete nanoparticles. These structures can provide a path relatively free of grain boundaries for the majority carriers (electrons in the case of TiO_2) and an easier transport of holes to the surface of the electrode. For such nanostructures, photogenerated holes have a shorter distance to travel to reach the electrode/electrolyte interface while the excited electrons move towards the back contact without crossing as high a density of grain boundaries and point defect traps. Electron transport in crystalline tube and wires are expected to be several orders of magnitude faster than percolation through a random polycrystalline network [5]. Hence, nanowires and nanotube

nanostructures should [11-13] reduce the recombination of charge carriers. This structural approach should also improve light harvesting, gravimetric and areal efficiencies due to the high surface areas that can be achieved.

Gold has been utilized as a material for coinage, jewelry, and electronics. Gold had been considered a relatively poor catalyst, until Haruta discovered that catalysts containing gold particles smaller than 5 nm possessed extraordinary activities for reactions including CO oxidation [14] (equation 3.1). Figure 3.1 shows a plot of turn over frequency (T.O.F., molecules reacting per active site in unit time) for the oxidation of CO as function of Au diameter. The rate of CO oxidation increases rapidly when the size of the metal particle size decreases below 5 nm. Since then nanostructured gold catalysts have been demonstrated to be highly active for a variety of reactions including water gas shift (equation 3.2), which involves the decomposition of water [15-17], and several photocatalytic reactions (i.e. equation 3.3) [4,18-22]. These results indicate that Au nanoparticles hold promise for significantly enhancing the water oxidation rates in PEC cells.

$$2CO + O_2 \rightarrow 2CO_2 \text{ , CO Oxidation} \tag{3.1}$$

$$CO + H_2O \rightarrow CO_2 + H_2 \text{ , Water Gas Shift} \tag{3.2}$$

$$C_2H_5OH + H_2O \xrightarrow{h\nu} CO_2 + CH_4 + 2H_2 \text{ , Photocatalytic Reaction} \tag{3.3}$$

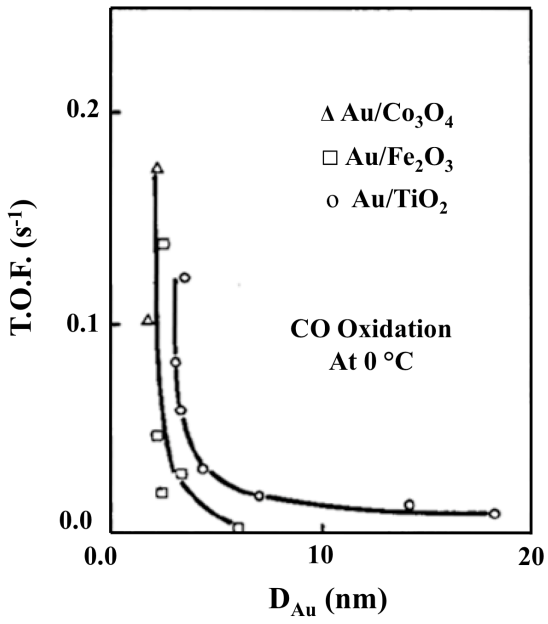

Figure 3.1: Particle size and support dependency for supported gold CO oxidation catalysts [23].

It has been reported that small Au nanoparticles (~5 nm in diameter) changed the optical and electronic properties of semiconducting oxides such as TiO_2 [21,22]. Gold nanoparticles on the surface of TiO_2 have shown to enhance the charge separation within the nanostructured network, thereby decreasing the recombination losses [4,18-21]. The metal works can act as a charge reservoir for electrons (otherwise accumulated on the traps Ti^{3+}) in the TiO_2, which improves the separation of the electron-hole pairs. A negative shift in the apparent flat band potential has also been observed in Au/TiO_2 [18]. The latter could be indicative of the ability of the Au/TiO_2 composite film to suppress the charge recombination by facilitating hole transfer to the redox couple in the electrolyte.

In their studies Subramanian *et al*. have shown that the maximum Au loading level for efficient photocurrent generation is of ~2.0 wt% [20]. As shown in Figure 3.2a, the photocurrent efficiency increases up to an Au loading of 2.0, and then levels off and decreases. We speculate that this is due, however, to a corresponding increase in Au

particle size and decrease in site density rather than a limit on the intrinsic activity of Au sites.

It has been shown (refer to 2.4.6) that the addition of Au nanoparticles on TiO_2 powders and TiNT films slightly reduced their bandgap (0.1-0.2 eV). This apparent reduction in bandgap energy could be related to the existence of impurity energy levels between the conduction (CB) and valence band (VB) of the oxide [24,25].

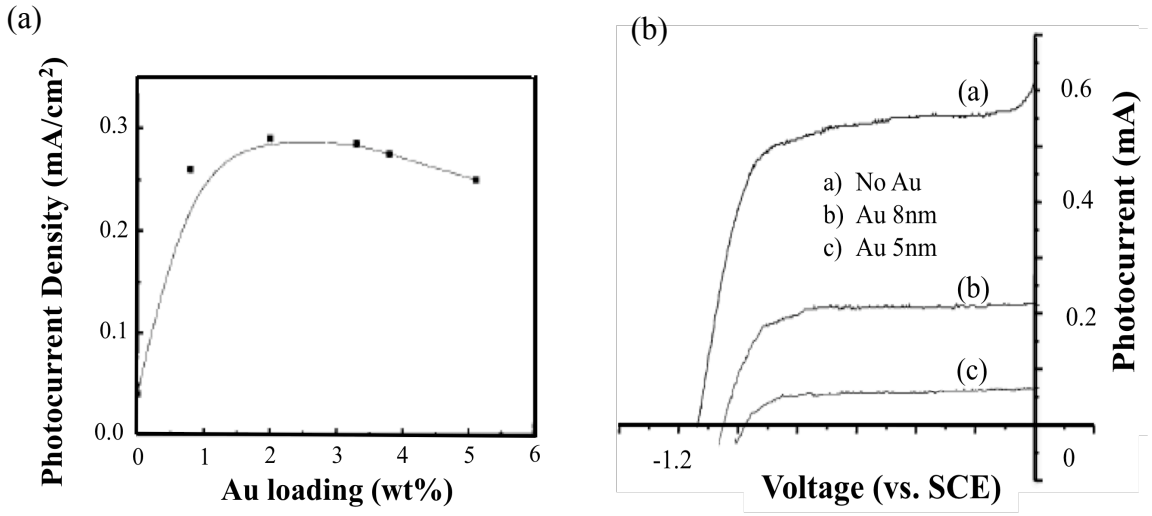

Figure 3.2 Photoanodes made with powder Au/TiO_2. (a) Plot showing the dependence of the photocurrent on the Au loading [20], the line was plotted to guide the eye. (b) Curves of i_{ph}-V characteristic for Au/TiO_2 loaded with different Au particle sizes [21]. The electrolyte used was 0.05 M NaOH and a Pt foil was the cathode.

The size of the metal particle as well as the method of deposition becomes crucial while tailoring the properties of a photocatalyst. It seems that the smaller Au particles induce a greater shift in the flat band potential than larger particles [21]. Also for other reactions such as CO oxidation, smaller particles are more catalytically active than larger particles [16]. Then, the catalyst with smaller Au nanoparticle is expected to be more

active catalytically, produce higher photocurrents, and oxidize water with greater photocatalytic efficiency than that composed of larger Au particles [26, 27].

The efficiency of photoelectrochemical cells will be the main determining factor of hydrogen production cost using PEC technology. Solar thermal processes are limited by the Carnot efficiency, whereas, solar photonic processes are limited by fundamental consideration associated with bandgap excitation [28].

Energy losses associated with energy conversion using PEC cells include several components that are associated with the following effects:

- Photons with $\lambda > \lambda_g$ (λ_g is the bandgap wavelength and $\lambda_g = hc/E_g$) cannot be absorbed and thus are lost to the conversion process [2,28].
- Photons with $\lambda \leq \lambda_g$ can be absorbed, but the excess energy (E-E_g) is lost as heat as the absorbed photon relaxes to the level of E_g. Unless some process can be devised to capture the excited states before they relax (like in multijunction PEC cells), this excess energy is not available to the conversion process [28].
- The energy of the excited state is thermodynamically internal energy and not Gibbs energy. Thus only a fraction (up to about 75%) of the excited state energy can be converted into useful work (e.g., electrical energy) or stored as chemical energy. This is why the open circuit voltage of a photovoltaic solar cell can never be as high as the bandgap potential. For example, a silicon photovoltaic cell, with $E_g = 1.1$ eV, exhibits an open-circuit voltage $V_{oc} \leq 0.8$ V. In a photoelectrochemical cell, these losses show up as part of the overpotential [2].
- When a PEC cell is illuminated, the excess chemical potential of the excited states is dependent on their concentration. The optimum condition (maximum power point) lies

somewhere between two extremes (short-circuit and open-circuit condition). Since a significant concentration of excited states exists at the optimum condition, there will always be some loss (1-2%) due to spontaneous emission (fluorescence) [1,2,28].

- There are irreversible processes associated with recombination of the electron-hole pairs, such as ohmic resistivity of the electrodes and electric connections, and overpotentials at the electrode/electrolyte interface.

The overall efficiency, which is known as the energy conversion efficiency (ECE) or solar-to-hydrogen efficiency (STH) is calculated using the following equation [29]:

$$\eta_{STH} = \frac{P_{out}}{P_{in}} \tag{3.4}$$

The output power (P_{out}) is the current density (mA/cm^2) multiplied by 1.23 V ($E°$, ideal potential for water splitting at 25 °C). And the input power (P_{in}) is the incident solar power (H_o, solar irradiation per irradiated area, in mW/cm^2). Then equation 3.4 becomes:

$$\eta_{STH} = \frac{E^o i_{ph}}{H_o} \tag{3.5}$$

The most unambiguous measurement of the photocurrent produced by a photoanode is to use two electrodes (no reference electrode). These two electrodes are the photoelectrode and a large-area counter electrode (typically Pt). Then, measure the short-circuit current between them while the sample is being illuminated. This of course assumes that the system works spontaneously and does not need an external bias voltage.

If a bias voltage is used then the convention is to subtract the bias voltage from the 1.23 V. The assumption here is that part of the output energy is used to generate the bias needed to make the reaction proceed. It should be noted here that one could get a negative efficiency if the bias voltage is high enough. That basically means that the light

energy is not adding anything and the process happening is standard water electrolysis [29]. Thus, equation 3.5 can be expressed as:

$$\eta_D = \frac{(1.229 - V_{bias})i_{ph}}{H_o} \tag{3.6}$$

Another way to measure efficiency is to measure the hydrogen generation rate directly. Then, following equation can be used:

$$\eta_{STH} = \frac{\Delta G^o_{H_2O} R_{H_2}}{H_o} \tag{3.7}$$

The input power here is the incident light intensity, and for this case, the output power is calculated by converting the volume H_2 per time, R_{H2}, which is the rate of hydrogen generation. In equation 3.7 ΔG^0 is the standard Gibbs free energy (237.141 kJ/mol).

The highest efficiency PEC cell based on TiO_2 (sigle bandgap photoanode, oxide without ion doping) has been reported for highly ordered titania nanotubes [11-13]. Grimes and Schmucki have shown currents up to 1.0 mA/cm^2 for nanotubes as long as 10-15 μm which corresponde to efficiencies in excess of 0.6-0.8 % [11]. Nitrogen and carbon ions have been used as dopants to reduce TiO_2 nanotubes bandgaps. Thermal treatments and ion implantation have been used [12, 30-33]. Current densities up to 0.9 mA/cm^2 have reported for nanotubes doped with carbon ions, the tube length was ~ 2 μm [33].

Based on the precedent from the literature sources cited above, it is evident that (a) producing the photocatalyst in the form of nanotubes to improve collection efficiencies, and (b) incorporating nanocrystalline gold onto the nanotubes to improve the

water oxidation activation, will significantly influence the PEC performance. This chapter details effects of these two strategies in the performance of the PEC cell.

3.2 EXPERIMENTAL

3.2.1 Photoelectrochemical Testing Setup

The photoelectrochemical experiments were carried out in a 3-electrode cell; Figure 3.3 shows the experimental set up. The components of the 3-electrode cell are a photoanode, platinum foil as the cathode, and an Hg/HgO (saturated in KOH) reference electrode (0.098 V vs. SHE). These electrodes were immersed in 1M KOH electrolyte, which was made by mixing potassium hydroxide (Fisher Scientific, ACS grade 88% w/w) with ultra pure water (Resistance = 18 Ω.cm). The electrolyte was bubbled with ultra high purity (UHP) nitrogen gas (99.99%) to remove oxygen.

A computer-controlled potentiostat (Gamry Instruments Series G750) was employed to perform linear sweep voltammetry, cyclic voltammetry, and chronoamperometry.

The simulated solar light was given by a 300 W solar source (Solar Light 16S-300). The 16S solar simulator replicates full spectrum sunlight and meets light sources by ASTM 892. The simulator had an AM 1.5 filter and gave an irradiation output of 100 mW/cm^2 of visible solar light (beam diameter 2 cm). Figure 3.4 shows a comparison between the actual AM 1.5 solar input and the 16-S solar simulator light output. The intensity of the light was measured using a power and energy meter (Newport Corporation, Model 70260). The solar light output was calibrated using a 2 cm x 2 cm solar cell that was originally calibrated at the National Renewable Energy Laboratory.

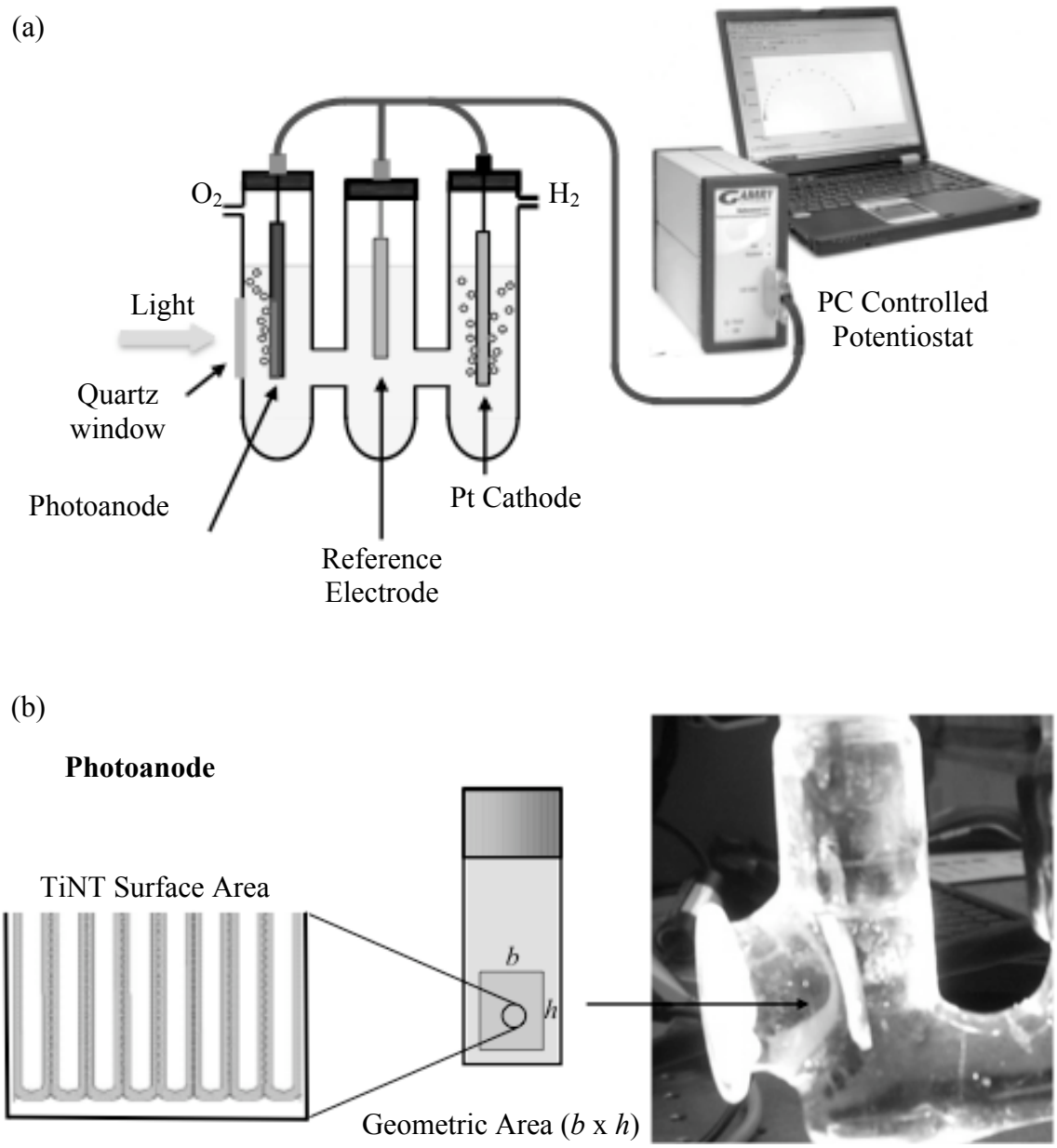

Figure 3.3: (a) Photoelectrochemical characterization testing set up: a 3-electrode cell, a potentiostat, a solar light simulator, and a power supply. (b) Photograph showing the photoanode under illumination, and a scheme showing the geometric electrode area and total nanotube surface area.

The glass cell included a 2.5 cm diameter quartz window for the light to pass and reach the photoanode. The optical losses due to transmission, reflection and absorption from the window, electrolyte column and photoelectrode were taken into account for the

final photocurrent and efficiency calculations. The optical transmission (Varian UV-Vis spectrometer) for quartz and the electrolyte column were 0.95 and 0.82, respectively; and the reflection from the photoanode was about 0.15.

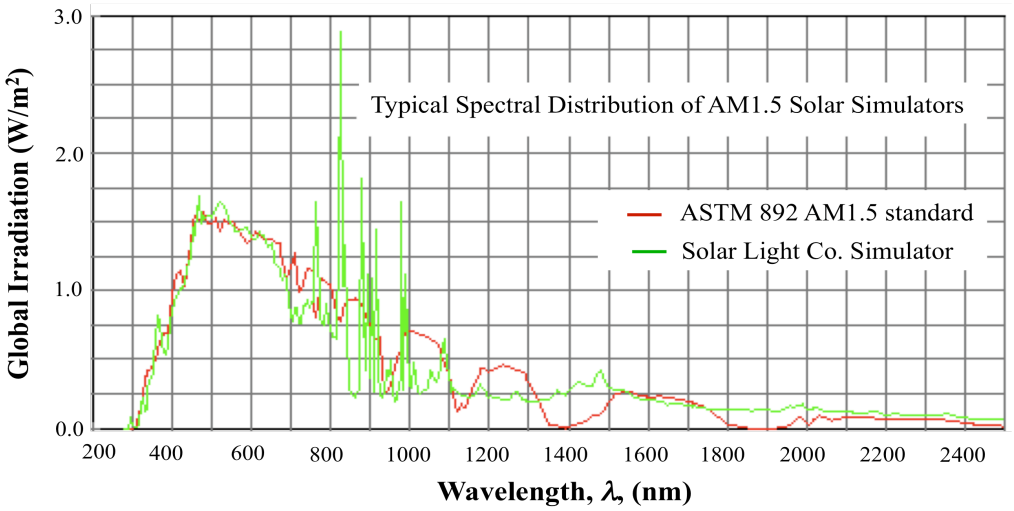

Figure 3.4: Plots showing the solar light spectrum for AM1.5 and the spectrum from the 16S Solar Simulator [34].

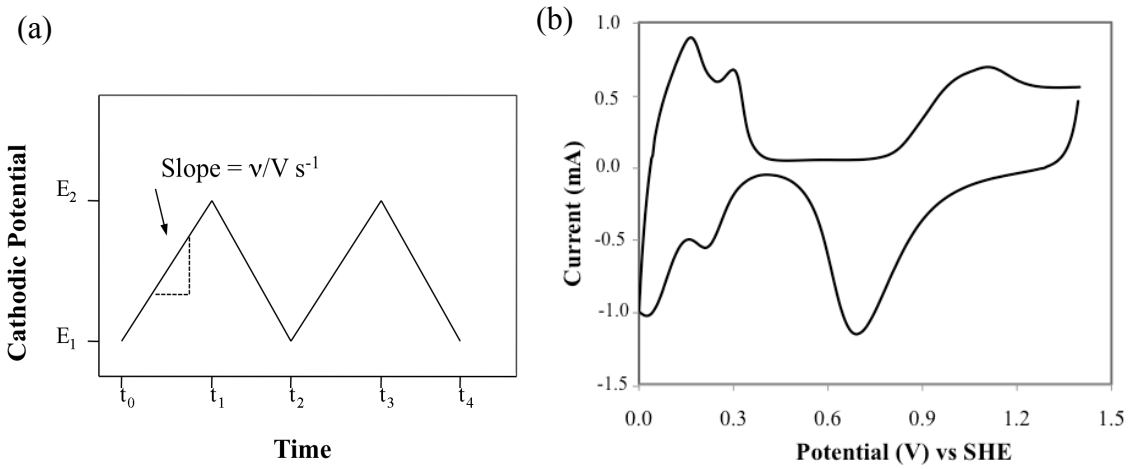

Figure 3.5: (a) Potential waveform applied to the working electrode in the cyclic voltammetry experiments. (b) Characteristic CV for Pt electrode in 0.5 M H_2SO_4, using a 50 mV/s scan rate.

3.2.1.1 Electrochemical Techniques

Cyclic Voltammetry (CV): involves applying a potential to the working electrode that changes with time as it is shown in Figure 3.5. The current flowing through the working electrode is measured as a function of the applied potential. The plot of current versus voltage is known as a voltammogram [35].

Linear Swept Voltammetry (LSV): similar to CV except that the potential is varied linearly with time with sweep rates ν ranging from 10 V/s to 200 V/s. The current is again measured as a function of potential, which is equivalent to recording current versus time [36]. Figure 3.6 shows the potential applied during a LSV experiment and the resulting current density versus voltage.

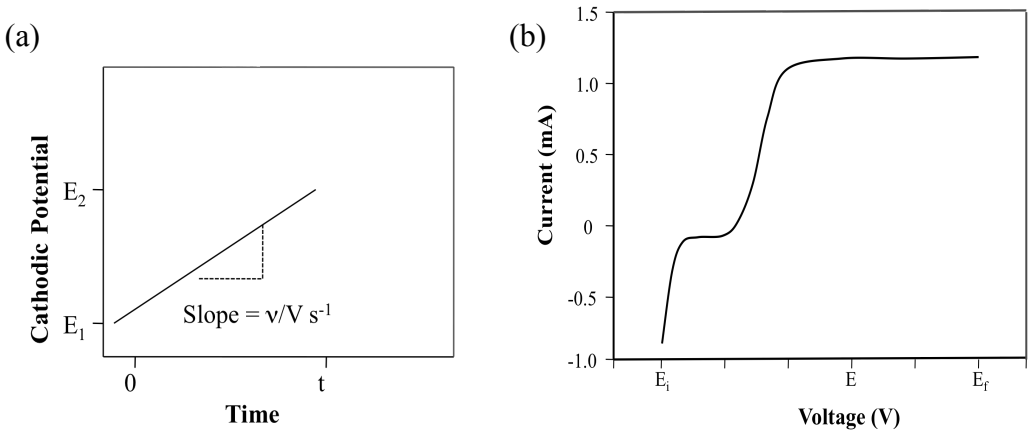

Figure 3.6: (a) Linear potential sweep or ramp. (b) Resulting i_{ph}-V curve for a PEC cell.

Chronoamperommetry (CA): this case a constant potential is applied to the working electrode for given period of time. The resulting plot is a current as a function of time (Figure 3.7) [35].

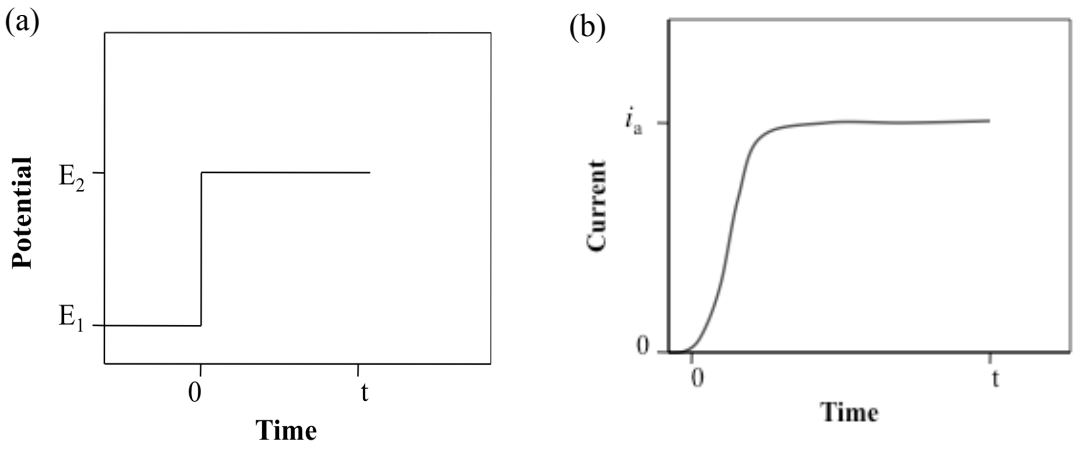

Figure 3.7: (a) Waveform for the step voltage applied during chronoamperometry. (b) Current flow recorded as a function of time.

3.2.1.2 Electrode Preparation

The photoelectrodes were prepared as described in section 2.3.6. In summary, electrodes were prepared with powder (TiO_2 and Au/TiO_2) by making a paste with polyethylene glycol solution. The paste was deposited onto indium tin oxide (ITO, electrically conductive) coated glass. The deposition on conductive glass was done using the doctor-blade technique. The electrodes made with the TiNT films, were prepared by attaching the TiNT film to a glass substrate. The excess surface of the film was painted with white enamel, leaving a small uncovered area of ~ 0.3 cm^2 for testing. The electrodes are connected to the potentiostat or power supply using alligator clamps.

3.2.2 Efficiency Measurements

There are two ways to make the measurements for efficiency calculations: one is to measure the rate of hydrogen (or oxygen) evolution directly, while the second is to measure the current flow between the electrodes and then assume a 100% current

efficiency (also called Faraday efficiency) for the production of hydrogen. The easiest and most common method to calculate the STH efficiency is to measure the current flow between the photoelectrode and the counter electrode, and then calculate the power out of the PEC cell and compared it to the input solar power.

In this work, equations 3.5 and 3.6 were used to calculate the efficiencies for the different photoelectrodes. The photoanode and the Pt counter electrode (two-electrode cell) were short-circuited and the photocurrent produced was measure along with V_{oc} of the cell under illumination. The electrolyte used was 1.0 M KOH (saturated with N_2 gas).

When external voltage was applied to the photoelectrodes, equation 3.6 was used. The efficiencies reported using the latter equation were not true STH efficiencies; because the extra energy supplied to the system to split water needed to be substracted from the STH equation [29]. These efficiency values are called diagnostic efficiencies or applied bias photon-to-current efficiency as used in reference by Chen *et al* [29], and were used to compare photoelectrode performances.

3.2.3 Trap Sites Location

Electron traps in nanostructured TiO_2 can be studied by means of electrochemical methods, such as chronoamperometry and cyclic voltammetry [7-9].

CV measurements were used in this work. The voltammograms were taken at room temperature in a standard 3-electrode cell with and without illumination. The electrolyte used was 0.1 M H_2SO_4 purged with UHP N_2 gas, along with an Hg/Hg_2SO_4 (0.658 V vs. SHE) reference electrode, and a Pt foil counter electrode. Measurements were performed with the computer-controlled G750 potentiostat. The CVs were recorded

at three scan rates 25, 50 and 100 mV/s between -0.4 and 0.4 V (vs. SHE). The current densities for this test were reported on the basis of the geometric area.

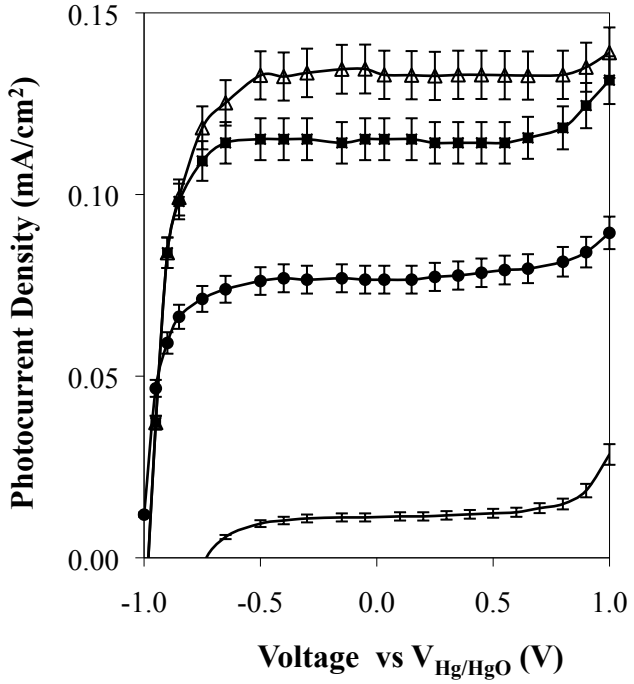

Figure 3.8: Photocurrent density-Voltage (i_{ph}-V) plots for 3 photoelectrodes fabricated with powder photocatalysts. (-) P25 dark case was taken without illumination. (•) P25 powder photoanode. *tint* photoelectrodes calcined at (■) 650 °C, and (▵) 500 °C.

3.3 RESULTS AND DISCUSSION

3.3.1 Influence of TiO_2 Structure on the Photoanode Performance

The structure of the photocatalyst affects the transport of the charge carriers in the photoelectrode films. The transport of majority carriers (electrons) in nanoparticulate TiO_2 proceeds by trapping and detrapping [5,39]. During this process some of the photogenerated electrons recombine with holes. This phenomenon occurs especially

when spherical-like nanoparticulates of TiO_2 are used (i.e. P25), and it is one of the major sources of energy losses. It has been suggested that changing the structure of the TiO_2 from spherical to nanotubes or nanofibers would reduce the recombination process and help the transport and separation of majority carriers [11,13,24].

Preliminary work was done using disordered TiO_2 nanotubes powders to study the influence of the different oxide structures on the separation and transport of charge carriers. Photoelectrochemical measurements were done using *LSV* to record the photocurrent density produced by the *tint*-based photoanodes under applied bias potential. The photocurrents were compared to the ones produced by electrodes made with only P25. Figure 3.8 shows i_{ph}-V curves for three photoanodes, the photocurrent densities were calculated using the geometric surface area of the electrode. The photocurrents produced by the disordered nanotube electrodes were higher than the one for P25 by about 80 %. The i_{ph} produced by nanotube powder calcined at temperature, higher than 500 °C gave lower photocurrents. The latter can be due to the phase (from anatase to rutile) and structure (from nanotubes to nanorods) transformation that the nanotube suffered during the high temperature thermal treatment (refer to section 2.4.1). The influence of thermal treatment on photoanode performance will be discussed in section 3.3.2.

When nanoparticulate TiO_2 is used ~5% of the charge carriers produced in the photoanode under illumination are used to produce current. Conversely, if *tint* are used the photocurrent produced increased by a factor of two, then in this case ~10% of the electron and holes generated were used in the photocatalytic reaction. Even though the increment of photocurrent generated by these nanotube-based electrodes was significant

compared to the commercial photocatalyst, these values are still low for a feasible photoelectrolysis application. Losses due to recombination and low photocatalytic rates are still major drawbacks in the operation of PEC cells.

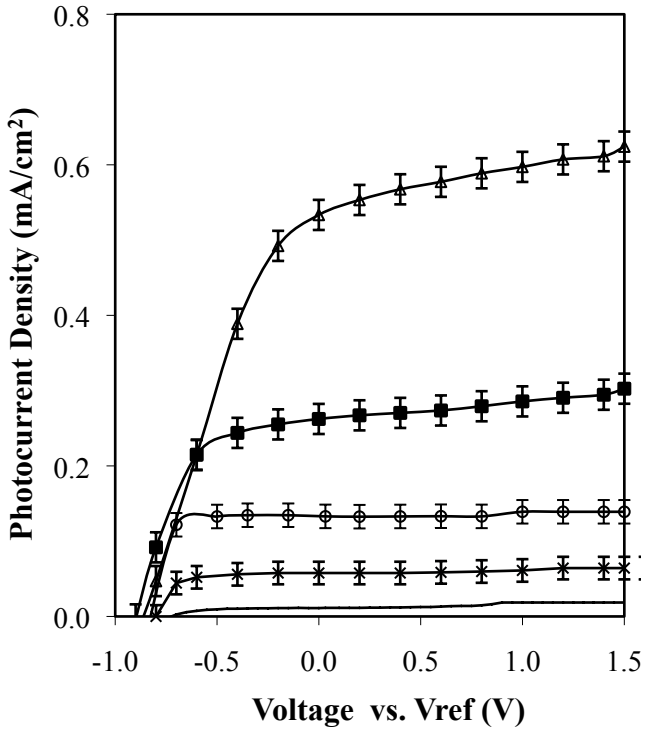

Figure 3.9: i_{ph}-V plots for different photoanodes. (-) P25 taken in the dark, and measurement taking under illumination (x) P25, (o) *tint* with L = 500 nm, (■) TiNT with L = 3 μm, (Δ) and TiNT with L= 8 μm. All the nanotube samples were calcined at 500 °C in air for 3 hours.

An ideal photocatalyst structure for water splitting is one that can help an efficient separation and transport of electron/hole pairs. These structures should allow the transport of electrons to the back of the photoelectrode without crossing any boundaries and the facile movement of holes to the surface of the photocatalyst. The usage of highly ordered vertical oriented TiO_2 nanotubes have been reported to enhance charge

separation and transport [11-13]. TiNT arrays were prepared under different fabrication conditions and tested as photoanodes in a PEC cell.

Figure 3.9 shows the i_{ph}-V plots comparing P25, *tint* and TiNT electrodes. The solid line at the bottom of the graph was taken in the dark (data from a P25 photoanode). The photocurrents produced by the TiNT-based electrodes were almost one order of magnitude (TiNT L = 8 μm) greater than the photocurrents produced by the both powders (P25 and *tint*) photocatalyst electrodes. Thus, for the 8 μm length TiNT electrode, it could be said that the usage of the photogenerated charge carriers also increased one order of magnitude, from 5 to ~50%. This enhancement could be because the nanotube structure has boosted the separation and transportation of electrons before they can recombine with holes [11-13,37].

3.3.2 Highly Ordered Titanium Dioxide Nanotubes

In the previous section it was shown that the current density produced by TiNT-based electrodes was much greater than the current densities for powder catalysts. The effect of nanotube dimensions and crystalline phase on the performance of the TiNT based electrodes will be discussed in this section.

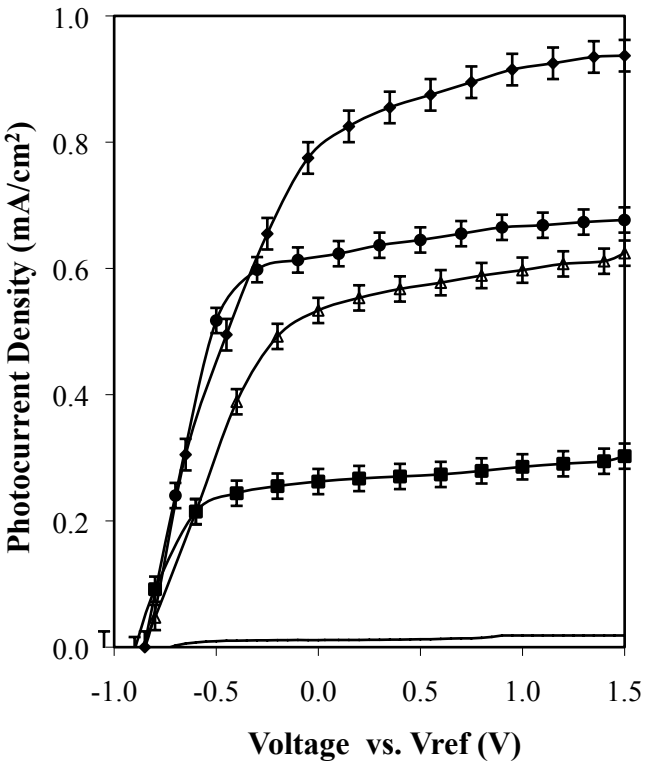

Figure 3.10: i_{ph}-V curves for TiNT photoelectrodes prepared by anodization. (-) Data obtained in the dark for TiNT photoanode. Illuminated photoanodes with nanotube length L (■) 3 μm, (▵) 8 μm, (◆) 15 μm, and (•) 45 μm. All the samples were calcined in air at 500 °C for 3 hours.

3.3.2.1 Nanotube Dimensions: Influence on the Photocurrent

Figure 3.10 shows the photocurrent density as a function of voltage for several different TiNT photoelectrodes; the i_{ph} values are given based on electrode geometric surface area. The bottom solid line is the dark case for tubes with length 15 μm (dark plots for the longer tubes were also recorded with similar results). In general, as the nanotube lengths increased, the i_{ph} increased as well. The increase may have been consequence of increased light absorption and active site number for water oxidation due to the higher surface areas. In contrast, the i_{ph} obtained with nanotubes with length of ~

45 μm actually decreased. In order to better understand the latter issue, nanotubes with different length were fabricated. The anodization time was varied and the applied voltage was kept constant. It was shown in 2.4.2 that the nanotube length varies almost linearly with anodization time.

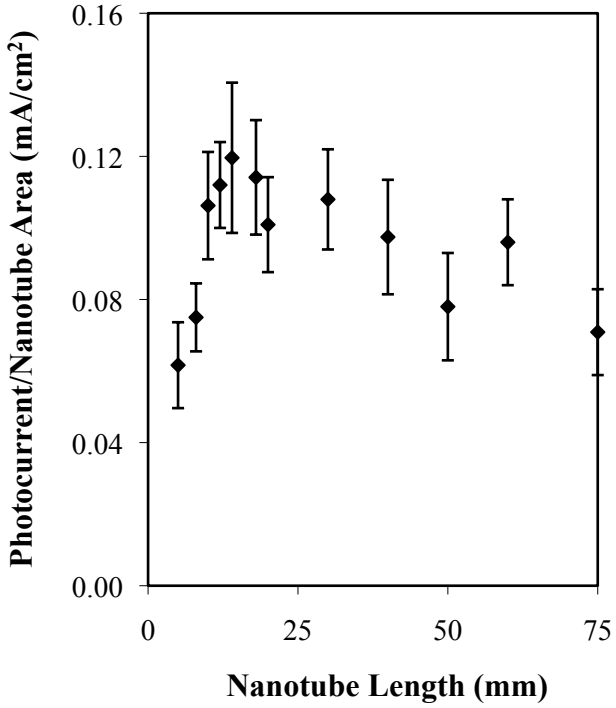

Figure 3.11. Specific current as a function of nanotube length. The specific currents were calculated using the saturation current measured at 0.5 V and dividing it by the TiNT total surface area.

Nanotubes with length between 5 and 75 μm where tested using LSV and CA. Photocurrents at 0.5 V (vs. Hg/HgO) applied bias voltage were recorded and normalized by the total nanotube surface area calculated using CV (section 2.4.7). This normalized current was called specific photocurrent, j_{ph}.

While TiNTs longer than 75 μm were readily produced, the results indicated that there was no performance benefit associated with using tubes longer than 15-20 μm (Figure 3.11). The diffusion length of electrons generated with visible light (AM 1.5) in long TiNTs is 15-20 μm suggesting. That is, for tubes longer than 20 μm; charge carriers could recombine before participating in reactions [37,38]. Also, due to shadowing, the light might not be able to reach the bottom of the nanotubes, therefore producing tubes longer than 20 μm could lead to inefficiencies. Based on these results, titania nanotubes with average lengths of ~15 μm were used for most of the following experiments.

3.3.2.2 Thermal Treatment

The photocatalytic properties of titania depend on its crystalline phase. X-ray diffraction showed that the as-prepared TiNTs structure was amorphous. Annealing the nanotubular arrays resulted in the transformation of the amorphous material into crystalline phases. It was shown in section 2.4.3 that the heating and cooling rates affected the final structure and integrity of the nanotubes. Faster heating ramps (i.e. 10 °C/min) led to the collapse of the nanotube structure. In terms of the annealing temperature, it was demonstrated that the anatase phase starts to appear at 300 °C, and complete transformation occurs at 500 °C. The rutile phase starts to appear at temperatures higher than 500 °C.

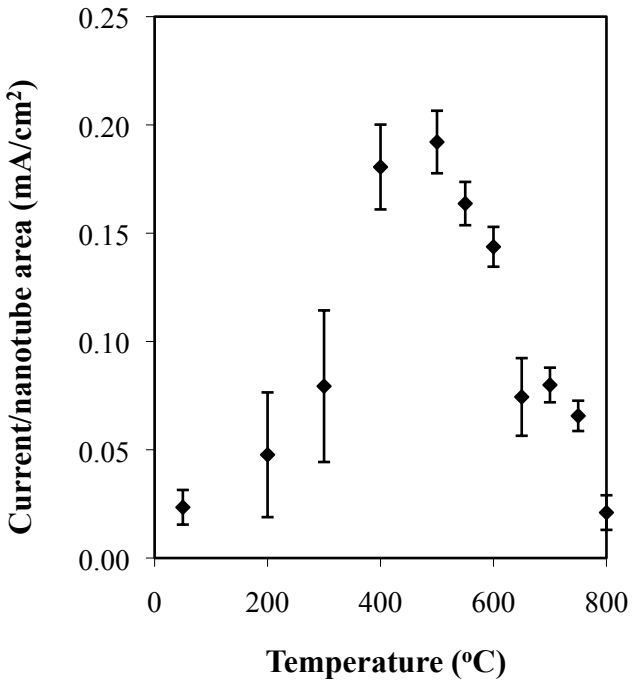

Figure 3.12: Specific photocurrent as a function of calcination temperatures. The nanotube average length for all the samples used was ~15 mm and the external diameter was ~150 nm.

In Figure 3.12 the specific photocurrent was plotted versus calcination temperature. The j_{ph} increases with calcination temperature until it reached a maximum at about 550 °C, after which it subsequently decreased. At this temperature the tubular structure completely collapsed leaving dense rutile crystallites. From this plot, it can be concluded that the best calcination temperature is 500 °C, which corresponds to a pure anatase phase.

As mentioned previously, the photocatalytic properties of TiO_2 depend on its crystalline phase. The anatase phase is typically preferred for electrochemical applications over the rutile phase, because the anatase phase appears to be more active for water oxidation [13,39-41]. Differences between the phases could be a consequence of the differing conduction band energies. The conduction band energy for rutile TiO_2 is

essentially coincident with the reversible hydrogen potential at all pH values, whereas for anatase TiO_2 the E_{CB} is more negative by 0.20 V. The latter means that rutile needs more external bias than anatase to oxidize water.

3.3.3 Charge Trapping

During illumination TiO_2 absorbs photons with energy equal to or greater than its bandgap, thus generating an electron-hole pair. Following this, the pair is separated into free electrons and free holes. The electron and hole randomly 'walk' to the bulk of the electrode and to the surface of the photocatalyst, respectively, and are trapped. Electrons travel to the back of the electrode and the holes react with donor molecules. Holes can also be trapped at bulk trapping sites and recombine there with electrons, releasing heat. The reaction between the reduced acceptor and hole can occur after the initial charge transfer, especially when the species are strongly adsorbed on the TiO_2 surface [39].

Photogenerated charge carriers, either free or trapped, can be probed by various spectroscopic techniques. Trapped holes and electrons absorb light in the visible and near-infrared spectral regions, whereas free electrons absorb in the infrared or microwave regions [39]. These techniques allow one to measure the time scales of photoelectrochemical processes by means of transient spectroscopies, such as transient absorption (TA) spectroscopy [42,43]. Studies using TA suggested that the charge recombination in a titania photocatalyst could be a slow process due to efficient charge trapping, and that interfacial charge transfer can be competitive to charge recombination [5,39,43].

Traps for electron and holes are needed in the photocatalyst process to suppress recombination and increase the probability of interfacial charge transfer [9,39]. In addition, the use of long enough nanotubes (~15 μm) can also help to facilitate transfer of electrons before recombination. Electron paramagnetic resonance (EPR) is frequently used to trace trapped electrons and holes in TiO_2 nanoparticles after UV illumination [9,43]. At low temperatures, trapped electrons can be detected in the form of Ti^{3+} (equation 3.9) [42,43]. Trapped holes can be observed using EPR as well, thus traps are considered to be localized deep trap states [9]. However, there is no consensus on the exact nature of the state: several types of species, such as sub-surface oxygen radicals connected to surface hydroxyls (Ti-O$^{\bullet}$-Ti-OH) surface oxygen radicals (Ti-O-Ti-O$^{\bullet}$) generated from basic surface hydroxyls, lattice O$^{\bullet}$ radical, etc. are postulated to exist in various cases [39]. On the basis of EPR Berger *et al.* specified the following charge transfer steps [9]:

$$TiO_2 + h\nu \rightarrow e^-_{CB} + h^+_{VB} \tag{3.8}$$

$$e^-_{CB} + Ti^{4+} \rightarrow Ti^{3+} \text{ , trapped electrons} \tag{3.9}$$

$$h^+_{VB} + O^{2-} \rightarrow O^- \text{ , trapped holes} \tag{3.10}$$

3.3.3.1 Electron Accumulation in Nanostructured TiO_2 Electrodes

In a nanostructured electrode the electrolyte penetrates the porous structure (absolute surface area exceeds the geometric surface area), because of that no significant macroscopic electric field exists in the semiconductor film [44]. Thus, electron transport occurs by diffusion. Consequence of this charge recombination depends on the nature of the film (porosity, particle size, etc.) as well as on the interfacial reaction rate [45]. The

latter implies that charge carrier recombination cannot be suppressed by an external bias voltage [46]. The electron diffusion coefficient in porous TiO_2 electrodes is orders of magnitude smaller than in the case of a single crystal electrode. This slow e^- transport has been attributed to the high concentration of localized states, which act as electron trapping sites. In TiO_2 the traps states are point defects such as oxygen and titanium vacancies and hydroxyl groups [46].

Charge carrier traps are energetically located below the conduction band (CB) edge of the semiconductor, they can be filled either by bandgap illumination with enough intensity or by means of an external bias voltage (using a potentiostat) [47]. Applying potentials negative to flat band potential (E_{fb}) leads to electron accumulation accompanied by CB filling according [45,46]:

$$TiO_2 + e^- + H^+ \rightarrow TiO_2\left(e^-_{CB}\right)\left(H^+\right)_{ads} \tag{3.11}$$

That is, electrons occupy conduction band states with the accumulated charge being compensated by adsorption of a proton from the electrolyte. Band filling gives rise to an apparent increase in the band gap energy, known as a Burstein shift [44]. On the other hand, at positive applied potentials close to E_{fb}, electron accumulation is accompanied by trap filling. That is, electrons occupy surface Ti^{4+} states with the accumulated charge being compensated by adsorption of a proton from the electrolyte [45,46] according to:

$$Ti_s^{4+}OH + e^- + H^+ \rightarrow TiO_s^{3+}(OH)\left(H^+\right)_{ads} \tag{3.12}$$

The applied potential at which the spectral changes assigned to the accumulation of electrons in surface trap and conduction band states observed is related to the energy of the trap and conduction band states being filled [44]. Then the E_{fb} plays an important role in the determination of the location and density of electrons traps. The flat band

potential of a semiconductor in contact with an electrolyte varies with the solution pH [44-48] according to:

$$E_{fb(vs.SHE)} = E_{fb,PZC} - 2.3kT\left[pH - PZC\right] \quad (3.13)$$

Where $E_{fb,PZC}$ is the flat band potential at the PZC (point of zero charge), k Boltzmann constant and T is the temperature of the electrolyte.

3.3.3.2 Electron Trap in Nanostructured TiO_2 Films

Electron traps at nanostructured TiO_2 (powder and TiNT films)/electrolyte interface have been studied by means of electrochemical methods (CV). The electrodes were made with TiO_2 (P25) and Au/TiO_2 powders and TiNT and Au/TiNT arrays. The flat band potentials for TiO_2 and TiNT (0.1 H_2SO_4, pH = 1.4) were calculated using equation (3.7) and were -0.14 V and -0.06 V (versus SHE), respectively.

Cyclic voltammograms of electrodes made with TiO_2 (P25) are shown in Figure 3.13.a. At potential negative to the E_{fb} of TiO_2 (-0.143 V) there is electron accumulation in the conduction band; in this section the plot follows an exponential trend [44-48]. Current peaks appear at potential positive to the E_{fb}, these peaks are associated with filling electron traps (Ti^{3+}) [49-51]. At positive potential ($E >> E_{fb}$) a nearly constant capacitance section is found, corresponding to the exposed surface of the conductive substrate [50].

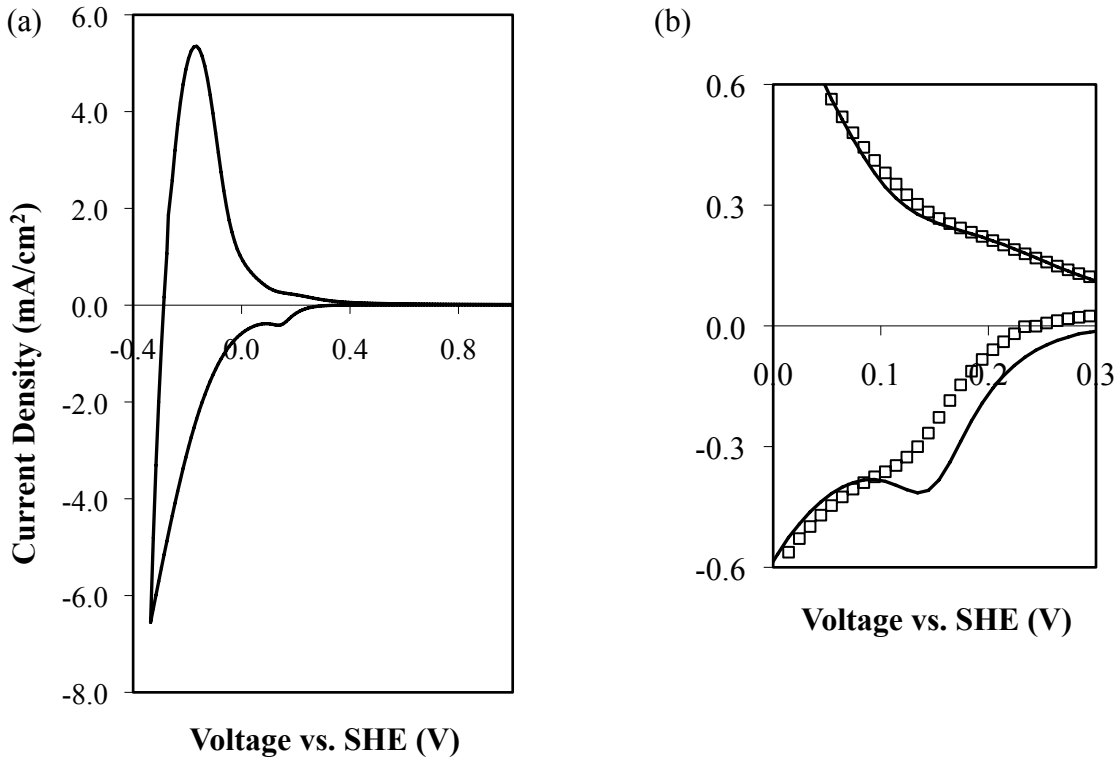

Figure 3.13: (a) Characteristic CV plot for a TiO_2 (P25) powder photoelectrode. TiO_2 powder was deposited on a conductive glass substrate; then scan rate was 50 mV/s. No light was used (dark). (b) Magnification of the region where the electron traps are located; (-) dark, (□) light.

Figure 3.13.b shows CVs of TiO_2 photoelectrodes taken without (dark) and with (light) illumination. The height of the current peak is smaller for the light case than the one for the dark. While holes are scavenged by the electrolyte (to oxidize water), electrons can move through the film and fill up part of the available traps. The shorter peaks might be explained by assuming that the light created additional traps, which would result in a slower photocurrent response and a decreased collected charge [52]. Also, trapped photogenerated electrons might recombine with holes releasing heat and decreasing the final photocurrent.

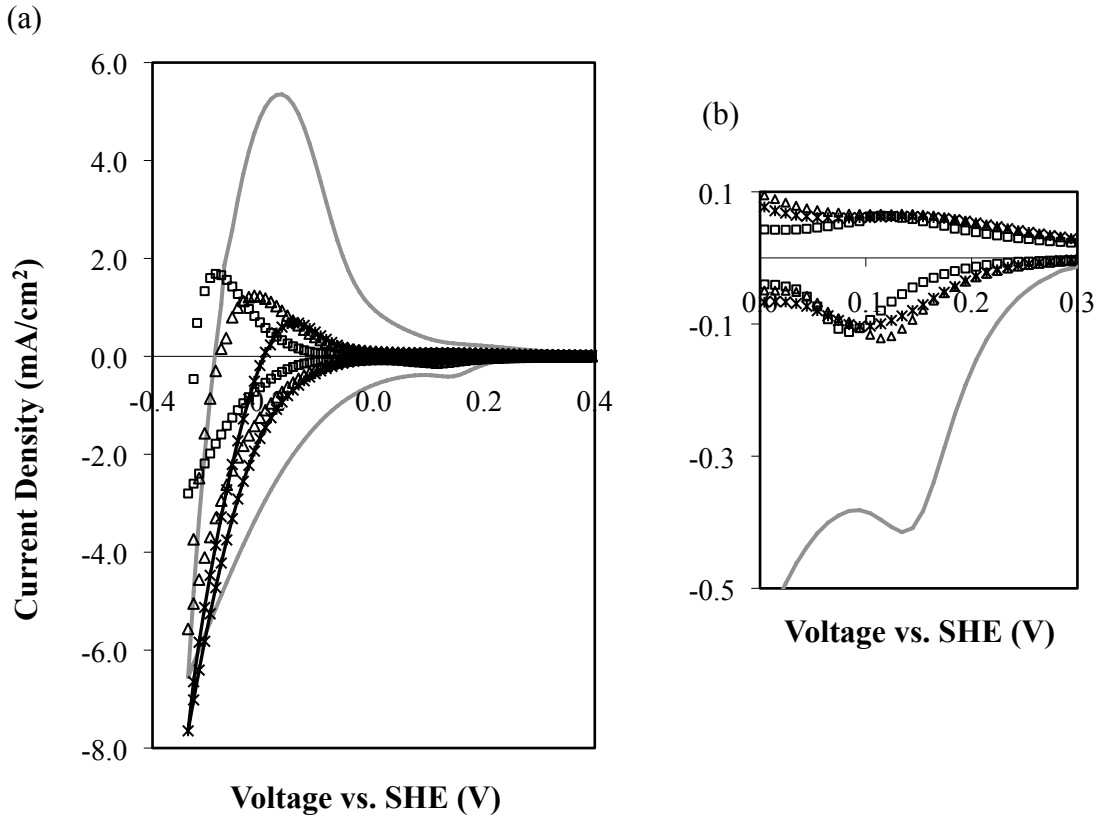

Figure 3.14: (a) CV plots for photoelectrodes made with powder (-) TiO_2, and Au/TiO_2. The gold loadings were (□) 0.7, (Δ) 1.7 and (x) 3.1 wt%. (b) Zoom in of the CV regions, which show the peak associated to charge trapping.

CV voltammograms were taken for Au/TiO_2 photoelectrodes (Figure 3.14). Adding Au to the surface of TiO_2 changed the shape of the accumulation section of the CV curve. Instead of an exponential variation, the current exhibits an approximately linear growth. This behavior indicates that current losses dominate, although there is still charge accumulation until certain extent [53]. An increase in the Au content maximizes these characteristics in CV plots. Higher Au loading (wt > 3.1%) and negative applied potential would make the photoanode behave like a cathode producing hydrogen gas at lower potential than pure TiO_2. The latter indicates that the addition of Au nanoparticles reduces the flat band potential to more positive values. Figure 3.13.b shows a

magnification of the region where electron trapping occurs. The trap peaks for Au/TiO_2 (3 different Au loadings) photoelectrodes were much smaller than the peak for TiO_2. This could be because the electrons were consumed in the hydrogen evolution reaction (HER).

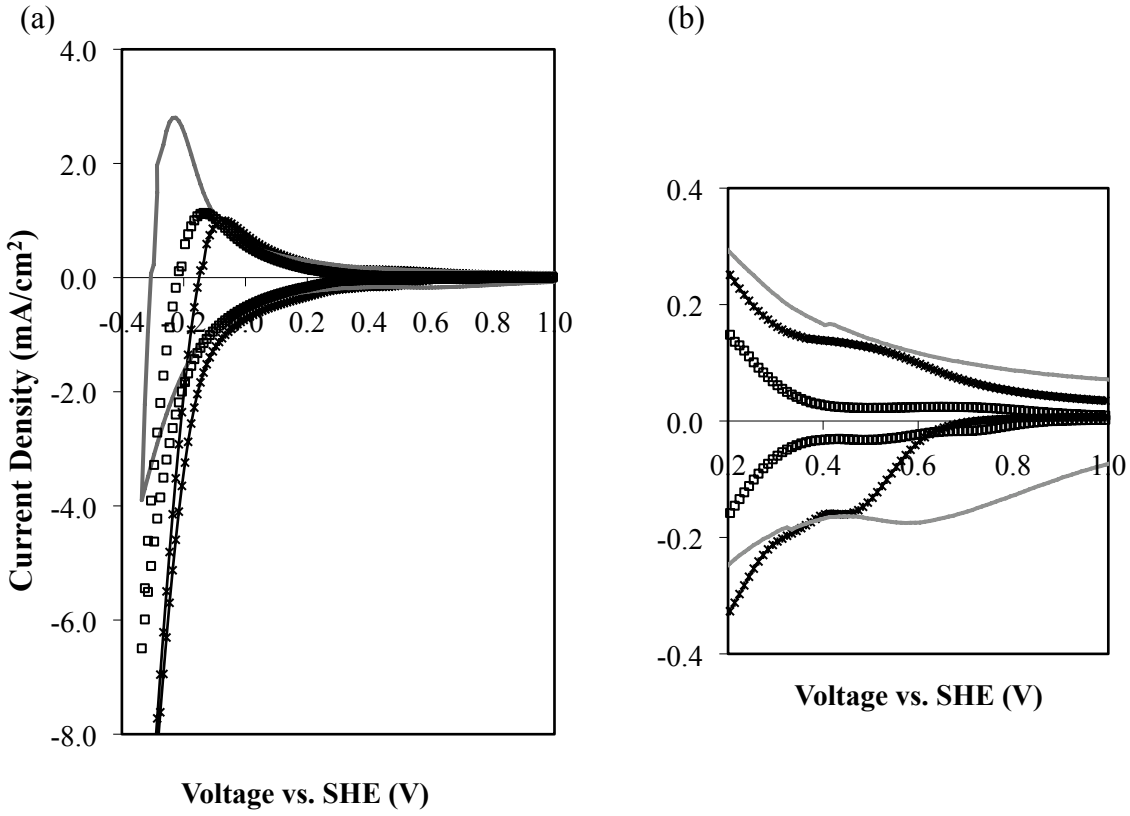

Figure 3.15: (a) CV plots for (-) TiNT, and Au/TiNT (□) photoelectrodes. The gold loadings and particle sizes were 0.4 wt% Au and 8.5 nm particle size and (*) 2.1 wt% Au and 3.1 nm particle size respectively. (b) Close up of the peak associated to charge trapping.

Figure 3.15 shows CV plots for TiNT and Au/TiNT. The TiNT voltammogram looks very similar to the one for TiO_2, however there is a shift in the location of the trap peaks (between 0.4 and 0.6 V). The later, was consequence of the more positive E_{fb} obtained for TiNT in 0.1 M sulfuric acid. At $E < E_{fb}$ a region for electron accumulation is also observed. In the case of Au/TiNT the tendency of the electrode to behave as a

cathode as the Au loading increases is similar Au/TiO_2. Charge accumulation in trap sites for TiNT is in general (with and without Au) lower than the amount for TiO_2. That could be result of the better electron separation and transport in long nanotubes (L ~15 μm) in contrast to smaller spherical particles (ϕ ~20 nm).

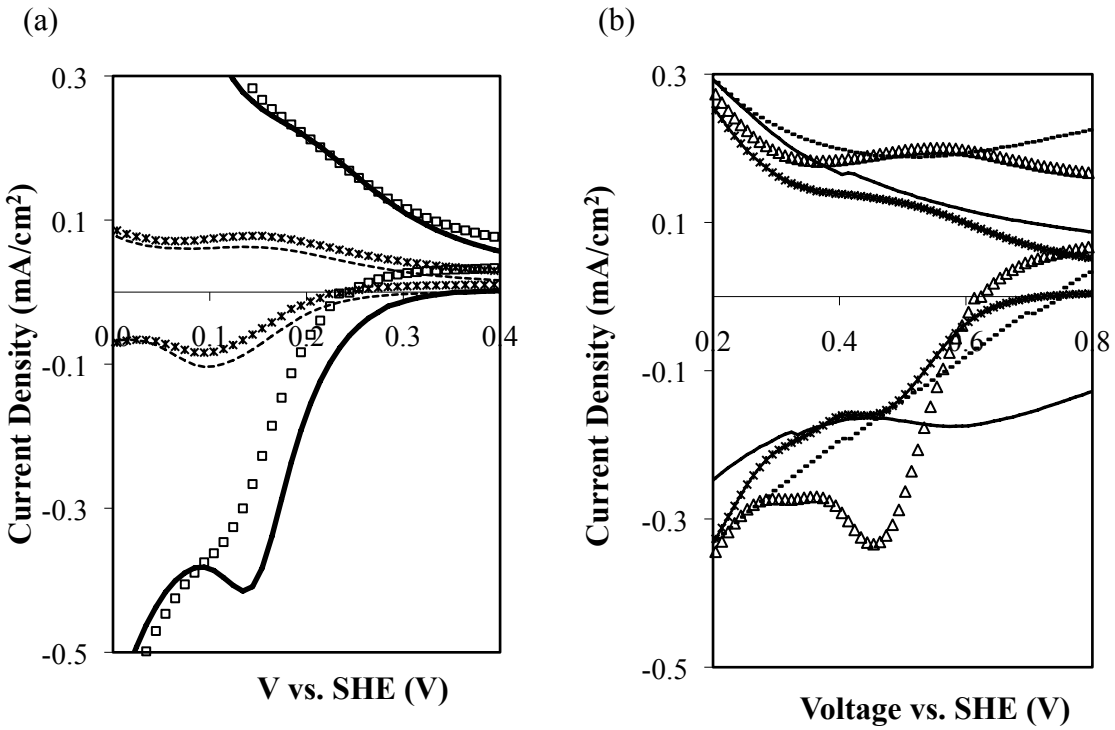

Figure 3.16: Cyclic voltammograms plots of gold loaded TiO_2 and TiNT. (a) Films made with powder TiO_2 (-) dark and (□) light, and Au/TiO_2 3.1 wt%, (--) dark and (*) light. (b) Films made with TiNT (-) dark and (•••) light, and Au/TiNT 2.1 wt% (*) dark and (Δ) light.

Under illumination Au/TiO_2 (Au/P25) behaves similarly to TiO_2; the peak height decreases as the incident light is removing trapped electrons (Figure 3.16.a). That is not the case for Au/TiNT, during illumination the current peak at the trap states actually increased (Figure 3.16.b). It seems that light created more trap states on the surface of the nanotubes and also more electrons due to the reduction of the E_g of Au/TiNT. In addition,

more light could have been absorbed by Au/TiNT (due to surface plasmons) and electrons were injected into the conduction band of TiNT.

3.3.4 Gold Deposited on TiO_2 Photocatalyst

Gold nanoparticles were successfully loaded on TiO_2 nanostructures. It was learned that the loading parameters influence the final structural characteristics of the Au/TiO_2 photocatalyst, and that the addition of Au nanoparticles changes the optical and electric properties of titania. Results presented earlier suggested that Au nanoparticles also influence the trapping of electrons in the bulk of the semiconducting electrode.

3.3.4.1 Au/TiO_2 Powder Photoelectrodes

Figure 3.17 shows the photocurrent curves as a function of bias voltage for photoanodes built using powder TiO_2 and Au loaded on TiO_2 and *tint* supports. The bottom solid line represents the results obtained in the dark (called dark case) for the Au/TiO_2 electrode. The photocurrents produced by both Au supported photocatalysts were about 60% greater than the one for TiO_2 alone. Subramanian *et al.* obtained similar results when they tested photoanode made from powder Au/TiO_2 [20,21]. The increment in photocurrent was attributed to charging of the metal nanoparticles by electrons followed by Fermi level equilibration between the metal and semiconductor in the composite nanotube array [18-21]. This charging phenomenon seems to enhance charge separation within the TiO_2 network, thereby decreasing recombination losses and increasing photocatalytic activity. Also, the dispersed gold nanoparticles are expected to decrease the overvoltage necessary for hole transfer to the redox reactions in the electrolyte. By promoting the interfacial hole transfer, the gold nanoparticles facilitate

charge stabilization within the nanostructured TiO_2 films so that the electrons can be transported with minimal charge recombination losses [19-21].

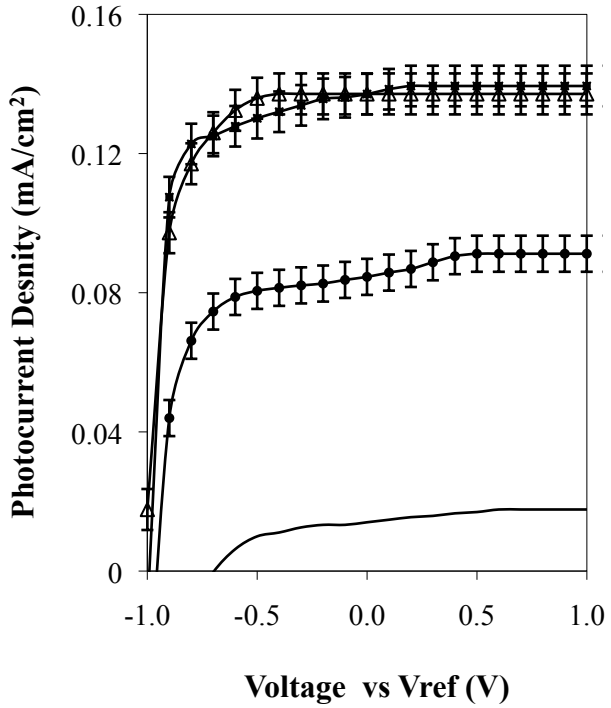

Figure 3.17: Photocurrent density-voltage plots for photoelectrodes prepared with powder photocatalysts (-) dark, (•) TiO_2, P25, (■) Au/TiO_2, and (▵) Au/*tint.* The nominal Au loadings were 2.4 and 0.9 wt% for Au/TiO_2 and Au/*tint*, respectively.

Bandgap Reduction

The addition of Au nanoparticles, with average diameter 5.2 nm, to the TiO_2 powder caused a slight decrease in the bandgap (E_g from 3.35 to 3.17 eV). Using the solar energy spectrum (photon flux versus wavelength, Figure 3.4) and calculating the amount of energy that can be generated by reducing the TiO_2 bandgap ~0.2 eV, it was found that this E_g reduction should increase the photocurrent produced by ~20%.

The highest E_g reduction (~0.2 eV) was obtained when the actual Au loadings were 2.0 wt% (± 0.5 wt%) and the average particle size was 4.5 nm (± 0.5 nm). Lower loadings with the same metal particle size gave lower bandgap reduction (as low as 0.05 eV). On the other hand, higher Au loadings and bigger Au particles (5 nm < ϕ < 10 nm) led to no significant reduction in the E_g further than 0.2 eV for Au/TiO_2 powders.

Gold Loading

The photocurrent produced by Au/TiO_2 photocatalysts depended on the amount of metal deposited on the oxide support. The highest photocurrent was produced with Au loading of about 2.2 wt%, which can be related to the bandgap reduction being the maximum for this amount of Au. The photocurrent produced by the Au/TiO_2 increase was about 60% more than the TiO_2 alone. Higher loading (2.5-3.5 wt%) did not show higher increase in current density. It has been argued that higher amounts of Au might block some of the light used to produce charge carriers [21].

Gold Particle Size

The Au particle size changed the photocurrent delivered by Au/TiO_2; the highest i_{ph} observed was obtained with average Au size of 4.5 nm. Metal particles bigger than 6 nm did not increase the photocurrent densities. Besides, slightly reducing the bandgap of TiO_2, Au has been reported to increase the catalytic activities of TiO_2 [4,21,24]. However, this increase in performance has been reported only when particles smaller than 5nm are used [21].

For powder Au/TiO_2 photocatalysts a rise of ~60% in the photocurrent was observed. About 20% of this increment could be due to the bandgap reduction. Therefore the remaining 40% can be attributed to an enhancement in catalytic performance.

3.3.4.2 Au/TiNT Film Photoelectrodes

Early results obtained with Au/TiO_2 powders lead to the investigation of Au on TiNT as an effective photocatalyst for water splitting. Gold was loaded onto TiNT using a modified DP process. The Au loading and particle size were successfully modified by change the deposition parameters.

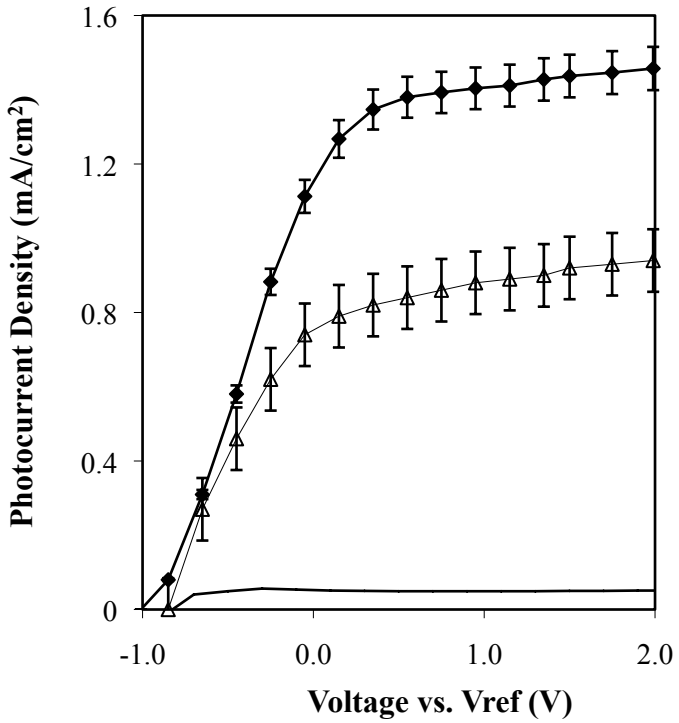

Figure 3.18: Photocurrent-voltage plots for a (▵) TiNT and (◆) an Au/TiNT electrode. Solid line represents the (-) dark case. The voltage was measured versus Hg/HgO reference electrode. TiNTs were fabricated at 40 V for 4 h. The average dimensions of the nanotubes were *L* ~15 μm, *OD* ~150 nm. The films were calcined at 500 °C.

Figure 3.18 presents a photocurrent versus voltage for two electrodes a TiNT and an Au/TiNT. The saturated photocurrent (maximal extraction of charges into the electrolyte) density produced by the Au/TiNT electrode was ~75% greater than that of

the TiNT alone. The Au loading and particle size were 2.5 wt% and 3.8 nm, respectively.

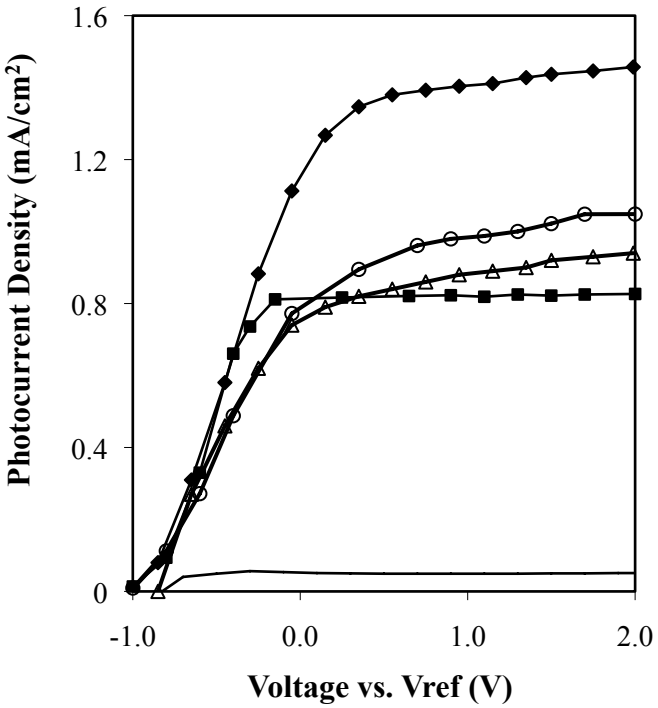

Figure 3.19: Photocurrent-voltage plots for a (∆) TiNT and Au/TiNT electrodes with different Au nanoparticles sizes (■) 12 nm, (o) 8 nm and (◆) 4 nm. Solid line represents the (-) dark case. The average dimensions of the nanotubes were L ~15 μm, OD ~150 nm.

Bandgap Reduction

In section 2.4.6 a reduction in bandgap of the Au/TiNT photocatalyst system was observed when nanocrystalline Au was added to titania nanotubes. Gold nanoparticles smaller than 10 nm reduced the E_g. This reduction was in the range of 0.05 and 0.25 eV, which was similar to the bandgap decrease obtained for powder TiO_2. The bandgap reduction of Au/TiNT was shown to depend on the metal particle size and loading. Gold particles bigger than 10 nm shifted the light absorption to the visible region due to the surface plasmon resonance effect [54-61]. The latter led to a bigger reduction in the E_g of

Au/TiNT system to values in the vicinity of 0.7 eV. It was mentioned previously that the apparent bandgap reduction of the Au/TiNT systems was due to absorption of photons by the metal nanoparticles. Figure 3.19 shows i_{ph}-V plots for Au/TiNT electrodes with different Au particle sizes. Even though, the E_g could reduce further using big Au particles (ϕ > 10 nm) the output currents are not increases due to the lower catalytic properties of this large metal particles.

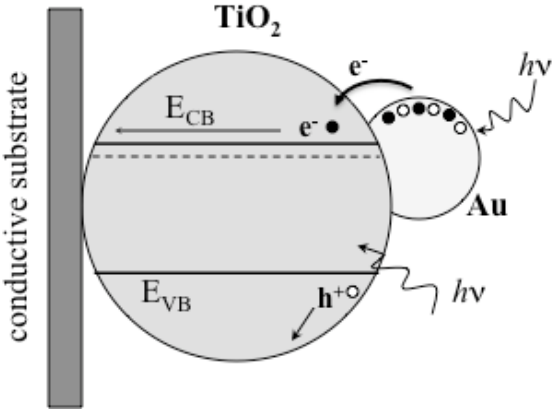

Figure 3.20: Propose electron transfers mechanism for Au/TiO_2 systems. In Au particle charge carriers are separated by light due to surface plasmom resonance, then transfer to the conduction band of TiO_2. In the diagram the open circles (o) represent holes (h^+) and closed circles (•) electrons (e^-).

The metal and the semiconducting film form a Schottky barrier [54-56], which is potential barrier formed at a metal–semiconductor junction. The largest differences between a Schottky barrier has typically low junction voltage (~1.0 eV), and decreased (almost nonexistent) depletion width in the metal [55]. Photoinduced electron transfer from plasmon excited gold nanoparticles to semiconductors has been reported by Tian [54] and Du *et al.* [55]. Tian et al. gave details on electron transfer in Au/TiO_2 (P25)

system; they suggested that Au/TiO_2 could be used as photosensitizers in place of common dye molecules in dye-sensitized solar cells. Figure 3.20 shows a schematic of the proposed charge separation and electron transfer for Au/TiO_2 based on Tian's work [54].

Gold Loading

For Au/TiNT the gold loading increases as the solution pH increases reaching the maximum at pH close to and slightly above the point of zero charge for TiNT (the measured PZC was 6.2). The addition of Au nanoparticles to TiNT enlarged the photocurrent production of the photoelectrode. The i_{ph} further increases as the Au loading rises up to about 2 wt%, past this point the photocurrent density seems to slightly decrease. Kamat *et al*. reported similar for Au/TiO_2 (P25) [20]. Figure 3.21 shows the photocurrent densities vs. Au loading plot, the data points on the vertical axes correspond to TiNT alone. The photocurrent densities were measure at 0.5 V (versus Hg/HgO reference electrode) bias voltage. Note that the gold particles were not similar for all these Au loadings (they were loaded at different solution pH), which might also influence the current production.

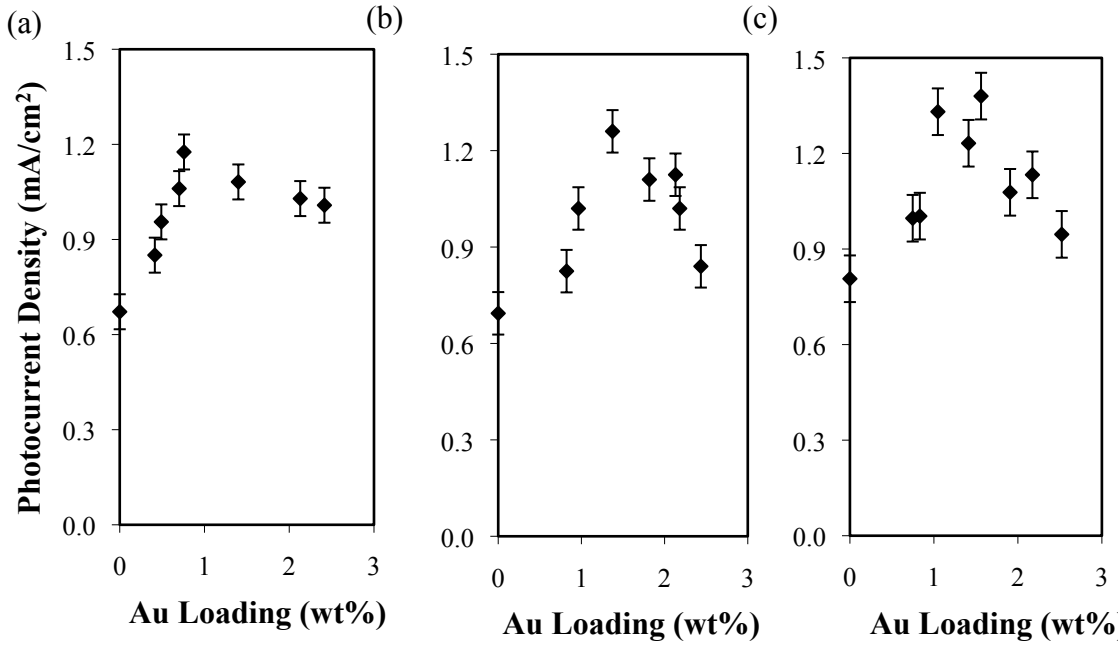

Figure 3.21: Photocurrent as a function of Au loading plots for TiNT with various dimensions (a) L ~ 12 µm, OD ~ 80 nm (b) L ~ 15 µm, OD ~ 150 nm, and (b) L ~ 18 µm, OD ~ 200 nm. The Au was loaded using deposition precipitation and Na_2CO_3 to control the solution pH. Photocurrent densities measure at 0.5 V (vs. Hg/HgO) bias voltage.

Particle Size

Figure 3.22 shows that the highest photocurrent was obtained for Au particle size in the range of 3-6 nm. Particles bigger than 9 nm did not enhance photocurrent densities; the numbers were comparable to the photoelectrodes without Au (data points on the vertical axis). Even though, Au nanoparticles bigger than 10 nm absorb light through SPR and the excited electron in the metal get transfer to the semiconductor, the photocurrents were not higher than those of smaller sizes. It seems that these extra electrons recombined before they could be used for water oxidation because of the low catalytic activities of Au/TiNT.

The i_{ph} increment due to a 0.20 eV E_g reduction was estimated to be ~25%. This means that more than half of the increase in photocurrent density might be due to a magnification in the catalytic activities of the composite photocatalyst.

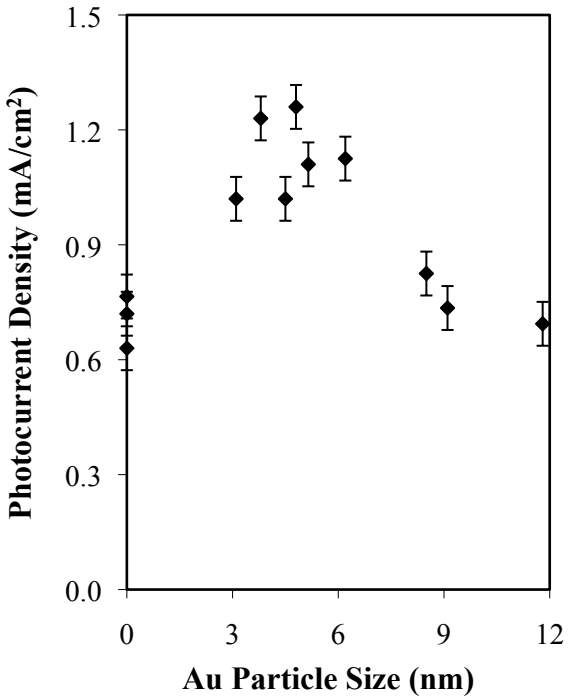

Figure 3.22: Photocurrent density as a function of Au particle size plots for Au/TiNT photoelectrodes. The photocurrent was measured at 0.5 V (vs. Hg/HgO) bias voltage. The nanotubes average dimension were *L* ~15 μm and *OD* ~150 nm.

Photocurrent densities were measured at 0.5 V (vs. Hg/HgO) bias voltage for a TiO_2, Au/TiO_2 (Figure 3.17), TiNT and Au/TiNT (Figure 3.18) and these values were normalized by the total electrochemical surface area. These results are ploted in Figure 3.23. This figure illustrates the increased photoanode performace due to both the change in TiO_2 structure and the addition metal sites for water oxidation.

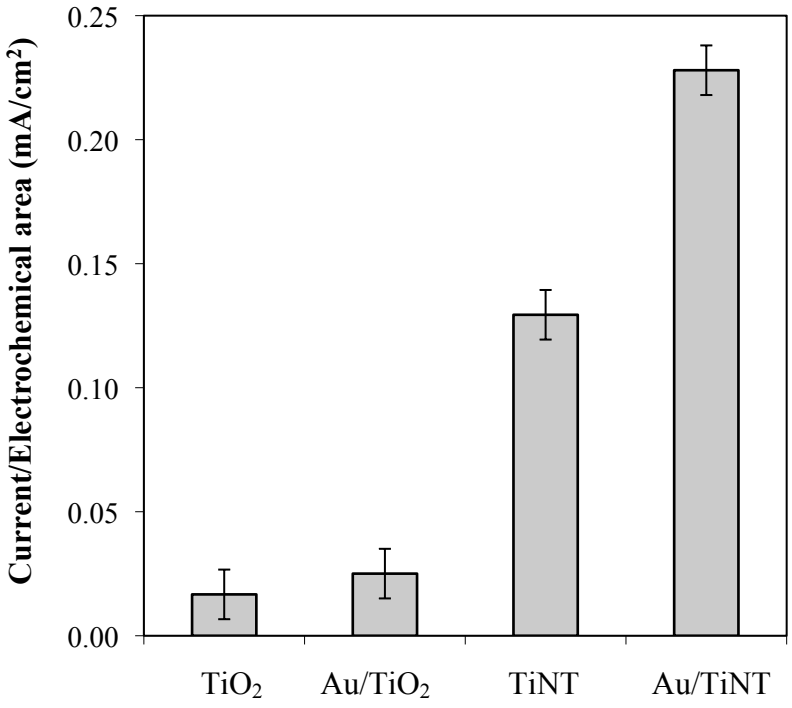

Figure 3.23: Current normalized by total electrochemical surface area of four photoanodes. The Au loadings were 2.4 and 2.5 wt% for Au/TiO_2 and Au/TiNT respectively.

3.3.5 Photoelectrochemical Water Oxidation

3.3.5.1 Photoelectrochemical Cells for Water splitting

The photocatalysis of water is based on back-to-back photoelectrochemical and electrochemical reactions, involving electrogenerated electrons and holes. It involves an oxygen evolution (OER) and the hydrogen evolution (HER) reaction. The later reaction can occur on the surface of the titania or at a different electrode [39].

The elementary reactions involved in the mechanism of water decomposition in a PEC cell, as proposed by Nowotny *et al.* [1,2], are given as follow:

- Adsorption of water (*ads*) derived from liquid (*l*) on surface active centers resulting

in the formation of catalytically active complexes.

$$H_2O_{(l)} \rightarrow H_2O^*_{(ads)} \tag{3.14}$$

- Dissociation of the adsorbed water molecules on the surface of the photoanode.

$$H_2O^*_{(ads)} \rightarrow OH^-_{(ads)} + H^+_{(ads)} \tag{3.15}$$

- Formation of electron-holes pairs, through light excitation of the semiconducting photoanode bandgap near the surface (s).

$$h\nu \rightarrow \left\{e^- + h^+\right\}_s \tag{3.16}$$

- Separation of light formed charge carriers near the surface of the photoanode, leading to transfer of holes (h^+) towards the surface (s) and the electrons (e^-) towards the bulk (b) of the electrode.

$$\left\{e^- + h^+\right\}_s \rightarrow e^-_b + h^+_s \tag{3.17}$$

- Reaction of OH^- radicals with the holes (at the surface of the photoanode) leading to the formation of O^- chemisorbed species and hydrogen ions.

$$OH^-_{(ads)} + h^+ \rightarrow O^-_{(ads)} + H^+_{(ads)} \tag{3.18}$$

- Reaction between the surface oxygen species O^- and holes resulting in the formation of atomic oxygen radicals.

$$O^-_{(ads)} + h^+ \rightarrow O^*_{(ads)} \tag{3.19}$$

- Desorption of oxygen radicals and their subsequent association leading the formation of gaseous oxygen (gas).

$$O^*_{(ads)} \rightarrow O^*_{(g)} \rightarrow \tfrac{1}{2} O_{2(gas)} \tag{3.20}$$

- Formation of hydronium ions near de vicinity of the photoanode.

$$H^+_{(ads)} + H_2O_{(l)} \rightarrow (H_3O^+)_a \tag{3.21}$$

- Transport of electrons from the bulk of the photoanode to the surface of the cathode through an external wire (external circuit).

$$(e_b^-)_a \rightarrow (e_b^-)_c \tag{3.22}$$

- Migration of hydronium ions from the vicinity if the photoanode (a) to the vicinity of the cathode (c).

$$(H_3O^+)_a \rightarrow (H_3O^+)_c \tag{3.23}$$

- Adsorption of hydrogen ions on the surface of the cathode.

$$(H_3O^+)_c \rightarrow (H^+_{(ads)})_c + H_2O_{(l)} \tag{3.24}$$

- Reaction between adsorbed hydrogen ions and electrons leading to the formation of hydrogen radicals in the vicinity of the cathode.

$$(H^+_{(ads)})_c + e^- \rightarrow (H^*_{(ads)})_c \tag{3.25}$$

- Transfer of hydrogen radicals from the adsorbed layer (ads) to the electrolyte (l) in the vicinity of the cathode.

$$H^*_{(ads)} \rightarrow H^*_l \tag{3.26}$$

- Association of hydrogen radicals leading to the formation of gaseous H_2 molecules (gas)

$$2H^*_l \rightarrow H_{2(gas)} \tag{3.27}$$

3.3.5.2 TiO_2 Interaction with Water: Active Sites for Water Oxidation

TiO_2 is a transition metal oxide whose d-electron orbitals are usually empty at room temperature. Thus, in the case of stoichiometric (defect free) TiO_2, there are no d-electrons available for charge transfer with adsorbed species. Consequently, the presence

of point defects is required to allow charge transfer [39,68,69].

Water can be adsorbed on titania surfaces molecularly or dissociatively [39]. For reduced TiO_2 surfaces water dissociates at oxygen vacancies (Ti^{3+} sites) produced during thermal treatment [70,71]. Henderson reported a high-resolution electron energy loss spectroscopy (HREELS) temperature programmed desorption (TPD) study that concluded that the adsorption of water on rutile (110) is molecular on the stoichiometric surface and dissociative on the reduced surface [70]. In addition, experimental studies [39] have shown molecular water adsorption on anatase (101) surface and dissociative on the (001) surface.

It has been recently shown by reactivity model that oxidation of TiO_2 (oxygen activity in the gas phase during processing or subsequent annealing) leads to the formation of titanium vacancies at the surface and their subsequent transport to the bulk [68,69]. These defects are the only acceptor-type intrinsic defects in undoped TiO_2, which must be considered as responsible for photoreactivity between TiO_2 and H_2O and the related charge transfer.

In summary, reported data on surface properties of TiO_2 allow the following points to be made: the presence of defects at the TiO_2 surface is essential for its reactivity with H_2O; the oxygen vacancies have been considered as the predominant surface defects; the dark (no illumination) reactivity between defected TiO_2 and H_2O results in the formation of two OH^- species [72], Ti vacancy might also be considered as active sites for water adsorption [68,69].

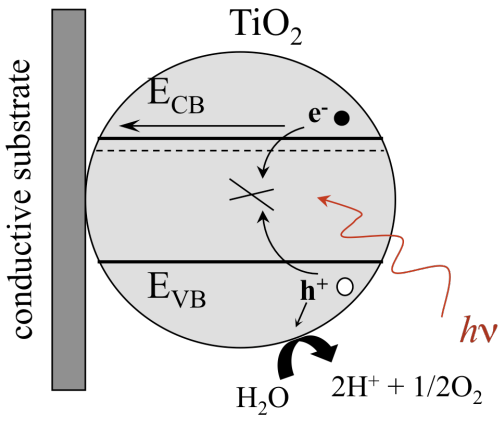

Figure 3.24: Schematic of the interfacial charge transfer process in TiO_2 photoanodes. Light creates electrons and holes. Holes move to the surface of the electrode to be consumed by water species. Electrons move to the back of the electrode.

3.3.5.3 Water Photooxidation on Titania and Au Loaded Titania

Water can be split on the surface of TiO_2 (or TiNT) using solar light (mainly the UV portion). Equations (3.8) to (3.21) describe one of the literature proposed mechanisms for water oxidation on TiO_2 surfaces. Figure 3.24 shows a schematic of the photoelectrochemical decomposition of water on TiO_2. Light excites the electrons in the VB, moving the electrons to the CB and leaving holes that will be used in the oxidation of water. Electrons are trapped at Ti^{3+} and holes at deep traps O^- [9]. If there are holes also trapped in bulk of the electrode they can recombine with electrons producing heat. In the case of TiNT the separation, and transport of electron should be more efficient than in the case of TiO_2 nanoparticulates, because electrons do not have to overcome grain boundaries to reach the back of the photoelectrode like in the case of P25. The latter reduces recombination and increases water oxidation rates. Water is absorbed on the defective surface of TiO_2 (either oxygen and/or titanium vacancies). The adsorbed water species will be oxidized by the holes produced during the light excitation of the

photoelectrode, realizing O_2 gas and producing hydronium ions. These H^+ ions travel to the vicinity of the cathode to be reduced by the electrons producing H_2 gas.

In contrast, when Au nanoparticles are added to TiO_2 and TiNT, the interfacial charge transport process changes. Light is absorbed by TiO_2 and by Au nanoparticles (due to SPR if the metal particles are bigger than 10 nm). Illumination with light on the TiO_2 electrode creates electron-hole pairs. If the potential produced is bigger than the E_{fb} electrons will be transport to the back of the electrode, and holes will move to the surface to oxidized water. Electrons are transferred from the semiconductor to the metal particle until their Fermi levels equilibrate [4,18-22,25]. Due to SPR the Au can absorb light and excite surface electrons. A Schottky barrier is formed in the metal-semiconductor interface, and if there is enough potential to overcome the barrier (E ~1 eV) electrons can be transferred to the CB of TiO_2, the electron lost in this way can be compensated by receiving an electron (transfer a hole) to reduce an acceptor specie (such as hydroxy ion) and produce oxygen. In addition, it has been argued that holes can also be transfered from the semiconductor to the metal particles if there is enough potential to do so. In the latter case, water oxidation might take place if there is water or hydroxyl species absorbed on the surface of the metal. The oxidation of water on gold surfaces has already been reported [75]. The surface area of Au is actually measured using the oxidation of water on the metal surface using CV on gold electrodes and Au/TiNT. The water oxidation on Au/TiO_2 scheme is shown in Figure 3.25.

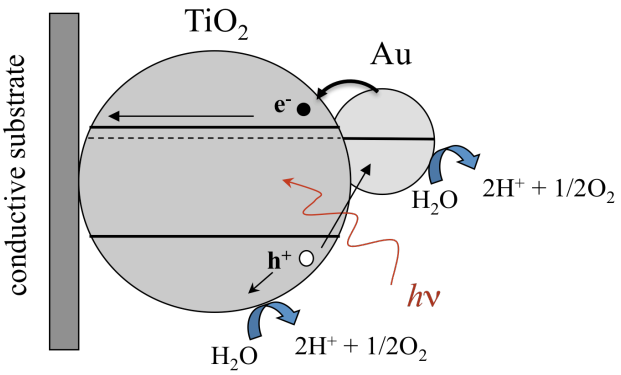

Figure 3.25: Schematic of the interfacial charge transfer process in Au/TiO_2 photoanodes. Light creates electrons and holes. Gold nanoparticles might also absorb light exciting metal electron, which can later be transfer to the CB of the semiconducting oxide.

3.3.5.4 Au Photocatalytic Active Sites

While the surface of massive gold exhibits modest catalytic properties, with highly dispersed forms of the metal the activity per unit mass will increases depending on the fraction of atoms at the surface [62]. Physical properties of the particle vary uniformly as the particle gets smaller, such as fractions of edge and corner atoms, the length of the particle perimeters, etc [64]. Furthermore, there is a metal to non-metal transition, this occurs when the size of the particle is so small (200-400 atoms, ~2-3nm) that the electron bands cannot form [65]. Thus, at this scale the gold particle behaves more like a semiconductor.

Results presented in this work shown enhancement of catalytic activity with the addition of Au nanoparticles onto the surface of TiO_2 and TiNT. It is known that TiO_2 oxidizes water when it is illuminated with UV light. It has been reported that the active sites for water adsorption (molecularly or dissociative) on TiO_2 are oxygen vacancies created during the fabrication of TiO_2 (mainly during thermal treatment) [39,71-73]. On

the other hand water can be oxidized on Au surfaces if there is enough high potential [70,74,75], according to density functional theory (DFT) calculations this potential is 1.8 V [74]. At lower potentials, water can dissociate to form adsorbed O atoms, and only after the surface has oxidized sufficiently will oxygen evolution start. The process therefore takes place on an oxidized surface [74]. Therefore, the addition of Au nanoparticles on TiO_2 adds active sites for water to adsorb and later to produce O_2; these sites are located on the surface of the metal. Furthermore, the addition of metal nanoparticles can create defects on the surface of the support creating extra sites for water oxidation.

In an attempt to understand the basis for the improved activity that resulted from adding Au nanoparticles, we measured the total nanotube and Au electrochemical surface areas of electrodes. Different loadings and particles sizes for Au where used. The Au loadings ranged from 0.2 to 3.5 wt%. The nanotube surfaces contained relatively high densities of particles with sizes ranging from 3 to 12 nm.

Figure 3.26 illustrates the photocurrent normalized by the total electrochemical surface area of the electrode as a function of the Au average particle size. Similar results were also obtained for nanotubes with different dimensions (Figure 3.27). The maximum specific photocurrent was obtained for films containing Au nanoparticles between 4 and 5 nm in size. These results indicate that sites associated with the Au nanoparticles contributed significantly to the water oxidation activity, and that this activity was influenced by the Au particle size. A variety of sites could be associated with the Au nanoparticles: sites on the nanoparticles, sites at the nanotube-nanoparticle interface, and/or sites on the TiO_2 that were modified by Au.

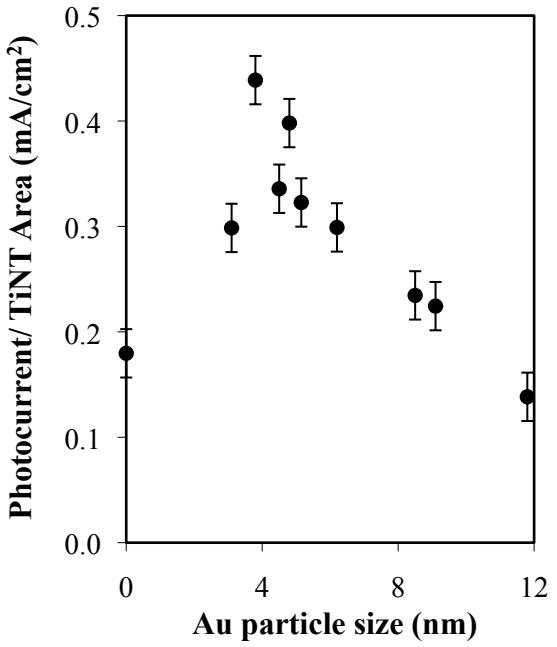

Figure 3.26: The total electrochemical surface area normalized photocurrent (specific photocurrent) as a function of average Au particle size. The length and outer diameter for the TiNTs were 15 μm and 150 nm, respectively.

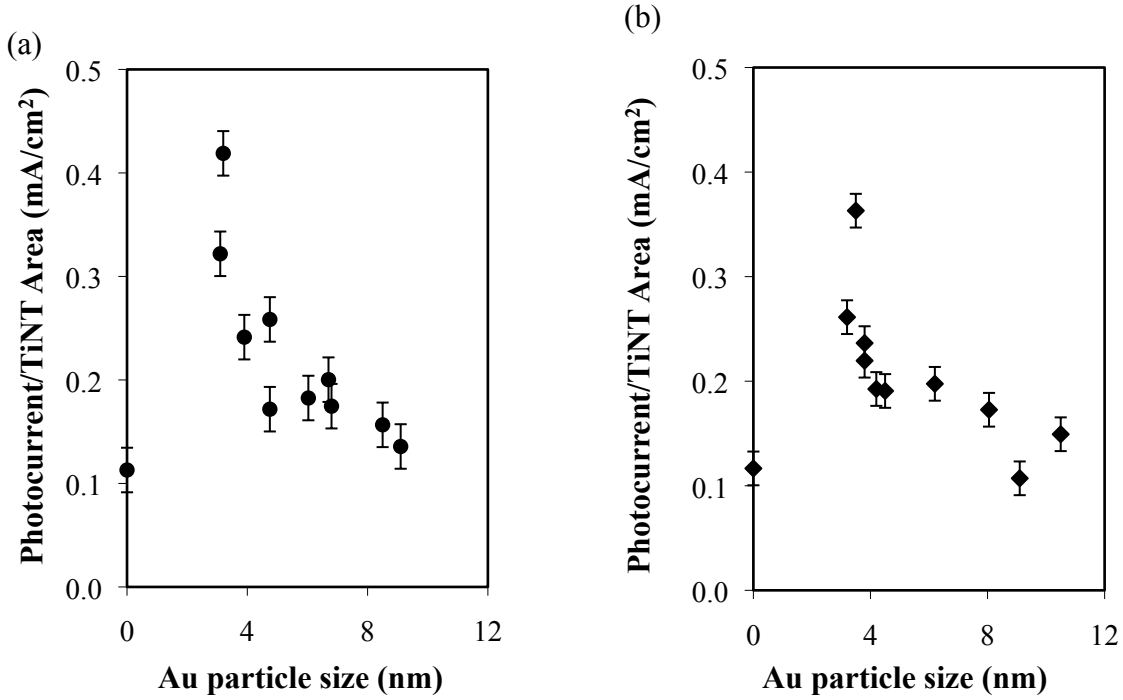

Figure 3.27: Specific photocurrent as a function of average Au particle size plots for TiNTs with average dimensions of (a) *OD* ~80 nm and *L* ~12 μm, and (b) OD ~200 nm and *L* ~18 μm.

If the most active sites for water oxidation added to titania are located solely on the surface of metal, a measurement of photocurrent produced (equivalent to H_2 production rate) normalized by the Au surface area versus particle size should give a almost horizontal line. The Au electrochemical surface area normalized photocurrents increased dramatically as the size of Au nanoparticles decreased below ~5 nm as shown in Figure 3.28. Similar trends where observed for photocurrents produced by photanodes made with nanotubes with dimensions (Figure 3.29). Assuming that the electrochemical measurements sample sites on the Au nanoparticles, the nonlinear correlation illustrated in Figure 3.28 and Figure 3.29 suggests that sites on the Au nanoparticles were not the only active sites for water oxidation. The specific rate for CO oxidation [16] has also been reported to increase dramatically for Au nanoparticles smaller than ~4 nm. Bond and Thompson suggested that the increased activities were due to a combination of effects: loss of metallic character, changes in particle morphology, and stronger interactions between Au and the support [62].

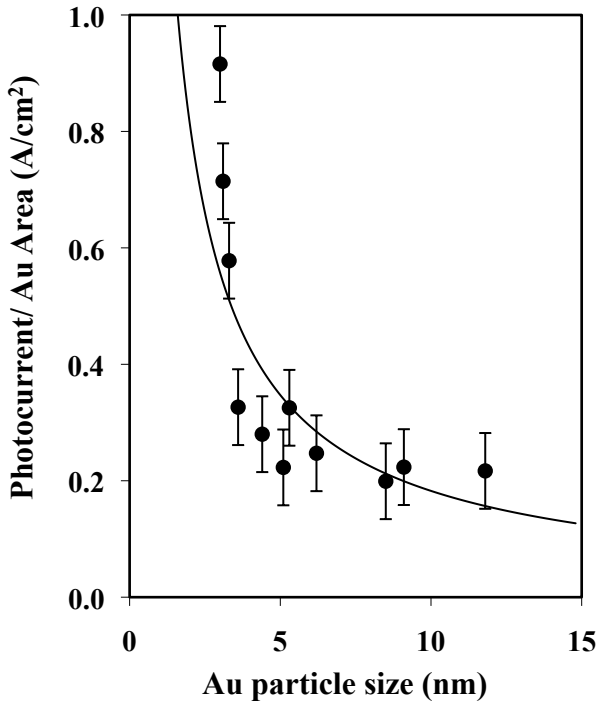

Figure 3.28: The Au electrochemical surface area normalized photocurrent as a function of average Au particle size. The length and outer diameter for the TiNTs were 15 mm and 150 nm, respectively.

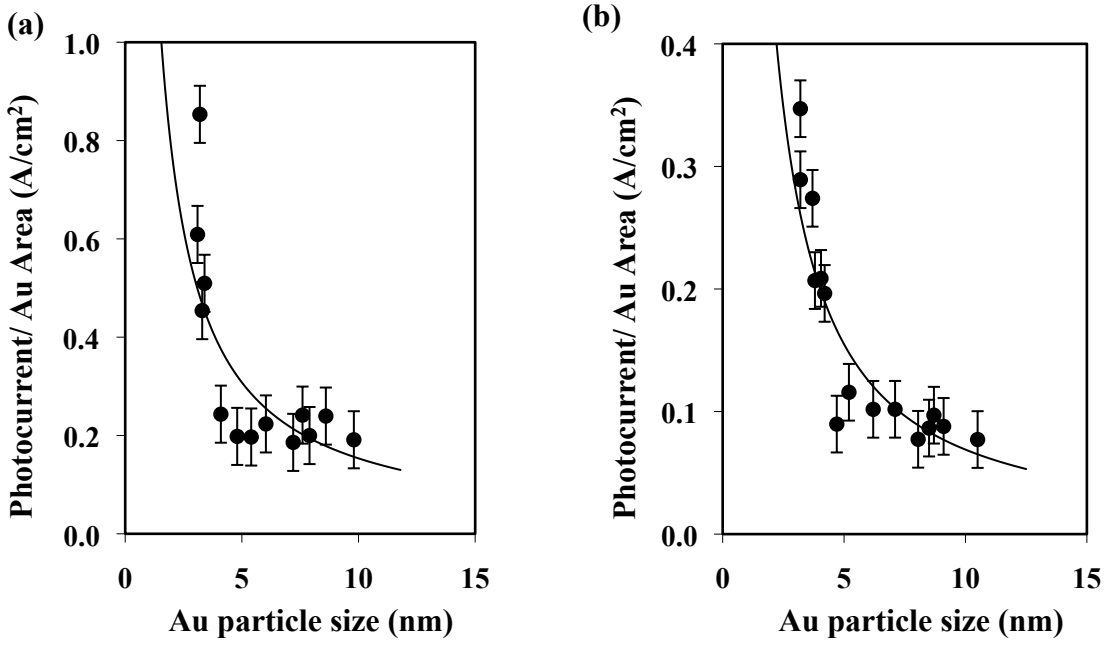

Figure 3.29: Photocurrent normalized by Au surface area as a function of average Au particle size plots for TiNT with (a) *OD* ~ 80 nm and *L* ~ 12 μm: and (b) *OD* ~ 200 nm and *L* ~ 18 μm.

In addition, hydrogen production rates have been calculated to study the relationship between Au particle size and rate per active Au specie. The hydrogen production rate (N [mol/s]) can be calculated directly using the photocurrent produced by the PEC cell as shown in equation 3.28. In this equation η_F is the Faraday efficiency (assumed to be 100%, i.e. all the photogenerated electrons are used to produce hydrogen), I_{ph} is the photocurrent, *2* is the number of electrons used in the reaction and F is the Faraday constant (96485.34 C).

$$N = \eta_F \frac{I_{ph}}{2F} \tag{3.28}$$

Furthermore, the rates were normalized by amount of Au in the photoanode (specific rate R [mol H_2/mol Au.s]) as shown in equation 3.29, where n_{Au}, m_{Au} and M_{Au} are moles, mass and molecular weight of gold.

$$R = \frac{N}{n_{Au}} = \frac{I_{ph}}{2F\left(\frac{m_{Au}}{M_{Au}}\right)} \tag{3.29}$$

Further insight regarding the nature of the active sites for water oxidation can be obtained from models relating the rate and Au particle size [66]. Then, the specific rate of reaction can be written as:

$$R = \left(\frac{\mathrm{N_{sites}}}{m_{Au}\left(\frac{1}{M_{Au}}\right)}\right)\left(\frac{\text{Molecules of } \mathrm{H_2}}{\text{site} \cdot \text{s}}\right)\left(\frac{1}{N_A}\right) = \left(\frac{M_{Au}}{N_A}\right)\left(\frac{\mathrm{N_{sites}}}{\mathrm{m_{Au}}}\right)TOF \tag{3.30}$$

In equation 3.30 N_{sites} is the number of active sites, N_A is Avogadro's number, and TOF is the turnover frequency. Therefore, the rate is proportional to the ratio of the number of sites to mass of Au present in the nanotubes. The Au weight loading can be express as a function of the Au particle diameter as shown in equation 3.31. The number of active

sites is assumed to be proportional to the Au cluster surface area or to the Au perimeter in contact with the support (equation 3.32) depending on the location of these sites.

$$m = \frac{N\rho\pi D_{Au}^3}{12} \tag{3.31}$$

for surface sites $SA = \frac{N\pi D_{Au}^2}{2}$ and for perimeter sites $P = N\pi D_{Au}$ (3.32)

By assuming that the TOF remains constant with changes in particle size [66,67] the ratio of the surface area or perimeter to the weight loading becomes proportional to specific rate. The rate, *R*, as a function of Au particle diameter vary approximately as D_{Au}^{-1} if the active sites are on the surface of the Au nanoparticle and as D_{Au}^{-2} if the sites are located on the perimeter between the metal and the oxide support (equation 3.33 and 3.34).

$$\frac{SA}{m} = \frac{6}{\rho D_{Au}} \quad \text{and} \quad \frac{P}{m} = \frac{12}{\rho D_{Au}^2} \tag{3.33}$$

for surface sites $R \propto \frac{SA}{m} \propto D_{Au}^{-1}$ and for perimeter sites $R \propto \frac{P}{m} \propto D_{Au}^{-2}$ (3.34)

Experimental data (*R* versus Au particle size plot) shown in Figure 3.30 does not shown a clear trend for the whole range of Au cluster sizes. However, if the data is divided in two sections, one for particles smaller and one for bigger than 5 nm, two exponential trends can be observed. Then, for all the data presented (Figure 3.30 and Figure 3.31) the rate varies roughly with particle size as $D_{Au}^{-0.7}$ for Au particles bigger than 5 nm and $D_{Au}^{-1.7}$ for Au diameters smaller than 5 nm. These results suggest that for Au particles bigger than 5 nm the most active sites might be located on the surface of the metal; and for Au clusters smaller than 5 nm the most active sites could be at the contact between the metal and the support.

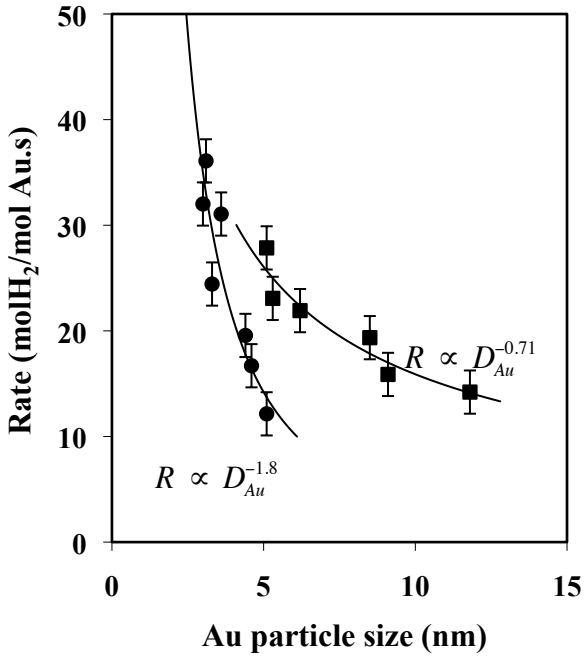

Figure 3.30: Hydrogen production rate normalized by Au moles as a function of Au particle size plot. (•) Au particles smaller than 5 nm, (n) Au particle bigger than 5 nm. The Au was deposited on TiNT with L ~ 15 μm and OD ~ 150 nm.

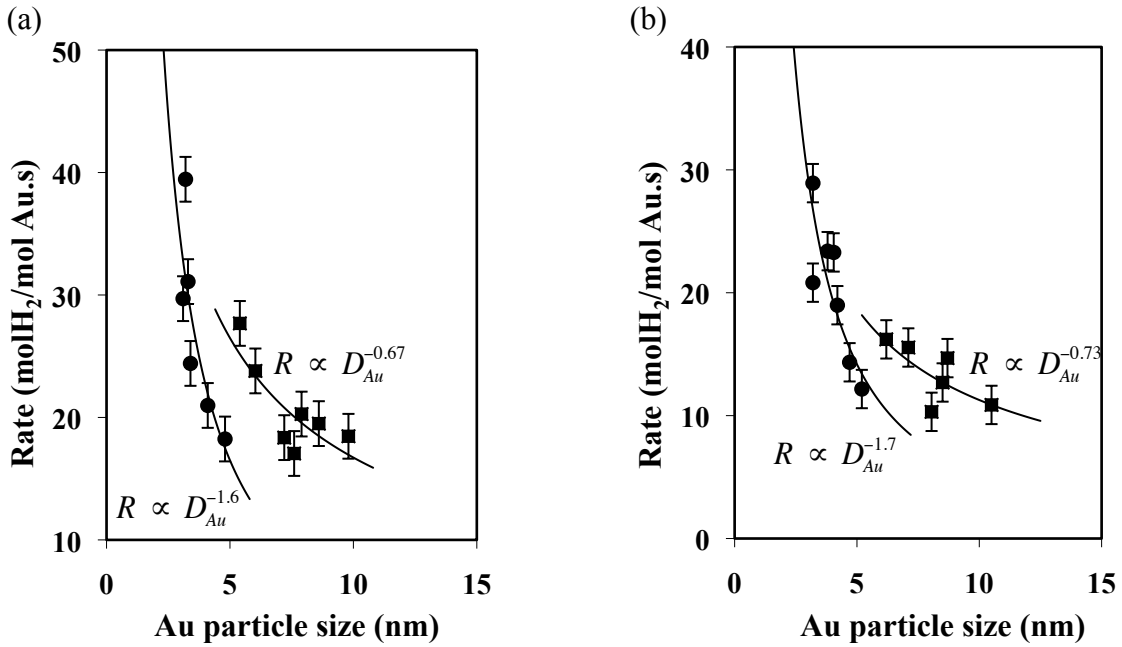

Figure 3.31: Specific hydrogen production rate as a function of Au particle size plots for TiNTs with dimensions (a) L ~ 12 μm and OD ~ 80 nm and (b) L ~ 18 μm and OD ~ 200 nm. (•) Au particles smaller than 5 nm, (n) Au particle bigger than 5 nm.

3.3.6 PEC Cell Efficiency

Overall STH efficiency (or energy conversion efficiency) is the most important measurement to characterize a PEC device. The STH is defined as the ratio of the maximum energy output that can be obtained from the H_2, to the energy supplied in the form of light. In terms of power, it is defined as the ratio of the maximum power output that could be obtained from H_2 to the power input from the incident light [29]. Depending on the flat band position of the photoelectrode in the electrolyte and work function of the counter electrode, PEC cells in most cases require an electrical bias from an external source or a chemical bias for driving the water splitting reaction [29,76,77]. The need of this additional energy input changes the way to calculate and report PEC efficiencies. In this case the efficiency is a diagnostic efficiency and not the STH.

Murphy *et al.* [78] calculated the maximum possible efficiencies of different materials according to their bandgap, for TiO_2 in anatase phase with E_g of 3.2 eV a maximum efficiency possible of 1.3% under AM 1.5 illumination, and 1.7% using an Xe arc lamp. However, it is know that the V_{oc} of a semiconductor can never be as high as the bandgap potential because of the inherent losses due to the entropy [2,29,77]. The efficiencies of the photoanode reported in this section (single band gap) needed external bias voltage to overcome overpotential and start the oxidation of water. When a potentiostat was used to gather data for efficiency measurements, the following equation was employed [11,29]:

$$\eta = \frac{\left[E^o - V_{app}\right] i_{ph}}{H_o} \times 100 \tag{3.35}$$

In equation 3.28, V_{app} is the voltage given by the potentiostat (bias potential) and it is

calculated as $V_{app} = V_{bias} = V_{oc} - V_{meas}$, where V_{meas} is the voltage recorded versus the counter electrode.

Two ways of measuring the currents and voltages (applied bias) were used in this work. A two-electrode cell was used along with a potentiostat to record LSV curves. No reference electrode was used, and the potentiostat recorder voltages respect to the Pt counter electrode. The efficiencies for this case was calculate using equation 3.28. Conversely, a power supply (connected to the two-electrode cell) and a multimeter (Fluke FLU87-5 Digital Multimeter) were used to apply an external bias voltage and to measure the current produced by the PEC cell. For the latter case equation 3.6 was used in the calculations.

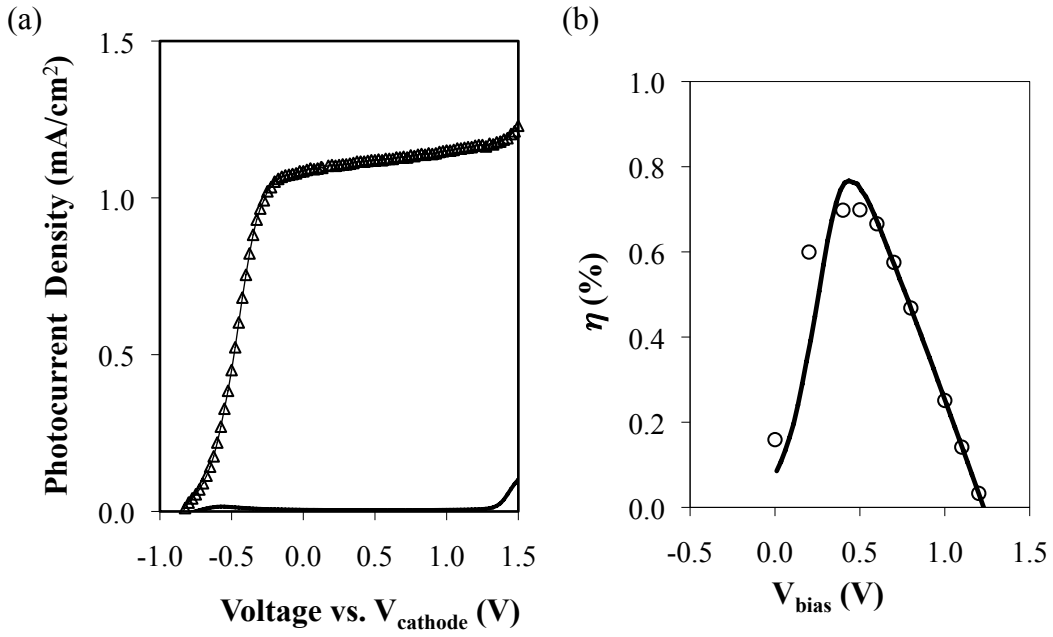

Figure 3.32: (a) i_{ph}-V plots for a TiNT photoelectrode, (-) dark, (Δ) light. (b) Diagnostic efficiency versus applied bias voltage curves for photoanodes. (o) Efficiency calculated using equation 3.6. (−) Efficiency calculated using data taken with a potentiostat and equation 3.28. Photoanode made with a film of TiNT with OD = 80 nm and L = 12 μm.

3.3.6.1 Efficiency Measurements Methods Comparisson

In order to compare the two methods of data collection used to calculate the PEC diagnostic efficiencies a photoanode made with TiNT film (*OD* ~ 80nm and *L* ~ 12 μm) was used. The open circuit voltage and saturation photocurrent were 0.83 V and 1.1 mA/cm^2 (Figure 3.32.a). Figure 3.32.b shows a curve of efficiency versus applied bias voltage. The circles represent the data obtained using equation 3.6 and the solid line was calculated with equation 3.28. The maximum efficiency for both cases was ~ 0.7% and it was reached at V_{bias} of 0.5 V.

Based on the similarity of the values obtained for both methods used to calculate the diagnostic efficiency, and due to the fact that the potentiostat records data much faster than manually measuring current and voltages, LSV was used to gather current-voltage data for efficiency calculations.

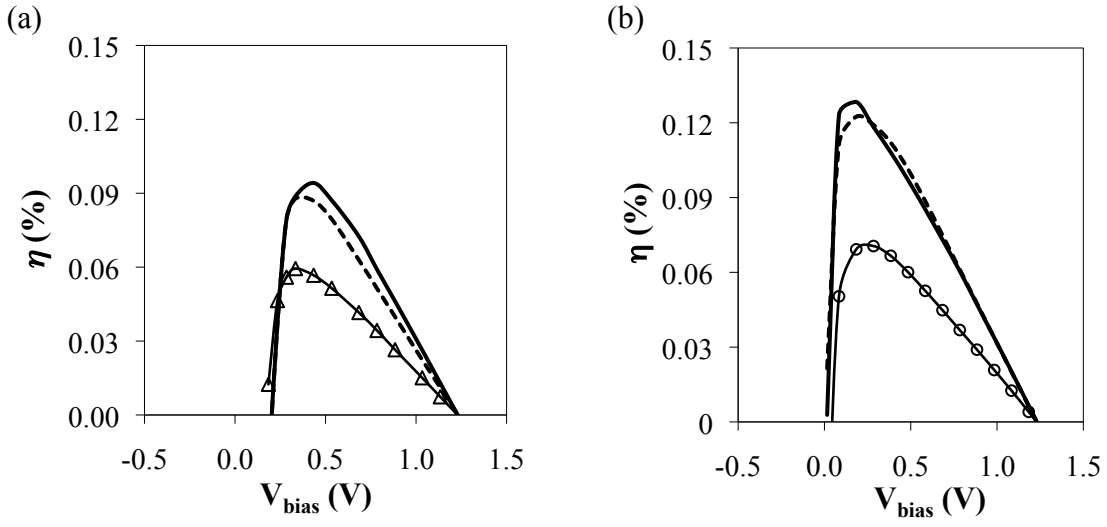

Figure 3.33: Efficiency as a function of V_{bias} curves for photoelectrode made with powder photocatalysts. (a) Titanium dioxide photocatalysts (Δ) TiO_2, (---) *tint* calcined at 650 °C, (−), and *tint* calcined at 500 °C. (b) Au loaded on TiO_2 (o) TiO_2, (---) Au/TiO_2 2.7 wt% gold loading, (−) Au/*tint* 0.8 wt% gold loading and calcined at 500 °C.

3.3.6.2 Diagnostic Efficiencies for PEC Cells

Efficiencies plots photoanodes made with TiO_2 powders and TiNT films are presented in Figure 3.33 and Figure 3.34 respectively. Table 3.1 summarizes the efficiencies for all the photoanodes characterized in this work. The results indicate that the efficiency increases one order of magnitude (for both TiO_2 and Au/TiO_2) when the structure of the oxide is changed from spherical discrete particles to long ordered nanotubes. The highest efficiency recorded was ~ 1.2%, which corresponded to an Au/TiNT photoanode with 2.3 wt% Au, and L ~ 200 nm and OD ~ 18 μm.

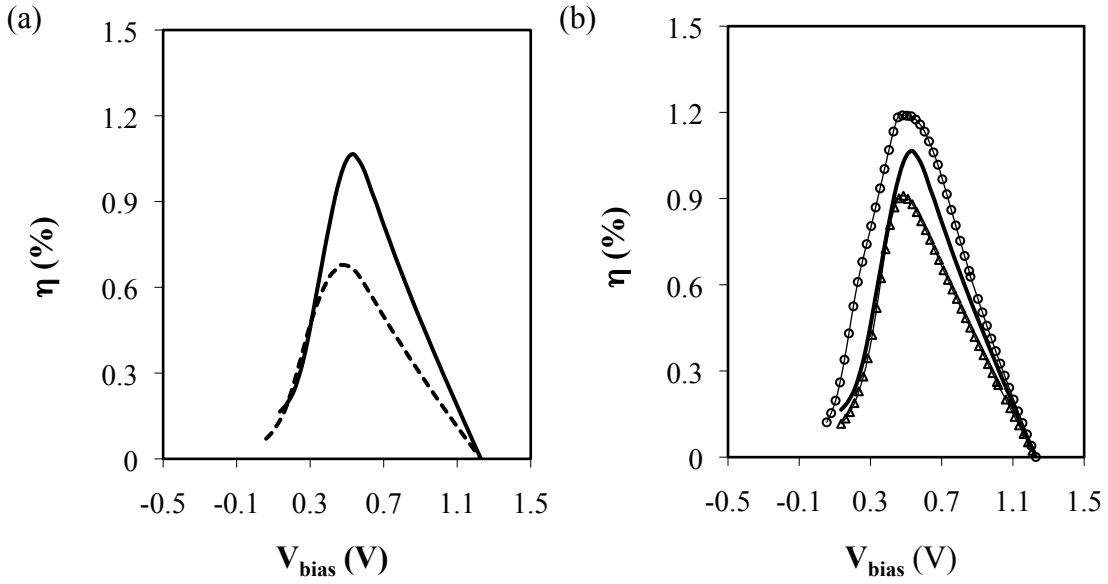

Figure 3.34: Efficiency as a function of V_{bias} plots for TiNT photoanodes. (a) TiNT (---) without Au and (−) with Au 2.3 wt%, nanotube L ~ 15μm and OD ~ 150 nm. (b) Au loaded on TiNT with different dimensions (Δ) L ~ 12 μm and OD ~ 80 nm, (−) L ~ 15 μm and OD ~ 150 nm, (o) L ~ 18 μm and OD ~ 200 nm.

Table 3.1: Summary of diagnostic efficiencies for photoanodes fabricated with powder and TiNT photocatalysts.

Electrode	i_{ph} **(mA/cm^2)**	V_{oc} **(V)**	V_{bias} **(V)***	**η (%)**
TiO_2 (P25)	0.09	0.72	0.50	**0.06 ± 0.02**
t*int*	0.13	0.72	0.50	**0.09 ± 0.02**
Au/TiO_2	0.14	0.78	0.45	**0.12 ± 0.02**
Au/*tint*	0.15	0.8	0.45	**0.13 ± 0.03**
TiNT	1.12	0.82	0.46	**0.75 ± 0.2**
Au/TiNT	1.76	0.92	0.50	**1.2 ± 0.3**

* V_{bias} at maximum efficiency

3.4 SUMMARY AND CONCLUSIONS

In this chapter the electrochemical, photoelectrochemical and performance characterizations of different TiO_2 photoanodes were presented. Characterization techniques such as cyclic voltammetry, chronoamperometry, linear sweep voltammetry and UV-Vis photospectrometry were used.

The photocurrents produced by nanoparticles of TiO_2 were hindered by recombination and poor photocatalytic performance. The i_{ph} were less than 0.1 mA/cm^2. This low production can be the consequence of poor charge separation and high recombination losses under illumination. Electrons are transferred to the back contact of the photoelectrode by trapping and detrapping events and crossing grain boundaries. In this process many of this electrons get recombined with holes before they can be used for water oxidation.

Changing the structure of powdered TiO_2 from spherical to short (and disordered) nanotubes boosted the production of photocurrents. There was an increase in i_{ph} of about 50%. It appears that the structural dimensions and shape of the nanotubes improved the separation of carriers and reduced recombination.

The usage of longer and highly ordered TiO_2 nanotubes further improved the photoelectrochemical performance of the photoelectrode. One order of magnitude increase in photocurrent was observed when TiNTs with 15 μm in length were used. The smooth and straight path that electrons follow in these systems upgraded the separation and transport of charge carrier limiting recombination. Also, the larger surfaces areas of these nanotubes enhance the light collection. Photocurrent production increased as the nanotubes got longer, up to a length similar to the electron diffusion length in TiO_2. This length has already been measured by other authors and reported to be between 15 to 20 μm.

The photocatalytic properties of TiO_2 depend on its crystalline phase. Thermal treatment converted the amorphous as-prepared material to anatase and later to rutile. Specific photocurrent measurements indicated that the anatase phase is the most active and effective for photoelectrochemical water decomposition. Even though rutile has a bandgap lower than anatase (E_g = 3.0 eV) its conduction band is not negative enough compared to the reduction potential of water, which means that it will need more bias voltage to oxidize water.

An important process during charge carrier transport and separation is the trapping and detrapping of electrons and holes. Electrons are trapped in titanium sites forming Ti^{3+}. Cyclic voltammetry was used to study the filling of these trapping sites. The structure and surface modification (with Au nanoparticles) modified the trapping of electrons in the bulk of the semiconductor.

The incorporation of Au nanoparticles significantly improved the rates for water oxidation in TiO_2 powders and nanotube films. The incorporation of Au nanoparticles

increased the photocurrent densities up to 50% and 75% of the original values without the metal for P25 and TiNT films, respectively. Gold nanoparticles smaller than 8 nm seem to decrease the E_g of TiO_2. The latter could be the consequence of addition of surface states between the band edges of TiO_2 and reductive modification of TiO_2 during the loading process. Gold particles as big as 30-50 nm were also found in some Au/TiNT samples. These metal particles can absorb light due to surface plasmon resonance exciting electrons that can later be transfered to the conduction band of TiO_2.

As the Au nanoparticle size decreased, the photocurrent produced by the photoanode increased suggesting that Au introduced highly active sites to the TiNTs. Additionally, during the metal loading point defect might be created which can act as active sites for water oxidation. In addition, if the potential in the Schotty barrier formed between the Au nanoparticle and TiO_2 is larger enough (~ 1 V) water can be decomposed increasing the overall performance of the Au/TiO_2 photocatalyst system. Studies relating Au particle size and hydrogen rate per active Au species suggested that for Au particles bigger than 5 nm the most active sites might be located on the surface of the metal, and for Au particles smaller than 5 nm the most active sites seemed to be at the perimeter in contact with the oxide support.

The energy efficiencies for different photoanodes were calculated. Changing the structure of the photocatalyst from spherical particles to highly ordered nanotubes increased the efficiency one order of magnitude. The highest efficiency recorded in this work for a single bandgap photoelectrodes was 1.2 ± 0.3 %.

3.5 REFERENCES

1. Bak, T.; Nowotny. J.; Rekas, M.; Sorrel, C. C. Int. J. Hydrogen Energy 2002, 27, 991-1022.
2. Bak, T.; Nowotny, J.; Rekas, M.; Sorrel, C. C. Int. J. Hydrogen Energy 2002, 22, 19-26.
3. Nault, R. M. Basic Research Needs for Solar Energy Utilization; US Department of Energy: 2005, 117-120.
4. Kamat, P.V. J. Phys. Chem. C 2007, 111, 2834-2860.
5. Law, M.; Greene, L.; Johnson, J.; Saykally, R.; Yang, P. Nature Materials 2005, 4, 455-459.
6. Meekins, B. H.; Kamat, P. V. ACS Nano 2009, 11, 3437–3446.
7. Boschloo, G.; Fitzmaurice, D. J. Phys. Chem. B 1999, 103, 7860-7868.
8. Wang, H.; He, J.; Boschloo, G.; Lindstrm, H.; Hagfeldt, A.; Lindquist, S. E. J. Phys. Chem. B 2001, 105, 2529-2533.
9. Berger, T.; Sterrer, M.; Diwald, O.; Knzinger, E.; Panayotov, D.; Thompson, T. L.; Yates, J. T. J. Phys. Chem. B 109 (2005) 6061-6068.
10. Kokorin, A.; Bahnemann, D. Chemical Physics of Nanostructured Semiconductors, 1st ed., Utrecht: Boston, MA, 2003; 83-110.
11. Mor, G.K., Varghese, O. K.; Paulose, M.; Shankar, K.; Grimes, C. A. Sol. Energy Mater. Sol. Cells 2006, 90, 2011-2075.9
12. Shankar, K.; Bashman, J. I.; Allen, N. K.; Varghese, O.K.; Mor, G. K.; Feng, X.; Paulose, M.; Seabold, J.A.; Choi, K.; Grimes, C.A. J. Phys. Chem. C 113 (2009) 6327-6347.
13. Ghicov, A.; Schmuki, P. Chem. Commun. (Cambrige, U. K.) 2009, 2791-2808.
14. Okazaki, K.; Ichikawa, S.; Meda, Y.; Haruta, M.; Kohyama, M., Appl. Catal. A 2005, 291, 45-54.
15. Kim, C.H.; Thompson, L.T. J. Catal. 2006, 244, 248.
16. Haruta, M.; Date, M. Appl. Catal. A 2001, 222, 427.
17. Kim, C. H.; Thompson, L.T., J. Catal. 2005, 230, 66.
18. Chandrasekharan, N.; Kamat, P.V. J. of Phys. Chem. B 2000, 104, 10851.
19. Chandrasekharan, N., Kamat, P.V., Nano Letters 2001, 2, 67-70.
20. Subramanian, V., Wolf, E., Kamat, P.V., J. Phys. Chem. B 2001, 105, 11439.
21. Subramanian, V.; Wolf, E. E.; Kamat, P.V. J. Am. Chem. Soc. 2004, 126, 4943.
22. Lana-Villarreal, T.; Gomez, R. Electrochem. Commun. 2005, 7, 1218–1224.

23. Haruta, M., Tsubota, S., Kobayashi, T., Kageyama, H., Genet, M. J. and Delmon, B. J. Catal. 144 175. (1993).

24. Aurora P.H., Kim CH, Thompson LT, Editors: Goswami DY; Zhao YW, Proceedings of ISES Solar World Congress 2007: Solar Energy And Human Settlement, Vol. I-V, 2781-2785, 2007

25. M. Debeila, M. Raphulu, E. Mokoena, M. Avalos, V. Petranovskii, N. Coville, M. Scurrell, Mater. Sci. Eng. A 396 (2005) 70.

26. A. Currao, V. R. Reddy, G. Calzaferri, ChemPhysChem 5 (2004) 720-724.

27. H. Yoshihiro and K. Hiromitsu, Thin Solid Films, 476 (2005) 264-271.

28. J. R. Bolton, Solar Photoproduction of Hydrogen, IEA Agreement on the Production and Utilization of Hydrogen, September 1996.

29. Z. Chen, T. F. Jaramillo, T. G. Deutsch, A. Kleiman-Shwarsctein, A. J Forman, N. Gillard, R. Garland, K. Takanabe, C. Heske, M. Sunkura, E. W. McFarland, K Domen, E. L. Miller, J. Turner, H. N. Dinh, J. Mater. Res. (2010) 25, 1, 3-16.

30. R. P. Vitiello, J. M. Macak, A. Ghicov, H. Tsuchiya, L. F. P. Dick, and P. Schmuki, Electrochemistry Communications 8 (2006) 544–548.

31. R. Hahn, A. Ghicov, J. Salonen, V. Lehto and Patrik Schmuki, Nanotechnology 18 (2007) 105604-7.

32. A. Ghicov, J. M. Macak, H. Tsuchiya, J. Kunze, Volker Haeublein, S. Kleber, and P. Schmuki, Chemical Physics Letters 419 (2006) 426–429.

33. Zhaoyue Liua, Batric Pesicb, Krishnan S. Rajaa, Raghu R. Rangarajua, and M. Misra, International Journal of Hydrogen Energy 34 (2009) 3250 – 3257.

34. Solar Light Inc. www.solarlight.com

35. R. G. Compton and C. E. Banks, Understanding Voltammetry, Published by World Scientific Publishing, London, 2007, 107-109.

36. A. J. Bard and L. R. Faulkner, Electrochemical Methods, Wiley 2004, p. 226-230.

37. R. P. Lynch, A. Ghicov, and P. Schmuki, J. Electrochem. Soc., 157, G76 (2010).

38. A.C. Fisher, L.M. Peter, E.A. Ponomarev, A.B. Walker, and K.G.U. Wijayantha, J. Phys. Chem. B, 104, 949 (2000).

39. A. Fujishima, X. Zhang, and D.A. Tryk, Surf. Sci. Rep., 63, 515 (2008).

40. Xiaobo Chen and Samuel S. Mao, Chem. Rev. 2007, 107, 2891-2959

41. Carp, O., Huisman, C.L., Reller, A. Prog. Solid State Chem. 2004, 32, 33–177.

42. T. L. Thompson and J. T. Yates, Jr., Chemical Reviews 106 (2006) 4428−4453.

43. T. L. Thompson, and J. T. Yates, Journal of Physical Chemistry B 109 (2005), 18230-18236.

44. G. Boschloo and D. Fitzmaurice, Journal of Physical Chemistry B, 103 (1999) 7860-7868.

45. T. Berger, T. Lana-Villarreal, D. Monllor-Satoca and R. Gomez, Electrochemistry Comunications, 8 (2006) 1713-1718.

46. T. Berger, T. Lana-Villarreal, D. Monllor-Satoca and R. Gomez, Journal of Physical Chemistry 111 (2007) 9936-9942.

47. H. Wang, J. He, G. Boscholoo, H. Lindstrom, A. Hagfeldt, and S. Lindquist, Journal of Physical Chemistry 105 (2007) 2529-2533.

48. A.G. Muñoz, Electrochimica Acta 52 (2007) 4167–4176

49. L. Kavan, K. Kratochvilovfi and M. Gratzel, Journal of Electroanalytical Chemistry 394 (1995) 93-102.

50. J. Bisquert, F. Fabregat-Santiago, I. Mora-Sero, G. Garcia-Belmonte, E. Barea, and E. Palomares, Inorganica Chimica Acta 361 (2008) 684–698.

51. A. Hagfeldtt and M. Gratzel, Chemical Reviews 95 (1995) 49-68.

52. N. Beermann, G. Boschloo, and A. Hegfeldt, Journal of Photochemistry and Photobiology A, 152 (2002) 213-218.

53. F. Fabregat-Santiago, I. Mora-Sero, G. Garcia-Belmonte, and Juan Bisquert, Journal of Physical Chemistry B 107 (2003) 758-76.

54. Yang Tian and Tetsu Tatsuma, Journal American Chemical Society, 127 (2005) 7632-7637.

55. L. Du, A. Furube, K. Yamamoto, K. Hara, R. Katoh, and M. Tachiya, Journal of Physiscal Chemistry C 113 (2009) 6454–6462.

56. A. J. Bard and M. A. Fox, Accounts Of Chemical Research 28 (1995) 141-145.

57. T. Toyoda, S. Tsugawa, and Q. Shena, Journal Of Applied Physics 105 (2009) 034314.

58. S. Link and M. A. El-Sayed, Journal of Physical Chemistry B 103 (1999) 4212-4217.

59. E. Kowalska, O. Omar Prieto Mahaney, R. Abea and B. Ohtani, Physical Chemistry Chemical Physics 12 (2010,0) 2344–2355.

60. S. Pillai, K. R. Catchpole, T. Trupke, and M. A. Green, Journal of Applied Physics 101 (2007) 093105.

61. E. W. McFarland and J. Tang, NATURE 421 (2003) 616-618.

62. Bond, G.C., Louis, C., Thompson, D. T., Eds. Catalysis by Gold; Catalytic Science Series Vol. 6; Imperial College Press: London, 2006.

63. G. C. Bond, and D. T. Thompson, Catalysis Reviews 41 (1999) 319.

64. F. Moreau, G. C. Bond, and A. O. Taylor, Journal of Catalysis 231 (2005) 105–114.

65. G. Bond, Gold Bulletin, 4 (2010) 88-93.

66. N. Schweitzer, J. Schaidle, O. Ezekoye, X. Pan, S. Linic and L. Thompson, unpublished paper (2010).

67. W. D. Williams, M. Shekhar, W-S. Lee, V. Kispersky, W. N. Delgass, F. H. Ribeiro, S. M. Kim, E. A. Stach, J. T. Miller and L. F. Allard, Journal of the American Chemical Society 132 (2010) 14018–14020.

68. J. Nowotny, T. Bak, M. K. Nowotny, and L. R.

69. J. Nowotny, T. Bak, M.K. Nowotny, and L.R. Sheppard, International Journal of Hydrogen Energy 32 (2007) 2651 – 2659.

70. M.A. Henderson, Surface Science Reports 46 (2002) 1-308.

71. M. A. Henderson, Langmuir 12 (1996) 5093-5098.

72. Z. Zhang, O. Bondarchuk, B. D. Kay, J. M. White, and Z. Dohnalek, Journal of Physical Chemistry B 2006, 110, 21840-21845.

73. R. Schaub, P. Thostrup, N. Lopez, E. Lægsgaard, I. Stensgaard, J. K. Nørskov, and F. Besenbacher, Physical Review Letters, 87 (2001) 266104-4.

74. J. Rossmeisl, A. Logadottir, and J.K. Nørskov, Chemical Physics 319 (2005) 178–184.

75. Y. Nakato ad H. Tsubomura, Journal of Photochemistry, 29 (1986) 257-266.

76. O. K. Varghese and C. A. Grimes, Solar Energy Materials & Solar Cells 92 (2008) 374–384.

77. J. R. Bolton, Solar energy 57 (1996) 37-50.

78. A. B. Murphya, P. R. F. Barnesa, L. K. Randeniyaa, I. C. Plumba, I. E. Grey, M. D. Horneb, and J. A. Glasscocka, International Journal of Hydrogen Energy 31 (2006) 1999 – 2017.

CHAPTER 4
HYBRID PHOTOELECTROCHEMICAL SYSTEMS

4.1 INTRODUCTION

Solid-state multijunction PEC devices or hybrid PEC cells can split water for hydrogen production using a large fraction of the solar spectrum providing high efficiency [1-4]. Tandem PEC cells connect PV layers (p-n junctions) with different semiconductor bandgaps in series, one behind the other in a single monolithic cascade device. In a hybrid PEC cell, the top layer would absorb the visible light spectra and also catalyze the reaction (photocatalyst). The bottom junctions would absorb the lower energy photons (near-infrared portion of the spectrum) to give the extra voltage for water decomposition.

While this system takes two photons to produce one electron in the external circuit, the voltages of the two cells are combined, giving rise to a higher efficiency than a single device alone. Multijunction photovoltaic solar cells have an efficiency limit of 42% while single-gap electrodes have a conversion efficiency limit of 32% [1].

In a hybrid PEC cell, the unstable (in aqueous solution) material is located at the bottom junction and a stable and protective one on the top junction. The difficulty in this approach is matching the light absorption characteristics of the two materials. Since the cells are in series, the component cell with the lowest current will limit the system final photocurrent. [2]. These types of devices can absorb a larger portion of the solar spectrum

therefore, they generate large open circuit voltages (V_{oc}) [3]. The generated voltage is the sum of the potential of the individual bandgap layers minus cathodic and anodic polarization losses on generated to drive the electrolysis reaction [3-7]. Numerous works have been done combining different photovoltaic materials with different water oxidation catalysts and photocatalyst [8-16].

Webber and Dignam have calculated the upper limit for hybrid PEC cells between 10-18 %, their efficiency analysis took into consideration the free energy and various solid-state and electrochemical losses [17,18]. The free energy ($\Delta\mu$) per electron, or photovoltage ($\Delta\mu/e$), extracted from a semiconductor device is determined by the separation of the quasi-Fermi levels for electrons and holes in the space charge region. The latter is also true for a semiconductor-electrolyte junction. In the dark there is only one common Fermi level.

In the dark, the photoanode and cathode in the electrolyte (connected by an external circuit) have their Fermi levels in equilibrium. Upon illumination there is a separation of the Fermi level in the photoanode, creating quasi-Fermi levels (Figure 4.1) [3,17-19]. It is worth to mention that the oxidation (OH^-/O_2) and reduction (H^+/H_2) level and quasi-Fermi levels are both electrochemical potential for electrons ($E^*_{F,e}$) and holes ($E^*_{F,h}$). It is known that net electron flow is thermodynamically forbidden except from a higher to a lower electrochemical potential. Based on this, a more strict conception for photoelectrochemical water splitting is that the quasi-Fermi levels for electrons and holes must overlap the redox level for water oxidation with sufficient extra separation to allow for overvoltages [17-19]. Therefore, the open circuit potential ($V_{oc} = \Delta\mu_{max}/e$), not just the E_g, has to be larger than 1.23 V. Figure 4.1 shows a band energy diagram of a

semiconductor-electrolyte interface, in this figure the V_{oc} $(\Delta\mu_{max}/e)$ = 1.23 + η_{O2} – V_{fb}, where η_{O2} is the OER overpotantial and V_{fb} is the flat band potential.

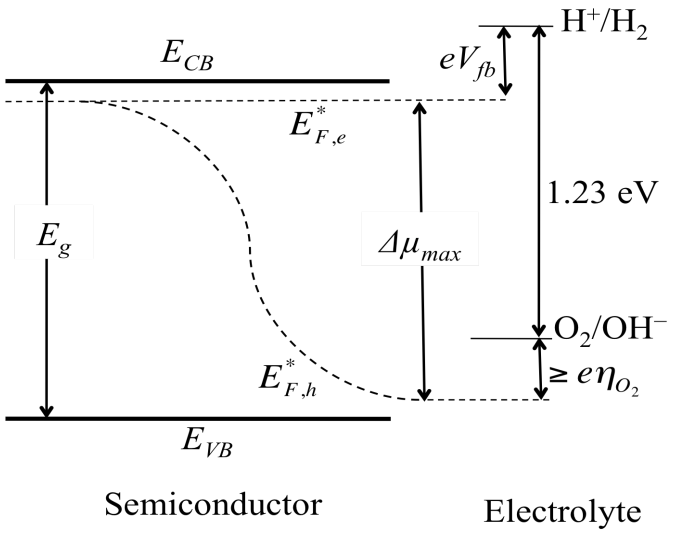

Figure 4.1: Energy diagram for a photoanode-electrolyte interface. The hole quasi-Fermi level must lie at least η_{O2} below the water oxidation potential for the holes to be transferred. In this case extra bias potential is needed to bend the conduction band enough to be more negative than H_+/H_2 [adapted from 17].

The upper limit for V_{oc} of a photovoltaic material is its bandgap. However, most times lower values are observed [24,25]. These diminished values are due to recombination processes occurring in the cell under illumination. Even in an otherwise ideal material, black body radiation will present a minimum amount of unavoidable radiative recombination, because solar cells operate at some finite temperature [23]. For powder TiO_2 (E_g ~ 3.2 eV) V_{oc} values around 0.7 V have been reported [24], and for Si (E_g ~1.14 eV) the typical values are around 0.6 V [18]. Values of V_{oc} between 0.8 and 1.0 V for TiNT films have been recorded in this work.

For two semiconductor devices connected in series, the total voltage is the sum of the voltages of each device. For this to occur in a tandem cell the hole quasi-Fermi level in semiconductor *I* must lie sufficiently below the O_2/OH^- redox level, and the electron quasi-Fermi level in semiconductor *II* must lie sufficiently above the H^+/H_2 level, in order to take care of the different energy losses. Figure 4.2 illustrates the energy diagram for two n-type semiconductors connected in series, the one in touch with the electrolyte absorbs the high energy photon and transmits the lower energy photons to the second semiconducting material.

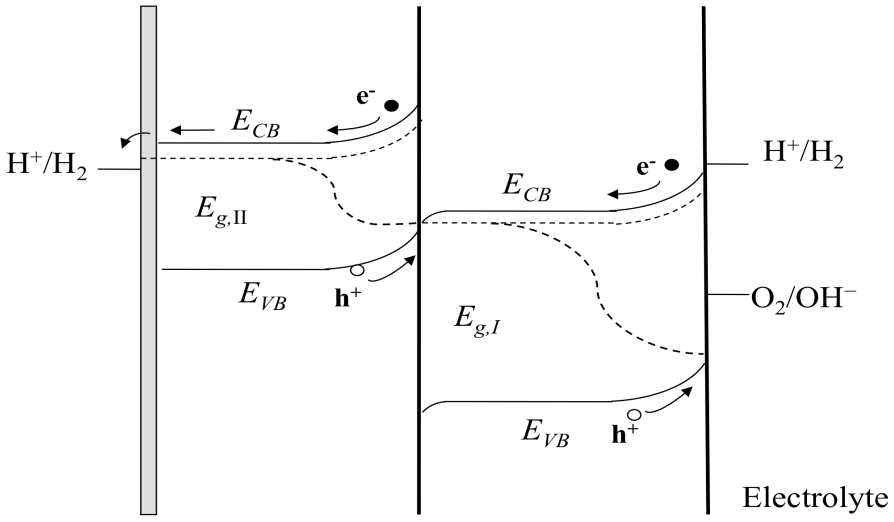

Figure 4.2: Tandem PEC cell energy diagram for n-type semiconductors immerse in an electrolyte. Electrons from the high bandgap material enter the valence band of the low bandgap where the low energy photons move them up to the conduction band [adapted from 18].

In a tandem PEC cell the photovoltaic junction acts to bias the photoanode to the required potential (V_{fb}). Because these two junctions are in series the operating condition will be limited by the element that produces the lower photocurrent. The photocurrent at the operating conditions, i_{OP}, is given by the intersection of the *i-V* curves of the

photoanode and the photovoltaic cell; this photocurrent must be equal for both interfaces. Any excess carriers would recombine as they do in a single bandgap photoelectrode. Figure 4.3.a illustrates and schematic of *i-V* curves for a photovoltaic solar cell and a photoanode. In this figure i_{SC}, i_{PL}, and i_{OP} are the solar cell short circuit, the photoanode saturation (or light-limited), and the tandem system operating current densities respectively. The photoanode onset, the solar cell open circuit and the tandem operation voltage are also indicated. The intersection of both curves denotes the operating point for the tandem system. Lower E_g materials give higher photocurrents but low potentials; Figure 4.3.b illustrates simulated *i-V* curves for three semiconductors (E_g = 1.14 (Si), 1.3 and 1.4 eV) and a photoanode with E_g = 2.2 eV [17] (this value corresponds to iron oxide). From the latter, only two solar cells might be able to produce enough voltage in combination with the photoanode to split water.

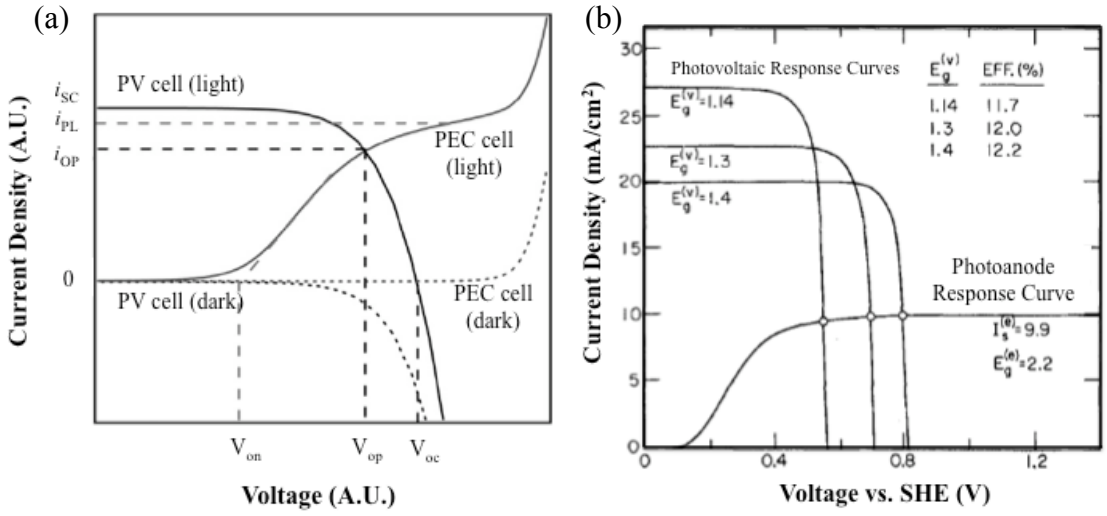

Figure 4.3: (a) Current-voltage curves for a photovoltaic solar cell and a photoanode in the dark (solid lines) and under illumination (solid lines) [adapted from 27]. (b) Current-voltage plots for 3 different bandgap solar cells and a photoanode with E_g = 2.2 eV [17].

Early work was done with photovoltaic-electrolysis (PVE) cells fabricated using commercial solar cells (single junction Si, double $GaInP_2$, and triple junction $GaInP_2$) and Pt catalyst. The main difference between these cells and PEC cells is that the only material in contact with the electrolyte is the catalyst, and the only material that captures sunlight is the solar cell. In addition alternative tandem PEC cells were fabricated using novel photocatalysts (TiNT and Au/TiNT) in combination with Si solar cells (single junction). The results of the fabrication, and material and performance characterization of these cells are presented in this chapter.

4.2 EXPERIMENTAL

Various multijunction cells (PEC and PVE) were fabricated using different solar cells and water oxidation catalysts (Pt loaded catalyst and TiO_2 photocatalyst). The solar cells used in this work were not fabricated in the laboratory; they were obtained from Spectrolab and Schott Solar Inc. Table 4.1 shows the electrical characteristics of the solar cells employed in these experiments.

4.2.1 Photovoltaic-electrolysis Cells

Three types of solar cells were used, a single junction Si (Schott Solar, Inc.), a double junction GaAs and a triple junction $GaInP_2$/GaAs/Ga (the last two from Spectrolab). The electrical characteristics of these solar cells are given in Table 4.1.

The electrocatalyst was prepared using Pt loaded on carbon black (with a nominal loading of 20 wt% Pt, Alfa Aesar). About 5 mg of the black powder was added to a solution of 200 μL of isopropanol alcohol (IPA, 2-Propanol, Certified ACS Plus, Fisher

Chemical) and 200 μL of DI water. The slurry was stirred vigorously to obtain an even paste.

Table 4.1: Summary of the electrical characteristics for various photovoltaic solar cells. The Si cells were received from Schott Solar Inc., and the GaAs cells were obtained from Spectrolab. The data was recorded using a parameter analyzer.

Characteristics	**p-n Si**	**p-n-Si (wafer)***	**Dual GaAs**	**$GaInP_2$/GaAs/Ga**
Area (cm^2)	0.94	0.77	0.21	0.5
V_{oc} (V)	0.52	0.54	0.9	2.4
i_{sc} (mA/cm^2)	24.9	15.7	9.8	12.1
P_{mp} (mW)	7.52	3.86	3.98	20.9
V_{mp} (V)	0.37	0.39	0.57	2.1
i_{mp} (mA/cm^2)	20.1	12.9	7.14	10.1
FF	57.9	59.9	42.0	72.7
η (%)	10.0	7.02	5.11	26.8

V_{oc}: open circuit potential
i_{sc}: short circuit current
P_{mp}: maximum power point
V_{mp}: voltage at the maximum power point
i_{pm}: current at the maximum power point
FF: fill factor, ratio of the maximum obtainable power, $(V_{mp} \times i_{mp})$ to the theoretical power, $(V_{oc} \times i_{sc})$
η : efficiency
* These cells do not have antireflection coating, bus bar, fingers, and metal contacts in either of their sides.

The solar cells were cut into small pieces of about 0.8 cm^2 in area. The aluminum coating on the back of the cell (positive side, p-side) was removed by sonicating the small cells in acetone. In order to prepare the cell, the Pt/carbon black (Pt/CBL) slurry was deposited on the back of the solar cells by carefully painting it with a small brush. Samples were dried under vacuum (-25 inches of Hg, Isotemp 280A, Fisher Scientific) for 5 minutes at 70°C.

The cells were then pasted on to a 1 mm thick quartz glass (GM Associates Inc.) using epoxy (DeVon 5 Minute® Epoxy), the epoxy served as adhesive and encapsulant.

A silver wire was attached to the back of the cell using silver paste (16032 Pelco® Colloidal Silver Paste, Ted Pella Inc.). To avoid contact between the silver wire and silver paste with the electrolyte, the connection was covered with the epoxy.

For these PVE cells, only the front side of the solar cell (protected by glass) was in contact with the light. The Pt catalyst was the only side in contact with the aqueous electrolyte.

4.2.2 TiNT Photocatalyst and Si Solar Cell Hybrid PEC Cell

4.2.2.1 Titanium Deposition on Si Substrates

A film of titanium metal (Ti pellets, Alfa Aesar 95% purity) was deposited onto 1 mm thick conductive glass (Indium Tin Oxide, ITO, film, R_s = 8-12 Ω, Delta Technologies Limited) and on Si solar cells (EFG Wafer diffused, from Schott Solar Inc.). Prior to the metal deposition, the substrates were cleaned with diluted KOH soultion to increase the roughness of their surfaces for better metal adhesion. After the etching procedure, the substrates were ultrasonically cleaned (Fisher Scientific Ultrasonic Cleaner, FS 360) in ethanol, acetone and water for 10 minutes each time, and then dried at 80 °C for 4-8 h. The metal deposition was done using an E-beam evaporator (Denton Vacuum LLC). The glass and Si solar cells were then attached to a round Si wafer and placed inside of the evaporator. The Ti deposition rate was varied between 2 and 4 Å/s, and the metal thicknesses obtained were between 1 and 2 μm.

4.2.2.2 Titanium Dioxide Nanotubes Fabrication on Si Substrates

The anodization of the Ti metal on Si substrates was done in the same manner as described in section 2.2.4. However, the two-electrode cell used for the anodization was

different. This cell was made out of glass, and it only allowed the side with the metal film to be in contact with the electrolyte. The substrate with the metal film was placed between two rubber o-rings and pressed against the cell and clamped. A silver wire was attached to the front of the sample (on top of the metal film) this wire was used to connect the cell to the power supply.

The electrolyte used was 0.3 wt% NH_4F in 98wt% ethylene glycol balance in DI water. Continuous magnetic stirring was needed to obtain good films with nanotubes. The applied voltage varied between 20 and 40 V. The anodization time depended on the initial thickness of the Ti film; in general the time was varied between 0.5 to 2 h. The latter was done in order to secure transparent films of TiO_2 nanotubes (complete usage of the Ti film) without disturbing the substrate (ITO and Si cell). Initial work varying voltages and anodization times was completed using regular non-conductive glass (1mm thick microscope glass slides, Fisher Scientific) to find the best-case scenario for transparent TiNT films.

After anodization, the TiNT films were rinsed in ethanol and dried under vacuum. Then, the samples were calcined in air at 500 °C for 3 hours with a 1 °C/min heating and cooling rates to obtain crystallinity. In order to ensure that calcination did not affect the electric performance of the cell, they were thermally treated at the calcination conditions. The open circuit potential and the short circuit current were measure before and after the thermal test, these measurements showed a decrease in less than 5 % for both current and voltage.

4.2.2.3 TiNT on Si Substrate Gold Loading

Gold nanoparticles were loaded onto the surface of the TiNT-Si supports. A preliminary test was performed by immersing the Si solar cells into Au precursor solution to see if there were any changes on the electric properties of the solar cell. This test indicated a small reduction (~ 4 %) in the V_{oc} occurred after the treatment, because the decrease in V_{oc} was not major, the side of the solar cell without the metal film was not protected during the Au loading.

The procedure of Au loading was already described in section 2.2.5. An aqueous solution of ~ 0.002 M $HAuCl_4 \cdot 3H_2O$ (Sigma Aldrich) was used and the solution pH was regulated adding small amounts of 0.01 M Na_2CO_3 solution. The substrates were rinsed various times by spinning the film in clean DI water for 30 minutes, then transferred to a vacuum oven (-25 inches of Hg, Isotemp 280A, Fisher Scientific) maintained at 80 °C and dried overnight.

4.2.2.4 Photoelectrode Fabrication

The photoelectrodes for the Hybrid PEC cell were made in a similar manner as described in 3.2.1. A silver wire was attached to back of the solar cells before the photoelectrode was attached to the glass. The excess surface of the film was painted with white enamel, leaving a small uncovered area of ~ 0.3 cm^2. The photoelectrode was connected to the potentiostat by clamping the silver wire with alligator connectors.

4.2.3 Material Characterization

The characterization of the nanotube films was accomplished by using SEM, TEM, and XRD. In order to measure the dimensions of the nanotubes a small portion of the film was cut and loaded onto the metal support without any further metal coating and introduced in the SEM chamber. Cross-sectional images of the nanotubes were obtained from layers cracked while cutting the sample film.

4.2.4 Performance Characterization

The photoelectrochemical performance experiments were carried out in a 3-electrode cell (Figure 3.3) connected to a potentiostat. The working electrode was the hybrid photoanode, the cathode was a Pt foil and an Hg/HgO electrode was the reference. The electrolyte used was a 1M KOH solution bubbled with ultra pure (UHP) nitrogen gas. The experiments under light were done using simulated solar light (AM1.5, 100 mW/cm^2 of visible solar light). The *i-V* characteristic curves for the photovoltaic solar cells were compiled using a parameter analyzer (HP 4145B Semiconductor Parameter Analyzer). All the photocurrent densities reported in this chapter were calculated using the geometric area of the photoanode in contact with the electrolyte.

4.3 RESULTS AND DISCUSSION

Preliminary work was completed using a PVE cell made with photovoltaic cells in and a very active water splitting electrocatalyst. High efficiency multijunction solar cells were used with the expectation of obtaining high solar-to-hydrogen (STH) efficiencies. Further, a lower cost photocatalyst (titanium dioxide nanotubes) was combined with Si

solar cells in a tandem PEC system. In order to increase water oxidation rates Au nanoparticles were also loaded on the surface of the nanotubes.

4.3.1 TiO_2 Nanotube Films on Si Substrates

Anodization of the Ti metal deposited on Si substrates resulted in formation of highly ordered nanotubes. The TiNT formation mechanism and the influence anodization parameters in the dimensions of the nanotubes were presented on section 2.4.2. TiO_2 nanotube growths on glass and silicon wafer have been reported previously [20-22].

The time of anodization was crucial during the nanotube growing process, because contact of the substrates with the electrolyte under applied voltage was not desired. The latter led to corrosion of the Si substrate. The applied voltage influenced the anodization time as well. Exploratory work done with ordinary microscope glass slides indicated that for 0.8 μm-thick Ti films anodization times of ~70 minutes at 20 V was sufficient to consume all the deposited metal. Films with thickness ranging between 1.5 and 2μm needed around 120 and 150 minutes respectively for the similar anodization voltage. Anodization times were reduced to almost half when 40 V was applied. With the latter potential films of 1μm and 2 μm thickness needed 45 and 90 minutes to consume all the metal.

Figure 4.4.a shows three samples of Ti deposited on conductive glass. The metal thickness before anodization was ~ 1.6 μm. Figure 4.4.b illustrates SEM micrograph showing a side and top view of the metal film deposited on the glass substrate. Anodization took up to two hours to obtain a transparent film composed of titania nanotubes. A SEM micrograph is given in Figure 4.4.c, which illustrates a cross section and top view of TiNT anodized for 1 h at 30 V. The TiNT average length and outer

diameter were 2.2 μm and 80 nm respectively. The bulk of the Ti film was not as uniform as the Ti foil. The nanotube walls obtained with the PVD deposited Ti were not as smooth as the ones resulted from Ti foils.

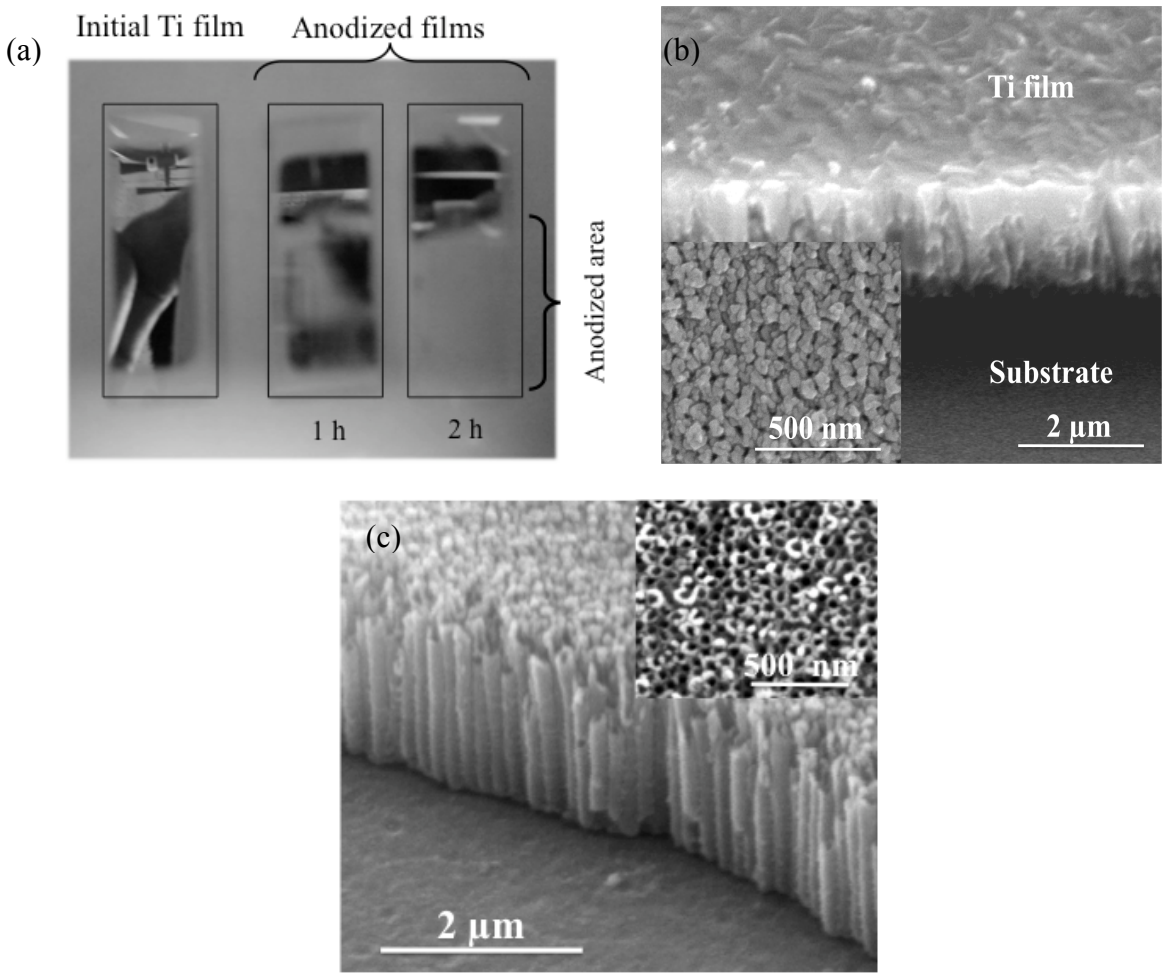

Figure 4.4: (a) Photographs of three films, on the left is an as-deposited on quartz Ti film, on the center and on the right are Ti films anodized anodized at 30V for 1 and 2 hours respectively. (b) SEM micrograph of a Ti film before anodization. (c) SEM micrographs of TiNTs on quartz, the initial Ti thickness was ~ 1.6 μm. The anodization time was 1 h.

Titanium dioxide nanotubes were fabricated from Ti films deposited on Si solar cells. The results were similar to the ones seen on glass substrates. Figure 4.5.a depicts a

side view of the nanotubes and a top view illustrating the entrances of the tubes. The average diameter of these tubes was ~ 100 nm for anodization performed at 30 V applied voltage and 1 h of electrochemical treatment. Similarly to TiNT fabricated from Ti foils, the nanotubes fabricated on Si substrates also have close bottoms with a semispherical shape as illustrate in Figure 4.5.b.

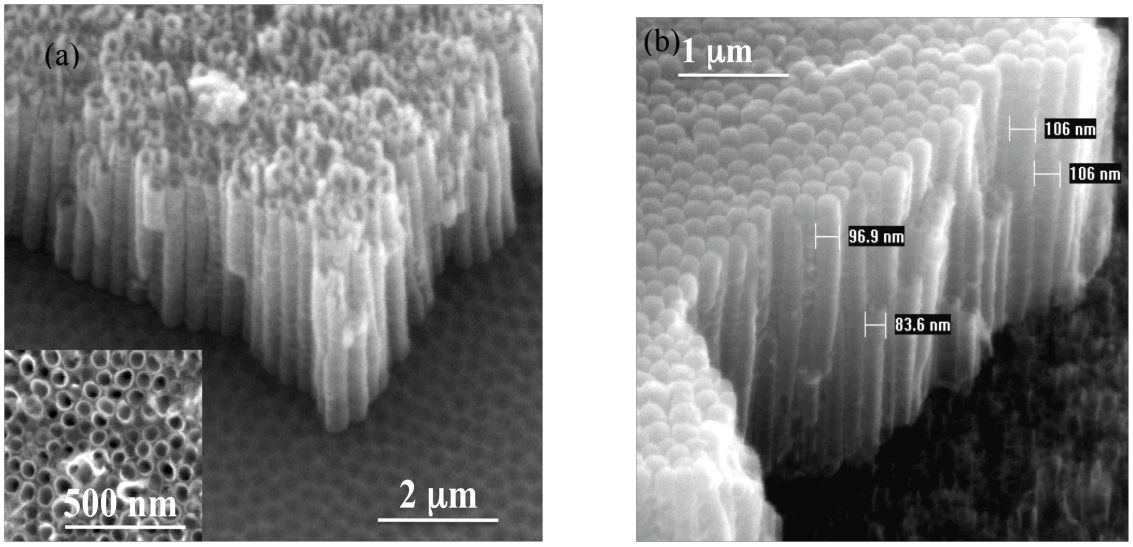

Figure 4.5: (a) SEM micrographs for the as-prepared nanotubes on Si Solar cells, the inset shows the open tops of the tubes. (b) Side view of the nanotube array, illustrating the semispherical closed bottom of the nanotubes. The nanotube dimensions were $L \sim 3$ μm and $OD \sim 100$.

In order to make a photoanode, a thin layer of Ti (later converted to TiO_2) was left between the nanotube array and the solar cell; this is illustrated in Figure 4.6.a. Therefore the tandem hybrid photoanode had four layers (Figure 4.6.b): an n-TiNT layer on top, a TiO_2 interface layer and a p-n junction solar cell.

The films were calcined in air for 3 hours at 500 °C in order to convert the as-prepared nanotubes to anatase. The heating and cooling ramps were kept to 1°C/min in order to preserve the structural integrity of the nanotubes. X-ray diffraction patterns

showed that the amorphous oxide nanotubes were converted to anatase after the thermal treatment (Figure 4.7). The XRD patterns were characterized by very intense Si peak and Ti signal emerging from solar cell and the remaining metal film underneath of the nanotubes.

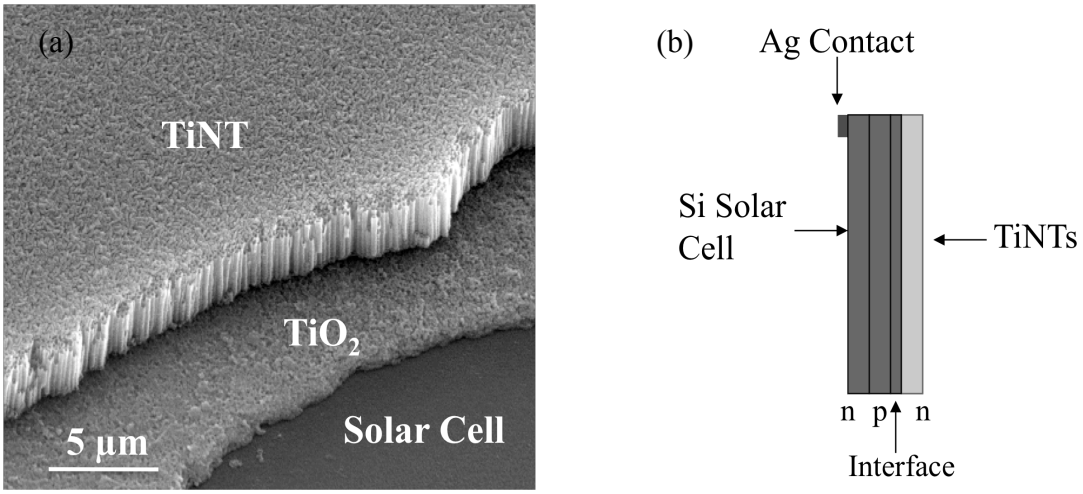

Figure 4.6: (a) SEM micrograph for a TiNT film on Si solar cell substrate. The initial Ti thickness was ~ 2 µm. The nanotube dimensions were L ~ 5 µm and OD ~ 100 nm. (b) Schematic representation of a tandem photoelectrode built with a pn-Si solar cell and n-TiNT film.

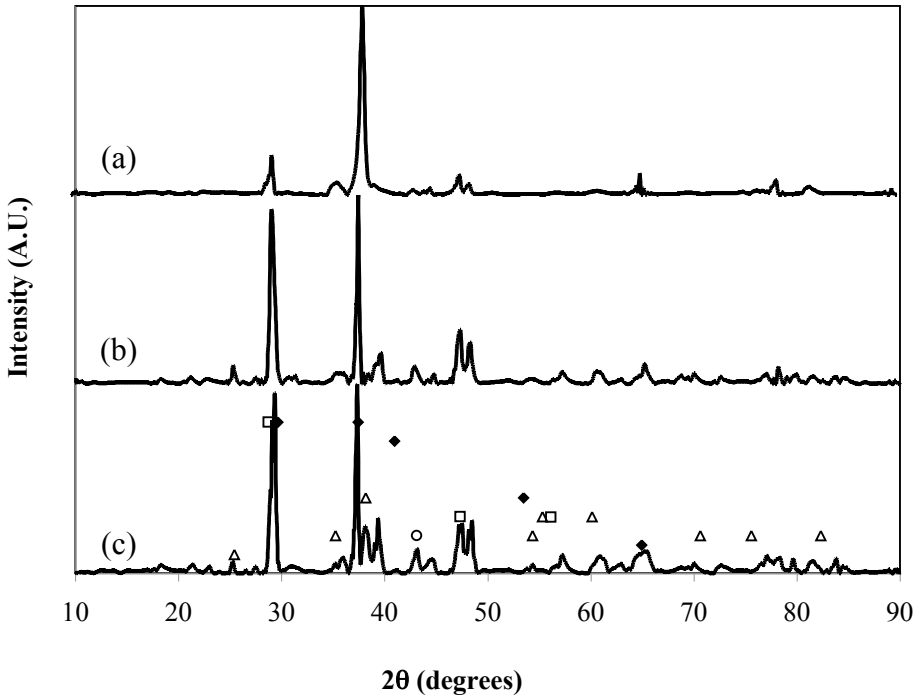

Figure 4.7: X-ray diffraction patterns for TiNT grown on Si photovoltaic cells. (a) As-anodized nanotubes and nanotubes calcined at 500 °C (b) TiNT and (c) Au/TiNT. The symbols represent (o) Gold, (◆) Titanium, (Δ) Silicon, and (□) Anatase. The Au loading for (c) was 2.1 wt%

4.3.2 Performance Evaluation

4.3.2.1 Electrocatalyst and Photovoltaic (PV) Solar Cells: PVE Cells

Three sets (three samples per set) of hybrid cells were prepared using a PV cell and Pt electrocatalyt as a photoanode. Characteristic i_{ph}-V plots for the solar cells are illustrated in Figure 4.8. Among these 3 cells only the triple junction cell can produce enough potential to split water. Even though the 1.23 V is the ideal potential for water decomposition; because of the overpotential related to oxygen evolution reaction (~ 0.4 V) and hydrogen evolution reaction (~0.05 V), the minimum potential needed is ~ 1.7 V [17, 18].

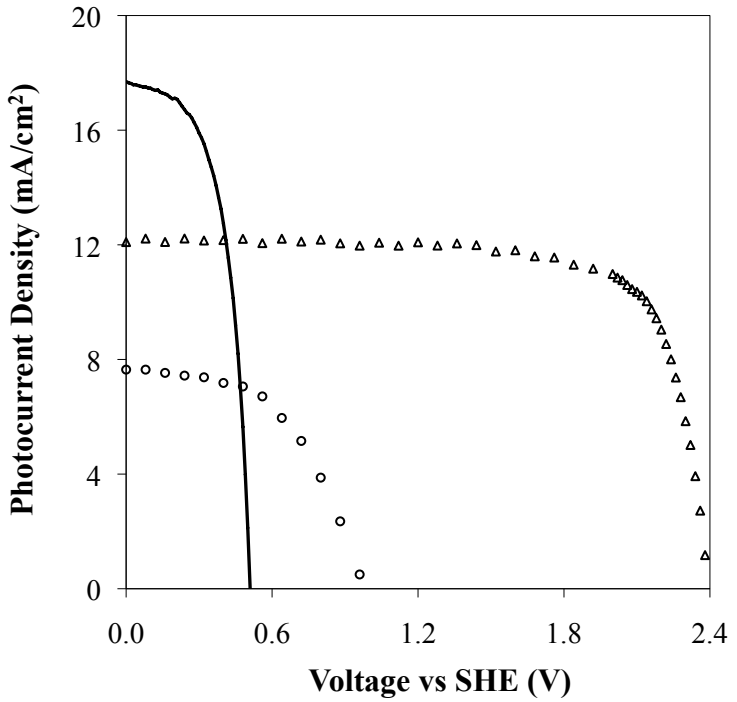

Figure 4.8: Current density-voltage plots for photovoltaic solar cells used to make hybrid PEC cells in combination with Pt catalyst. The symbols represent the (-) p-n Si, (o) double junction GaAs, and (Δ) triple junction $GaInP_2$/GaAs/Ga.

Figure 4.9.a shows the *i-V* curves for Si cells and Pt/CBL electrode (Pt/CBL deposited on a Ti foil). The operation point for the Pt/CBL-Si cell was very close to the V_{oc} for Si (0.52 V vs. SHE). This voltage is not enough to start the oxidization of water. However, a combination of three Si cells in series (in a triple junction p-n photovoltaic cell) might be and alternative cell that could supply enough bias voltage to start the OER with an operation current of ~ 4 mA/cm^2 (simulated values). More efficient solar cells (double and triple junction solar cells, efficiencies are shown in Table 4.1) were also used. Figure 4.9.b presents the *i-V* plots for these cells along with the Pt loaded anode. Figure 4.10.a illustrates the i_{ph}-*V* (bias voltage dependence of the photocurrent) plots for the Pt/CBL/GaAs (double junction solar cell) photoanode, the saturation current was ~ 0.52 mA/cm^2. The bias voltage characteristics were consistent with that expected from the *i-V*

characteristics shown in Figure 4.9.b. However, the potential produced by the double junction solar cell was not enough to oxidize water and external bias was needed to start oxygen production at the photoanode. Conversely, the triple junction solar cell has a V_{oc}, which is sufficient to overcome overvoltages and start the OER. The operation characteristics were ~2.1 V ~ 11.8 mA/cm^2 (Figure 4.10.b). This is very close to the maximum power point for this solar cell. This cell produced abundant amounts of O_2 and H_2 (bubbles on both electrodes) under simulated sunlight when the electrodes were short-circuited. The latter combination of a catalysts and a photovoltaic cell is very close to an ideal scenario, where the operating point for the photovoltaic-electrolysis system matches the maximum power point of the solar cell.

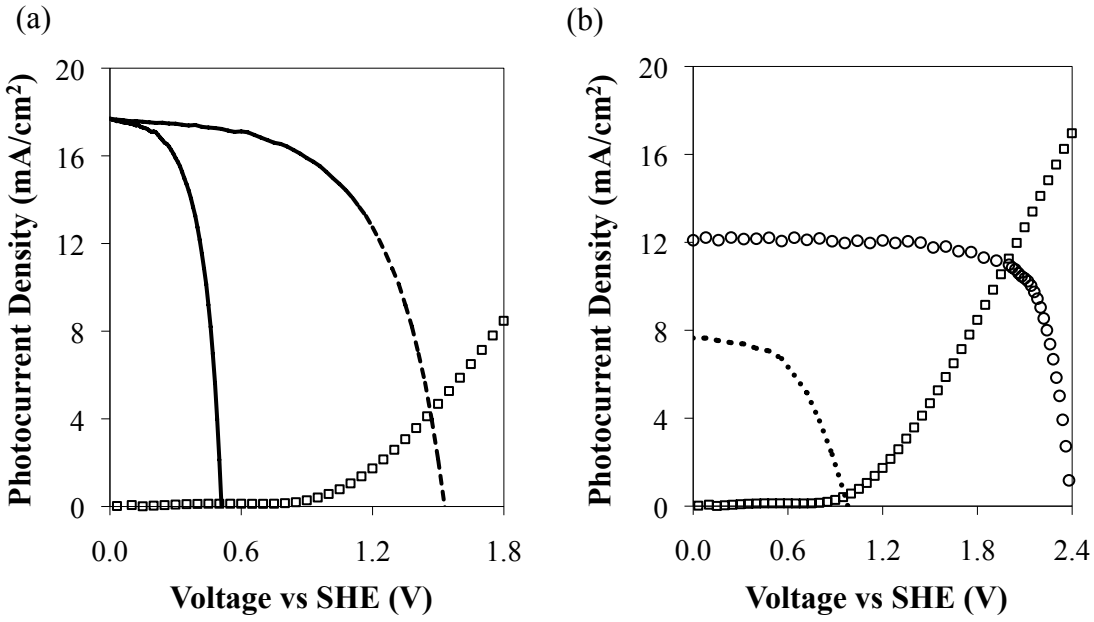

Figure 4.9: Photocurrent as a function of voltage for two photovoltaic cells and an (□) anode for water oxidation. (a) p-n Si solar cell, (−) single bandgap cell and (---) 3 Si cell in series. (b) Multijunction solar cells, (−) GaAs, and (o) triple junction $GaInP_2$/GaAs/Ga.

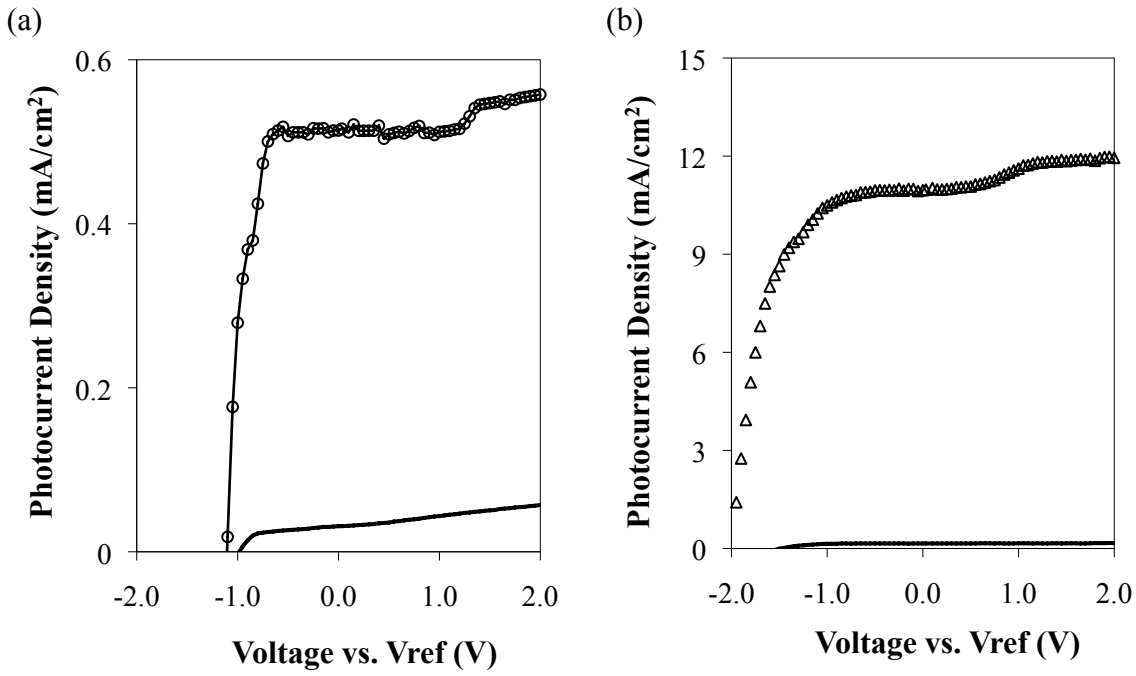

Figure 4.10: Measured i_{ph}-V characteristics plots for the (a) double junction GaAs and (b) triple junction $GaInP_2$/GaAs/Ga photoanodes (the catalyst was Pt on Carbon black). Plots were obtained by linear sweep voltammetry performed at 50 mV/s scan rate in 1.0M KOH electrolyte.

The efficiencies calculations were made for the different hybrid PEC and photovoltaic-electrolysis cells using equations 3.6 (STH) and 3.28 (diagnostic efficiency). The PEC with the triple junction cells did not required external voltage (note the values reported for a triple junction Si cell were simulations using the values of a single junction solar cell). In contrast, due to their low V_{oc} the single bandgap Si and the double junction PEC cells needed bias to run the reaction. Figure 4.11 shows the diagnostic efficiencies as a function applied voltage for the last two PEC cells. A summary of the operating conditions and efficiencies for these PEC cells are given in Table 4.2. The efficiency of the Pt/CBL-$GaInP_2$/GaAs/Ga given in the table is the actual STH. The simulated results

for a triple junction Si based photovoltaic-electrolysis cell suggested that this configuration could be a good option for a less expensive system.

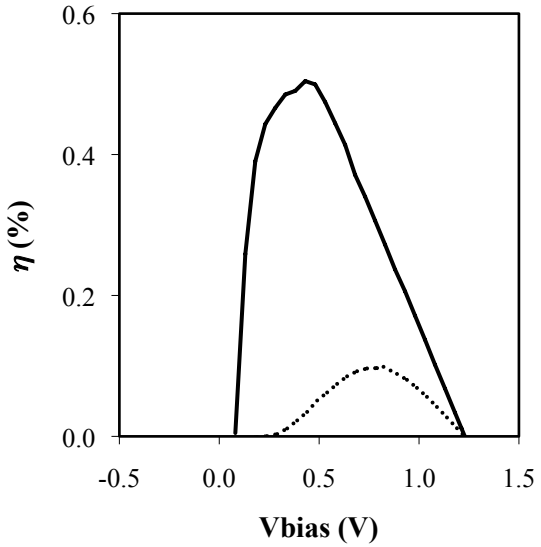

Figure 4.11: Efficiency as a function of applied bias voltage plots for (---) single bandgap Si and (−) double junction GaAs solar cells. The water catalyst was Pt (20 wt%) on carbon black.

Table 4.2: Summary of the characteristics of the PVE cells fabricated with photovoltaic solar cells and Pt/Carbon Black.

Characteristics	**p-n Si**	**p-n-Si (three)[a]**	**Dual GaAs**	**$GaInP_2$/GaAs/Ga**
V_{oc} (V)	0.54	1.62	0.98	2.4
i_{sc} (mA/cm^2)	17.7	17.7	7.65	12.1
V_{op} (V)	0.5	1.5	0.94	2.1
i_{op} (mW)	0.18	4.2	0.41	11.2
V_{bias} *(V)*	0.82	0	0.43	0
η (V)	0.1[b]	5.2	0.5[c]	13.8

V_{op}: operation voltage
i_{op}: operation current
[a] Simulated not measured

4.3.2.2 TiNT and PV Solar Cells as a Hybrid Photoanodes

Titanium dioxide nanotubes have been combined with Si solar cells to fabricate a hybrid PEC cell. Photocurrent-voltage characteristic plots for a Si solar cell and TiNT and Au/TiNT photoelectrodes (the nanotubes were fabricated from Ti foil, with dimensions $L \sim 15$ μm, $OD \sim 150$ nm) are shown in Figure 4.12. The intersection points (1, 2) indicated the expected operation points for hybrid PEC cells made with Si solar cell and TiNT photocatalysts. The main difference between these PEC cells and the Pt/CBL and solar cells is that the TiO_2 is a photocatalyst. Thus, in addition to catalyze the OER, TiO_2 also produces voltage and current to be used in the water splitting process. In the TiNT-SC cells, the TiNT and the solar cells are connected in optical and electrical series, so the efficiency is limited by the component with the lowest photocurrent (i.e. TiNT).

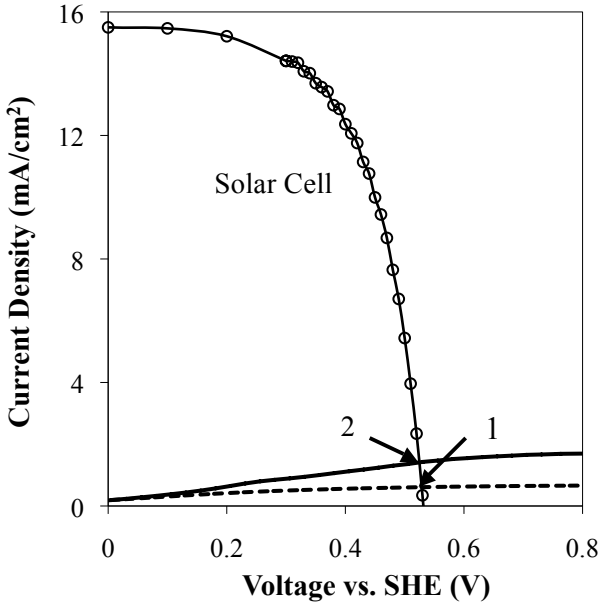

Figure 4.12: Photocurrent as a function of voltage plots for a (Δ) Si solar cell, and two photoanodes (---) and TiNT (−) Au/TiNT. The solar cell was specially fabricated without any coating on either of the sides. The nanotubes were

fabricated from Ti foils and the dimensions were $L \sim 15$ μm, and $OD \sim 150$ nm.

Before the fabrication TiNT on Si solar cells, ITO coated glass was used to test the performance of transparent TiNT films. Photoelectrodes were prepared with the TiNT-ITO films and tested as a photoanode in a PEC cell. Figure 4.13.a presents the i_{ph}-V for the TiNT-ITO and for TiNT-Ti (the nanotubes were grown from Ti foil) with similar dimensions (OD ~100 nm and L ~5 μm). The final saturation current (important for matching photoanodes with solar cells) is similar for both cases. Figure 4.13.b is a schematic representation of the photoelectrode used to obtain the data for Figure 4.13.a.

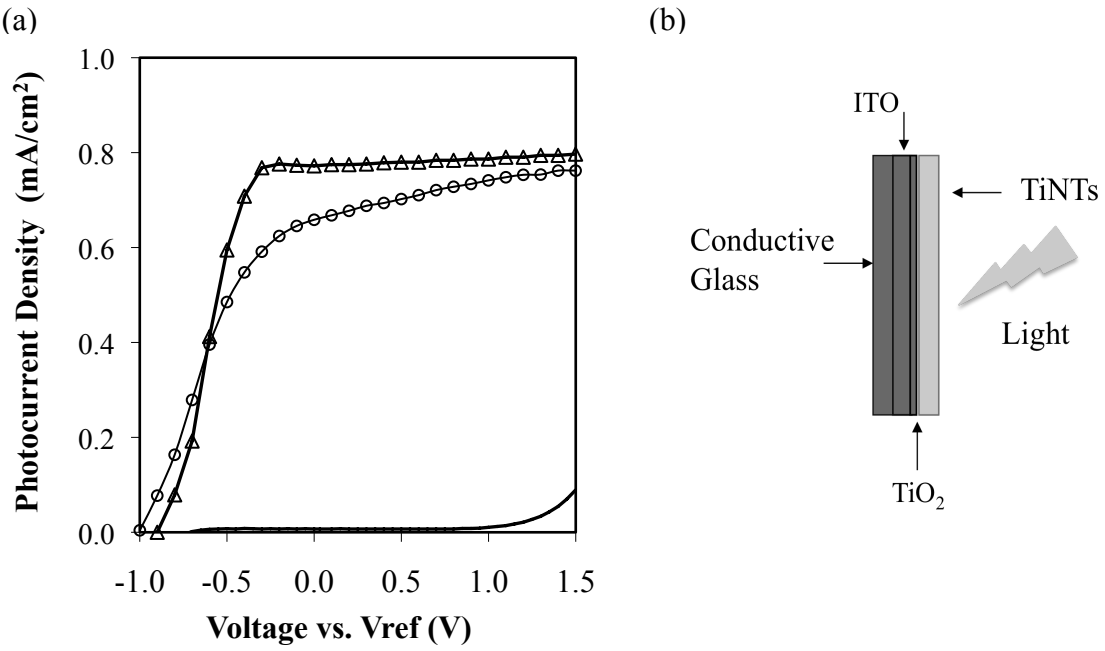

Figure 4.13: (a) Photocurrent as a function of applied voltage plots for TiNT photoelectrode: (-) dark and under simulated sunlight (o) TiNT-ITO and (Δ) TiNT-Ti. (b) Schematic representation of the TiNT-ITO photoelectrode.

In Figure 4.14 the photocurrent characteristics for a TiNT-SC PEC cell are given, the saturation currents were similar to the operating values obtained from Figure 4.12.

For the same nanotube dimensions, the photocurrent produced by the TiNT-SC photoelectrode doubled the current produced by TiNT-ITO. The light-limited current density was reached approximately at a zero bias, and this value was similar to the one produced by TiNT photoanodes with larger dimensions (L ~ 15 μm and OD ~ 150 nm). The latter might be result of the improved transport and separation of electrons and holes at the interface (between the solar cell and the TiNT layers) when a solar cell is used as a substrate instead of Ti or ITO. However, even though the photocurrent produced with the TiNT-SC photoelectrode was higher, the potential produced was not sufficient to initiate the oxidation of water.

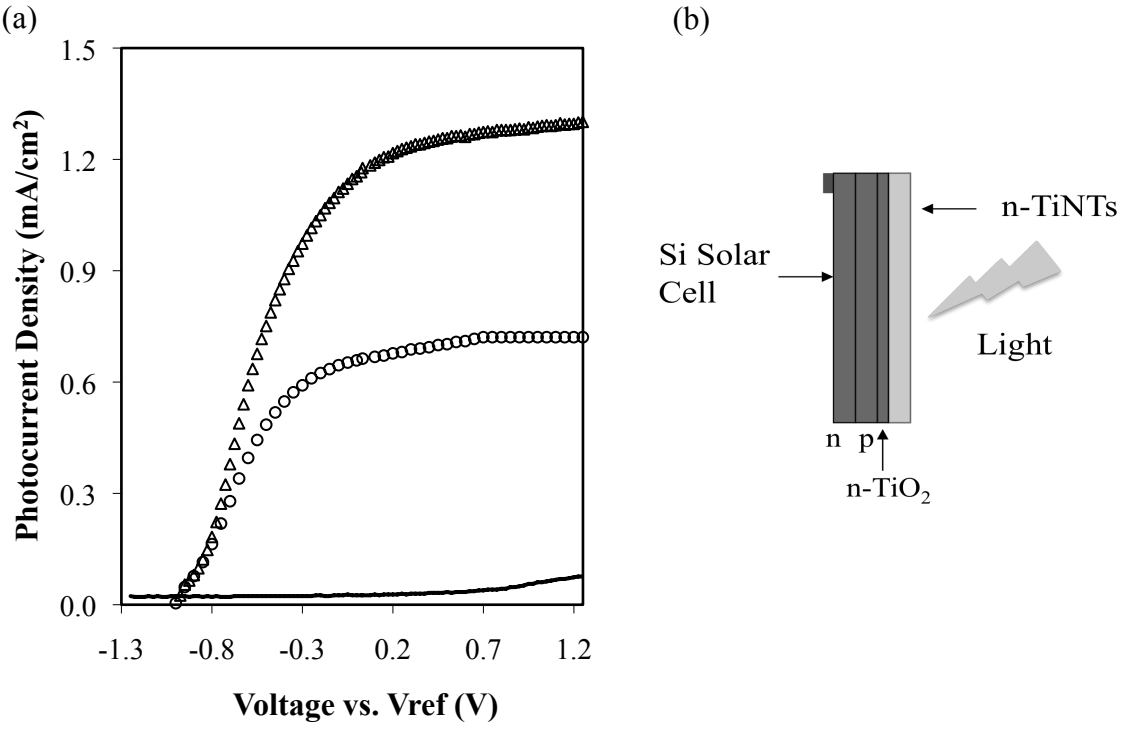

Figure 4.14: Photocurrent density as function of applied voltage curves for (−) a solar cell alone (SC), (o) TiNT-ITO, and (Δ) TiNT-SC. All the data were gathered under illumination. (b) Scheme illustrating a hybrid TiNT-SC photoanode.

Results presented in previous chapters indicated that the addition of Au nanoparticles on the surface of TiO_2 enhances the water oxidation rate by creating extra sites for the OER and capturing more light due to the modification of the oxide bandgap. Gold nanoparticles were loaded on the surface of the nanotubes grown on Si solar cells. Three different loadings and particle sizes were obtained by varying the loading solution pH.

Figure 4.15 shows photocurrent densities versus bias voltage for three electrodes with Au/TiNT photocatalyst. The metal loadings were 0.5, 0.9 and 2.1 wt%, and the particle sizes 9.5, 7.6, and 3.8 nm for the respective loadings. The combination of the highest amount of metal and the smallest particle size gave the highest photocurrent production.

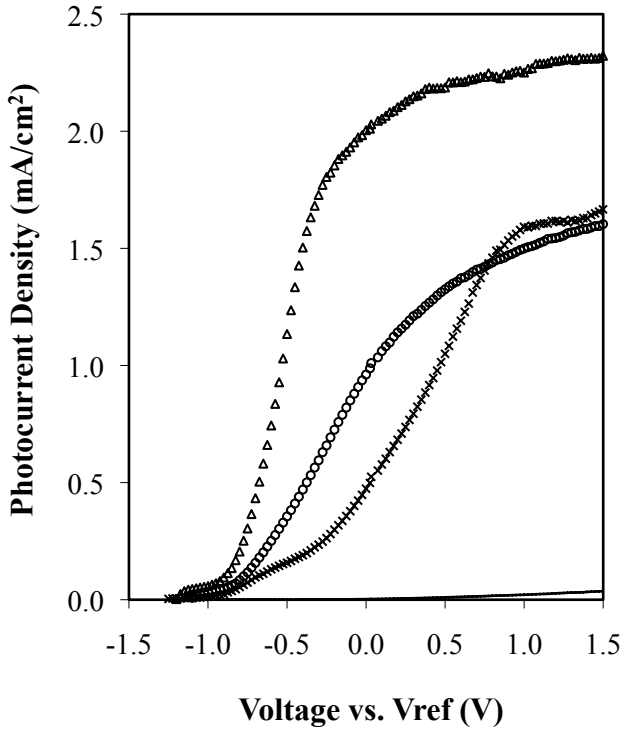

Figure 4.15: Photocurrent characteristic plots for Au/TiNT-Si photoanodes. The gold loading was done at solution pH of (×) 9.1 (o) 3.9, (Δ) 6.7. The metal loading and nanoparticle sizes corresponding to this pH values are (×)

0.5wt% and 9.5 nm, (o) 0.9 wt%, and 7.6 nm particle size, and (Δ) 2.1 wt%, and 3.8 nm. The nanotube dimensions were $L \sim 5$ μm and $OD \sim 100$ nm.

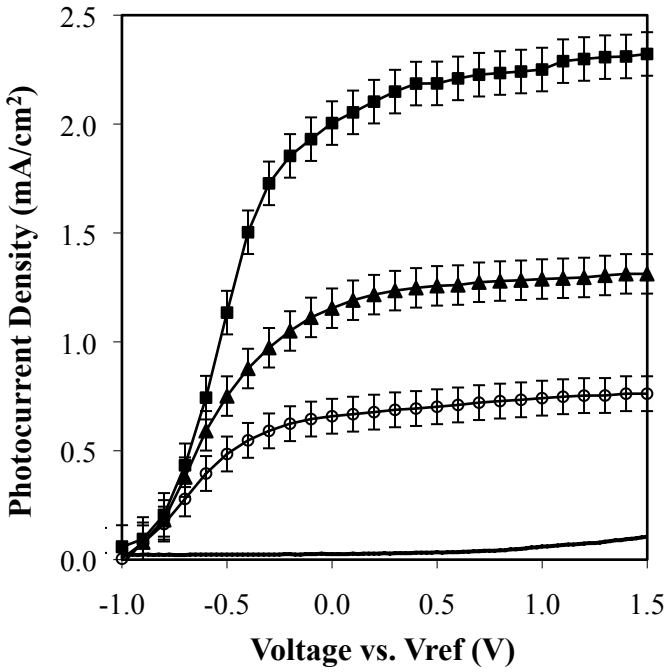

Figure 4.16: Photocurrent density as a function of bias voltage plots for hybrid photoelectrodes. The bottom line represents the dark case (−). While the other three were obtained under simulated sunlight (×) TiNT on ITO glass, (o) TiNT on Si SC, and (Δ) Au/TiNT-Si. In all the cases the nanotube dimensions were $L \sim 5$ μm and $OD \sim 100$ nm.

The saturation current for the Au/TiNT-SC photoelectrode was 2.5 mA/cm^2, which is similar to the one predicted from intersection of the *i-V* curves in Figure 4.12. And the photocurrent produced by the Au/TiNT-SC was 70% higher than the current produced by the photoanode without gold (the nanotubes dimensions were the same in both cases) as shown in Figure 4.16. The V_{oc} for the tandem PEC cell was ~1.3 V; this potential reflects the addition of the open circuit potentials for TiNT (0.85 V) and Si solar cell (0.54 V). However, in order to start producing O_2 gas the photoelectrode needed a 0.3 V bias voltage. Diagnostic efficiencies were calculated for the TiNT based hybrid

PEC cells. Figure 4.17 illustrates the efficiency curves for three PEC cells as a function of the applied bias potential. Table 4.1 summarizes the characteristic parameters and efficiencies for the hybrid PEC cells fabricated using TiNT and solar cells. The highest efficiency was accomplished by the Au/TiNT-SC with 2.1 wt% gold content.

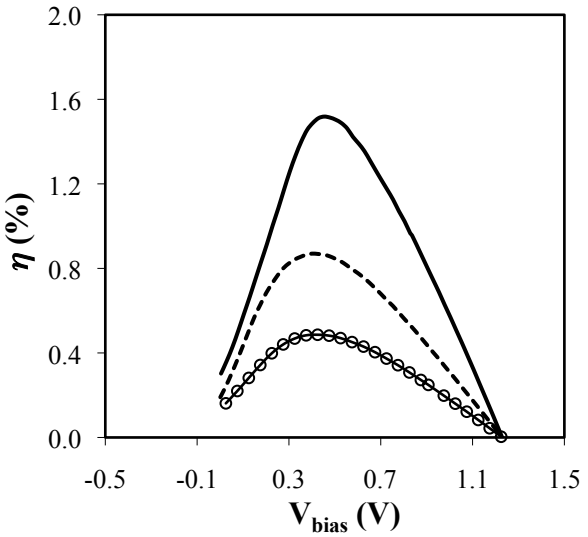

Figure 4.17: Efficiency as a function of applied bias voltage plots for hybrid PEC cells: (o) TiNT on ITO, (---) TiNT on Si solar cell, and (−) Au/TiNT on Si solar cell with 2.1 wt% Au. The average nanotube dimension for the three photoelectrodes were $L \sim 5$ μm and $OD \sim 100$ nm.

Table 4.3: Photocurrent, potential and efficiencies for hybrid PEC cell fabricated with TiNT and Si photovoltaic solar cells.

Characteristics	**TiNT-ITO**	**TINT-SC**	**Au/TiNT-SC**
V_{oc} (V)	0.80	1.1	1.2
i_{sc} (mA/cm^2)	0.81	1.2	1.9
V_{op} (V)	0.75	0.52	0.54
i_{op} (mA/cm^2)	0.83	1.1	1.9
V_{bias} (V)*	0.46	0.4	0.41
η (%)	0.4 ± 0.2	0.85 ± 0.2	1.5 ± 0.3

* V_{bias} obtained at maximum efficiency

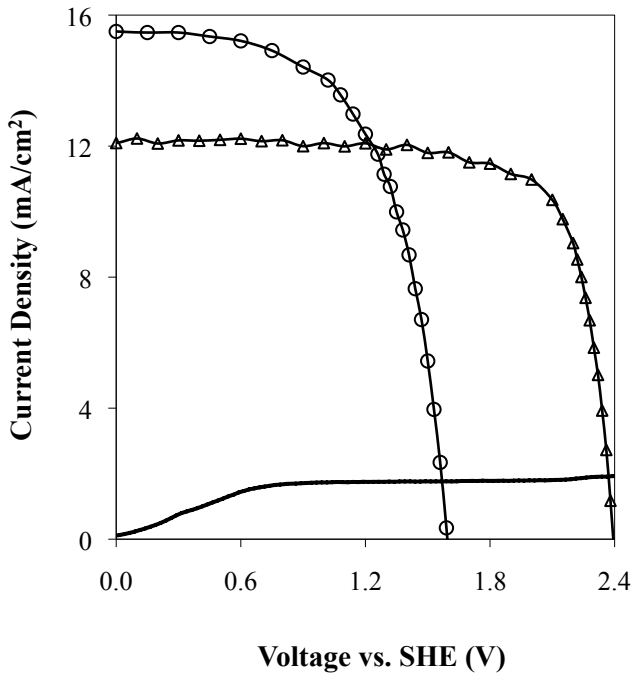

Figure 4.18: *i-V* curves for an (−) Au/TiNT photoanode, a (o) simulated triple junction Si solar cell, and a (Δ) triple junction $GaInP_2$/GaAs/Ga solar cells.

The performance efficiencies (calculated using equation 3.3) for the TiNT-SC hybrid PEC cells are almost on order of magnitude smaller than the one for the Pt/CBL-$GaInP_2$/GaAs/Ga. In either case the TiNT based PEC cell still needs extra bias voltage to produce hydrogen from water. These systems were designed and fabricated with the goal of studying the feasibility of combining TiNT films with solar cells and to study the behavior as a hybrid PEC cell. In spite of the low performance efficiency and the need of bias voltage, the PEC cell worked as a multijunction cell supplying higher potential than the Si cell or TiNT photoelectrode alone.

A major source of efficiency loss lies in the slow rate of the rise of the photocurrent with voltage for the photoelectrodes. In other words, photoelectrodes have a low fill factor. So unless fill factors can be greatly improved, PEC cells will not be able

to match efficiencies of photovoltaic cells. This could be accomplished by allowing the photocatalyst layer to absorb more sunlight (i.e. doping TiO2 with C or N). Photoelectrochemical cells are forced to operate at fixed potential of 1.23 V, and as a result when a high voltage (V_{oc} > 1.8 V) and *FF* solar cells (multijunction) are combined with a low fill factor photoanode (i.e. TiO_2) the final efficiencies will not be higher. Figure 4.18 depicts the characteristic *i-V* for an Au/TiNT photoanode and two triple junction solar cells (simulated triple junction Si, and triple junction $GaInP_2$/GaAs/Ga solar cell). In the latter case, even though the potential is enough to start the water oxidation reaction the operation current will be limited by the photoanode, and the excess charge carriers will recombine lowering the maximum efficiency of the PEC cell.

To maximize solar-to-hydrogen efficiency of the PEC system a multijunction photovoltaic solar cell should be specifically designed to match the electrical parameters for water splitting. For any direct solar-to-hydrogen conversion system, the maximum voltage is fixed by the chemical potential of hydrogen. Therefore, in order to increase the conversion efficiency, the current (and therefore the hydrogen rate) must be increased (increase fill factor).

4.4 SUMMARY AND CONCLUSIONS

The fabrication and characterization of different hybrid photoelectrochemical and photovoltaic-electrolysis cells for hydrogen production has been presented. Solar cells with different efficiencies were combined with a water oxidation catalyst (Pt/Carbon black) and a photocatalyst (Titanium dioxide nanotubes) to form hybrid cells.

The combination of highly efficient (triple junction $GaInP_2$/GaAs/Ga solar cell)

solar cells with a highly active water oxidation catalyst (Pt) was shown to give high solar-to-hydrogen efficiency. For this cell, the Pt supported catalyst was in contact with the electrolyte and the solar cell was the only one that absorbed light. Solar-to-hydrogen efficiency in excess of 14% was demonstrated for indoor measurements. A combination of Pt supported catalyst with a triple junction Si solar cell could be an alternative for a lower cost water photovoltaic-electrolysis cell. Calculations presented in this chapter based on modeled electric characteristics showed efficiencies on the order of 5 % for the latter cell.

The combination of less expensive materials such as TiO_2 nanotubes with Si photovoltaic solar cells in a hybrid PEC cell was investigated. Titania is a semiconductor that absorbs light in the UV region of the solar spectrum, as well as catalyzes the oxidation of water. When light is illuminating the surface of this PEC cell, the higher energy photon are absorbed by TiO_2, and the lower energy photons are transmitted to the Si solar cell to produce the extra bias voltage for water splitting. The open circuit potential for the Au/TiNT-SC was ~ 1.3 V, which indicated that the films were connected in electrical series. However, this potential was not enough to initiate water oxidation. The need of bias voltage and the low photocurrent produced limited the performance efficiency of the cell to ~ 1.5 %. In spite of the low efficiency, the combination of a less expensive photocatalyst and a Si solar cell proved to work in a tandem system. An alternative could be usage of a triple junction solar cell in combination with TiNT. In addition, in order to increase the solar-to-hydrogen efficiencies the fill factor of the photoelectrodes has to be increased, in other words, the photocurrents have to be enhanced.

4.5 REFERENCES

1. A. Luzzi, Photoelectrolytic Production of Hydrogen, IEA Agreement on the Production and Utilization of Hydrogen, IEA/H2/TR-02/ 2004.
2. E. L. Miller, R. E. Rocheleau, and S. Khan, International Journal of Hydrogen Energy, 29 (2004) 907-914.
3. S. Licht, in: A. J. Bard and M. Stratmann, (Eds.), Solar Photoelectrochemical Generation of Hydrogen Fuel: Encyclopedia of Electrochemistry, Wiley-VCH, Weinheim, Germany, 2002 v. 6, 346-357.
4. N. Lewis and G. Crabtree (Eds.), Basic Research Needs for Solar Energy Utilization, Report of the Basic Energy Sciences Workshop on Solar Utilization, US Department of Energy (2005).
5. H. Morisaki, T. Watanabe, M. Iwase, K. Yawaza, Applied Physics Letters, 29 (6) (1976) 338-340.
6. H. Gerischer, Semiconductor Electrodes and their Interaction with Light, Photoelectrochemistry, Photocatalysis and Photoreactors, Fundamentals and Developments, NATO ASI Series, 146 (1984) 39-106.
7. S. Chandra, Photoelectrochemical Solar Cells, Electrocomponent Science Monographs, Gordon and Breach Science Publisher, 1985, v. 5.
8. S. Licht, J. Physical Chemistry B 105 (2001) 6281-6294.
9. A. Goetzberger, C. Hebling, and H-W Schock, Material Science and Engineering 40 (2003) 1-46.
10. S. Litch, in: A. J. Bard and M. Stratmann, Encyclopedia of Electrochemistry, Semiconductor Electrodes and Photoelectrochemistry, Wiley-VCH, Weinheim, Germany, 2002 v. 6 358-394.
11. S. Maheshwar, in: A. J. Bard and M. Stratmann, Encyclopedia of Electrochemistry, Semiconductor Electrodes and Photoelectrochemistry, Wiley-VCH, Weinheim, Germany, 2002 v. 6, 346-357.
12. O. Khaselev, A. Bansal, and J. A. Turner, International Journal of Hydrogen Energy 26 (2001) 127-132.
13. O. Khaselev, J. A. Turner, Science 280 (5362)(1998) 425-427.
14. E. L. Miller, B. Marsen, D. Paluselli, and R. Rocheleau, Electrochemistryand Solid-State Letters 8 (2005) A247-A249.
15. E. L. Miller, D. Paluselli, B. Marsen, and R. Rocheleau, Hawaii Natural Energy Institute, University of Hawaii, II.E.2 Photoelectrochemical Hydrogen Production, DOE Hydrogen Program, FY 2004 Progress Report.
16. E. L. Miller, D. Paluselli, B. Marsen, R. E. Rocheleau, Solar Energy Material & Solar Cells 88 (2005) 131-144.

17. M. F. Weber and M. J. Dignam, Journal of the Electrochemical Society, 131 (1984) 1258-1265.

18. M. F. Weber and M. J. Dignam, international Journal Hydrogen Energy, 11 (1986) 225-232.

19. Y. V. Pleskov and Y. Y. Gurevich, Semiconductor Photoelectrochemistry, Consultants Bureau, New York, 1986.

20. A. J. Leenheer, A. Miedaner, C. J. Curtis, M. F.A.M. van Hest, and David S. Ginley, Journal of Materials Reserach, 22 (2007) 681-687.

21. J. M. Macak, H. Tsuchiya , S. Berger , S. Bauer , S. Fujimoto , P. Schmuki, Chemical Physics Letters 428 (2006) 421–425.

22. G. K. Mor, O. K. Varghese, M. Paulose, and C. A. Grimes, Advanced Functional Materials15 (2005) 1291-1296.

23. W. Schockley and H. J. Queisser, J. Appl Phys. 32(3) (1961) 510-519

24. Bak, T.; Nowotny. J.; Rekas, M.; Sorrel, C. C. Int. J. Hydrogen Energy 2002, 27, 991-1022.

25. R. E. Rocheleau and E. L. Miller, International Journal of Hydrogen Energy, 22 (1997), 771-782.

26. M. C. Hanna and A. J. Nozik, Journal of Applied Physics, 100 (2006) 074510-1-8.

27. J. Brillet, M. Cornuz, F. Le Formal, J. Yum, M. Gratzel, and K. Sivula, Journal of Materials Research, 25 (2010) 17-24.

CHAPTER 5
OTHER MATERIALS FOR PEC CELLS

5.1 INTRODUCTION

Along with TiO_2 two other semiconductor oxides have been widely investigated for photoelectrochemical water splitting. Tungsten trioxide (WO_3) and iron oxide (hematite, α-Fe_2O_3) have a relatively narrow bandgap, 2.6-2.8 and 2.0-2.3 eV respectively [1]. These materials are ideally capable to split water using visible light, and they have sufficient resistance against corrosion and photocorrosion in aqueous solutions [1,2]. Calculated theoretical maximum STH efficiency as a function of the material bandgap (assuming 100% faraday efficiency) has given 15 % and 6 % for α-Fe_2O_3 and WO_3 respectively, compared to ~ 1 % for TiO_2 [3]. However, these oxides have disadvantages as well that limit their use on PEC cells. Ferric and tungsten oxide have relatively slow charge transfer kinetics and high rate of hole-electron recombination resulting in low conversion efficiencies [5]. In both oxides the conduction band is more negative than the redox potential for hydrogen reduction [6,7] therefore it needs external bias to start the oxidation of water.

To overcome these disadvantages WO_3 and Fe_2O_3 have been combined (doped) with other metals showing increase in photocurrent production. WO_3 films doped with transition metal, such as Pt, Ru, Ni, Co, Cu and Li have been extensively study [5, 8].

The effect of doping α-Fe_2O_3 thin-films with Ti, Al, Sn, Pt, Ni, In, Cr has been reported [1]. TiO_2 has also been combined with WO_3 and Fe_2O_3 in a solid solution aiming to reduce the bandgap of the final oxide system [9,10]. In addition, WO_3 and Fe_2O_3 have been reported to be a good alternative in combination with solar cells in a tandem PEC cell [11-13].

Iron oxide in the hematite phase with different particle structures have been reported [6,14-19]. Misra [16,17] and Grimes [18,19] groups have shown that anodization in acidic organic electrolytes produce order vertical nanotubes of iron oxide. Current densities up to 1.2 mA/cm^2 have been reported when these nanotube films were used as photoanodes. Gratzel [6] group reported currents up to 2.6 mA/cm^2 using dendritic nanostructured a-Fe_2O_3.

Early anodization experiments were conducted testing both metals. Oxide nanotube structures were only obtained with Fe by making minor changes to the method used for the fabrication TiO_2 nanotubes. Based on the latter results and due to the lower bandgap of iron oxide, this metal was chosen as a potential alternative to TiO_2 for the fabrication of photoanodes. This chapter describes details regarding material fabrication and characterization, as well as performance evaluation of photoanodes based on iron oxide (hematite phase, α-Fe_2O_3). The results presented in this chapter are preliminary experiments that can lead to further investigation for future investigation.

5.2 EXPERIMENTAL

Iron oxide nanotube (FeNT) films were made using the anodization process [10, 14-20]. The technique had to be modified from the original used for Ti anodization. In

addition, gold nanoparticles were loaded onto the surfaces of the FeNT to study the influence of the metal nanoparticles on the photocatalytic performance of hematite. The details of the methods and procedures for the fabrication and characterization of FeNT films are described in following section.

5.2.1 Iron Oxides Nanotube Fabrication

An anodization method was used to fabricate vertically ordered iron oxide nanotubes [14-22]. The electrolyte used was a solution mixture of 0.3wt% ammonium fluoride (NH_4F, Sigma Aldrich, 98+%) in 98 wt% ethylene glycol (Fisher, less than 0.2 wt% H_2O) and balanced with deionized water.

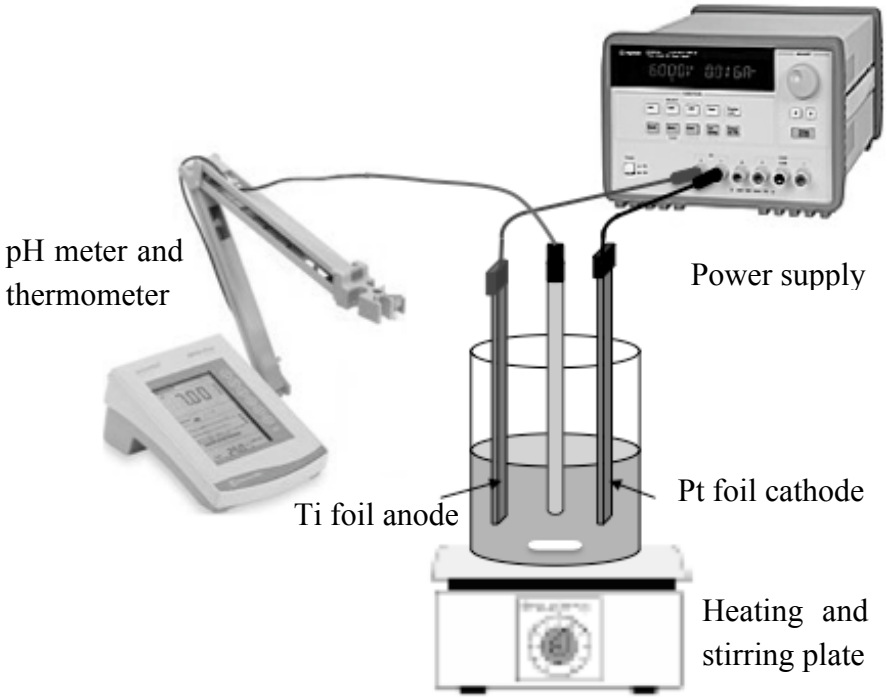

Figure 5.1: Schematic depiction of the two-electrode anodization cell used to fabricate iron oxide nanotubes (FeNT) films.

The anodization was carried out in a two-electrode cell (Figure 5.1), with a Fe foil as anode and Pt foil as the cathode. The iron foils (Alfa Aesar 99.7% purity, 0.127 mm

thickness) were cut into 2.5 × 0.8 cm^2 pieces. The metal surfaces were cleaned by sonicating the metal pieces in ethanol, then acetone and finally water for 10 minutes each time. Then, the foils were dried in air for 30 minutes at 90 °C. The electrodes were connected to a power supply (Agilent, E36474, maximum voltage 60V), and the voltage was increased to a final value that was varied between 20 and 60V. The rate at which the voltage was increased was varied between 0.1-0.01 V/s, and then held at the final potential for a defined period of time. The electrolyte was continuously magnetically stirred. The final potential, anodization time and the electrolyte temperature were varied to study the influence of these parameters on the final structure and dimensions of the nanotubes.

After anodization, the samples were rinsed in ethanol and then dried under vacuum at 90 °C for 30 minutes. Finally, the FeNT films were calcined to remove remaining organic compounds and to crystallize the samples.

5.2.2 Gold Loading on FeNT films

The modified deposition-precipitation method (refer to section 2.2.5) was employed to support Au nanoparticles on FeNT films [23-25]. Two concentrations of Au precursor solution ($HAuCl_4 \cdot 3H_2O$ in DI water) were used, 0.5 and 1.0 mg/mL. The foils were continuously spun in water before and after the gold solution was added. The temperature of the solution was maintained at 30-40 °C for 30 minutes. The solution pH was regulated adding small amounts of 0.01 M Na_2CO_3 solution. After adding the Au precursor solution, the temperature of the loading solution was maintained at 40 °C for 1 h. After the deposition of Au, the substrates were rinsed various times by spinning the

film in clean DI water for 30 minutes, then transferred to a vacuum (-25 psi) oven maintained at 80 °C and dried overnight.

5.2.3 Material Characterization

The bulk characterization of the FeNT films was carried out using SEM and XRD, in similar way done for TiNT and depicted in section 2.3.1.

ICP OES was used to determine the Au loadings. The gold content in the nanotube films was estimated by measuring the gold remaining in the solution after the loading. Approximately 2 mL of the left solution was added to a test tube and diluted with DI water to a 1:7 dilution factor. This mixture was analyzed for Au content using the ICP spectrometer. The amount of Au loaded on the FeNT films was calculated based on the difference between the concentration before and after deposition.

The PZC of the iron oxide was calculated using the potentiometric mass titration method. FeNT powders (peeled from the substrate and grained, S_{BET} = 20 m^2/g) were used. About 28 mg of the oxides were suspended in 6 mL of DI water at ambient temperature for 20 h to reach an equilibrium pH value. Small volume of Na_2CO_3 (0.01 M) and H_2SO_4 (0.01 M) solution were added to protonate and deprotonate the iron oxide solution. The initial and final pH values were recorded in each case.

5.2.4 Performance Characterization

Photoelectrochemical performance evaluations were carried out in a 3-electrode cell, as shown in Figure 3.3. In this cell the photoanode (working electrode) was the FeNT film, the cathode was a Pt foil, and the reference electrode used was and a Hg/HgO. The electrolyte was a 1M KOH solution saturated with UHP N_2 gas. Linear sweep

voltammetry and cronoamperometry measurements were done using a potentiostat. The experiments under illumination were done using simulated sunlight. The i_{ph}-V characteristic curves were calculated using the geometric area (in contact with the electrolyte) of the photoanode. The open circuit voltage in the dark and under illumination was measured using a multimeter. The photoelectrodes were made in a similar manner as described in section 3.2.1. The excess surface of the film was covered with white enamel, leaving a small uncovered area of ~ 0.3 cm^2.

5.3 RESULTS AND DISCUSSION

Anodization of iron foils in fluoride solution resulted in the formation of vertically ordered nanotubes. The method was slightly modified from the TiNT recipe used earlier. Similarly to the results seen in titania nanotubes, the anodization parameter influenced the nanotube dimensions and structure. The FeNT films were decorated with nanocrystalline gold particles to study the effect of the metal on the overall photocatalytical performance of the Au/FeNT composite. In addition, the electrolyte temperature had a crucial role in the formation and structure of FeNTs. These results along with photoelectrochemical evaluation outcomes are highlighted in this section.

5.3.1 FeNT Fabrication

The iron oxide nanotubes growth mechanism was as a competition between an electrochemical oxide formation and a chemical dissolution of the oxide by the fluoride ions [10,15,21,22] similar to the TiNT. The nanotubes achieved had very delineated cylindrical-shape walls and semispherical closed bottoms. The film surface changed color

during the electrochemical process from light yellow to dark red depending on the voltage used and the film thickness.

5.3.1.1 Influence of the Anodization Parameters

Nanotubes only started to grow at potentials equal or higher than 20 V. Furthermore, the formation of nanotubes depended not only on the applied potential but also on the rate of at which the potential was raised. For instance, for a final voltage of 30 V, when the rate was 0.5 V/s no nanotubes were observed. Figure 5.2 shows a SEM micrograph of a Fe foil, which was anodized at 30 V and 1 h and the voltage increment rate was 0.5 V/s. The SEM shows a nanoporous structure, but instead of nanotubes there was a disordered matrix of connected nanorods. Decreasing the voltage ramp to 0.01 V/s lead to the formation of nanotubes smooth nanotubes.

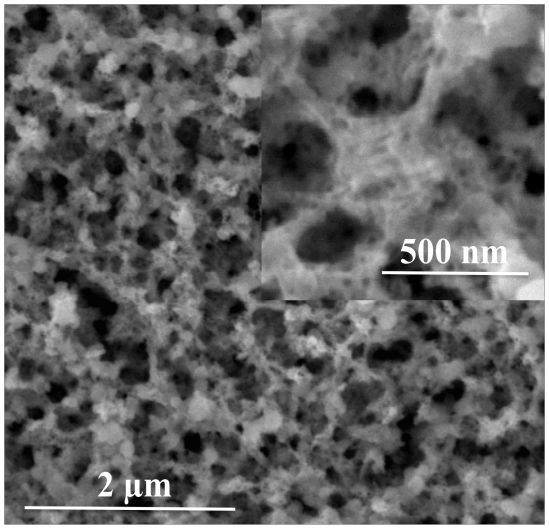

Figure 5.2: SEM micrograph for an as-anodized iron foil prepared using 30V voltage for 1 h and a voltage ramp of 0.1 V/s. The inset is a close up illustrating details of the nanoporous structure. The anodization was accomplished at room temperature (23 °C).

Similarly to the titania nanotubes formation, FeNTs dimensions depended on the anodization time and voltage. While longer periods of anodization increased the nanotube length almost linearly, the diameter depended on the applied voltage. However, anodization times longer than 1 h did not increase the nanotube length for anodization potentials higher than 40 V.

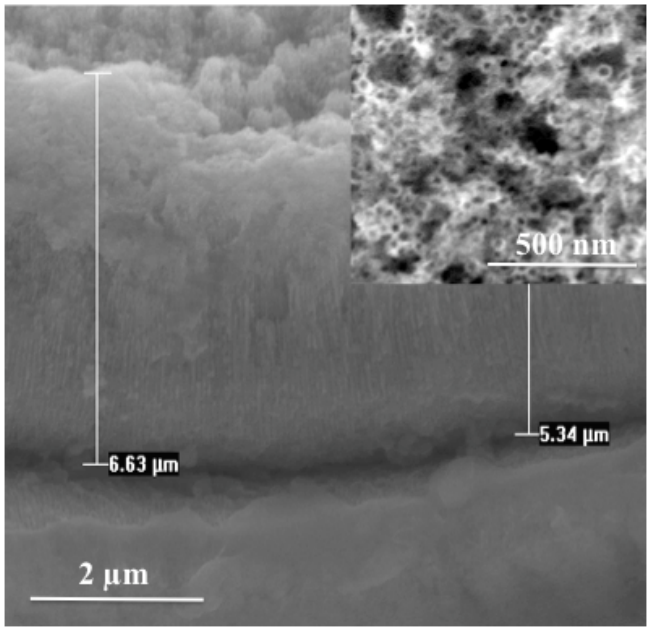

Figure 5.3: SEMs of as-prepared iron foil anodized using 30V for 1 h. The anodization voltage was increased by 0.01 V/s. The inset shows a top view of the FeNTs. The anodization was performed at room temperature (23 °C).

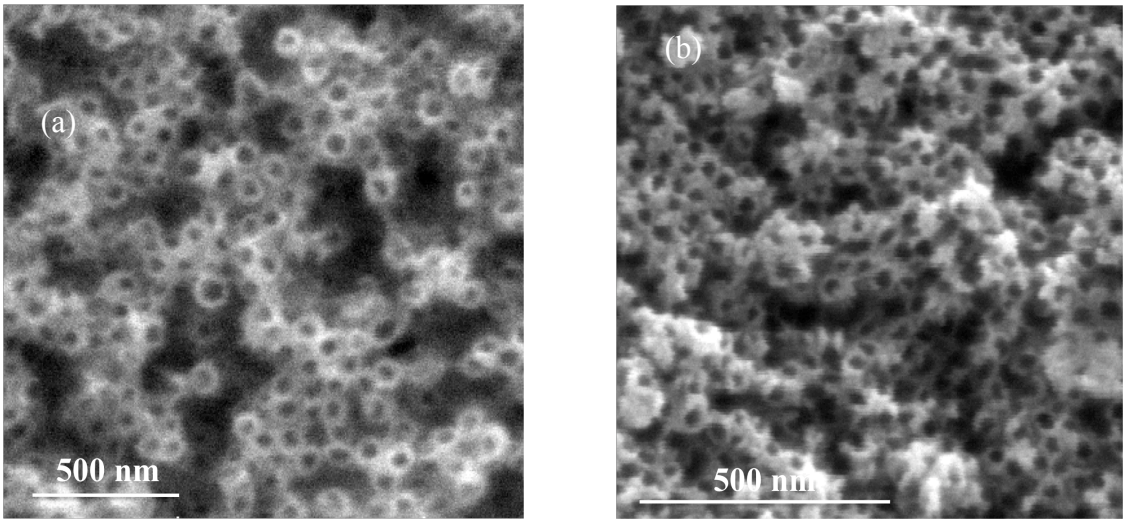

Figure 5.4: As-anodized FeNT films at applied voltage (a) 30 V and (b) 60 V. The average ODs for these samples were 60 and 120 nm.

The temperature of the electrolyte influenced the formation of iron oxide nanotubes [16-19]. For the same voltage, increasing the electrolyte temperature from room temperature (23 °C) up to 60 °C decreased the anodization time to almost half. In both cases nanotubes with similar lengths were achieved. The faster growth of the FeNTs was due to an increase in current densities. For 30 V applied voltage the current density went from ~ 30 mA/cm^2 at room temperature to ~ 60 mA/cm^2 at 60 °C. The features of the nanotubes (i.e. diameters and walls) were smoother and more demarcated when the electrolyte was heated at least 40 °C (Figure 5.5). However, at electrolyte temperatures higher than 60 °C (for any anodization voltage between 20 and 60 V) the iron foil corroded in short period of times to later disintegrate in the electrolyte solution.

The former results aided in the identification of the optimal settings for FeNT fabrication. Thus, the following recipe was used for the rest of the experiments: 40 V applied voltage (which gave nanotubes with *OD* of ~ 100 nm), 1 h anodization time (giving nanotube length of L ~ 5 μm) and ~ 40 °C electrolyte temperature.

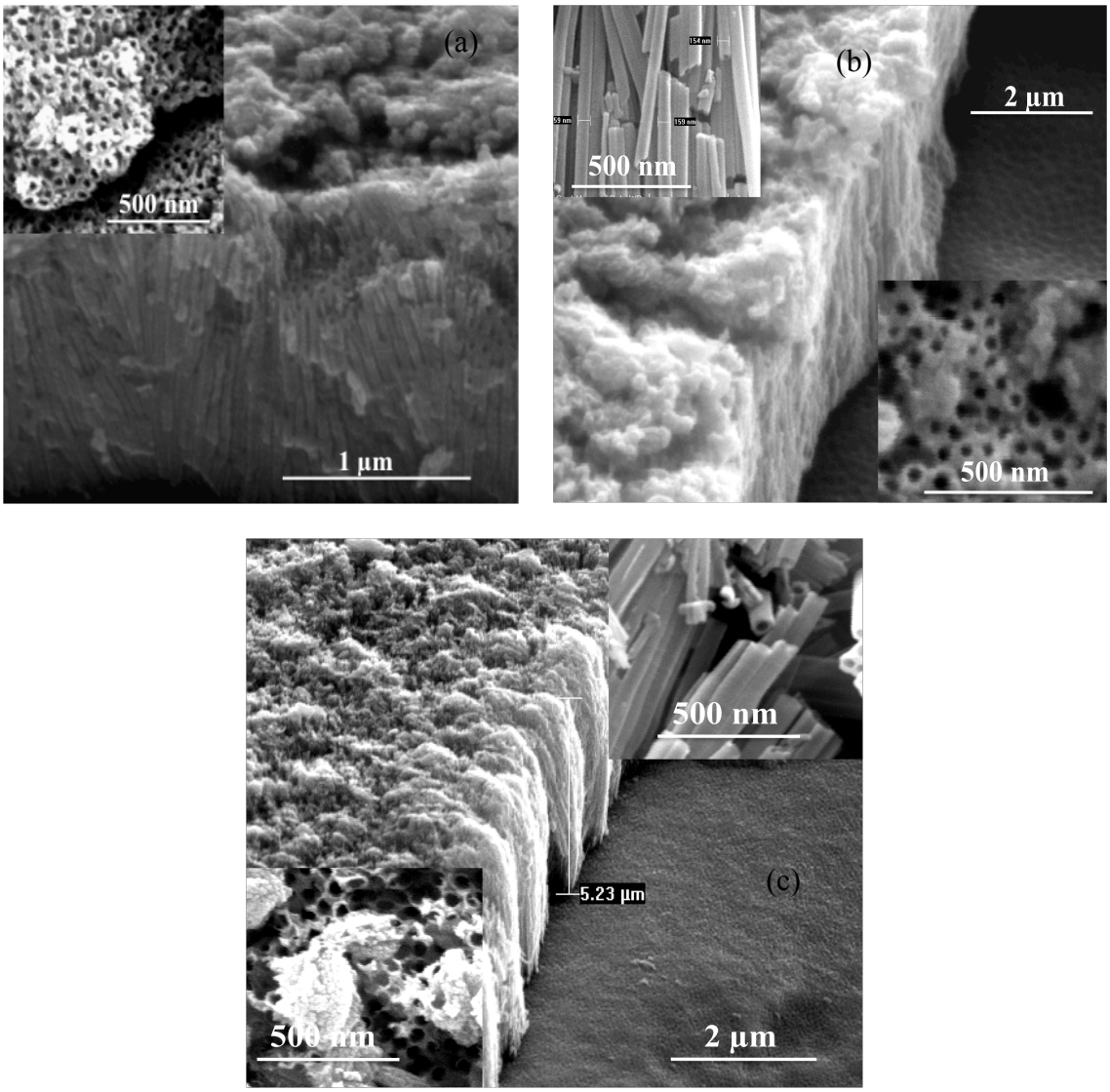

Figure 5.5 SEM micrographs for iron oxide nanotubes anodized using 40 V for 1 h. The temperature of the electrolyte was (a) 23 °C, (a) 40 °C and (a) 60 °C. The electrolyte employed was 98 wt % ethylene glycol mixed with 0.3wt% NH_4F and balanced with DI water.

5.3.1.2 Thermal treatment

The photoelectrochemical properties of iron oxide depend on its structure and crystalline phase. Hematite (α-Fe_2O_3) is the phase of iron oxide preferred for photocatalytic reactions [6,8,16-28].

The as-prepared FeNT films were amorphous in nature, and crystallinity was

obtained by high temperature calcination. X-ray diffraction patterns for TiNTs are shown in Figure 5.6. The XRD plots indicated that the as-prepared FeNT were amorphous, and strong characteristic peaks for Fe metal were observed. Thermal treatments above 300 °C started to convert the amorphous film into hematite, and further oxidize the iron metal under the nanotube film (substrate). The XRD results and the outcomes from thermal gravimetric analysis (TGA) suggested that the calcination temperature should be set to ~ 450 °C to convert most of the nanotubes into hematite. At temperatures higher than 450 °C conversion of the films into magnetite was observed. The FeNT film thickness was ~ 5 μm, because of this Fe peaks were still detected in the XRD patterns even after calcination at 500 °C.

5.3.1.3 Gold Loading

Gold nanoparticles were loaded onto FeNT surface by the deposition-precipitation method. As mentioned previously (section 2.4.4) the DP method works best for supports with a PZC higher than 5. According to the literature the PZC of hematite varies between 6.5 and 8 [29]. Therefore, Au should be able to get deposited on the surface of the iron oxides nanotubes using DP. The solution pH was varied in order to change the Au loading and metal particle size. Ideally, a pH lower than the PZC should give bigger particle sizes; while pH above but still close to the PZC should give higher loading with smaller particles; and pH much higher than the PZC could lead to smaller particles but lower loadings.

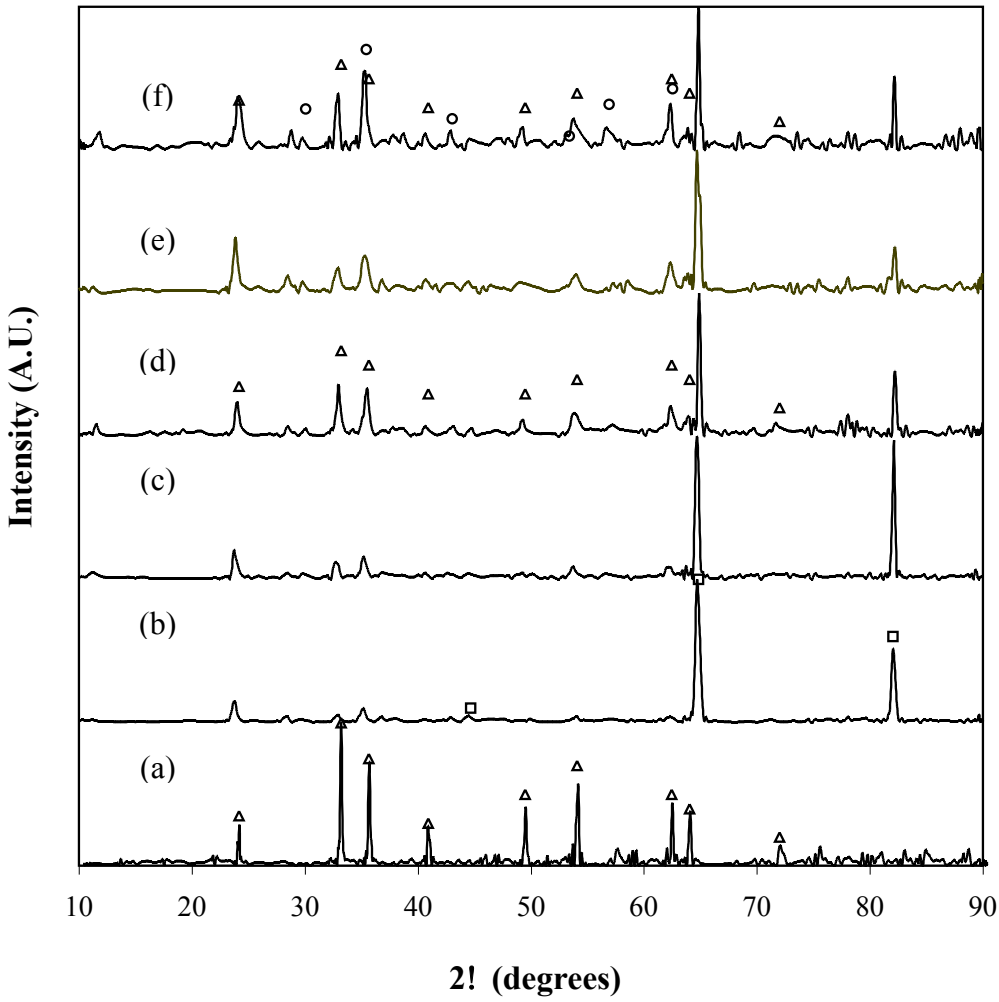

Figure 5.6: XRD patterns for (a) iron oxide (hematite) powder and FeNT films calcined at different temperatures (b) as-prepared, (c) 250 °C, (d) 350 °C, (e) 450 °C, and 500 °C. Calcination was accomplished in air for 1h. The symbols represent (Δ) hematite, (□) iron metal, and (o) magnetite.

Initially 1 mg of Au precursor (1 mg/mL) was added to the FeNT films. The iron oxide mass in the film was 4 mg, which should give a maximum Au loading of ~ 13 wt%. Figure 5.7 illustrates Au loading as a function of solution pH. The maximum loading (which is very close to the ideal) was achieved at lower pH. This indicated that at this pH most of the Au presented deposited on the FeNTs. The solution pH was varied from 5 to 10, which changed the amount of metal deposited. Lower pHs led to the agglomeration of

the metal making big particles and giving high loading. Raising the pH decreased the Au loading but the particles were still quite large, and they were detected under XRD (crystallite sizes were calculated to be ~ 25 nm, Figure 5.8).

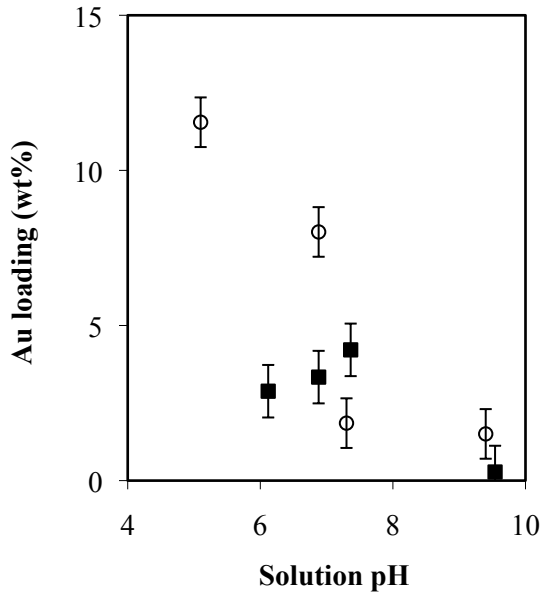

Figure 5.7 Gold loadings for Au/FeNT film photocatalysts. The mass of Au precursor added to the films were (o) 1 mg and (■) 0.5 mg. The nanotube dimensions were L ~ 5 μm and OD ~ 100 nm.

The volume and concentration of the Au precursor added during the deposition was decreased (1 mL of 0.5 mg/mL), which gave an Au mass of ~ 0.25 mg. This amount should give a maximum Au loading of ~ 6 wt%. In fact, this modification resulted in lower Au loadings and smaller particle sizes (Figure 5.7). The maximum gold uptake was reached at pH ~ 7.3, giving 4.2 wt%. No characteristic Au peaks were detected by XRD, which could indicate that the Au particles were smaller than 15 nm (detection limit of the diffractometer).

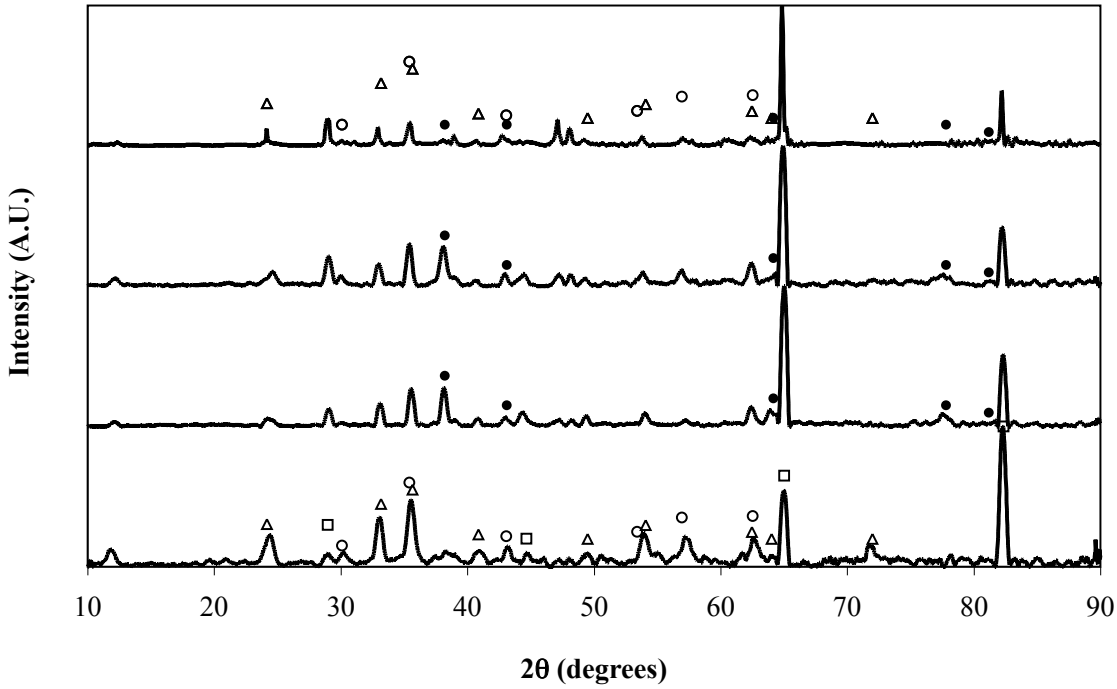

Figure 5.8: XRD diffraction patterns for (a) FeNT and Au/FeNT Au loaded at solution pH of (b) 5.1 and (c) 7.3 the mass of Au added was 0.5 mg; and (c) pH 7.5 and Au mass 0.25 mg. The symbols indicate (∆) hematite, (o) magnetite, (□) Fe metal and (•) Au metal.

These results led to establish the best conditions for Au loading on hematite nanotubes for the rest of the experiments. On the other hand, actual Au particle sizes measurements for Au/FeN photocatalysts have not been done in this work. A more detailed study of the variation on particle sizes needs to be done and it will be suggested as future work.

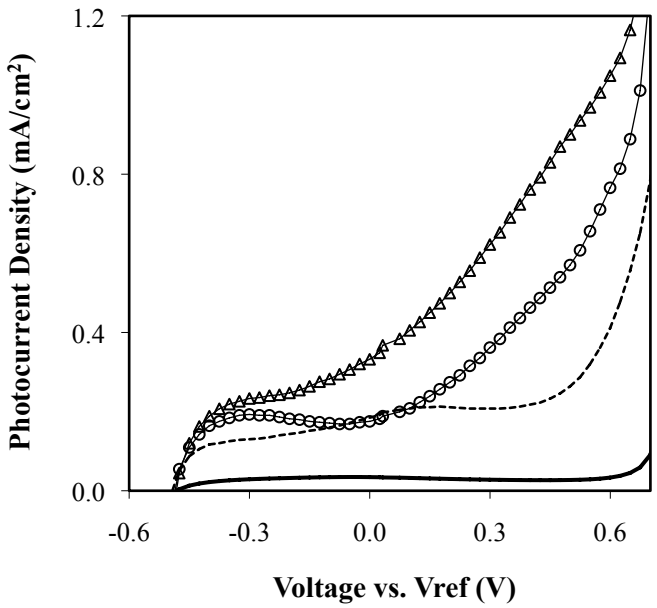

Figure 5.9: Photocurrent-voltage characteristics plots for iron oxides nanotube in the (−) dark and under illumination of simulated sunlight. FeNT were fabricated using 40 V for 1h and the electrolyte temperature was (---) 23 °C, (o) 40 °C and (Δ) 60 °C.

5.3.2 Performance Evaluation

5.3.2.1 Iron Oxides Nanotubes Performance as Photoelectrodes

The FeNT films were used to construct photoelectrodes, which were later photoelectrochemically tested in a 3-electrode cell. Figure 5.9 illustrates the photocurrent-voltage curves for different FeNT photoanodes in the darkness and under simulated sunlight. All the FeNT films shown in this figure were anodized at 40 V, however the electrolyte temperature was not the same. The dark current (for the sample anodized at room temperature) was negligible up to about 0.65 V (vs. Hg/HgO) where electrocatalytic oxygen evolution occurs indicated by a rapid increase in current. The photocurrent under illumination rose at around zero voltage for the film anodized at room temperature and -0.3 V for electrodes made at 40 and 60 °C. The nanotubes fabricated at

60 °C gave the highest i_{ph} value. Under light the photocurrents did not reach saturation, because the electrocatalytic oxidation of water starts around 0.5 V (electrolyte pH = 13.2) and dominates the current production.

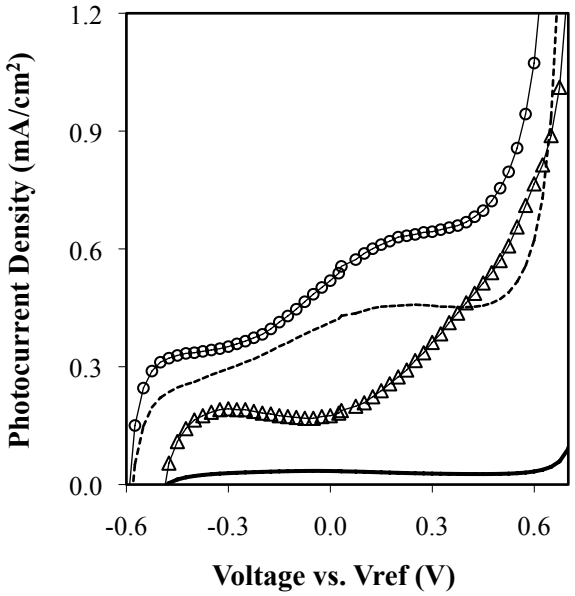

Figure 5.10: Photocurrent versus voltage plots for a FeNT and an Au/FeNT photoanodes. Anodization was done at 40 V for 1h and 40 °C electrolyte temperature. (−) Dark and under simulated sunlight (∆) FeNT, (---) Au/FeNT with 0.4 wt% Au, (o) Au/FeNT with 4.1 wt% Au. The nanotube dimensions were L ~ 5 μm and OD ~ 100 nm.

5.3.2.2 Au/FeNT photocatalyst

An increament in photocurrent (which leads to an increase in hydrogen production) of ~75 % was shown earlier (section 3.3.4) when Au nanoparticles were added to TiNT films. This enhancement was attributed to modification in optical properties (apparent E_g reduction) and the increased photocatalytic activity in the Au/TiNT system. These results led to the investigation of Au loaded onto FeNT films, with the expectation of obtaining similar results.

Figure 5.10 shows i_{ph}-V plots for FeNT and Au/FeNT photoanodes. The photogenerated current densities for the Au/ FeNT compared to the values for FeNT until water electrocatalytic oxidation started (~ 0.5 V vs. Hg/HgO). These results suggested that the inclusion of Au nanoparticles have modified the photoelectrochemical properties of FeNT. It can be speculated that the metal nanoparticles suppressed recombination of charge carriers by helping in the separation of electrons. Nanoscale gold particles could generate active sites for water oxidation on iron oxide. Furthermore, the light absorption might have also been upgraded by the addition of Au, which could had enhanced the photocurrent production.

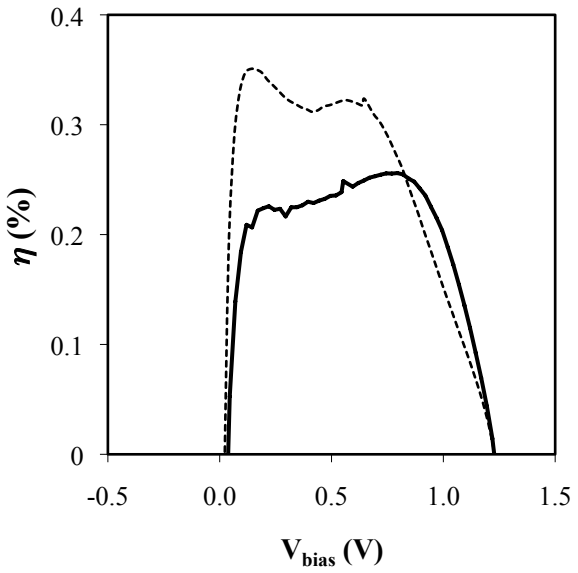

Figure 5.11: Diagnostic efficiency as a function of applied bias voltage plots for (−) FeNT and (---) Au/FeNT with 4.1 wt% of gold.

Figure 5.11 illustrates the diagnostic efficiencies for FeNT and Au/FeNT photoanodes. These efficiencies were calculated using data collected in a 2-electrode cell (working electrode: FeNT, cathode: Pt, 1 M KOH). The addition of gold to hematite

nanotubes increased the photoanode performance in 30% compared to the values for photoelectrodes with pure hematite.

5.4 SUMMARY AND CONCLUSIONS

The fabrication and characterization of the photocatalyst materials, FeNT and Au/FeNT, as well as their performance were presented.

Highly ordered α-Fe_2O_3 nanotubes were fabricated using the anodization process. The dimensions of the FeNTs depended on the anodization parameters, and the nanotube features depended more on the electrolyte temperature. The as-prepared amorphous nanotubes were calcined in air, at 450 °C for 1 hour to convert the film into hematite phase. Higher calcination temperatures led to the formation of the magnetite phase.

The most advantageous condition for the loading of gold nanoparticles onto α-Fe_2O_3 was obtained for solution pH in the range of pH 7-8, which corresponds to the point of zero charge for this oxide. The incorporation of Au nanoparticles improved the rates of photocurrent production in FeNT films. The highest efficiency observed among all the FeNT photoelectrodes fabricated was ~ 3.5 %, which corresponded to the Au/FeNT photoanode with 4.1 wt% Au.

Further study needs to be conducted in order to understand the effects of Au on the optical, electrical and electrochemical properties of hematite. TEM studies need to be done in order to find the Au nanoparticle size distribution. Studies regarding the influence of Au particle loading and size on the performance of the photocatalyst are suggested for future wok. Optical transmission or total reflection measurements should be performed to

calculate the bandgap of FeNT and Au/FeNT. The latter can aid to find if Au nanoparticles change the E_g of the Au/FeNT system.

5.5 REFERENCES

1. A. Luzzi, Photoelectrolytic Production of Hydrogen, IEA Agreement on the Production and Utilization of Hydrogen, IEA/H2/TR-02/ 2004.
2. C. Santato, M. Ulmann, and J. Augustynski, Advanced Materials 13 (2001) 511-514.
3. Z. Chen, T. F. Jaramillo, T. G. Deutsch, A. Kleiman-Shwarsctein, A. J Forman, N. Gillard, R. Garland, K. Takanabe, C. Heske, M. Sunkura, E. W. McFarland, K Domen, E. L. Miller, J. Turner, H. N. Dinh, Journal of Materials Research 25 (2010) 3-16.
4. M. Radecka, P. Sobas, M. Wierzbicka, and M. Rekas, Physica B, 364 (2005) 85-92.
5. J. C. Sartoretti, M. Ulmann, B. D. Alexander, J. Augustynski, and A. Weidenkaff, Chemical Physics Letters 376 (2003) 194-200.
6. A. Kay, C. Ilkay, and Michael Gratzel, Jounral of the American Chemical Society. 128 (2006) 15715-21.
7. A. Kokorin, and D. Bahnemann (Eds.), Chemical Physics of Nanostructured Semiconductors, Utrecht: Boston, MA, 2003, 83-110.
8. W. B. Ingler, and S. U. M. Khan, International Journal of Hydrogen Energy 30 (2005) 821-827.
9. B. Tryba, M. Piszcz, and A. W. Morawski, International Journal of Photoenergy, 7 (2009) 29731-9.
10. G. K. Mor, H. E. Prakasam, O. K. Varghese, K. Shankar, and C. A. Grimes, Nano Letters 7 (2007) 2357-63.
11. E. L. Miller, R. E. Rocheleau, and S. Khan, International Journal of Hydrogen Energy, 29 (2004) 907-914.
12. E. L. Miller, D. Paluselli, B. Marsen, R. E. Rocheleau, Solar Energy Material & Solar Cells 88 (2005) 131-144.
13. Heli Wang, Todd Deutsch, and John A. Turner, Journal of The Electrochemical Society, 155 (2008) F91-F96.
14. G. K. Mor, O. K. Varghese, M. Paulose, K. Shankar, C. A. Grimes, Solar Energy Materials and Solar cells 90 (2006) 2011-2075.
15. J. Macak and P. Schmuki, Electrochimical Acta 52 (2006) 1258–1264.
16. R. R. Rangaraju, A. Panday, K. S. Raja and M. Misra Journal of Physics D: Applied Physics 42 (2009) 135303-135310.
17. R. R. Rangaraju, K.S. Raja, A. Panday, M. Misra, Electrochimica Acta 55 (2010) 785–793.
18. T. J. LaTempa, X. Feng, M. Paulose, and C. A. Grimes, Journal of Physical Chemistry C 113 (2009) 16293–16298.

19. H. E. Prakasam, O. K. Varghese, M. Paulose, G. K. Mor and C. A. Grimes, Nanotechnology 17 (2006) 4285–4291.

20. P. Aurora, P. Rhee, L. Thompson, Journal of the Electrochemical Society 157 (2010) 152-155.

21. A. Ghicov and P. Schmuki, Chemical Communications (Cambridge, United Kingdom) 2009, 2791-2808.

22. J. M. Macak, H. Hildebrand, U. Marten-Jahns, and P. Schmuki, Journal of Electroanalytical Chemistry 621 (2008) 254–266.

23. G. C. Bond, C. Louis, and D. T. Thompson (Eds.) Catalysis by Gold; Catalytic Science Series, v. 6, Imperial College Press, London, 2006.

24. D. Andreeva, T. Tabakovaa, V. Idakieva, P. Christova, and R. Giovanoli, Applied Catalysis A: General 169 (1998) 9-14

25. A. M. Visco, A. Donato, C. Milone and S. Galvagno, Reaction Kinetics. Catalysis Letters 61 (1997) 219-226.

26. A. Watanabe and H. Kozuka , Journal of Physical Chemistry B 107 (2003) 12713-12720.

27. V. M. Aroutiounian, V. M. Arakelyan , G. E. Shahnazaryan, G. M. Stepanyan, John A. Turner and O. Khaselev, International Journal of Hydrogen Energy 27 (2002) 33–38.

28. C. J. Sartoretti, M. Ulmann, B. D. Alexander, J. Augustynski, A. Weidenkaff Chemical Physics Letters 376 (2003) 194–200.

29. M. Kosmulski, Journal of Colloid and Interface Science 298 (2006) 730–741.

CHAPTER 6
SUMMARY, CONCLUSIONS, AND RECOMMENDATIONS FOR FUTURE WORK

This research provided a study and analysis of various photoelectrochemical cells for the production of hydrogen from water using solar light. The influence of the TiO_2 photocatalyst structure and phase on the production rates was evaluated. The addition of active metal nanoparticles to TiO_2 to increase water oxidation rates was analyzed and discussed as well. PEC cells in hybrid configurations were investigated; these hybrid cells were fabricated using solar cells and catalysts for water splitting. Finally, an alternative material to titania was examined. A brief summary of these results along with concluding remarks and suggestions for the future direction of this research are provided in this chapter.

6.1 SUMMARY AND CONCLUSIONS

Titanium dioxide is the most studied material for photoelectrochemical water oxidation. TiO_2 is very stable against corrosion and photocorrosion in aqueous solution in a wide pH range [1]. Its conduction and valence band are located in the correct position with respect to the water oxidation potential and allow it to split water. In addition, it is inexpensive compared to other photovoltaic materials. In spite the latter advantages,

commercial nanoparticulate TiO_2 powders suffer from low photoelectrochemical efficiency for water oxidation [2]. This is due to its large bandgap, which only permits the usage of the UV portion of the solar spectrum [3-5]. The structure of the particles in powder TiO_2 allows recombination of the photogenerated electrons and holes [6]. Furthermore, TiO_2 alone it is not a good photocatalyst for water oxidation. Therefore, three strategies have been used in this work to improve PEC performance:

- Production of the photocatalyst in the form of nanotubes to improve collection efficiencies.
- Incorporation of nanocrystalline gold onto the nanotubes to improve the water oxidation activation.
- Utilization of a photovoltaic cell in conjunction with the photocatalyst in a multijunction hybrid PEC.

Different methods for the fabrication TiO_2 with different structural characteristics (i.e. high surface area, different particle structures) have been employed. High surface area titania in powder forms were fabricated by the precipitation of $TiCl_4$ (powder) and hydrothermal method (short disordered nanotubes). The dimensions of the nanosized structures and thus the surface areas changed with high temperature treatment in air enviroment. In addition, highly ordered TiO_2 nanotubes were fabricated using the anodization process. The dimensions of the TiNTs strongly depended on the process parameters. In order to obtain longer and smoother nanotubes organic solvents were used in combination with low concentrations of fluoride ions. The nanotube length was mainly a function of the anodization time, while the applied voltage governed the diameter of the nanotubes [7-10]. The nanotube films were thermally treated to obtain the desired anatase

crystalline phase. At temperatures between 450 °C and 550 °C the nanotube walls remained structurally intact in the anatase phase, whereas at temperatures higher than 750 °C the structure of the nanotubes started to transform and finally collapsed at temperatures higher than 850 °C.

Gold nanoparticles were loaded onto the titania surfaces using the deposition-precipitation method. For powder Au/TiO_2 the optimal conditions were at pH between 8-10. At this range the highest metal loading and smallest particles sizes were obtained, as reported in the literature [11-13]. Conversely, the deposition of gold on TiNT surfaces was different from the deposition of gold on powders. The optimal condition for Au/TiNT was obtained when the pH was in the range of pH 6-7, which corresponded to the PZC for titania.

Gold nanoparticles smaller than 8 nm decreased the E_g of TiO_2. This reduction was in the order of 0.2 eV, and it depended on the Au loading and particle size. It was speculated that this reduction could have been a consequence of the addition of surface states between the band edges of TiO_2, and reductive modification of TiO_2. These two phenomena could have occurred during the preparation of the photocatalyst (i.e. gold loading, thermal treatment). Gold particles bigger than 8 nm and up to 50 nm in diameter were found as well in some Au/TiNT samples. These larger metal particles can absorb light due to surface plasmon resonance exciting electrons that can later be transfer to the conduction band of TiO_2. The wavelength of the photons absorbed depends on the Au particle size. Thus, the addition of Au nanoparticle appears to enhance the collection of light in the visible region.

Several photoanodes were fabricated using the various photocatalysts fabricated; these electrodes were photoelectrochemically tested in a 3-electrode cell. The photocurrents produced by powder titania photoelectrodes were hindered by recombination and poor photocatalytic performance. The i_{ph} were less than 0.1 mA/cm^2. This low production can be the consequence of poor charge separation and high recombination losses during photoelectrochemical testing. Electrons are transferred to the back contact of the photoelectrode by trapping and detrapping events and crossing grain boundaries. In this process many of these electrons get recombined with holes before they can be used for water oxidation. Changing the structure of powdered titania from spherical to short (and disordered) nanotubes boosted the production of photocurrents. There was an increase in i_{ph} of 50% in current production. It appears that the structural dimensions and shape of the nanotubes improved the separation of carriers and reduced recombination.

Conversely, the usage of longer and highly ordered TiO_2 nanotubes further improve the photoelectrochemical performance of the photoanode. One order of magnitude increase in photocurrent was observed when 15μm-long TiNTs were used instead of power-based photocatalyst. The smooth and straight path that electrons follow in the nanotubes upgraded the separation and transport of charge carrier limiting recombination. The larger surface areas of these nanotubes enhance the light collection. The photocurrent produced increased, as the nanotubes got longer, up to a length similar to the electron diffusion length in TiO_2, which is about 15μm.

The incorporation of Au nanoparticles onto the surfaces of the different titania photocatalysts significantly improved the rates for water oxidation. Their addition

increased the photocurrent densities up to 75% of the original values without the metal. The reported drop in E_g was the cause of ~ 25% of this enhancement. The other 50 % were attributed to amplification in the photocatalytic properties of TiO_2 for water oxidation. Furthermore, as the Au nanoparticle size decreased the photocurrents increased suggesting that smaller metal particles introduced highly active sites to the TiNTs. Some of these additional sites seem to be located at the interface between the metal and the oxide. Besides, during the metal loading point defect might be created on the semiconducting oxide, which can act as active sites for water oxidation. If the potential in the Au-TiO_2 interface is large enough (~ 1 V) water can be decomposed on the surface of the Au nanoparticle increasing the overall performance of the Au/TiO_2 photocatalyst system.

The efficiencies for the single bandgap TiO_2 PEC cells were calculated using the current and voltages recorded using a 2-electrode cell (no reference electrode) [14-16]. Due to their low V_{oc} (highest value 1.2 V) the photoelectrodes needed external bias in order to produce H_2. Thus, the efficiency calculated was the so-called diagnostic efficiency. Changing the structure of the photocatalyst from spherical particles to highly ordered nanotubes increased the efficiency one order of magnitude. The highest efficiency recorded for these single bandgap photoelectrodes was 1.1 ± 0.2 %, which corresponded to the Au/TiNT photoelectrode.

Hybrid PEC cells combine a semiconductors with different bandgaps in a single monolithic cascade device. In a hybrid PEC cell, the top layer absorbs the visible light spectra and also catalyst the reaction (photocatalyst), and the bottom junctions would absorb the lower energy photons to give the extra voltage for water decomposition [17].

Photovoltaic cells with different efficiencies were combined with a water oxidation catalyst (Pt/Carbon black) and a photocatalyst (titanium dioxide nanotubes) for form a multijunction PEC system.

The combination of highly efficient (triple junction $GaInP_2$/GaAs/Ga solar cell) solar cells with a very active water oxidation catalyst (Pt) gave a STH efficiency in excess of 14%. Simulated results for Pt catalyst in conjunction with a triple junction Si solar cell shown STH efficiency in the order of 5 %. This result suggests that the latter cell could be an alternative configuration for a lower cost PEC cell.

The designed TiNT and Au/TiNT photocatalysts were integrated with Si photovoltaic solar cells to form a hybrid PEC cell. Titania absorbs light in the UV region of the solar spectrum producing photovoltage, as well as catalyzes the oxidation of water. The open circuit potential for the Au/TiNT-SC (V_{oc} ~ 1.2 V) resembles films connected in electric and optical series. However, the cell still needed external bias voltage to outclass overpotentials and to start the OER. This drawback along with the low photocurrent produced limited the performance efficiency of the hybrid cell to ~ 1.6 %. In spite of the low efficiency, the combination of a less expensive photocatalyst and a Si solar cell proved to work in a tandem arrangement.

Ordered α-Fe_2O_3 nanotubes were fabricated using the anodization process and the knowledge learn while working with TiNTs. Thermal treatment in air was used in order to convert the as-prepared amorphous FeNT films into hematite. Gold nanoparticles were loaded onto α-Fe_2O_3 nanotube. This addition seemed to change the photo and electrochemical properties of hematite, which in terms improved the photocurrent to 35% compared to pure hematite nanotubes.

6.2 RECOMMENDATIONS FOR FUTURE WORK

Titanium dioxide nanotubes and its combination with gold nanoparticles have shown to be better photocatalysts than commercial TiO_2 powders. In additon, the usage of hybrid PEC cells, which combine the former photocatalyst and photovoltaic cells, have shown to enhance hydrogen production efficiencies. To further enhance the performance of these PEC cells and avoid the usage of external bias potentials, there are several key areas that warrant further study.

Titanium dioxide nanotube films and their combination with Au nanoparticle have been show to be effective photocatalysts for water oxidation. The fabrication of vertically ordered TiNTs was optimized to obtain nanotube dimension that work best as a photocatalyst. In spite of these promising results, future investigation needs to be done regarding nanotube growing mechanism as well as diffusion of liquids during anodization, Au loading and performance characterization [7-8]. This type of studies will aid the fabrication and design of better photoelectrodes.

Photoelectrodes made with TiNT films were shown to enhance the production of photocurrent due to the better separation and transport of electrons and holes in the nanotubes. However, the open circuit potential for these PEC cells were ~ 0.9 V, which is not enough to start the oxygen evolution reaction. Also, the currents produced are very small due to the low absorption of photons. Doping the nanotubes with carbon or nitrogen might be an option to increase sunlight absorption by red-shifting the bandgap of the oxide [1,2,4-6]. The incorporation of these elements into the lattice of TiO_2 could be done by ion implantation or thermal treatments.

The PEC efficiencies reported in this work were calculated using equation 3.6 and

assuming that the electric current to hydrogen efficiency (Faraday efficiency) was 100%. A direct method of calculating the efficiency of the photoanodes is to collect the hydrogen produced under illumination in a two-electrode cell. Then measure its volume and purity (making sure the volumetric ratio between hydrogen to oxygen is 2 to 1) by an analytical method such as gas chromatography or mass spectrometry. The energy content in the hydrogen gas can be compared to the input solar energy to obtain the solar to hydrogen efficiency [16].

Another way to present the efficiency of a photoanode is to use the incident photon to current efficiency (IPCE). The IPCE is an important diagnostic figure of merit for PEC devices; it describes the photocurrent collected per incident photon flux as a function of illumination wavelength. In a PEC system, IPCE is usually obtained from a chronoamperometry measurement. The current generated by photoanode under with simulated light at various wavelengths is measured. IPCE is an extremely useful number because it yields device efficiency in terms of electrons out per photons in. In the context of PEC water splitting, IPCE describes the maximum possible efficiency with which incoming radiation can produce hydrogen from water, with an implicit assumption that all electrons are used for the evolution of H_2 instead of other by-products or corrosion (100% Faraday efficiency) [15,16].

Electrochemical impedance spectroscopy (EIS) is encouraged to pursue as future work to analyze the kinetic behavior of the PEC cell. This technique measures the impedance of a system over a range of frequencies, and therefore the frequency response of the system, including the energy storage and dissipation properties, is revealed. Often, data obtained by EIS is expressed graphically in a Bode plot or a Nyquist plot [18]. The

latter plot can give you an idea of the type of impedance associated with the PEC cell and can aid finding the electrical equivalent circuit [18-20]. In addition, Mott-Schottky plots (a measurement of capacitance as a function of the applied bias) which is called the) are very useful in a PEC cell. This technique can provide insight regarding the type of semiconductor material being used (n or p type), location of the flat band potential and band bending [16,18,19,21].

Nanocrystalline gold was successfully loaded onto titania nanotubes and the amount of Au and the particle size where varied changing the solution pH. However, the loading mechanism and location and type of the active sites that Au adds to TiNT have not been studied in this work. Further studies should aim to investigate the location of these active sites and also the nature of the Au, whether it is metallic or ionic. Characterization techniques such as in-situ X-ray photoelectron spectroscopy (XPS), X-ray fine structure spectroscopy (XAFS) and X-ray near edge structure spectroscopy (XANES) can be utilized [11-13] for these purposes.

Results presented in this work and in the literature have shown that hybrid PEC can effectively split water [17, 22-24]. Si photovoltaic cell in combination with Au/TiNT photocatalyst (L ~ 5 μm and OD ~ 100 nm) showed promise for a less expensive multijunction PEC cell. However, the former cell did not produce enough potential for water oxidation. Further, the length of the nanotubes was limited to ~ 5 μm, due to the limitation during the metal deposition process. Triple junction photovoltaic solar cell such as Si solar cell in combination with Au/TiNT should be able to produce enough potential to overcome overvoltages and start the OER. The calculated open circuit potential for a triple junction Si solar cell is ~ 1.5 V, this value plus the potential

generated by the Au/TiNT (~ 0.9V) should give a total voltage of ~ 2.4 V, which in turn should be enough for water decomposition. In addition, thicker films of Ti should deposited on the solar cells to obtain longer TiNTs, which in turns could lead to higher photocurrents. In order to avoid deterioration of the multiple bandgap solar cells during thermal treatment of the TiNTs, the anodization process can be slightly modified. Shankar *et al*. have suggested that an initial chemical treatment of the Ti (metal foil or film) with hydrogen peroxide (H_2O_2) and phosphoric acid (H_3PO_4) give nanotubes in the anatase phase after anodization without further calcination [25]. Future work covering these issues is recommended.

Iron oxide and tungsten trioxide have been widely investigated for photoelectrochemical water splitting. These oxides have relatively narrow bandgap, and should be capable to split water using visible light. Their theoretical maximum STH efficiency have been calculated to be 15 and 6 % for α-Fe_2O_3 and WO_3 respectively, compared to ~ 1 % for TiO_2 [16]. However, they suffer recombination and other inefficiencies that do not allow them to directly split water. Preliminary experiments have been done with hemamite nanotubes and Au loaded on FeNTs. These early results suggested that Au/FeNT could be a good option for an effective photocatalyst. Further material characterization needs to be done in order to understand the effect of the oxide structure and gold loading on the performance of the photoanodes. Both α-Fe_2O_3 and WO_3 can also be combined with photovoltaic solar cells in a tandem PEC cell to reach higher STH efficiencies [22-26]. Titanium can be mixed with either Fe or W in a solid solution and this film can be used to grow nanotubes, which should give a mixture of oxides that could have lower bandgap [1,22].

6.3 REFERENCES

1. S. Licht, in: A. J. Bard and M. Stratmann, (Eds.), Solar Photoelectrochemical Generation of Hydrogen Fuel: Encyclopedia of Electrochemistry, Wiley-VCH, Weinheim, Germany, 2002 v. 6, 346-357.
2. N. Lewis and G. Crabtree (Eds.), Basic Research Needs for Solar Energy Utilization, Report of the Basic Energy Sciences Workshop on Solar Utilization, US Department of Energy (2005).
3. Bak, T.; Nowotny. J.; Rekas, M.; Sorrel, C. C. Int. J. Hydrogen Energy 2002, 27, 991-1022.
4. Bak, T.; Nowotny, J.; Rekas, M.; Sorrel, C. C. Int. J. Hydrogen Energy 2002, 22, 19-26.
5. A. Luzzi, Photoelectrolytic Production of Hydrogen, IEA Agreement on the Production and Utilization of Hydrogen, IEA/H2/TR-02/ 2004.
6. A. Fujishima, X. Zhang, and D.A. Tryk, Surf. Sci. Rep., 63, 515 (2008).
7. G. K. Mor, O. K. Varghese, M. Paulose, K. Shankar, C. A. Grimes, Solar Energy Materials and Solar cells 90 (2006) 2011-2075.
8. J. Macak and P. Schmuki, Electrochimical Acta 52 (2006) 1258–1264.
9. P. Aurora, P. Rhee, L. Thompson, Journal of the Electrochemical Society 157 (2010) 152-155.
10. A. Ghicov and P. Schmuki, Chemical Communications (Cambridge, United Kingdom) 2009, 2791-2808.
11. G. C. Bond, C. Louis, and D. T. Thompson (Eds.) Catalysis by Gold; Catalytic Science Series, v. 6, Imperial College Press, London, 2006.
12. Bond, G.C., Louis, C., Thompson, D. T., Eds. Catalysis by Gold; Catalytic Science Series Vol. 6; Imperial College Press: London, 2006.
13. C. H. Kim. 2005. Catalytic and Surface Properties of Nanocrystalline Gold Water Gas Shift Catalysts. In Chemical Engineering. University of Michigan, Ann Arbor, MI.
14. C. Santato, M. Ulmann, and J. Augustynski, Advanced Materials 13 (2001) 511-514.
15. J. R. Bolton, Solar energy 57 (1996) 37-50.
16. Z. Chen, T. F. Jaramillo, T. G. Deutsch, A. Kleiman-Shwarsctein, A. J Forman, N. Gillard, R. Garland, K. Takanabe, C. Heske, M. Sunkura, E. W. McFarland, K Domen, E. L. Miller, J. Turner, H. N. Dinh, Journal of Materials Research 25 (2010) 3-16.
17. A. Kay, C. Ilkay, and Michael Gratzel, Jounral of the American Chemical Society. 128 (2006) 15715-21.
18. A. J. Bard and L. R. Faulkner, Electrochemical Methods, Wiley 2004, p. 226-230.

19. S. Chandra, Photoelectrochemical Solar Cells, Gordon and Breach Science Plublishers 1985, p. 88-103.

20. F. Fabregat-Santiago, G. Garcia-Belmonte, J. Bisquert, A. Zaban, and P. Salvador, Journal of Physical Chemistry B, 106 (2002) 334-339.

21. A. G. Muñoz, Electrochemical Acta, 52 (2007) 4167-4176.

22. G. K. Mor, H. E. Prakasam, O. K. Varghese, K. Shankar, and C. A. Grimes, Nano Letters 7 (2007) 2357-63.

23. E. L. Miller, R. E. Rocheleau, and S. Khan, International Journal of Hydrogen Energy, 29 (2004) 907-914.

24. E. L. Miller, D. Paluselli, B. Marsen, R. E. Rocheleau, Solar Energy Material & Solar Cells 88 (2005) 131-144.

25. K. Shankar, J. I. Bashman, N. K. Allen, O. K. Varghese, G. K. Mor, X. Feng, M. Paulose,J. A. Seabold, K. Choi, and C. A. Grimes, Journal of Physical Chemistry C 113 (2009) 6327.

26. Heli Wang, Todd Deutsch, and John A. Turner, Journal of The Electrochemical Society, 155 (2008) F91-F96.